Universitat Autònoma de Barcelona

# Development of pixel detectors for the IBL and HL-LHC ATLAS experiment upgrade

**Marta Baselga Bacardit**

CENTRE NACIONAL DE MICROELECTRÒNICA (CSIC)

PHYSICS DEPARTMENT OF THE UNIVERSITAT
AUTÒNOMA DE BARCELONA

# Development of pixel detectors for the IBL and HL-LHC ATLAS experiment upgrade

*Ph. D. Thesis in Physics of:*

Marta BASELGA BACARDIT

*Thesis director:* Dr. Giulio PELLEGRINI

*Thesis tutor:* Dr. Maria Pilar CASADO LECHUGA

12th January 2016

## Abstract

This thesis presents the development of advanced silicon technology detectors fabricated at CNM-Barcelona for High Energy Physics (HEP) experiments. The pixel size of the tracking silicon detectors for the upgrade of the HL-LHC will have to decrease in size in order to enhance the resolution in position for the measurements and they need to have better occupancy for the electronics. The future experiments at CERN will cope with fluences up to $2 \times 10^{16}\,\mathrm{n_{eq}/cm^2}$, and the smaller 3D silicon detectors will have less trapping of the electron-holes generated in the bulk leading to a better performance under high radiation environment. This thesis studies silicon detectors fabricated at CNM-Barcelona applied to HEP experiments with two different kinds of novel projects: 3D and Low Gain Avalanche Detectors (LGAD). The 3D detectors make it possible to reduce the size of the depleted region inside the detector and to work at lower voltages, whereas the LGAD detectors have an intrinsic gain which increase the collected signal with a multiplication mechanism. Chapter 1 introduces the silicon detectors applied to HEP experiments. Chapters 2 and 3 explore the new designs for 3D silicon detectors fabricated at CNM-Barcelona. 3D silicon detectors were first introduced in a HEP experiment in 2013 for a new ATLAS layer, the Insertable B layer (IBL), and some of them are characterized in this work. Now, it is expected that 3D silicon detectors with smaller pixel size will be operative for the next ATLAS upgrade, and they are also simulated in this thesis. Chapter 4 is devoted to segmented LGAD detectors fabricated on epitaxial wafer with the intention to decrease the thickness of the detector and increase the charge collected with the multiplication mechanism. This thesis shows technological simulations, fabrication process, electrical simulations and electrical and charge characterization of those devices.

# Acknowledgements

This thesis would not have been possible without (little or much) help of quite a lot of people. I will try to include all of them. If anyone feels excluded, please report it to the author.

First of all, thanks to Dr. Giulio Pellegrini for giving me the opportunity of doing the Ph. D. at CNM and for his help and guidance during the four years of thesis. Without him this work would not have been possible. Thanks to Dr. Richard Bates and Dr. Hartmut Sadrozinsky for their help during the scholarship at the University of Glasgow and at UCSC, which gave me a great opportunity to learn with them and their staff.

This research has been partially financed by Spanish Ministry of Economy and Competitiveness through grant FPA2013-48308-C2-2-P.

I did not carried out all the measurements presented in this work. Dr. Celeste Fleta, Sergi Esteban help me take the current voltage curves of IBL 3D sensors. The IFAE group helped me get some data of the IBL sensors and provided the data of their testbeam at large $\eta$ angles. Thanks to Dr. Gregor Kramberger for the measurements of the 3DSS with the $^{90}Sr$ radioactive source. I must also acknowledge Christian Gallrapp, Marcos Fernandez and Michael Moll for the TCT measurements at CERN of the sensors 3D-SS 50 µm fabricated with low resistivity wafers. They have a very good setup and did a really great job. The Diamond testbeam was carried out with the help of Dr. Dima Maneusky and Dr. Richard Bates who really help me with the setup and the measurements. The testbeam at CNA would have been impossible without the help of Dr. Javier Gracia, and the collaboration of Dr. Celeste Fleta and Sergi Esteban. And finally, thanks again to Sergi Esteban (again) for the Geant4 simulations.

A well deserved round of acknowledgements goes to all the radiation detector(s) group. Their help has proven invaluable during the performance of this thesis, such as Dr. David Quirion, Dr. Pablo Fernandez, Victor Benítez, Dr. Salvador Hidalgo, etc... A big thanks to the clean room staff for their help and great work. And a general thanks to the people at CNM for all the good moments during these 4 years.

And finally, a special thanks to my family, for obvious reasons, and to Joan and Gol·lum, for their help.

# List of publications

## Publications

[i] G. Pellegrini, **M. Baselga**, M. Carulla, V. Fadeyev, P. Fernández-Martínez, M. Fernández García, D. Flores, Z. Galloway, C. Gallrapp, S. Hidalgo, Z. Liang, A. Merlos, M. Moll, D. Quirion, H. Sadrozinski, M. Stricker, I.Vila, *Recent Technological Developments on LGAD and iLGAD Detectors for Tracking and Timing Applications*, Nuclear Instruments and Methods in Physics Research A, Article in press.

[ii] H. F.-W. Sadrozinski, A. Anker, J. Chen, V. Fadeyev, P. Freeman, Z. Galloway, B. Gruey, H. Grabas, C. John, Z. Liang, R. Losakul, S. N. Mak, C. W. Ng, A. Seiden, N. Woods, A. Zatserklyaniy, B. Baldassarri, N. Cartiglia, F. Cenna, M. Ferrero, G. Pellegrini, S. Hidalgo, **M. Baselga**, M. Carulla, P. Fernández-Martínez, D. Flores, A. Merlos, D. Quirion, M. Mikuž, G.Kramberger, V. Cindro, I. Mandić, M. Zavrtanik, *Ultra-Fast Silicon Detectors (UFSD)*, Nuclear Instruments and Methods in Physics Research A, Article in press.

[iii] **M. Baselga** on behalf of RD50 collaboration, *Radiation hard semiconductor devices for very high luminosity colliders*, Proceedings of Science, 24th International Workshop on Vertex Detectors, 2015.

[iv] N. Cartiglia, R. Arcidiacono, **M. Baselga**, R. Bellan, M. Boscardin, F. Cenna, G.F. Dalla Betta, P. Fernández-Martínez, M. Ferrero, D. Flores, Z. Galloway, V. Greco, S. Hidalgo, F. Marchetto, V. Monaco, M. Obertino, L. Pancheri, G. Paternoster, A. Picerno, G. Pellegrini, D. Quirion, F. Ravera, R. Sacchi, H.F.-W. Sadrozinski, A. Seiden, A. Solano, and N. Spencer, *Design optimization of ultra-fast silicon detectors*, Nuclear Instruments and Methods in Physics Research A, 796 (2015) 141-148.

[v] E. Cavallaro, J. Lange, I. Lopez Paz, S. Grinstein, **M. Baselga**, V. Greco, D.

---

Quirion, G. Pellegrini, *First measurements of segmented silicon tracking detectors with built-in multiplication layer*, Nuclear Instruments and Methods in Physics Research A, 796 (2015) 136-140.

[vi] C. Fleta, S. Esteban, **M. Baselga**, D. Quirion, G. Pellegrini, C. Guardiola, J. Garcia Lopez, M.C. Jimenez Ramos, F. Gomez, and M. Lozano, *3D cylindrical silicon microdosimeters: fabrication, simulation and charge collection study*, Journal of Instrumentation, Vol. 10, October 2015, P10001.

[vii] G. Kramberger, **M. Baselga**, V. Cindro, P. Fernández-Martínez, D. Flores, Z. Galloway, A. Gorisek, V. Greco, S. Hidalgo, V. Fadeyev, I. Mandic, M. Mikuž, D. Quirion, G. Pellegrini, H.F-W. Sadrozinski, A. Studen, M. Zavrtanik, *Radiation effects in Low Gain Avalanche Detectors after hadron irradiations*, Journal of Instrumentation, 10, July 2015, 07006.

[viii] G. Pellegrini, P. Fernández-Martínez, **M. Baselga**, C. Fleta, D. Flores, V. Greco, S. Hidalgo, I. Mandic, G. Kramberger, D. Quirion, M. Ullan, *Technology developments and first measurements of Low Gain Avalanche Detectors (LGAD) for high energy physics applications*, Nuclear Instruments and Methods in Physics Research A 765 (2014) 12-16.

[ix] H. F. -W. Sadrozinski, **M. Baselga**, S. Ely, V. Fadeyev, Z. Galloway, J. Ngo, C. Parker, D. Schumacher, A. Seiden, A. Zatserklyaniy, N. Cartiglia, G. Pellegrini, P. Fernández-Martínez, V. Greco, S. Hidalgo, D. Quirion, *Sensors for ultra-fast silicon detectors*, Nuclear Instruments and Methods in Physics Research A, 765 (2014) 7-11.

[x] N. Cartiglia, G. Dellacasa, S. Garbolino, F. Marchetto, G. Mazza, A. Rivetti, R. Arcidiacono, M. Obertino, V. Fadeyev, H. F-W. Sadrozinski, A. Seiden, N. Spencer, A. Zatserklyaniy, R. Bellan, F. Cenna, V. Monaco, A. Picerno, F. Ravera, R. Sacchi, A. Solano, G. Pellegrini, P. Fernández-Martínez, **M. Baselga**, V. Greco, S. Hidalgo, D. Quirion, *Timing Capabilities of Ultra-Fast Silicon Detectors*, Acta Physica Polonica B Proceedings Supplement No 4, Vol. 7 (2014) 657-664.

[xi] N. Cartiglia, **M. Baselga**, G. Dellacasa, S. Ely, V. Fadeyev, Z. Galloway, S. Garbolino, F. Marchetto, S. Martoiu, G. Mazza, J. Ngo, M. Obertino, C. Parker, A. Rivetti, D. Shumacher, H. F-W. Sadrozinski, A. Seiden, A. Zatserklyaniy, *Performance of ultra-fast silicon detectors*, Journal of Instrumentation, Vol. 9, No 2 (2014).

[xii] G. Pellegrini, **M. Baselga**, M. Christophersen, S. Ely, V. Fadeyev, C. Fleta, A.

Gimenez, S. Grinstein, I. Lopez, M. Lozano, A. Micelli, B. F. Phlips, D: Quirion, H. F-W. Sadrozinski, S. Tsiskaridze, *Recent results on 3D double sided detectors with slim edges*, Nuclear Instruments and Methods in Physics Research A 731 (2013) 198-200.

[xiii] S. Grinstein, **M. Baselga**, M. Boscardin, M. Christophersen, C. Da Via, G. Dalla Betta, G. Darbo, V. Fadeyev, C, Fleta, C. Gemme, P. Grenier, A. Jimenez, I. Lopez, A. Micelli, C. Nelist, S. Parker, G. Pellegrini, B. Phlips, D. Pohl, H. F-W. Sadrozinski, P. Sicho, S. Tsiskaridze, *Beam test studies of 3D pixel sensors irradiated non-uniformly for the ATLAS forward physics detector*, Nuclear Instruments and Methods in Physics Research A 730 (2013) 28-32.

## Oral presentations

[xiv] M. Baselga on behalf of RD50, *RD50: radiation-hard technology developments*, Proceedings of Science, VERTEX2015: The 24th International Workshop on Vertex Detectors, June 2015.

[xv] M. Baselga et al., *Measurements with strips LGAD p-type detectors fabricated at CNM-Barcelona*, 10th Trento workshop on Advanced Silicon Radiation Detectors (3D and p-type technologies), February 2015.

[xvi] M. Baselga, G. Pellegrini, D. Quirion, *New 3D fabrication at CNM-Barcelona for pixel ATLAS upgrade*, 10th Trento workshop on Advanced Silicon Radiation Detectors (3D and p-type technologies), February 2015.

[xvii] M. Baselga et al., *First measurements of new p-type strip and pad detectors with LGAD in epitaxial wafers*, 9th Trento workshop on Advanced Silicon Radiation Detectors (3D and p-type technologies), February 2014.

[xviii] M. Baselga, *First results of new p-type strip and pad detectors with LGAD in epitaxial wafers*, 23rd RD50 Workshop (CERN). November 2013.

[xix] M. Baselga, *Fabrication of new p-type pixel detectors with enhanced multiplication effect in the n-type electrodes*, 8th Trento workshop on Advanced Silicon Radiation Detectors, (3D and p-type technologies), February 2013.

# Contents

Chapter 1

# Introduction

## 1.1 High Energy Particle Detectors

In 1896 Henry Becquerel found that rays emanating certain minerals could go through paper but they were stopped on a photographic plate. It was obvious that some particles could go through matter without being noticed. Since then there has been an interest for detecting and studying those high energy particles (known as radiation).

There are different methods to detect radiation and most of them use the property that high energy charged particles ionize the atoms along their path[1]. During the first part of the 20th century the ionization chamber was widely used, but nowadays different kinds of high energy particle detectors exist, such as scintillators or Geiger detectors, all suitable for different applications. In the seventies the first semiconductor detector was developed[2]. As electronics were evolving, semiconductor radiation detectors were decreasing in size, making it possible to detect particles with a position precision of a few micrometers by using an array of small individual detectors (pixel detectors). This arrangement has proven to be the best candidate for tracking high energy particles[3].

Germanium, silicon and diamond are semiconductor materials suitable for different applications in radiation detection. Due to its small band-gap, germanium detectors should be operated at low temperatures to limit their noise, but they perform well in gamma ray measurements. Diamond, on the other hand, is a very expensive semiconductor and it has a very large band-gap (it takes more energy than the other semiconductors to create an electron-hole pair) but it tolerates high fluences of radiation, making it a good material for high radiation environments. Silicon is one of the best candidates for semiconductor detectors due to a moderate band gap, low leakage current, low noise and low cost.

In this work we study different types of silicon detectors for high energy particles developed and fabricated at CNM-Barcelona[4] in the radiation detectors group[5]: 3D columnar detectors and Low Gain Avalanche Detectors (LGAD).

### 1.1.1 High Energy Particle physics

The Standard Model in physics predicts new particles not yet observed. In order to observe them we need accelerators and colliders to create nuclear reactions, separate the most fundamental particles and interact among them. All matter is composed by elementary particles, and are responsible for strong, weak, electromagnetic and gravity forces (according to standard model). Fundamental particles are difficult to detect thus they need huge experiments so the high energy particles can leave a print and show its track, as Becquerel noticed the emanating particles with the photographic plate. Collisions at high energy between elementary particles leads to elementary interactions, allowing to observe particles that in regular conditions will never occur. The Large Hadron Collider (LHC) in the European Organization for Nuclear Research (CERN) was build to observe the most fundamental particles and corroborate their existence.

On 4th July 2012 a new particle was discover in two of the general purpose experiments in the LHC. This particle has a mass of $m_H = 125.06 \pm 0.21(stat) \pm 0.11(syst)$ GeV/c$^2$[6] and it is associated to the Higgs boson. The Higgs boson was predicted in 1964, and it is associated to the Higgs field which explains why some particles have mass.

### 1.1.2 LHC

The LHC is the biggest hadron collider ever built. It has a ring of 27 km of perimeter (4.3 km radii), built 100 m underground in Geneva, between the Swiss and French border. It contains two pipes with opposite proton beams of 7 TeV and intending to reach 13 TeV. The opposite beams meet at certain collision positions where the experiments are located, such as ATLAS, CMS, ALICE and LHCb (as shown in figure 1.1). ATLAS and CMS are general-purpose experiments. ALICE (A Large Ion Collider Experiment) is a dedicated heavy-ion detector to exploit the unique physics of nucleous-nucleous interctions. LHCb (the Large Hadron Collider beauty) experiment investigates the matter and antimatter differences, studying the quark beauty.

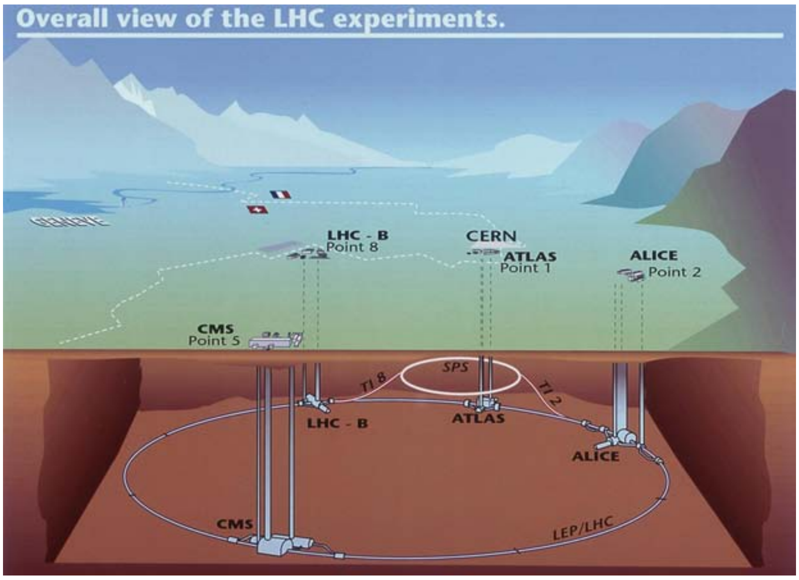

Figure 1.1: LHC experiments[7].

The protons of the beams are grouped in bunches separated by 25 ns. Each bunch has approximately 1 billion protons and in average 20 protons collide at each interaction. The experiments will detect the particles that outcome from the proton-proton collision.

The organization operating the LHC is CERN and has 21 european member states. The LHC belongs to CERN's accelerator complex.

### 1.1.3 ATLAS experiment

A Toroidal LHC ApparatuS (ATLAS) is the biggest general-purpose experiment in the LHC (see figure 1.2)[9], it aims to cover any new phenomena appearing through proton-proton interaction. It is focused on the investigation of the nature of electroweak symmetry breaking and the study of the Higgs boson. The ATLAS experiment[10] has a cylindrical shape covering the beam line. Close to the beam-line is the inner detector, consisting on tracking detectors. The inner detector is

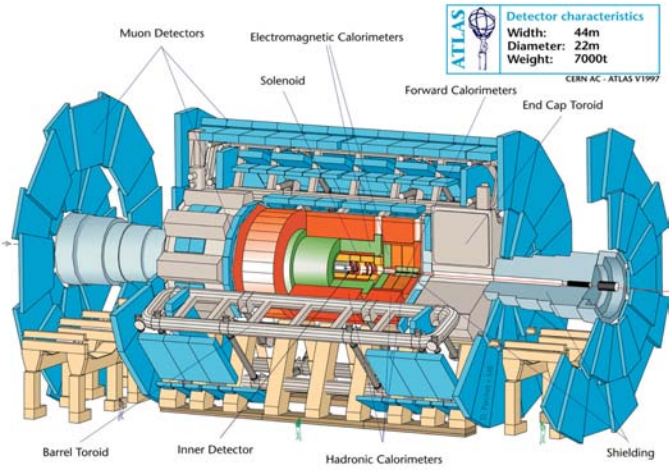

Figure 1.2: Atlas experiment in LHC. The innermost layer of detectors are the silicon detectors.

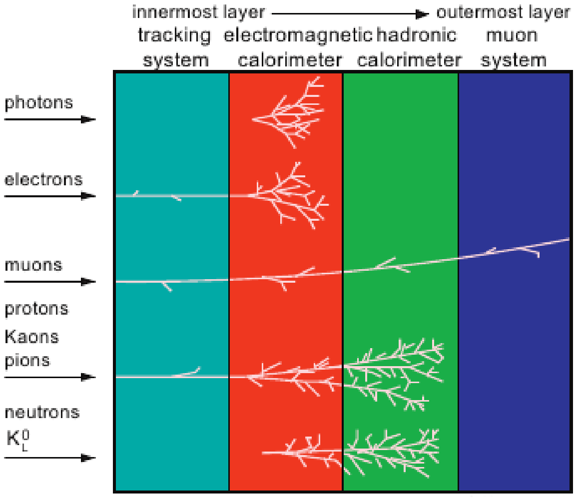

Figure 1.3: Scheme of the different layers of the ATLAS detectors and the corresponding particle they detect[8].

covered by the electromagnetic calorimeter, followed by the hadron calorimeter. Finally the muon chamber covers all the ATLAS structure. Each of those parts are meant to detect different particles (figure 1.3 shows the detectors layers of the ATLAS experiment) since each one leaves a different print[8].

The inner tracker detector has an outer radius of 1.15 m and a total length of 7 m. It is contained in a solenoid of 2 T nominal magnetic field and is composed of high resolution pixel and strip detectors. Pixel detectors are silicon detectors with very small size, the electronic currently used is 50 µm×250 µm and silicon microstrip

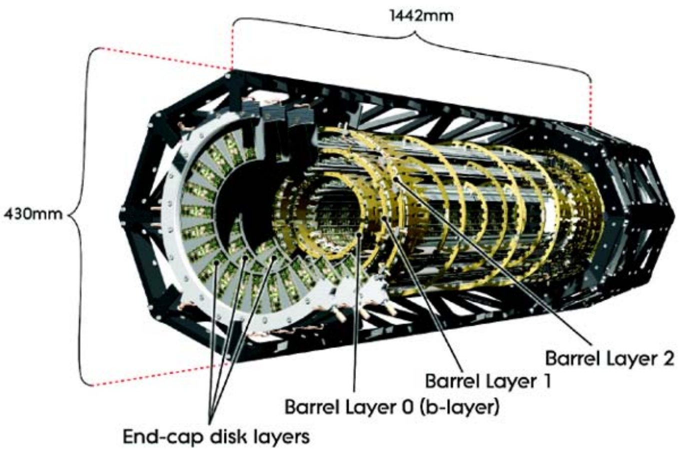

Figure 1.4: ATLAS pixel detector. The IBL is the barrel layer 0.

detectors are those with one dimension much bigger than the other (80 µm×10 mm). The pixel are in the inner part of the tracker detector and consist of about 2 m$^2$ of pixel detectors, and at an intermediate radii there is an area of 60 m$^2$ silicon strip detector called historically Semiconductor Tracker or SCT (as shown in figure 1.4). The outer radii of the Inner detector consist of 400000 straw tube drift cells, and is named the Transition Radiation Tracker or TRT.

The detectors inside the ATLAS experiment are in constant radiation exposure, damaging the silicon during operation. The inner part of the detector will receive fluences up to $2 \times 10^{16}\,\mathrm{n_{eq}/cm^2}$ in the next upgrade. RD50 is a collaboration from CERN of worldwide groups called *Radiation hard semiconductor devices for very high luminosity colliders*[11]. Their work is focused on improving radiation hardness performance of silicon detectors.

During the long shutdown 1 in 2013-2014 the IBL (Insertable B Layer) was inserted in the ATLAS Pixel Detector (see photos in figure 1.5). It consists of 14 staves covering a cylindrical shape of 3.2 cm radii inserted between the beam pipe and the pixel B-layer. IBL has silicon pixel detectors of size 50 µm × 250 µm with planar and 3D geometry[12]. 84 3D detectors were fabricated in CNM-Barcelona[4] and inserted in the IBL.

The IBL should provide better resolution in the tracker detector for the ATLAS experiment, as well as to give tracking robustness, detect at higher luminosity and receive larger radiation doses.

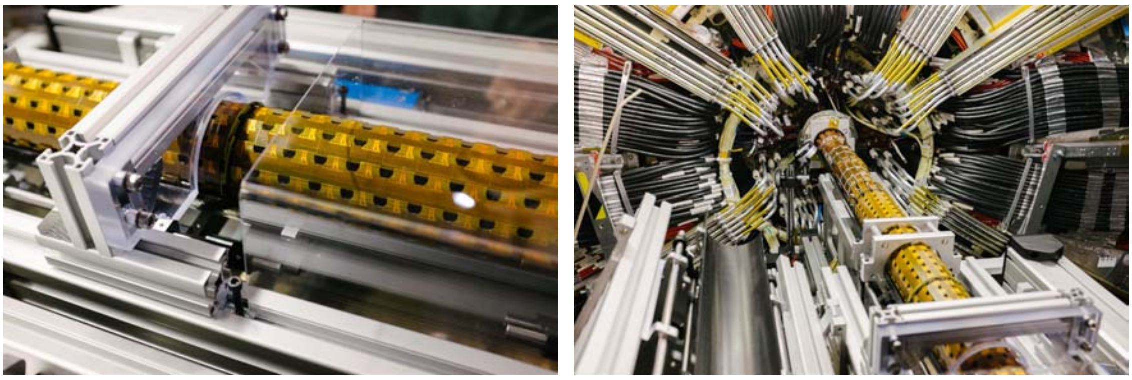

(a) Detail of the staves (b) IBL getting inside ATLAS experiment

Figure 1.5: Photos of the IBL getting inside the ATLAS experiment[13].

## 1.2 Silicon

### 1.2.1 Crystal structure

Silicon is a semiconductor with a diamond crystal structure, as shown in figure 1.6. The diamond crystal structure is based in two interpenetrating face-centered cubic (fcc) lattices.

All semiconductors have a forbidden region in the energy band structure (silicon energy bands are shown in figure 1.7). The band gap is an energy barrier that separates the conduction band and the valence band. At low temperatures all valence electrons remain bound to their atom but at higher temperatures the covalent bond may break creating a free electron and leaving a hole in the valence band. Silicon has an indirect band gap, which means that in order to move an electron from the maximum of the valence band to the minimum of the conduction band it needs to increases both its energy and momentum.

#### Intrinsic and extrinsic semiconductors

Figure 1.8 shows a 2 dimensional silicon crystal lattice sketch. In figure 1.8 a), silicon atoms share 4 electrons with the neighboring atoms forming four covalent bonds (silicon is a group IV material, with four valence electrons). Those atoms have the last atom shell with 8 electrons as a noble gas. This is the configuration for intrinsic silicon. Adding impurities with 5 valence electrons (such as phosphorus in figure 1.8 b)) one electron of the external shell of the phosphorus atom remains free and is donated to the conduction band. Those impurities are called donors and

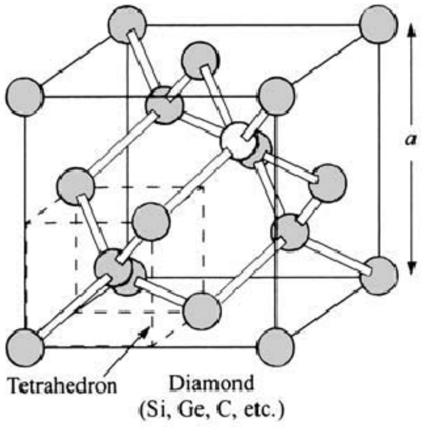

Figure 1.6: Crystal structure for silicon, diamond and germanium, (among other materials). Figure from [14].

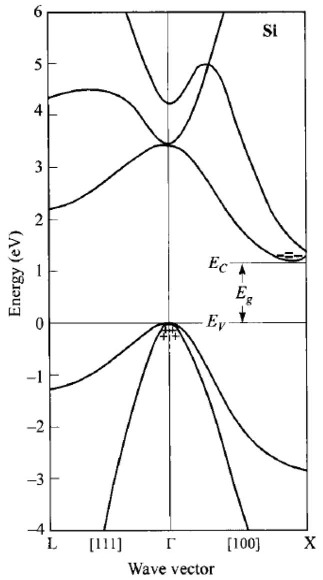

Figure 1.7: Energy band structure for Silicon, $E_g$ is the band gap. Figure from [14].

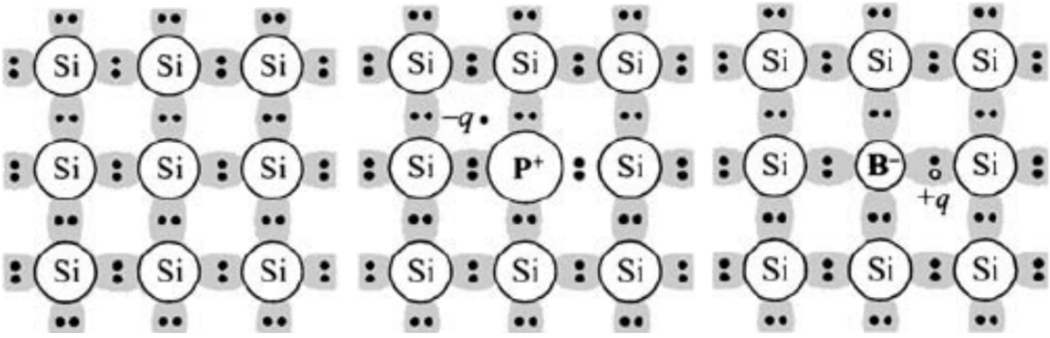

(a) intrinsic silicon (b) n-type silicon (c) p-type silicon

Figure 1.8: Silicon bonds in intrinsic and extrinsic doping.

their addition turns intrinsic silicon into n-type. On the other hand if impurities with 3 valence electrons are added (such as boron in figure 1.8 c)), there is a missing electron in the bonds and a free positive charge (or hole) will be created in the valence band. Those impurities are called acceptors and they make the original intrinsic silicon turn into p-type silicon.

An intrinsic semiconductor is one with a very low concentration impurities. In that case, the number of electrons $n$ in the conduction band and holes $p$ in the valence band is equal and it is called intrinsic concentration:

$$n_i = n = p$$

In thermal equilibrium the occupancy probability of one state at the energy $E$ and at temperature $T$ is governed by the Fermi-Dirac statistics:

$$f(E,T) = \frac{1}{e^{(E-E_F)/kT} + 1}$$

where $k$ =8.617 × $10^{-5}\,\mathrm{eV\,K^{-1}}$ is the Boltzmann's constant and $E_F$ is the Fermi level defined as the energy for exactly half of the available levels are occupied. The Fermi level changes depending on the impurities.

The density of free electrons is given by:

$$n = 2\left(\frac{2\pi m_e^* kT}{h^2}\right)^{\frac{3}{2}} \cdot e^{-\frac{E_C - E_F}{kT}} = N_C \cdot e^{-\frac{E_C - E_F}{kT}}$$

$N_C$ is the effective state density in the conduction band, $m_e^*$ is the effective mass for electrons, and $E_C$ is the minimum energy of the conduction band. The density of free holes $p$ is:

$$p = 2\left(\frac{2\pi m_h^* kT}{h^2}\right)^{\frac{3}{2}} \cdot e^{-\frac{E_F - E_V}{kT}} = N_V \cdot e^{-\frac{E_F - E_V}{kT}}$$

$N_V$ is the effective state density in the valence band, $m_h^*$ is the effective mass for holes and $E_V$ the maximum energy of the valence band. For an intrinsic material the intrinsic carrier concentration fulfills:

$$n_i^2 = n \cdot p = N_V \cdot N_C \cdot e^{\frac{-E_g}{kT}}$$

The energy gap of silicon is $E_g = E_C - E_V = 1.12eV$ at room temperature but since it has an indirect gap, silicon needs 3.6 eV to create an electron-hole pair.

### Carrier Transport in Semiconductors

In semiconductors under an external electric field the free charges are accelerated. The average drift velocity for electrons is:

$$\vec{v}_n = -\frac{q \cdot \tau_c}{m_n} \cdot \vec{E} = -\mu_n \cdot \vec{E}$$

$\mu_n$ is the mobility of the electrons, that depends on the temperature and the mean free time between two collisions $\tau_c$ and for silicon at 300 K is $\mu_n$ =1415 cm$^2$/Vs. The drift velocity for holes is:

$$\vec{v}_p = \frac{q \cdot \tau_c}{m_p} \cdot \vec{E} = \mu_p \cdot \vec{E}$$

where $\mu_p$ is the mobility of the holes for silicon and at 300 K is $\mu_p$ =480 cm$^2$/Vs[15].

The drift current for electrons per unit area can be calculated as:

$$\vec{J}_{n,\text{drift}} = -qn\mu_n\vec{E} \tag{1.1}$$

and the drift current for holes is:

$$\vec{J}_{p,\text{drift}} = qp\mu_p\vec{E} \tag{1.2}$$

A free charge in a gradient of carrier concentration will probably move from a high concentration region to a low concentration region. That random movement is called diffusion. The diffusion current for electrons is described as:

$$\vec{J}_{n,\text{diff}} = -D_n\vec{\nabla}n$$

where $D_n$ is the diffusion coefficient and is given via the Einstein equation:

$$D_n = \frac{kT}{q}\mu_n \tag{1.3}$$

where $T$ is the temperature, $q$ is the electron charge and $k$ is the Boltzmann's constant. The diffusion for holes is:

$$\vec{J}_{p,\text{diff}} = D_p\vec{\nabla}p$$

and the diffusion coefficient for holes is:

$$D_p = \frac{kT}{q}\mu_p \tag{1.4}$$

The total current density is the sum of the drift current and the diffusion current. The total current density for electrons is:

$$\vec{J}_n = q\mu_n n\vec{E} + D_n\vec{\nabla}n$$

and for holes is:

$$\vec{J}_p = q\mu_p p\vec{E} - D_p\vec{\nabla}p$$

**Resistivity**

The mobility of the electrons and holes determines how fast they can move inside the material. This allows us to define the conductivity:

$$\sigma = q(\mu_n n + \mu_p p) \tag{1.5}$$

The resistivity is defined as the inverse of the conductivity:

$$\rho = \frac{1}{\sigma} \tag{1.6}$$

The units of the resistivity are $\Omega \cdot \mathrm{cm}$. With the resistivity we can define the resistance, which is:

$$R = \rho\frac{L}{A}$$

Where $L$ is the length of the material and $A$ is its cross-sectional area. The unit of the resistance is $\Omega$.

### 1.2.2 P-N Junction

Adjoining a p-type semiconductor with a n-type one, a p-n junction or diode is created (figure 1.9 shows an scheme of a p-n junction). Electrons from the $n$ side will diffuse towards the $p$ side, leaving positively charged atoms behind. Correspondingly, holes from the $p$ side will diffuse towards the $n$ side, leaving negatively charge atoms behind. When this happens, an electric field builds up between the positive and negative atoms that opposes the diffusion. When the electric field builds up to the point where it cancels the diffusion, the system reaches thermal equilibrium with the so called build-in voltage $V_{bi}$ between the $n$ and $p$ sides of the junction. The region of the junction where electrons have diffused to the $p$ side and holes to the $n$ side is called *space-charge region* or *depleted region*. Figure 1.10 shows an sketch of the rseistivity, the electric field and the voltage within a p-n junction.

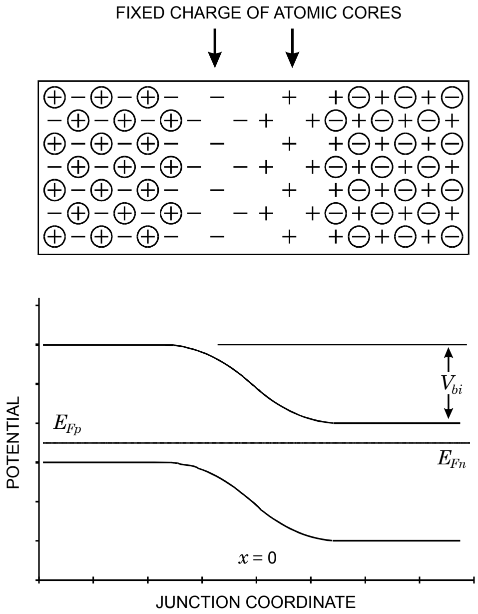

Figure 1.9: The upper figure shows the charge distribution in a pn-junction. The bottom figure shows the electric potential as a function of the position within the junction. The Fermi level remains constant but the distance to the conduction band and the valence band changes[16].

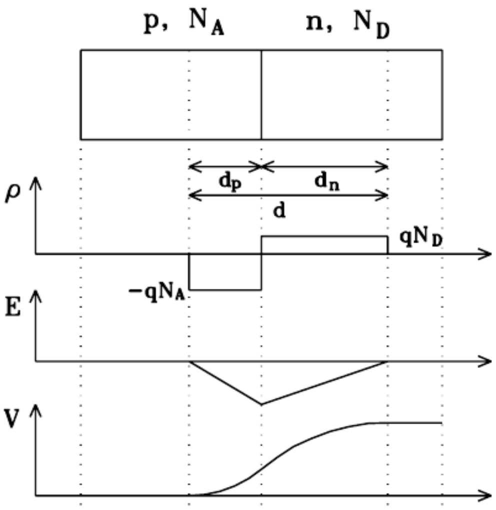

Figure 1.10: Scheme of the p-n junction charge density, electric field and voltage (figure from [17]).

When a p-n junction is in thermal equilibrium (not in electrical stress) the Fermi levels of both regions get leveled as in the bottom part of figure 1.9. The band structure deforms and surge a gradient of carriers concentration where holes from the $p$ region move to the $n$ region in order to recombine with other electrons. In both sides of the junction there are non compensated charge.

Applying a direct or reverse bias voltage the pn-junction functions in two different modes:

**Forward bias -** The applied voltage reduce the potential barrier.

**Reverse bias -** The applied voltage increase the potential barrier, increasing the depleted region of free charge.

Forward bias leads to a large current flow whereas the reverse bias leads to a small current flow and an increase of the depletion region.

Under the reverse bias $V_b$, we can describe the diffusion of the electrons with the Poisson equation:

$$\frac{d^2V}{dx^2} + \frac{Nq}{\epsilon} = 0$$

where $N$ is the dopant concentration, $q$ the electron charge and $\epsilon$ the permittivity of the medium. In silicon the permittivity is $\epsilon = \epsilon_{Si}\epsilon_0$, where $\epsilon_0$ =8.854 × $10^{-12}$ F m$^{-1}$ is the vacuum permittivity and $\epsilon_{Si} = 11.68$ is the relative permittivity of silicon at room temperature.

We can consider $x_n$ and $x_p$ the limits of the depletion region in the $n$ and $p$ sides, respectively. Integrating for the depleted region for the n-region:

$$\frac{dV}{dx} = -\frac{qN_d}{\epsilon}(x - x_n)$$

where $N_d$ is the donor concentration. Integrating again:

$$V(x) = -\frac{qN_d}{\epsilon}\frac{x^2}{2} + \frac{qN_d x x_n}{\epsilon} + V_j$$

where $V_j$ is the junction potential (the potential in the $x = 0$ in figure 1.9). Considering $V_b$ the applied reverse bias voltage, the contribution of the n-region to the total reverse bias when $x = x_n$ is:

$$V_b - V_j = \frac{qN_d x_n^2}{2\epsilon}$$

and you can solve the equation for the p-region. Considering $V_b = 0$ in the p-region, for $x = x_p$ is:

$$V_j = \frac{qN_a x_p^2}{2\epsilon}$$

and the total potential is:

$$V_b = \frac{q}{2_\epsilon}(N_d x_n^2 + N_a x_p^2) \tag{1.7}$$

Due to overall charge neutrality $N_d x_n = N_a x_p$ and we can obtain the depletion widths on the $n$ and the $p$ side of the junction:

$$x_n = \sqrt{\frac{2\epsilon V_b}{qN_d(1 + N_d/N_a)}} \qquad x_p = \sqrt{\frac{2\epsilon V_b}{qN_a(1 + N_a/N_d)}}$$

The total depletion width is

$$W = x_n + x_p = \sqrt{\frac{2\epsilon V_b}{q}\frac{N_a + N_d}{N_a N_d}}$$

The doping concentration can be expressed in terms of the resistivity using equations 1.5 and 1.6. For a material with $N_d \ll N_a$

$$W \approx x_n = \sqrt{\frac{2\epsilon V_b}{qN_d}} = \sqrt{2\epsilon\mu_n\rho_n V_b} \tag{1.8}$$

A similar expression can be reached if $N_a \ll N_d$:

$$W \approx x_p = \sqrt{\frac{2\epsilon V_b}{qN_a}} = \sqrt{2\epsilon\mu_p\rho_p V_b} \tag{1.9}$$

### Breakdown voltage

A reversely biased diode might have electrons with high kinetic energy that can break the lattice bonds and create new electron-hole pairs. The new electron-hole pair can again reach high velocity and generate new electron-hole pairs, in a multiplication mechanism as depicted in figure 1.11. This normally happens in silicon for electric fields higher than $3 \times 10^5\,\mathrm{V\,cm^{-1}}$. This process can irreversibly damage the diodes. For that reason it is important not to reach those electric fields.

But if the multiplication mechanism is controlled, not leading to an early break down it can lead to an avalanche mechanism[16].

Moderate gain APD's are used for high energy particle detection. Intrinsic gain helps to amplify the signal before it reaches the readout electronics. The detectors

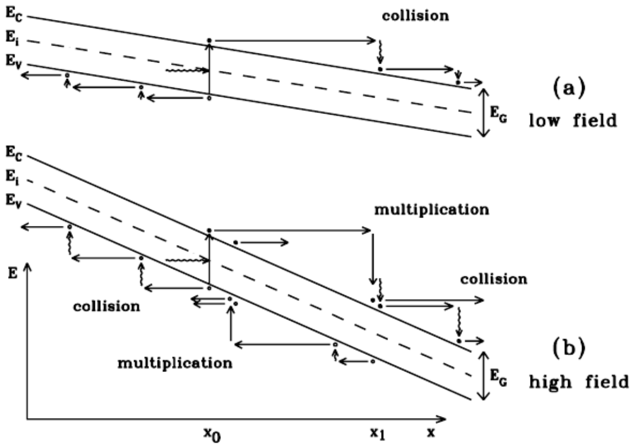

Figure 1.11: Multiplication scheme under high field[17].

that use that mechanism are known as Low Gain Avalanche Detectors (LGAD)[18]. A moderate gain (G=10∼20) is preferred in some applications because amplification also affects the noise[19]. Chapter 4 is devoted to strips, pixel and pad LGAD.

### Leakage current

A reversely biased pn-junction increases the width of the depleted region in the silicon and reduces the diffusion current.

The current-voltage behavior for an ideal diode is:

$$I = I_S(e^{\frac{qV}{k_BT}} - 1) \tag{1.10}$$

where

$$I_S = \frac{qD_p p_{n0}}{L_p} + \frac{qD_n n_{p0}}{L_n}$$

where $D_p$ the diffusion coefficient of holes and $D_n$ the diffusion coefficient of electron (given by equations 1.3 and 1.4). $p_{n0}$ is the density of holes in the $n$ region and $n_{p0}$ is the density of electrons in the $p$ region in thermal equilibrium, $L_p = \sqrt{D_p \tau_{rp}}$ is the diffusion length for holes and $L_n = \sqrt{D_n \tau_{rn}}$ is the diffusion length for electrons. $\tau_{rp}$ is the recombination time for holes and $\tau_{rn}$ is the recombination time for electrons. According to equation 1.10, for a forward bias ($V > 0$) the current increase exponentially and in reverse bias ($V < 0$) the current saturates at $I_S$. The generation and recombination process is not taken into account.

Free charge carriers are also thermally generated, contributing to a leakage current in addition to the ideal current of equation 1.10. They are created due to silicon defects introduced during the fabrication process. This generation is described by the Shockley-Read-Hall model for indirect semiconductors[20; 21] and it strongly depends on the temperature.

### Capacitance

The p-n junction stores some charge in the bulk like a capacitor. The capacitance of a parallel plate silicon capacitor is defined as:

$$C = \epsilon_0 \epsilon_{Si} \frac{A}{d} \approx 1[pF/cm] \frac{A}{d} \tag{1.11}$$

Being $A$ the area of the capacitor and $d$ the width of the capacitor. Using the width $W$ of the depleted region calculated in equation 1.9:

$$\frac{C}{A} = \frac{\epsilon_0 \epsilon_{Si}}{W} = \sqrt{\frac{q \epsilon_0 \epsilon_{Si} |N_{eff}|}{2(V_{bi} + V)}}$$

or

$$\frac{A^2}{C^2} = \frac{2(V_{bi} + V)}{q \epsilon_0 \epsilon_{Si} |N_{eff}|} \tag{1.12}$$

From a plot of $\frac{1}{C^2}$ versus $V$ information of the p-n junction can be extracted such as the effective doping concentration $|N_{eff}|$ and the full depletion voltage ($V_{FD}$):

$$|N_{eff}| = \frac{2 \epsilon_0 \epsilon_{Si}}{q d^2} V_{FD}$$

For a non depleted p-type pad sensor, the doping profile can be extracted from equation 1.12 with a $1/C^2$-voltage:

$$|N_{eff}| = \frac{2}{\frac{d(1/C^2)}{dV}} \frac{1}{q \epsilon_0 \epsilon_{Si} A^2} \tag{1.13}$$

Where $A$ is the area of the sensor and $\epsilon_0$ is the vacuum permittivity constant and $\epsilon_{Si}$ is the relative permittivity of the silicon.

## 1.3 Radiation-Matter Interaction

Charge generation inside a semiconductor may appear by thermal agitation, optical excitation and ionization by penetrating charged particles[1; 22].

At room temperature electrons may be excited directly from the valence band to the conduction band, thermally generating electron-hole pairs. This is true for semiconductors with very low band-gap such as germanium but for silicon the probability is very low. In this work we want to study the electron-hole generation mechanism through radiation-silicon interaction, such as electromagnetic generation or by charged particles.

### 1.3.1 Electromagnetic radiation

Electromagnetic generation happens when a photon generates an electron-hole pair. Depending on the energy, photons interact with matter differently. For low energy photons, the most probable interaction mechanism is the photoelectric effect. For moderate energies the most probable effect is the Compton scattering, and for high energies the photon will probably create an electron-positron pair. Figure 1.12 shows a scheme of the three electromagnetic generation mechanisms.

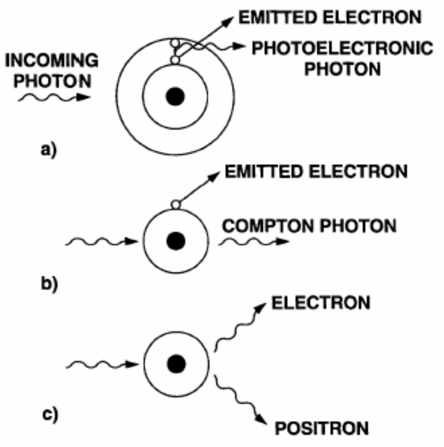

Figure 1.12: Scheme of the electromagnetic interaction, a) shows the photoelectric effect, b) the Compton scattering and c) the pair production.

### Photoelectric effect

When a photon impinges a material with a moderate energy the photon may interact with an electron in such a way that the electron is promoted to a higher energy state. This phenomena is called the photoelectric effect. The photoelectric effect is the most probable interaction mechanism for photons with energies of a few electron volts to some keV.

The energy absorbed by the electron is:

$$E_e = h\nu - E_b$$

where $E_e$ is the energy of the electron, $h = 4.136 \times 10^{-15}\,\mathrm{eV\,s}$ is Planck's constant, $\nu$ is the frequency of the electron and $E_b$ is the binding energy of the photoelectron in its original shell.

### Compton scattering

In the Compton scattering, the incoming photon is deflected by an angle $\theta$ while it scatters an electron of the target material. The outcome is a deflected photon and a recoiling electron. The relation between the outgoing electron energy and the deflection angle is:

$$h\nu' = \frac{h\nu}{1 + \frac{h\nu}{m_0 c^2}\left(1 + \cos\theta\right)}$$

where $h\nu'$ is the outgoing electron energy, $m_0 c^2 = 0.511\,\mathrm{MeV}$ is the electron rest mass and $h$ is Planck's constant. It happens with more probability with photons of energy between a few keV to 1 MeV.

### Pair production

If a photon has an energy higher than the rest-mass energy of two electrons (1.02 MeV) the most probable process to happen is pair production. The energy of the photon is used to generate an electron-positron pair. It normally occurs when the photon is near a nucleus since it helps to preserve the momentum.

### Different absorption of light through silicon

Depending on the energy (or wavelength $\lambda$ since they are related with $E = hc/\lambda$) of the photons impinging silicon, it will respond differently.

According to Beer-Lambert's law the attenuation of a light beam inside a material is given by the relation:

$$I(x) = I_0 e^{\alpha x} \tag{1.14}$$

$I(x)$ is the intensity at any given point of the beam, $I_0$ is the initial intensity, $\alpha$ is the absorption coefficient and $x$ is the position inside the material. The absorption coefficient for the silicon as a function of the wavelength is presented in figure 1.13 in the optical range.

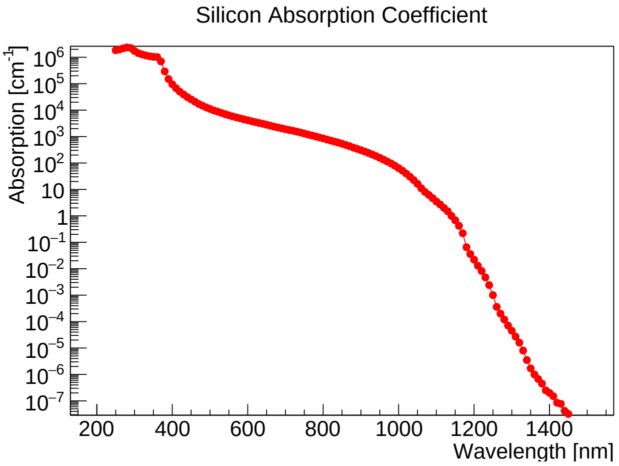

Figure 1.13: Light absorption coefficient of the silicon in the optical range for cm$^{-1}$ [23].

From figure 1.13 we note that for long wavelengths the absorption coefficient of silicon is very low, thus the light may go through all silicon, whereas for shorter wavelengths (more energetic light) most photons are absorbed within a few microns.

## 1.3.2 Charged particles

Charged particles traversing any material lose some energy through coulumbian or nuclear interaction. The charged particles interact with electrons, exciting the electrons or ionizing them. Thus the charged particles will create electron-hole pairs along their path. The mean rate of energy loss by moderately relativistic charged heavy particles is described by the Bethe equation[15; 24]:

$$-\langle\frac{dE}{dx}\rangle = Kz^2\frac{Z}{A}\frac{1}{\beta^2}\left[\frac{1}{2}ln\frac{2m_ec^2\beta^2\gamma^2T_{max}}{I^2}-\beta^2-\frac{\delta(\beta\gamma)}{2}\right]$$

$\frac{dE}{dx}$ gives the energy loss of the particle

$K = 4\pi N_{Av}r_e^2m_ec^2$ =0.307 075 MeVcm$^2$

$z$ charge of he traversing particle in units of the electron charge

$Z$ atomic number of the absorbing medium (14 for silicon)

$A$ atomic mass of the absorbing medium (28 for silicon)

$m_ec^2$ is the energy of the electron at rest 0.511 MeV

$\beta$ velocity of the particle in units of the speed of light

$\gamma$ Lorentz factor $1/\sqrt{1-\beta^2}$

$I$ mean excitation energy (137 eV for silicon)

And $T_{max}$ is the maximum kinetic energy which can be transferred to an electron by a particle of mass $M$:

$$T_{max} = \frac{2m_ec^2\beta^2\gamma^2}{1+2\gamma m_e/M+(m_e/M)}$$

The Bethe formula describes the mean rate of energy loss in the region $0.1 < \beta\gamma < 1000$ for intermediate-Z materials quite accurately. Figure 1.14 presents the stopping power against the muon momentum on copper. The curve is separated by different regions such as Linhard-Scharff, Anderson-Ziegler, Bethe and Radiative region and those regions depends on the energy of the incident particle. In the Bethe region is the minimum ionization point. Particles whose mean energy loss through matter is close to the minimum are defined Minimum Ionizing Particles (MIP).

Figure 1.15 presents the number of electron-hole pairs generated by muons and protons in silicon as a function of the kinetic energy.

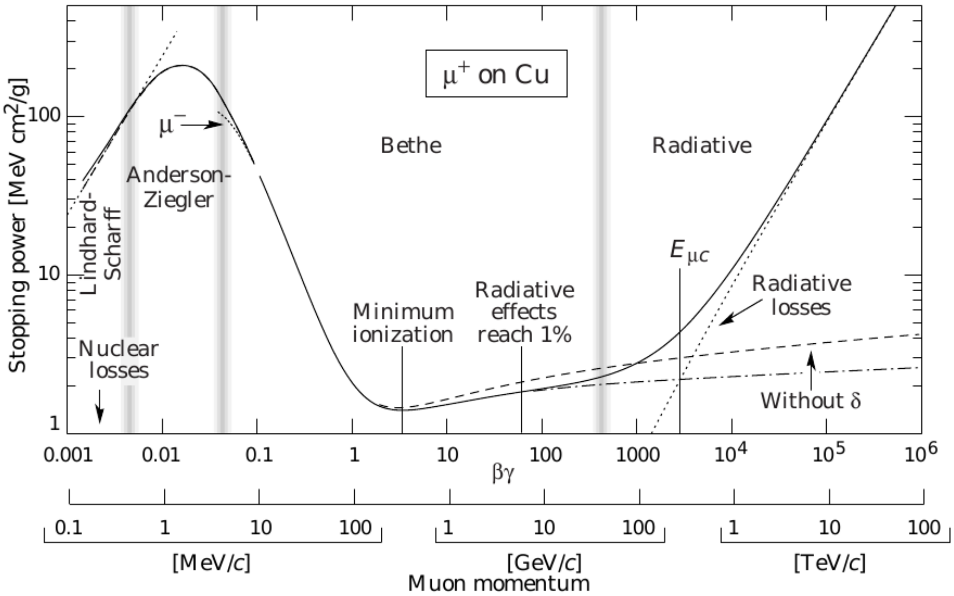

Figure 1.14: Stopping power for muons on copper (figure from [24]).

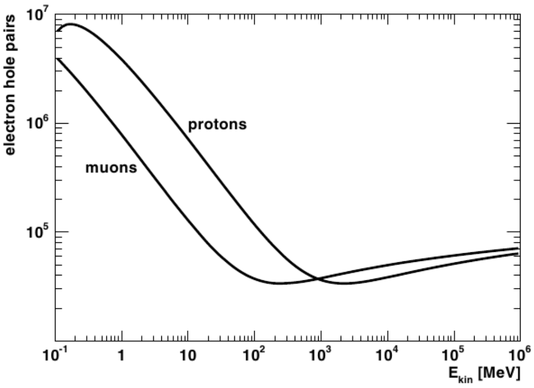

Figure 1.15: Number of electron-hole pairs generated by muons and protons in 300-µm thick silicon[15] as a function of the kinetic energy.

## 1.4 Silicon detectors

Silicon detectors operate as a reversely biased diode[25]. Regarding the substrate, we distinguish between n-type and p-type detectors, for detectors with $n$ doped and $p$ doped substrates, respectively.

Since the electrode of the detector can also be n-doped or p-doped, we have four possible combinations of substrate and electrode doping, as shown on table 1.1.

p-on-p and n-on-n typically correspond to a 2 sided process of fabrication, mean-

|  | Substrate |  |
|---|---|---|
| Electrode | p-type | n-type |
| p-electrode | p-on-p | p-on-n |
| n-electrode | n-on-p | n-on-n |

Table 1.1: The four different kinds of detectors according to the wafer substrate doping and the electrode doping.

ing that the fabrication steps have to be performed in the front and back side of the wafer and align them. Two sided fabrication processes normally are more expensive than a single sided process (as the p-on-n and n-on-p process) since more masks are needed.

### 1.4.1 Geometries

High energy particle tracking detectors are typically fabricated in two different layouts: microstrip and pixel. Microstrip detectors have one of their dimensions much larger than the other (e.g. 10 mm × 80 µm). Figure 1.16 (a) shows the mask of a strip detector and 1.16 (b) shows a photo of a strip taken with an optical microscope. They yield a very good 1 dimensional position. Positioning two of them together with some misalignment angle gives a very precise 2D position of the particle. They need one connexion readout for each strip.

Pixel detectors are small diodes with a pixel cell of some microns, normally they are embedded in a bigger detector. Figure 1.17 (a) shows the mask of a pixel detector and 1.17 (b) shows a picture of a FE-I3 pixel. Since they are very small they give good two dimensional position precision, but they need to be individually bonded to the electronic through bumps.

Microstrip and pixel detectors can be fabricated as planar detectors (implanting the surface of the wafer) or 3D detectors (etching a column that almost reach both sides of the wafer and filling it with doped polysilicon):

#### Planar sensors

Planar detectors are fabricated with their two electrodes in each side of the wafer. The main bulk of the wafer remains intrinsic silicon (see left part of figure 1.18). Depending on the thickness of the wafer the detector has a different volume to deplete.

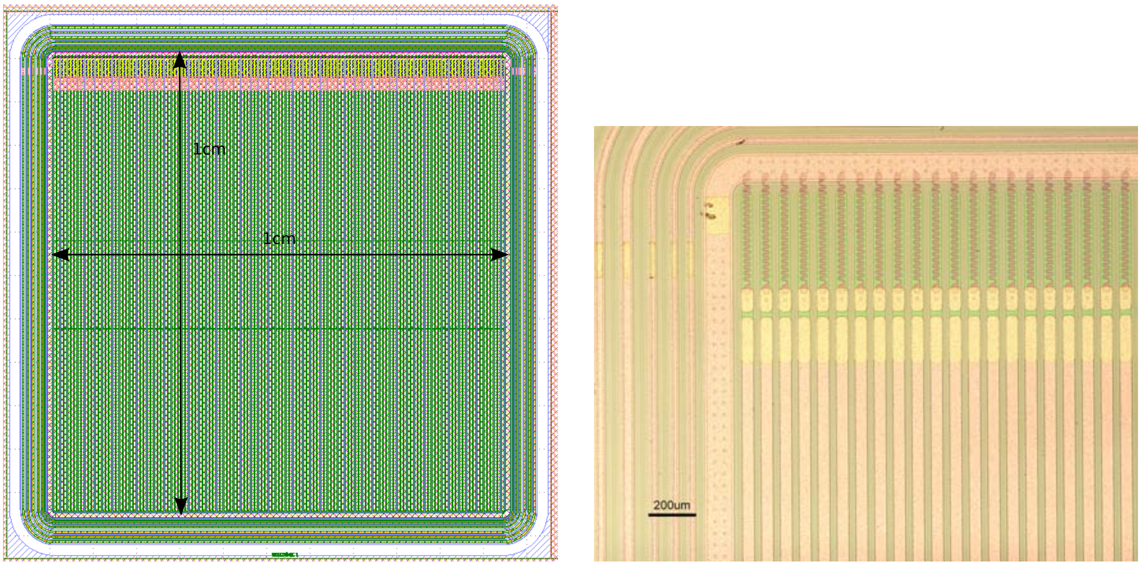

(a) Mask of strip detector. The strips take all the vertical length. There are 130 strips embedded in the total detector area.

(b) Photo that shows a detail of a strip detector.

Figure 1.16: Strip mask (a) and strip photo (b).

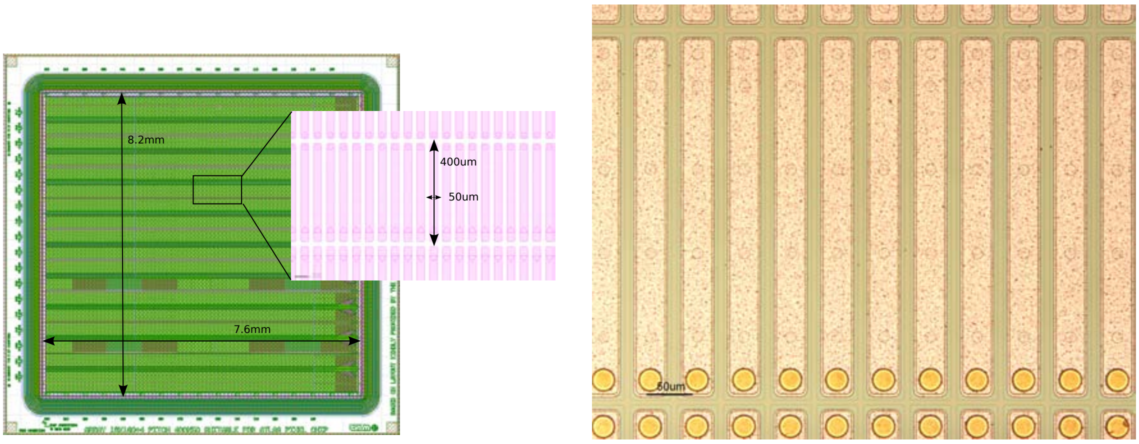

(a) Mask of a pixel detector. It is a FE-I3 pixel detector.

(b) Photo of a FE-I3 pixel detector.

Figure 1.17: Pixel mask (a) and pixel photo (b).

The photos taken in figure 1.16 and 1.17 belong to planar detectors.

### 3D sensors

Columnar implants were proposed to fabricate a new kind of silicon detectors, called 3D sensors[27; 28] where the electrodes are laterally separated instead of vertically

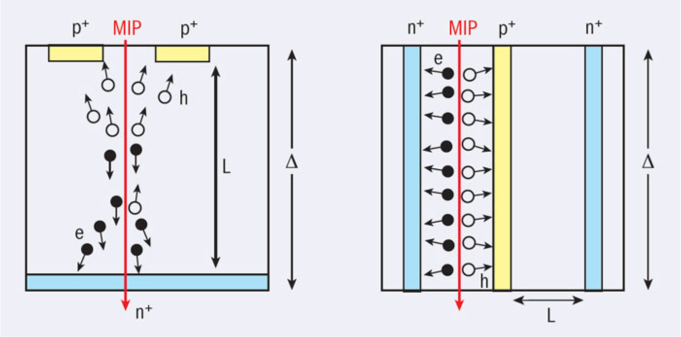

Figure 1.18: Cross section of a planar strip sensor (left) and a 3D sensor (right)[26].

(figure 1.18 right). The silicon is etched with a Deep Reactive Ion Etching (DRIE) technique and the column is filled with doped polysilicon. The volume to deplete is the volume between columns. Since the volume between columns is typically smaller than the thickness of the wafer 3D detectors needs less bias voltage to deplete all its volume.

### 1.4.2 Collected charge

When a charged particle crosses the detector, it creates a track of electron-hole pairs inside the depleted silicon bulk. If a total amount of energy $E$ is absorbed in the detector from incoming high energy particles, the number of electron-hole pairs for silicon is given by:

$$N = \frac{E}{3.6eV}$$

where 3.6 eV is the average energy to create an electron-hole pair in silicon.

### 1.4.3 Ramo's theorem

Simon Ramo[29] showed that the instantaneous current received by a given electrode due to a mobile charge motion is equal to:

$$i = \vec{E}_v q \vec{v}$$

where $q$ is the charge, $\vec{v}$ is the instantaneous velocity and $\vec{E}_v$ is the field component in the direction $\vec{v}$ and is called weighting field. The induced charge on the electrode is given by:

$$Q = q\Delta\varphi_0$$

where $q$ is the charge of the carrier, and $\Delta\varphi_0$ is the difference in the weighting potential. To find the weighting potential one must solve the Laplace equation:

$$\nabla^2\varphi = 0$$

for the geometry of the detector with the conditions:

1. The chosen electrode voltage is set to 1V.
2. The other electrodes are set to 0V.
3. The trapping state of the charge (trapped, untrapped) is not taken into account.

## 1.5 Radiation Damage

One of the main problems of silicon detectors is that when they are exposed to high fluences of radiation and suffer microscopic degradation in the crystal lattice[30]. It leads to a degradation of the performance of the detector. In 2013 the LHC is supposed to reach an integrated luminosity of $3000\,\mathrm{fb}^{-1}$, and the detectors will receive fluences up to $2 \times 10^{16}\,\mathrm{n_{eq}/cm^2}$. The received fluence of the detectors of the ATLAS inner tracker versus the distance of the beamline is presented in figure 1.19.

### 1.5.1 Microscopic effects

The damage produced by high energy particles to the silicon detectors can be[32]:

1. Bulk damage. Displacement of the silicon atoms.
2. Surface damage: Ionization of the isolating layers such as $SiO_2$.

#### Bulk damage

Charged or non charged particles impinging into a crystallographic lattice at high energy may displace atoms in the crystal. That effect does not depend on the kind

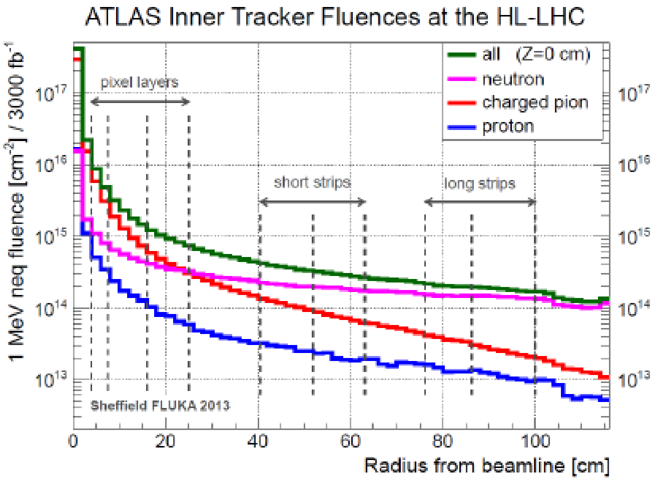

Figure 1.19: Simulation of the received fluence for the tracker detectors depending on the distance of the beamline[31].

of particles but on its energy. The particles interact with the atoms via the electromagnetic and strong forces. They create interstitials, di-interstitials, vacancies, di-vacancies or even triple-vacancies (some of those atomic displacements are depicted in figure 1.20). An extensive list of the defects can be found in [17; 30; 33; 34]. If the energy is higher than 25 eV (called the displacement energy) they create single Frenkel defects, since 25 eV is the energy at which the displacement probability is one half. The recoil atom can create new atom displacements if the energy is high enough. After a heavy recoil it can create clusters of defects in the lattice as simulated in figure 1.21. The approximate energy for creating a defect cluster is 5 keV. Depending on the energy and the particle the cluster defects layout may change[35]. The bulk damage is the main damage effect of the radiation[36].

In order to neutralize the dependence on the type of radiation and its energy a scaling quantity called Non-Ionizing Energy Loss (NIEL) is created (figure 1.22) which shows the damage normalized to 1 MeV neutrons.

### Surface damage

Surface damage is due to electron-hole pairs created in the insulator layers, in this case the $SiO_2$. The electrons are fast collected in the electrode whereas the holes stay as a positive charge in the oxide because of their lower mobility. That leads to a flat band displacement and increases the charge in the oxide till it saturates around $Q_{ox} = 3 \cdot 10^{12} cm^{-2}$. Surface damage depends on the kind of radiation since

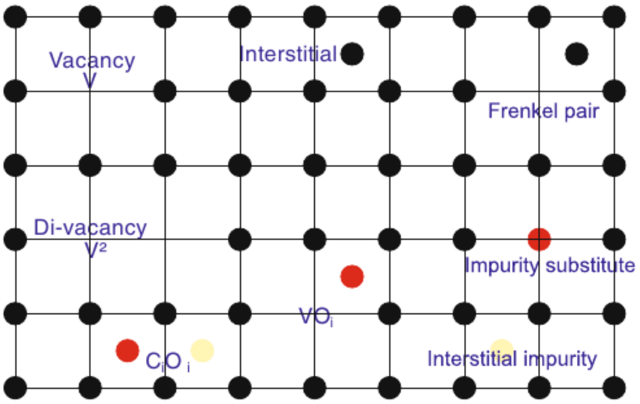

Figure 1.20: Scheme of the silicon crystal lattice with vacancies, di-vacancies, interstitial, frenkel pair, and other possible radiation damage to the silicon[37].

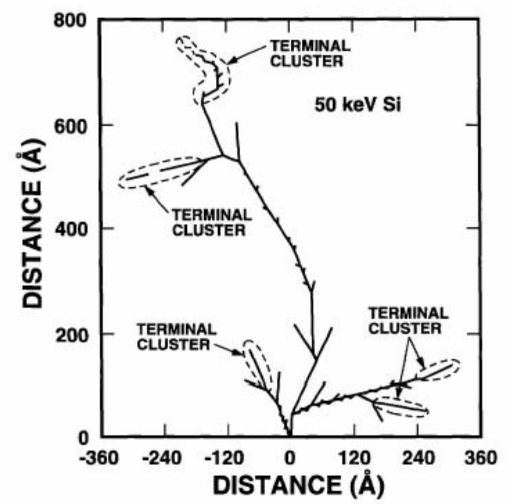

Figure 1.21: Simulation of a cluster damage from a recoil of an atom with an energy of 50 keV (figure from [38]).

electron-hole pairs are created by charged particles or photons.

### 1.5.2 Macroscopic effects

High energy particles generate defects in the crystalline lattice creating new states within the band-gap[30]. The consequences of those defects are the increment of the full depletion voltage, the increment of the leakage current, degradation of the charge collection efficiency and the shift of the effective doping profile of the detector. Those defects depend on the time of the irradiation and on the fluence.

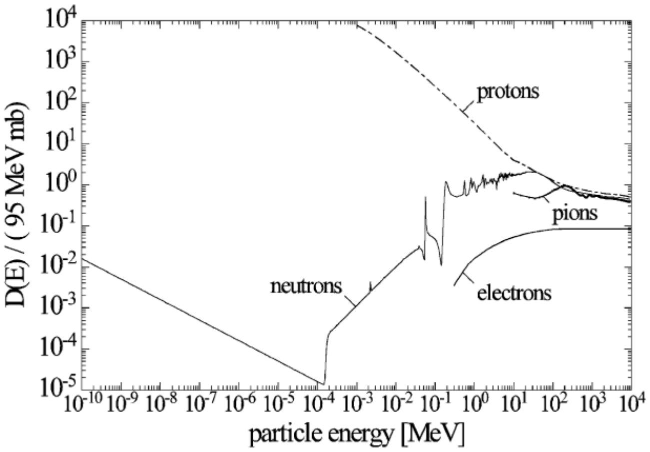

Figure 1.22: Displacement damage functions $D(E)$ versus the energy. The damage is equivalent to 1 MeV of neutrons[39].

For a n-type detector, radiation creates acceptor defects. For low fluences it decreases the full depletion voltage but after fluences around $2 \times 10^{12}\,\mathrm{n_{eq}/cm^2}$ the substrate inverts and becomes p-type (as in figure 1.23). p-type detectors do not invert and they show a higher charge collection after irradiation (in figure 1.24 is an example of charge collection for strips of p-type and n-type wafers)[40]. n-on-p detectors collect electrons which they are faster, they can multiply and they are less probable to be trapped. Currently, n-on-p detectors are the baseline for RD50 collaboration as for strip upgrades of ATLAS and CMS experiments[41].

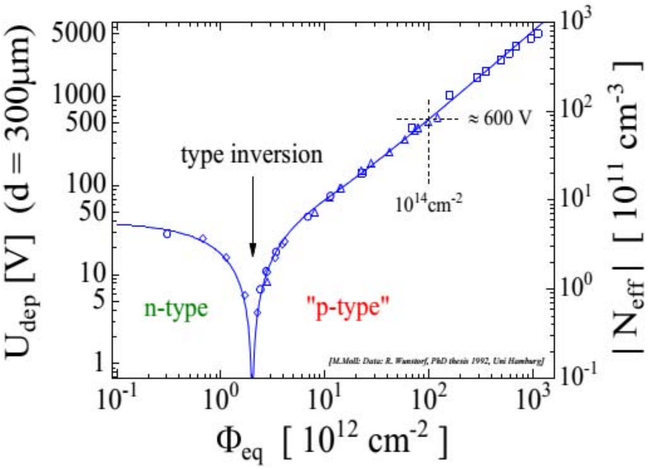

Figure 1.23: Full depletion voltage against fluence for a n-type detector[42].

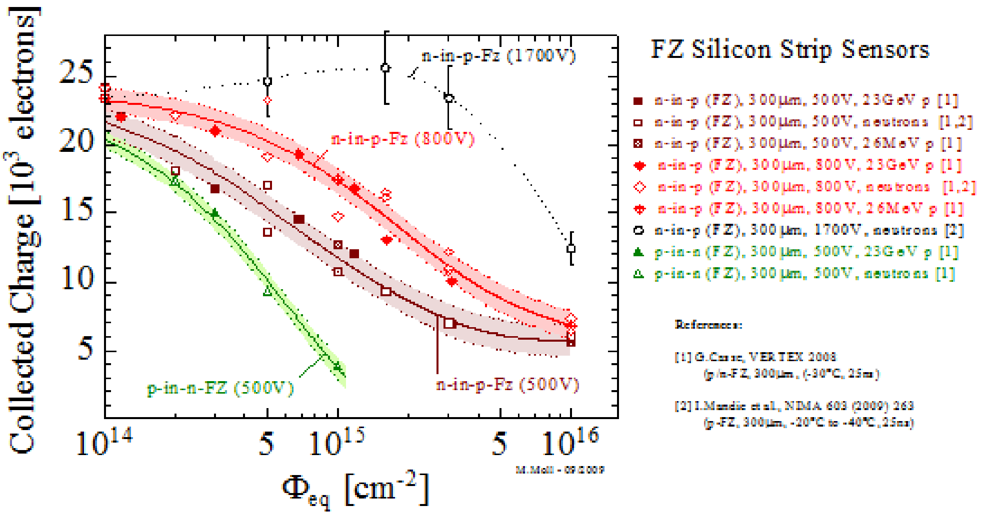

Figure 1.24: Collected charge after irradiation for p-type and n-type strip detectors.

The generation of traps within the detector increases the reverse leakage current. Thus the leakage current is directly proportional to the fluence as:

$$\Delta I/V = \alpha \cdot \Phi$$

where $\Delta I$ is the increment of the current, $\Phi$ is the fluence, $\alpha$ is the current-related damage rate and $V$ is the active volume of the detector.

The radiation diminish the collected charge since the electron-hole pairs created by the particles are easy to recombine with the traps inside the damaged detector. But as shown in figure 1.24, since radiation increases the electric field it can lead to a multiplication mechanism and have more charge collected.

After irradiation, the increase of trapping, leakage current and effective doping change diminishes with time, as with the temperature, nevertheless it is shown that the defects might induce a charge multiplication mechanism due to high electric fields, as shown in [40; 43; 44]. The disappearance of radiation-damage evidence through defects is called *annealing*[45], and it will make decrease the deffects H116(-/0), H140(-/0) and H152(-/0)[46].

## 1.6 TCAD Simulation

One of the powerful tools for designing silicon detectors is a TCAD (Technology Computer Aided Design) simulator. In this thesis the TCAD simulator used is Synopsys TCAD Sentaurus toolkit[47]. The simulations use some models defined for the TCAD simulator which adjust better to the detectors fabricated at CNM-Barcelona[33].

For a simulation first a simple single pixel cell with Sentaurus Structure Editor is created, and with Sentaurus Device a potential voltage is applied between the two electrodes. The simulator proceeds to solve the Poisson equation in the structure[48][49].

Synopsys TCAD Sentaurus has several models to choose for each physical parameter of the device being simulated, such as the mobility of the free carriers or recombination. Choosing the models that better describe the real system goes a long way towards getting good results from the simulations. In the following sections the TCAD models for the electrical simulations used in this work will be explained.

### 1.6.1 Mobility

The electrical simulations use several mobility models. Mobility models for the simulations are combined with the Mathiessen's rule:

$$\frac{1}{\mu} = \frac{1}{\mu_1} + \frac{1}{\mu_2} + \dots \tag{1.15}$$

where $\mu$ is the total mobility and $\mu_1$, $\mu_2$ ... are the different contributions such as doping dependence, enhanced Lombardi, high field saturation or carrier-carrier scattering.

#### Doping dependence

For doped semiconductors, scattering of the carriers by charged impurity ions leads to degradation of the carrier mobility. For this reason the simulations use a doping dependent mobility that adjust better to the reality of the semiconductor physics. For silicon it is the Masetti model[50]:

$$\mu_{dop} = \mu_{min1} e^{\left(-\frac{P_c}{N_{A,0}+N_{D,0}}\right)} + \frac{\mu_{const} - \mu_{min2}}{1 + (\frac{N_{A,0}+N_{D,0}}{C_r})^{\alpha}} - \frac{\mu_1}{1 + (\frac{C_s}{N_{A,0}+N_{D,0}})^{\beta}}$$

With the parameter values detailed in table 1.2.

| | Electrons | Holes |
|---|---|---|
| $\mu_{min1}$ | $52.2\,\mathrm{cm^2/Vs}$ | $44.9\,\mathrm{cm^2/Vs}$ |
| $\mu_{min2}$ | $52.2\,\mathrm{cm^2/Vs}$ | |
| $\mu_1$ | $43.4\,\mathrm{cm^2/Vs}$ | $29\,\mathrm{cm^2/Vs}$ |
| $P_c$ | | $9.26 \times 10^{16}\,\mathrm{cm^{-3}}$ |
| $C_r$ | $9.68 \times 10^{16}\,\mathrm{cm^{-3}}$ | $2.23 \times 10^{17}\,\mathrm{cm^{-3}}$ |
| $C_s$ | $3.43 \times 10^{20}\,\mathrm{cm^{-3}}$ | $6.10 \times 10^{20}\,\mathrm{cm^{-3}}$ |
| $\alpha$ | 0.68 | 0.719 |
| $\beta$ | 2 | 2 |

Table 1.2: Parameters for the Masetti model.

$\mu_{const}$ is given by the constant mobility model that accounts for phonon scattering:

$$\mu_{const} = \mu_L \left(\frac{T}{300K}\right)^{-\zeta}$$

where $T$ is the temperature, $\mu_L$ is the mobility due to bulk phonon scattering and $\mu_L$ =1417 $\mathrm{cm^2/Vs}$ for electrons and $\mu_L$ =470.5 $\mathrm{cm^2/Vs}$ for holes. For electrons $\zeta = 2.5$ and for holes $\zeta = 2.2$.

### Enhanced Lombardi model

The semiconductor mobility decreases at the interfaces because carriers are subjected to scattering by acoustic surface phonons and surface roughness. The mobility model used to take into account that effect is the enhanced Lombardi model, with a surface contribution due to acoustic phonon scattering:

$$\mu_{ac} = \frac{B}{F_\perp} + \frac{C((N_{A,0} + N_{D,0} + N_2)/N_0)^\lambda}{F_\perp^{1/3}(T/300K)^k}$$

And the contribution due to surface roughness scattering is given by:

$$\mu_{sr} = \left(\frac{(F_\perp/F_{ref})^2}{\delta} + \frac{F_\perp^3}{\eta}\right)^{-1}$$

With the coefficients given in table 1.3.

| | Electrons | Holes |
|---|---|---|
| $B$ | $4.75 \times 10^{7}\,\mathrm{cm\,s^{-1}}$ | $9.925 \times 10^{6}\,\mathrm{cm\,s^{-1}}$ |
| $C$ | $5.80 \times 10^{2}\,\mathrm{cm^{5/3}}\ /\mathrm{V^{2/3}s}$ | $2.947 \times 10^{3}\,\mathrm{cm^{5/3}}\ /\mathrm{V^{2/3}s}$ |
| $N_0 = N_2$ | $1\,\mathrm{cm^{-3}}$ | $1\,\mathrm{cm^{-3}}$ |
| $\lambda$ | 0.1250 | 0.0317 |
| $k$ | 1 | 1 |
| $\delta$ | $5.85 \times 10^{14}\,\mathrm{cm^2/Vs}$ | $2.0546 \times 10^{14}\,\mathrm{cm^2/Vs}$ |
| $A$ | 2 | 2 |
| $\eta$ | $5.85 \times 10^{30}\,\mathrm{V^2/cms}$ | $2.0546 \times 10^{30}\,\mathrm{V^2/cms}$ |

Table 1.3: Lombardi model coefficients for silicon.

Those mobilities are contributing to the total mobility through Mathiessen's rule (equation 1.15). The reference field is $F_{ref}$ =1 V cm$^{-1}$ and $F_{\perp}$ is the transverse electric field. $D$ is a damping parameter that switches off the inversion layer and is given by $D = exp(-x/l_{crit})$, where $x$ is the distance from the interface and $l_{crit} = 1 \times 10^{-6}$ cm is a fitting parameter for silicon.

### High Field Saturation

For high electric fields the mobility saturates. In order to account for that effect the Canali model is used. For high electric fields the velocity saturates at a value $v_{sat}$. The Canali model depends on $v_{sat}$:

$$\mu(F) = \frac{\mu_{low}}{\left[1 + \left(\frac{\mu_{low}F}{\nu_{sat}}\right)^{\beta}\right]^{1/\beta}} \tag{1.16}$$

where $\mu_{low}$ is the low field mobility and $\beta$ is:

$$\beta = \beta_0 \left(\frac{T}{300K}\right)^{\beta_{exp}}$$

where T is the temperature of the lattice. The other parameters are described in table 1.4.

| | Electrons | Holes |
|---|---|---|
| $\beta_0$ | 1.109 | 1.213 |
| $\beta_{exp}$ | 0.66 | 0.17 |

Table 1.4: Temperature dependence for the Canali model.

$v_{sat}$ is defined as

$$v_{sat} = v_{sat,0} \left( \frac{300K}{T} \right)^{v_{sat,exp}}$$

$v_{sat,0}$ and $v_{sat,exp}$ are defined in table 1.5.

| | Electrons | Holes |
|---|---|---|
| $v_{sat,0}$ | $1.07 \times 10^7\,\mathrm{cm\,s^{-1}}$ | $8.37 \times 10^6\,\mathrm{cm\,s^{-1}}$ |
| $v_{sat,exp}$ | 0.87 | 0.52 |

Table 1.5: Saturation parameters for the Canali model.

$F$ from equation 1.16 is the driving force, and is the component of the electric field parallel to the carrier current:

$$F_c = \vec{E} \cdot \left( \frac{\vec{j_c}}{|j_c|} \right)$$

where $\vec{E}$ is the electric field vector, and $\vec{j}$ is the electron or hole current vector.

### Carrier-Carrier Scattering

The simulations use the Conwell-Weisskopf carrier-carrier scattering, given by the mobility contribution:

$$\mu_{eh} = \frac{D \left( \frac{T}{T_0} \right)^{3/2}}{\sqrt{np}} \left[ \ln \left( 1 + F \left( \frac{T}{T_0} \right)^2 (pn)^{-1/3} \right) \right]^{-1}$$

where $n$ and $p$ are the electron and hole densities, $T$ is the lattice temperature and $T_0$ =300 K. $D$ and $F$ are defined parameters given by $D$ =$1.04 \times 10^{21}$ /cmVs and $F$ =$7.452 \times 10^{13}\,\mathrm{cm^{-2}}$.

## 1.6.2 Effective Intrinsic Density

The detectors used have an active region with doping profiles above $1 \times 10^{19}\,\mathrm{cm^{-3}}$. For higher effective doping it is important to take into account the band-gap narrowing. The effective band-gap is:

$$E_{g,eff}(T) = E_g(T) - \Delta E_g$$

Where $E_g(T)$ is the temperature depending band-gap given by

$$E_g(T) = E_g(0) - \frac{\alpha T^2}{T + \beta}$$

where $E_g(0)$ is the band-gap at $0\,\mathrm{K}$, $\alpha = 4.73 \times 10^{-4}\,\mathrm{eV\,K^{-1}}$ and $\beta = 636\,\mathrm{K}$.

$\Delta E_g^0$ is calculated using the Old Slotboom model:

$$\Delta E_g^0 = E_{ref}\left[\ln\left(\frac{N_{tot}}{N_{ref}}\right) + \sqrt{\ln^2\left(\frac{N_{tot}}{N_{ref}}\right) + 0.5}\right]$$

with $E_{ref} = 9.0 \times 10^{-3}\,\mathrm{eV}$ and $N_{ref} = 1.0 \times 10^{17}\,\mathrm{cm^{-3}}$.

### 1.6.3 Recombination

#### Shockley-Read-Hall recombination

Shockley-Read-Hall (SRH) recombination takes into account deep defects levels within the band gap. The recombination rate is described by the equation:

$$R_{net}^{SRH} = \frac{np - n_{i,eff}^2}{\tau_p(n + n_1) + \tau_n(p + p_1)} \tag{1.17}$$

with

$$n_1 = n_{i,eff} e^{\frac{E_{trap}}{kT}} \tag{1.18}$$

$$p_1 = n_{i,eff} e^{\frac{-E_{trap}}{kT}} \tag{1.19}$$

The silicon value for $E_{trap} = 0$. The lifetimes from equation 1.17 are defined as:

$$\tau_{dop}(N_{A,0} + N_{D,0}) = \frac{\tau_{max}}{1 + \frac{N_{A,0} + N_{D,0}}{N_{ref}}}$$

With $N_{ref} = 1 \times 10^{16}\,\mathrm{cm^{-3}}$, $\tau_{max} = 1 \times 10^{-5}\,\mathrm{s}$ for electrons and $\tau_{max} = 3 \times 10^{-6}\,\mathrm{s}$ for holes.

### Surface SRH recombination

At the interface of the detector it appears recombination mechanism. The surface Shockley-Read-Hall (SRH) recombination between two different regions is described as:

$$R_{surf,net}^{SRH} = \frac{np - n_{i,eff}^2}{(n+n_1)/s_p + (p+p_1)/s_n}$$

with $n_1$ defined in equation 1.18 and $p_1$ defined in 1.19. The surface recombination velocity is given by:

$$s = s_0 \left[1 + s_{ref}\left(\frac{N_i}{N_{ref}}\right)\right]$$

with $s_0 = 1 \times 10^3\,\mathrm{cm\,s^{-1}}$, $s_{ref} = 10^3$ and $N_{ref} = 1 \times 10^{16}\,\mathrm{cm^{-3}}$.

### Avalanche

If the space charge region is larger than the mean free path between two ionizing impacts a charge multiplication mechanism may happen and cause electrical breakdown.

The University of Bologna Impact Ionization Model covers the avalanche model for electric fields from $50\,\mathrm{kV\,cm^{-1}}$ to $600\,\mathrm{kV\,cm^{-1}}$ and temperatures from 300 K to 700 K. The ionization coefficient is

$$\alpha = \frac{F_{ava}}{a(T) + b(T) exp\left[\frac{d(T)}{F_{ava}+c(T)}\right]}$$

The temperature dependence for the electron parameters are:

$$a(T) = a_0 + a_1 t^{a_2} \qquad b(T) = b_0 \qquad c(T) = c_0 + c_1 t + c_2 t^2 \qquad d(T) = d_0 + d_1 t + d_2 t^2$$

and for holes are:

$$a(T) = a_0 + a_1 t \qquad b(T) = b_0 exp(b_1 t) \qquad c(T) = c_0 t^{c_1} \qquad d(T) = d_0 + d_1 t + d_2 t^2$$

with $t = T/1K$.

The coefficients are specified in table 1.6.

| | Electrons | Holes |
|---|---|---|
| $a_0$ | 4.3383 V | 2.376 V |
| $a_1$ | $-2.42 \times 10^{-12}$ V | $1.033 \times 10^{-2}$ V |
| $a_2$ | 4.1233 | 0 |
| $b_0$ | 0.235 V | 0.177 14 V |
| $b_1$ | 0 | $-2.178 \times 10^{-3}$ |
| $c_0$ | $1.6831 \times 10^{4}$ V cm$^{-1}$ | $9.47 \times 10^{-3}$ V cm$^{-1}$ |
| $c_1$ | 4.3796 V cm$^{-1}$ | 2.4924 |
| $c_2$ | 0.130 05 V cm$^{-1}$ | 0 |
| $d_0$ | $1.2337 \times 10^{6}$ V cm$^{-1}$ | $1.4043 \times 10^{6}$ V cm$^{-1}$ |
| $d_1$ | $1.2039 \times 10^{3}$ V cm$^{-1}$ | $2.9744 \times 10^{3}$ V cm$^{-1}$ |
| $d_2$ | 0.567 03 V cm$^{-1}$ | 1.4829 V cm$^{-1}$ |

Table 1.6: University of Bologna impact ionization coefficients.

### Auger Recombination

Auger recombination is important at high carrier densities. In the Auger recombination process, an electron relaxes from the conduction band to the valence band, transferring its energy to another electron that will relax through phonons. The band-to-band rate of Auger recombination is given by:

$$R^A_{net} = (C_n n + C_p p)(np - n^2_{i,eff})$$

it depends on the temperature according to:

$$C_n(T) = \left[A_{A,n} + B_{A,n}\left(\frac{T}{T_0}\right) + C_{A,n}\left(\frac{T}{T_0}\right)^2\right]\left[1 + H_n exp\left(-\frac{n}{N_{0,n}}\right)\right]$$

$$C_p(T) = \left[A_{A,p} + B_{A,p}\left(\frac{T}{T_0}\right) + C_{A,p}\left(\frac{T}{T_0}\right)^2\right]\left[1 + H_p exp\left(-\frac{n}{N_{0,p}}\right)\right]$$

with $T_0 = 300K$. The other values of Auger recombination can be found in table 1.7.

The contribution $\left[1 + Hexp\left(-\frac{n}{N_0}\right)\right]$ corresponds to the decrease of Auger coefficients at high injection levels[51].

| | Electrons | Holes |
|---|---|---|
| $A_A$ | $6.7 \times 10^{-32}\,\mathrm{cm}^6/\mathrm{s}$ | $7.2 \times 10^{-32}\,\mathrm{cm}^6/\mathrm{s}$ |
| $B_A$ | $2.45 \times 10^{-31}\,\mathrm{cm}^6/\mathrm{s}$ | $4.5 \times 10^{-33}\,\mathrm{cm}^6/\mathrm{s}$ |
| $C_A$ | $-2.2 \times 10^{-32}\,\mathrm{cm}^6/\mathrm{s}$ | $2.63 \times 10^{-32}\,\mathrm{cm}^6/\mathrm{s}$ |
| $H$ | 3.46667 | 8.25688 |
| $N_0$ | $1 \times 10^{18}\,/\mathrm{cm}^3$ | $1 \times 10^{18}\,/\mathrm{cm}^3$ |

Table 1.7: Auger recombination model coefficients.

### 1.6.4 Irradiation models for TCAD simulations

Irradiation models for simulations implement acceptor and donor defects in the silicon lattice. 3D simulations were studied in [52] and [53] as a modification of the Perugia model, all of them with 2 acceptor defects and one donor defect. The radiation defects list is longer with more acceptor and donor traps detailed in [33], but is not comuptable in a TCAD simulation. For that reason the simulations are simplified to 2 acceptor traps and one donor trap which might characterize the radiation damage.

The simulation of the trap defects used in this work use a modified version of Perugia traps by Pennicard[54] and can be found in tables 1.8 and 1.9.

| Type | Energy(eV) | Trap | $\sigma_e(cm^2)$ | $\sigma_h(cm^2)$ | $\eta(cm^{-1})$ |
|---|---|---|---|---|---|
| Acceptor | $E_C - 0.42$ | $V_2^{-/0}$ | $1.5 \cdot 10^{-15}$ | $0.9 \cdot 10^{-14}$ | 13 |
| Acceptor | $E_C - 0.50$ | $V_2O^{-/0}$ | $5 \cdot 10^{-15}$ | $3.5 \cdot 10^{-14}$ | 0.08 |
| Donor | $E_V + 0.36$ | $C_iO_i^{0/+}$ | $2.5 \cdot 10^{-17}$ | $3.1 \cdot 10^{-15}$ | 1.1 |

Table 1.8: Modified traps model for n-type silicon[54].

| Type | Energy(eV) | Trap | $\sigma_e(cm^2)$ | $\sigma_h(cm^2)$ | $\eta(cm^{-1})$ |
|---|---|---|---|---|---|
| Acceptor | $E_C - 0.42$ | $V_2^{-/0}$ | $9.5 \cdot 10^{-15}$ | $9.5 \cdot 10^{-14}$ | 1.613 |
| Acceptor | $E_C - 0.46$ | $V_2O^{-/0}$ | $5 \cdot 10^{-15}$ | $5 \cdot 10^{-14}$ | 0.9 |
| Donor | $E_V + 0.36$ | $C_iO_i^{0/+}$ | $3.23 \cdot 10^{-13}$ | $3.23 \cdot 10^{-14}$ | 0.9 |

Table 1.9: Modified traps model for p-type silicon[55].

The irradiation damage is scaled with the fluence, with a linear dependence for the concentration $N_t$ as:

$$N_t = \eta \cdot \Phi$$

where $\Phi$ is the fluence.

The $Si/SiO_2$ oxide after irradiation reaches saturation values of $3 \times 10^{12}\,\mathrm{cm}^{-2}$ for $< 100 >$ p-type wafers.

Chapter 2

# 3D sensors for the ATLAS experiment

## 2.1 3D detectors for IBL

In 1997 Kenney and Parker [27; 28] proposed a new structure with columnar electrodes along the silicon bulk, known as 3D detectors (introduced in chapter 1). The electrodes are n and p-doped columns with a pitch of a few micrometers. The depleted volume for a 3D detector depends on the distance between columns, typically set smaller than the wafer thickness. Hence, the detector will be fully depleted at lower voltages and the collection time for 3D detectors is reduced to just a few nanoseconds since they have shorter drift distances. All the surface of the detector, except the columns, is active since it does not need guard rings to delimit the area of the sensor. In HEP experiments, the dead area of the columns can be avoided since the detector is slightly tilted (15°), thus the particles always pass through some active area. The columnar electrodes are processed with a Deep Reactive Ion Etching (DRIE), an anisotropic reactive ion etching process that can etch deep holes in silicon material with high aspect ratios[56].

Before the LS1 (Long Shutdown 1 in 2013-2014), the silicon planar technology was the only used for high energy physics experiments. During LS1, an inner layer of silicon detectors of the ATLAS experiment positioned 3.2 cm from the beam, called IBL (Insertable-B Layer), was introduced. For the IBL, which consist on 14 azimuthal carbon fiber staves, it was agreed to use 75% of PPS (Planar) detectors and 25% 3D detectors, being the first time that 3D silicon detectors were used in a high energy physics experiments.

IMB-CNM (CSIC) in Barcelona[4] produced part of the 3D sensors for the IBL, and this chapter covers their characterization. 84 sensors fabricated at CNM-Barcelona are now installed and operative inside the IBL. The end of the chapter covers the simulation of new 3D detectors that will adapt to the next ATLAS pixel read out electronics for the inner tracker with smaller pixel sizes and smaller bump-bonds pitch[57].

### 2.1.1 3D IBL sensors description

3D sensors for IBL were fabricated on 230 µm thick wafers and the columns were 210 µm deep, with a diameter of 10 µm, following the IBL specifications[58]. Figure 2.1 shows the detectors layout, the fabrication details are given in ref. [59], and the simulations are covered in ref. [33]. Figure 2.2 shows a microsection of 3D detectors fabricated at CNM-Barcelona. The columns do not reach the other side of the wafer, they are 210 µm deep in order to have lower electric field at the column tip. The DRIE used a metallic mask to protect the surface from the etch of the holes, and the aspect ratio obtained (the ratio of deep etch divided by lateral etch) was 21:1. The wafers are quite thin and the DRIE etch holes through almost all the wafer, increasing the wafer bow and resulting in a low production yield due to the fragility of the fabrication process.

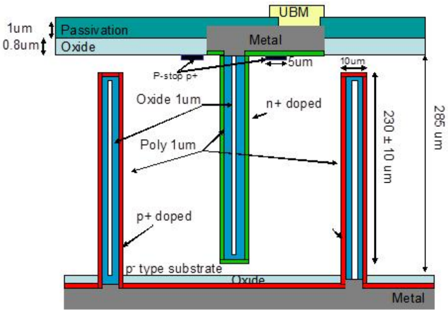

Figure 2.1: Scheme of a two sided 3D detector[60] fabricated at CNM-Barcelona.

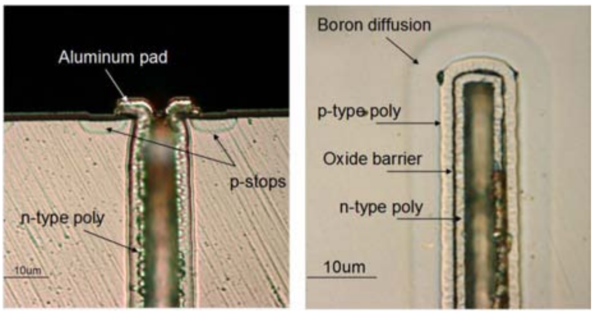

Figure 2.2: Microsection of a 3D column. On the left, an n-type column and on the right a p-type one.

Figure 2.3 shows the mask of the wafer for this production, with 8 FE-I4, 9 FE-I3, 3 CMS pixel detectors, four micro-strip and 8 diodes.

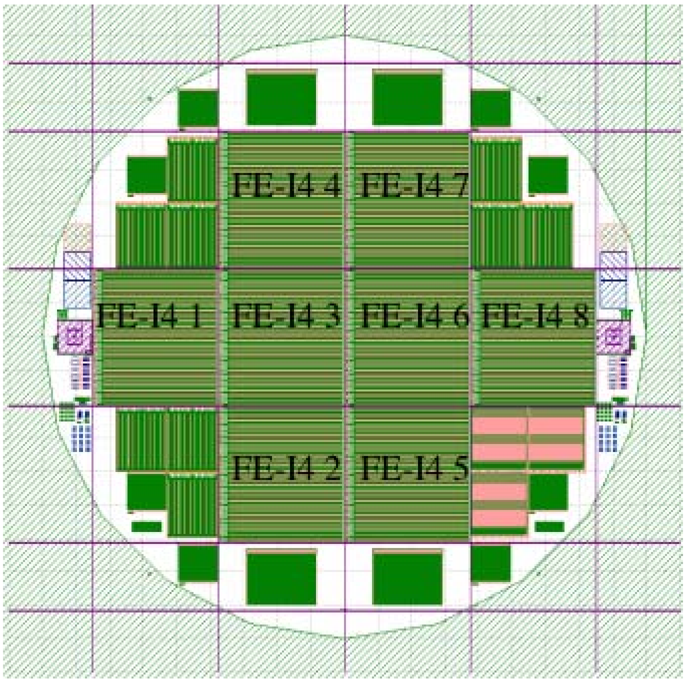

Figure 2.3: CNM mask used for the production of IBL 3D sensors.

After fabrication, the sensors needed to be electrically characterized with a current-voltage curve to identify high leakage currents or sensors with low break down voltages. Subsequently, the sensors were shipped at Fraunhofer IZM[61] for the deposition of Under Bump Metalization (UBM), an electro-plating copper deposition necessary for the flip chip. Figure 2.4 shows a photo of UBM, and figure 2.5 shows a SEM image of the UBM.

After the UBM deposition, the sensors went through the flip chip process, a step that bonds the pixels to the read out electronics. Later, the sensors were assembled into carbon fiber staves (figure 2.6), and introduced inside the ATLAS experiment 3.2 cm away from the beam (as shown in figure 1.5). Figure 2.7 shows a schematic cross section of the IBL detector.

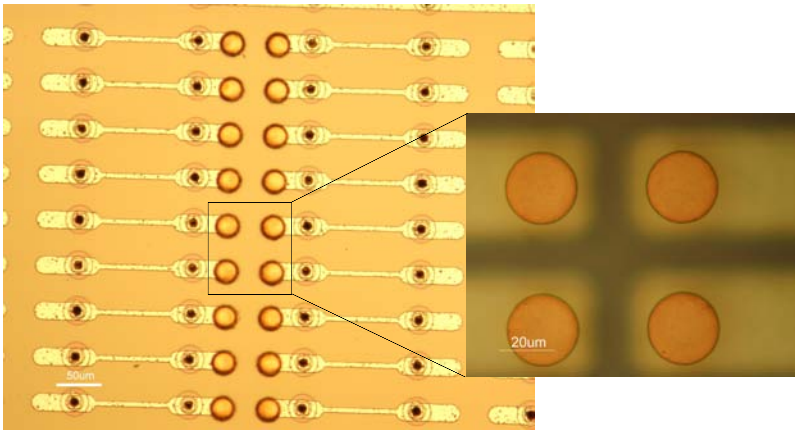

Figure 2.4: Photo of the UBM. The left picture shows the pixels, and the black dots are the holes of the columns. The right image shows a detail of four UBM pads.

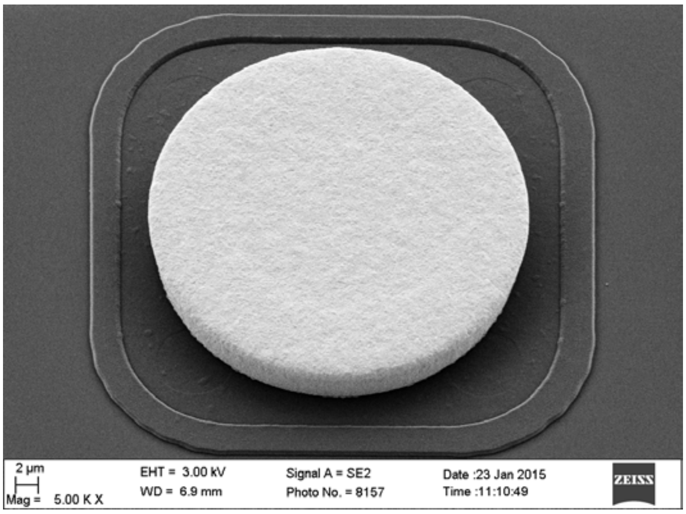

Figure 2.5: SEM image of one UBM pad, the height of the UBM pad is 4 µm.

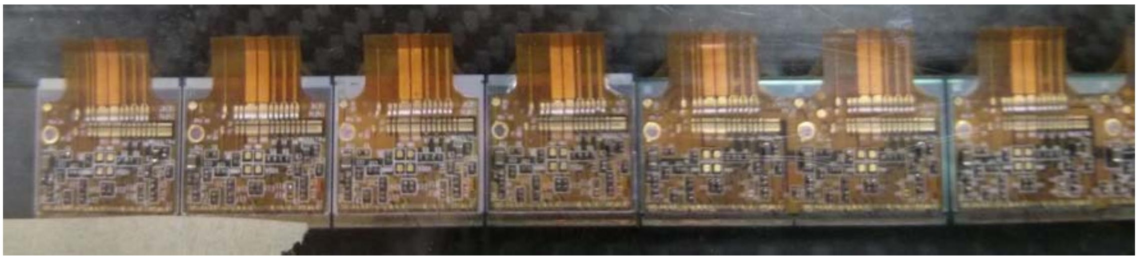

Figure 2.6: Photo of one IBL stave with 3D detectors connected to the FE-I4 electronics.

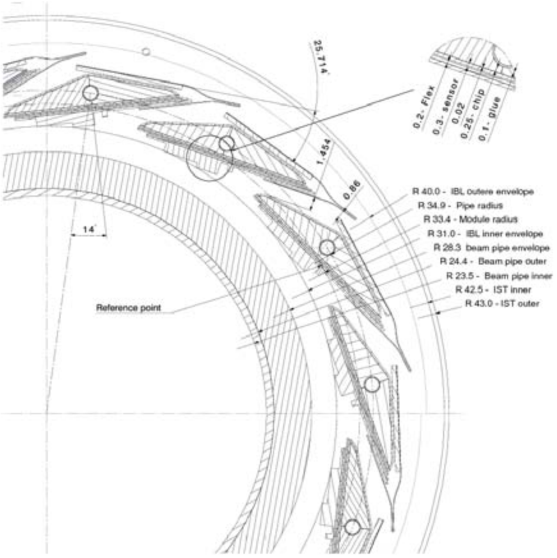

Figure 2.7: Cross section of IBL layout[62].

### 2.1.2 Electronics

Sensors for the Insertable B-Layer (IBL) have a geometry that fits the Front End-I4 (FE-I4) electronics[62]. Table 2.1 shows the details of the integrated cirquits FE-I4 and FE-I3 (used in the central layout of the ATLAS experiment) electronics. FE-I4 detectors are bigger and the pixel size is smaller compared to the previous read out electronics Front End-I3. FE-I3 pixel sensors were excluded from IBL design because the hit rate is lower, have lower occupancy and higher thresholds than FE-I4[63].

| | FE-I3 | FE-I4 |
|---|---|---|
| Pixel Size | $50 \times 400$ µm$^2$ | $50 \times 250$ µm$^2$ |
| Pixel Array | $18 \times 160$ | $80 \times 336$ |
| Chip Size | $7.6 \times 10.8$mm$^2$ | $20.0 \times 18.6$mm$^2$ |
| Active Fraction | 74% | 89% |
| Analog Current | 16 µA/pixel | 10 µA/pixel |
| Digital Current | 10 µA/pixel | 10 µA/pixel |
| Analog Supply Voltage | 1.6 V | 1.5 V |
| Digital Current | 2.0 V | 1.2 V |
| Data Rate | 40 Mb s$^{-1}$ | 160 Mb s$^{-1}$ |

Table 2.1: FE-I3 and FE-I4 pixel details.

## 2.2 Characterization of 3D detectors for IBL

In order to select the sensor to be mounted inside the IBL, all 3D sensors fabricated at CNM were characterized electrically with current-voltage curves that yield information about:

- Leakage current
- Break down voltage

The first measurements were carried out on wafer, biasing only the guard ring (figure 2.8 shows the position of the guard ring contact). The guard ring is not connected to any pixel, therefore the measurement only takes into account the leakage current of the ring. The measurement should show the bulk current from peripherial pixels through the puch-through mechanism. The punch-through mechanism happens when a depleted biased implant extends around a floating implant, at one point the depleted implant will deplete the volume of the floating one. The potential of the floating implant is called punch-through voltage and it is determined by the distance of the implants and the substrate doping[15].

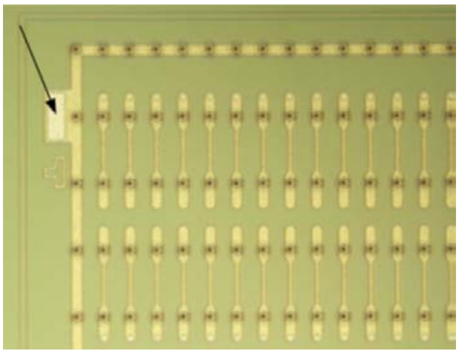

Figure 2.8: Position of the guard ring pad (black arrow).

After UBM, the detectors were diced, thus the detectors could be measured individually. The detectors were positioned upside-down, the bumps of the UBM facilitated the contact of the pixel with the surface of a metallic chuck, and once biased, the current was measured for all pixels. The following section will study the yield of the detectors and the reliability of the measurements of IBL detectors.

Current-voltage measurements before UBM were taken with a Semiconductor Parameter Analyzer (SPA) HP 4155B and a Cascade probe station. The measurements of the guard ring were carried on with a thermal chuck at 20 °C with a nitrogen flow to provide a dry environment. Current-voltage measurements after UBM were taken on a Cascade probe station at room temperature, and the detectors were biased with a Keithley 2410 power supply (figure 2.9 shows a photo of the setup).

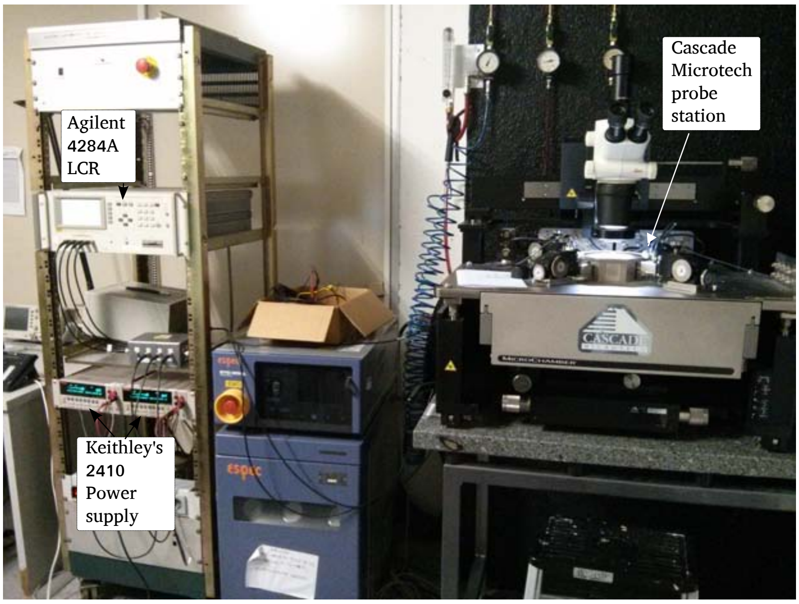

Figure 2.9: CNM characterization lab. The Cascade probe station is on the right side of the picture and the two power supplies are on the left.

### 2.2.1 Measurements on wafer

After fabrication, the FE-I4 detectors were tested on wafer, biasing the guard ring through the contact shown in figure 2.8. 51 wafers were fabricated and 412 sensors were tested. Figure 2.10 shows the current-voltage curve for all of them colored in red and green: in green are shown the detectors with a leakage current lower than 20 nA at 25 V and break down voltage higher than 35 V, whereas the red ones do not fulfill either of those conditions[12]. The measurements were taken at 20 °C in a nitrogen flow atmosphere.

Figure 2.11 shows the number of detectors for each current bin. The compliance of the measurement was set at $1 \times 10^{-5}$ A. The inset shows a zoom of the histogram corresponding to the range 0 µA to 1 µA) where the mean value is 0.1417 µA.

Figure 2.12 shows a scheme of all the wafers and the color corresponding to each FE-I4 sensor. The figure also reports the fabrication run, the wafer number and the detector number.

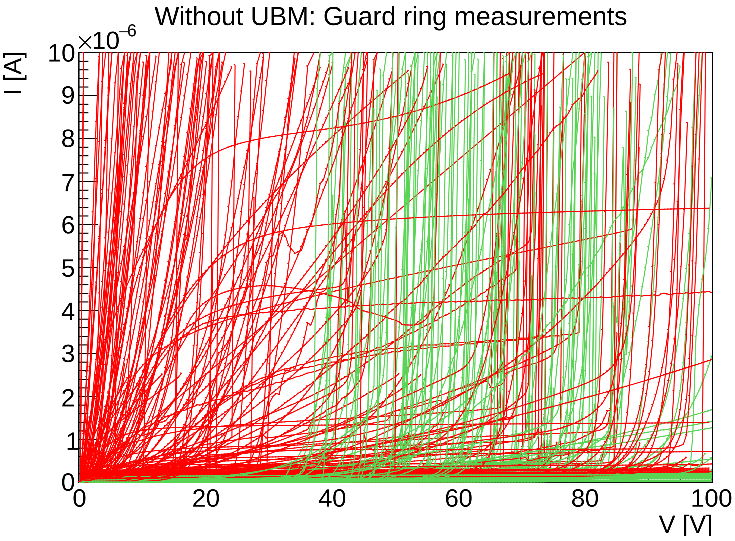

Figure 2.10: IV curves of the guard rings for the 412 sensors. Detectors with a leakage current higher than 200 nA at 25 V or a break down voltage lower than 35 V are shown in red, and the other ones in green.

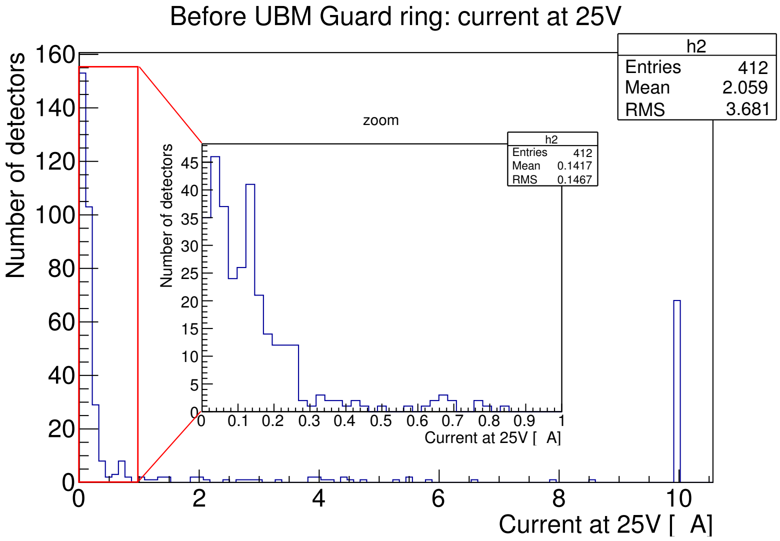

Figure 2.11: Histogram of the reverse currents at 25 V for all the sensors. The compliance of the SMU was set at $1 \times 10^{-5}$ A.

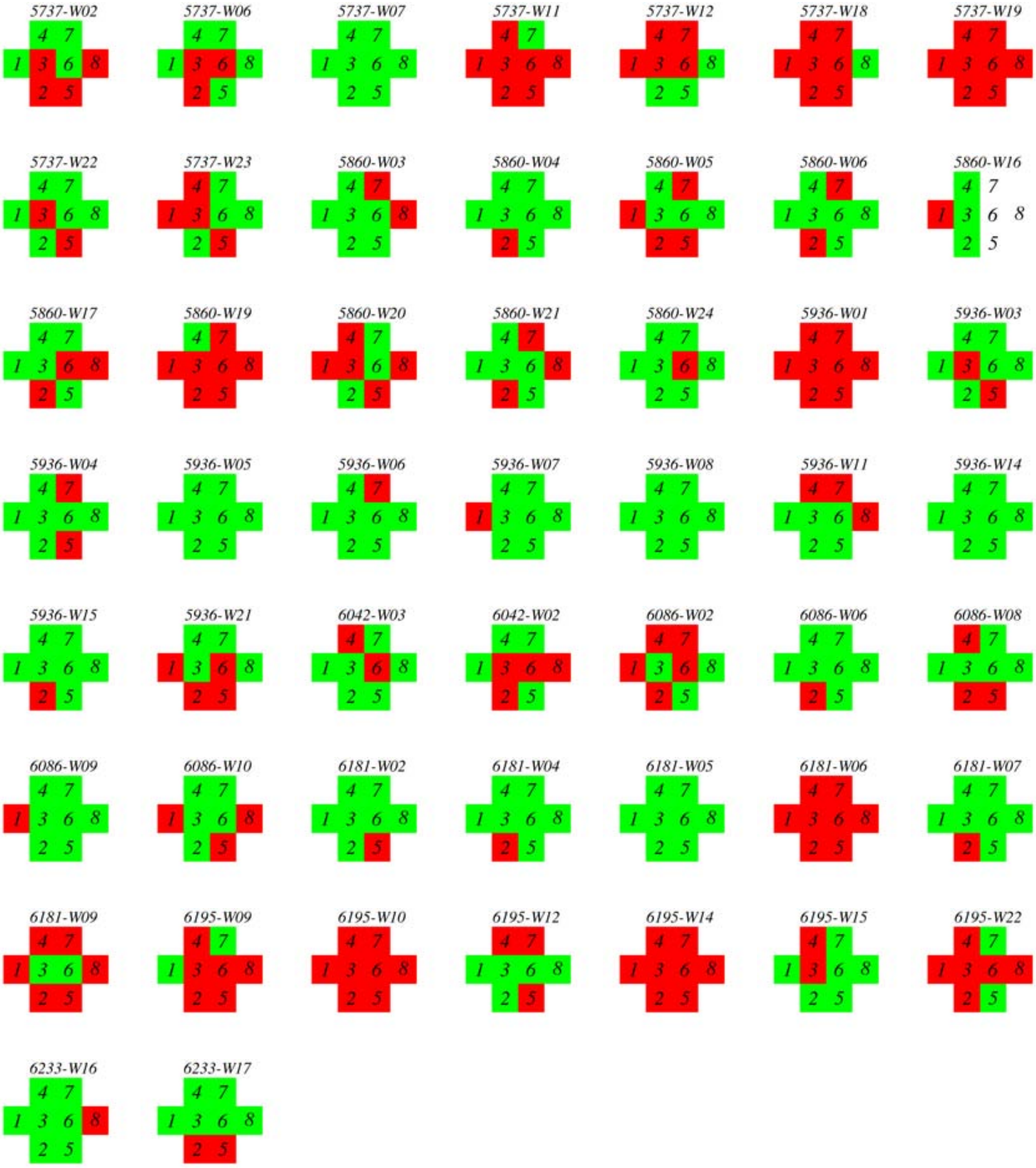

Figure 2.12: Guard ring current voltage measurements of the FE-I4 detectors, before dicing. In green are shown the ones with a leakage current lower than 20 nA at 25 V and break down voltage higher than 35 V, and in red the ones that do not fulfill either of those conditions

### 2.2.2 Measurements after UBM

IV measurements were used to select the good wafers from the UBM deposition and then they were diced. After UBM, some sensors where shipped for flip chip and others went back to CNM. The ones back to CNM where measured again with current-voltage curves to ensure the good electrical performance of those detectors. Once the detectors were diced they were positioned with the bumps contacting the chuck of the probe station, taking into account all the pixels of the detectors and making the measurement more reliable than the one through the guard ring. Nevertheless, after some measurements the detectors showed that the current-voltage curves depended on the position of the detector regarding the chuck (the vacuum of the chuck makes a different pixel contact depending on the bow). After the realization that the position of the probe and the detector on the chuck made a difference in the current-voltage measurement, the detectors were biased seven times with different positions. Figure 2.13 shows the different positions of the probes and the vacuum on the chuck of the probe station.

Table 2.2 shows green sensors and red sensors before and after UBM and dicing. Since not all the detectors underwent through the same measurements, after UBM, the green sensors are the detectors selected for the IBL, while the red ones were rejected.

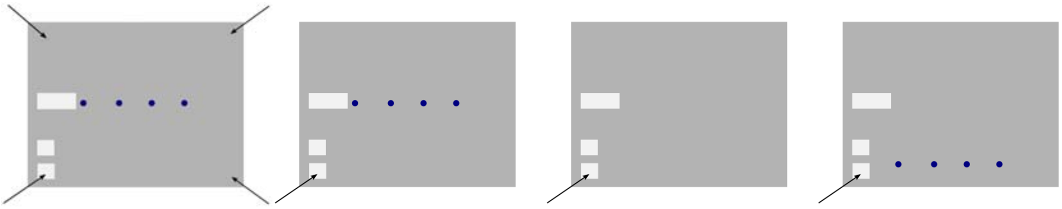

(a) 4 probes (b) Center (c) Without vacuum (d) Down

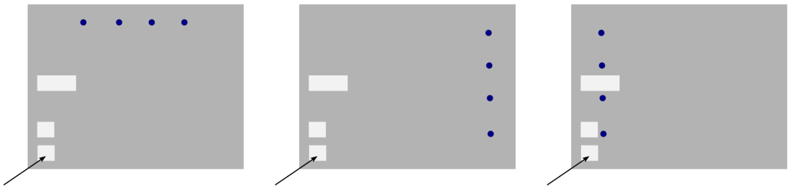

(e) Up (f) Right (g) Left

Figure 2.13: Measurements of the FE-I4 detectors after UBM. The vacuum holes of the probe station are sketched in blue, and the black arrows show the probe positions.

| | Before UBM | After UBM |
|---|---|---|
| Total FE-I4 | 412 | 412 |
| Green FE-I4 | 242 | 84 |
| Red FE-I4 | 170 | 324 |

Table 2.2: Number of green and red FEI4 detectors before and after UBM.

Finally, out of 412 sensors, 103 were shipped for IBL and 84 were introduced inside IBL. Figure 2.14 shows in green the detectors inside IBL. Due to the fact that there were not enough good detectors, some detectors with lower break down voltage were also used for the IBL. Blue detectors were also selected despite having a breakdown voltage under 30 V.

### 2.2.3 Comparison of measurements before and after UBM

Table 2.3 shows the number of green, red and blue sensors before and after UBM and the percentage of each one.

| Before UBM: | Green | Green | Green | Red | Red | Red |
|---|---|---|---|---|---|---|
| After UBM: | Green | Red | Blue | Green | Red | Blue |
| Number of sensors | 70 | 169 | 3 | 10 | 159 | 1 |
| Percentage | 17% | 41% | 0.7% | 2.4% | 38.6% | 0.3% |

Table 2.3: Number of green and red detectors before and after UBM.

Table 2.4 shows the number of green FE-I4 sensors before and after UBM separated by the detector position inside the wafer. Sensors 2 are the ones with lower yield before and after UBM, while, sensors 6 and 7 show the best yield in the wafer position.

Further measurements after flip chip for IBL FE-I4 3D detectors are reported in [64; 65]. During 2015, IBL did the first measurements with cosmic rays[66] and all the detectors mounted are operational.

### 2.2.4 3D detectors for Atlas Forward Physics

The ATLAS Forward Physics (AFP) is an experiment that aims to locate 3D pixel tracking detectors in the forward ATLAS region, around 210 m from the interaction point of the ATLAS experiment. The detectors will be located very close to the beam line, receiving high fluences with very inhomogeneous irradiations[67]. Those

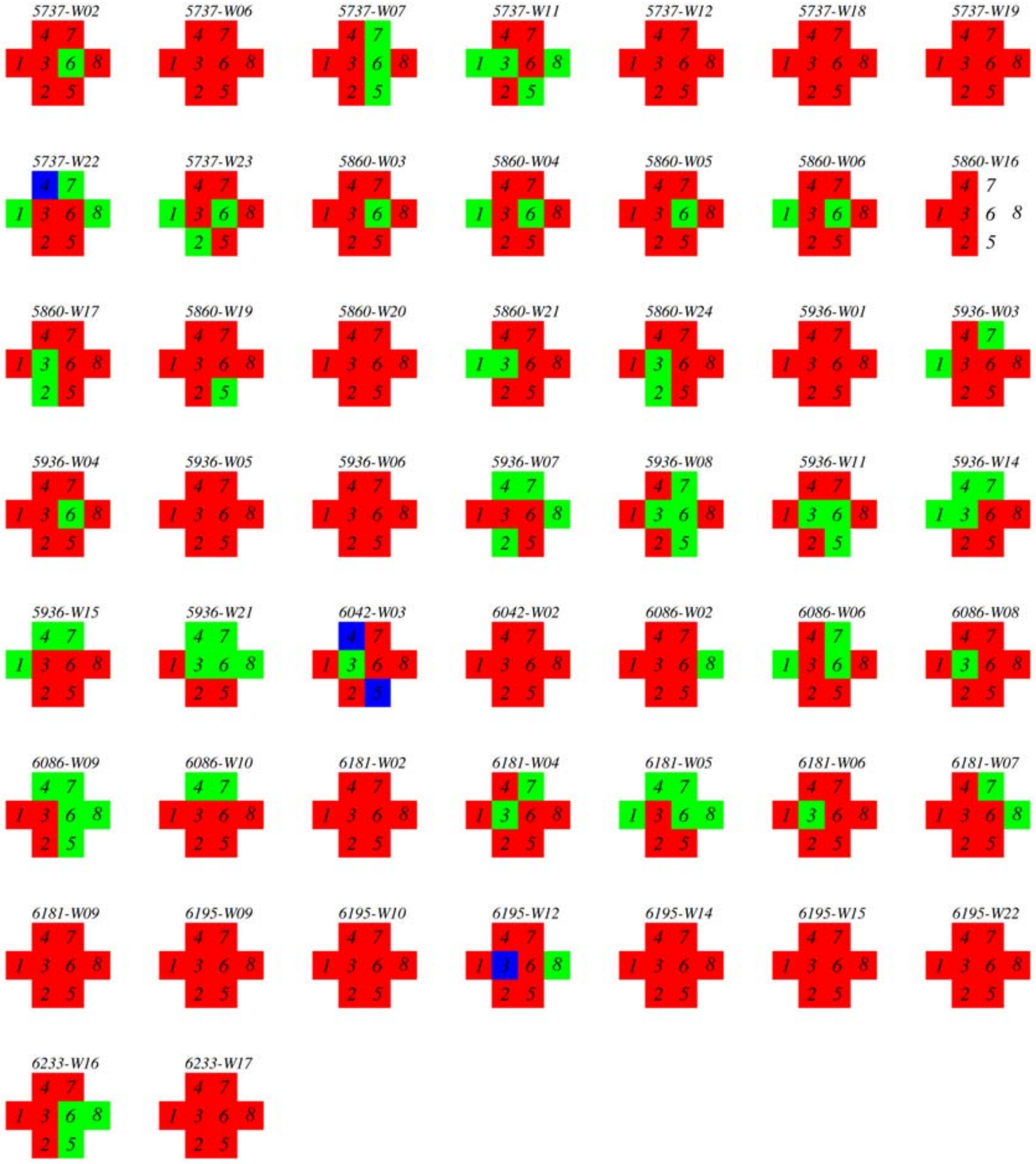

Figure 2.14: The green sensors are inside IBL and have a break down voltage higher than 30 V, blue sensors are inside IBL and have a break down voltage lower than 30 V and red sensors were discarded.

| Sensor position | Number of green sensors before UBM | Number of green sensors after UBM |
|---|---|---|
| 1 | 30 | 11 |
| 2 | 24 | 4 |
| 3 | 31 | 12 |
| 4 | 31 | 7 |
| 5 | 27 | 7 |
| 6 | 32 | 15 |
| 7 | 31 | 14 |
| 8 | 30 | 10 |

Table 2.4: Number of green sensors in each position at the wafer, before and after UBM.

detectors are expected to detect diffracted protons at 206 m and 214 m from the interaction point. Figure 2.15 shows a sketch of the location of AFP experiment. AFP will use similar 3D FE-I4 detectors as IBL (fabricated at CNM Barcelona).

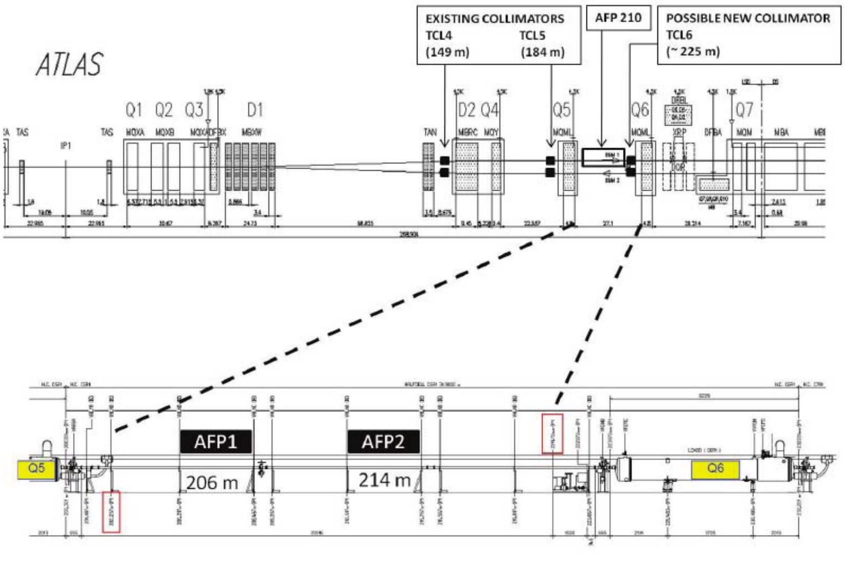

Figure 2.15: Sketch of the LHC position of AFP[67].

Due to its proximity to the beam, the detectors for AFP will have to be diced very close to the active area in one side of the detector[68]. The active area is the detector area occupied by pixels and hence, where the particles are detected. In order to study the electric behavior of FE-I4 detectors diced very close to the active area, the current-voltage curve of three FE-I4 detectors was studied with

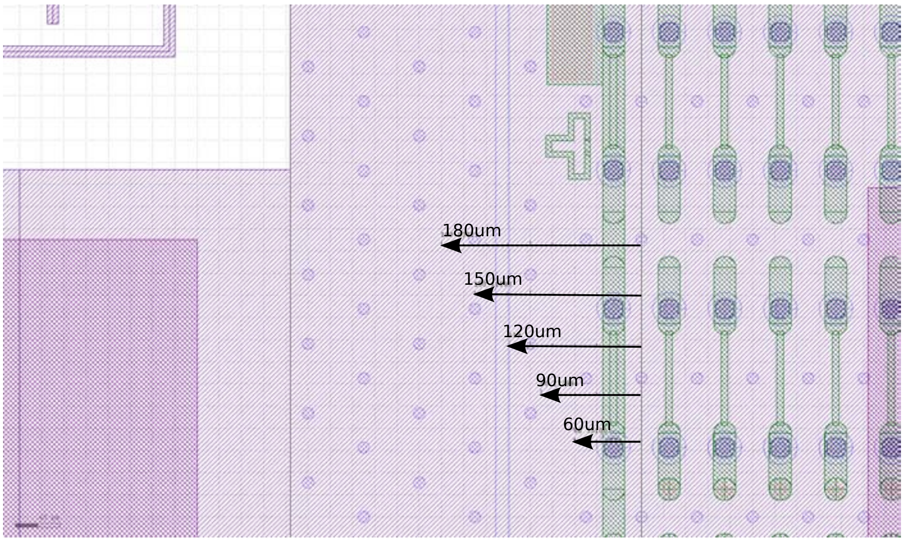

Figure 2.16: Cut positions at 180 µm, 150 µm, 120 µm, 90 µm and 60 µm, respectively.

different dicing positions in order to measure their leakage current. The detectors were diced with a diamond saw, which has an approximate width of 30 µm, and afterwards a current-voltage of the guard ring and a current-voltage of the detector were measured. Those steps were repeated after each cut. Figure 2.16 shows the different dicing positions from the active area of the FE-I4 detector. Table 2.5 shows the different cuts for the three sensors in order to observe how precise was the dicing saw. The dicing distances were measured from images taken with an optical microscope. The saw was aligned through all the wafer although there is some difference between the distance at the left and the right of the detector. The left cut and right cut are the measurements of the left distance from the active area and the right distance from the active area measurements respectively, and the difference between those cuts are due to the error associated to the alignment.

Figure 2.17 shows two cuts of the detectors, (a) shows the left cut and (b) the right cut of the same detector with a nominal distance of 150 µm from the active area. There is a difference of 6 µm between both distances, which is one of the largest dicing difference (cut 2 of sensor 2).

Figures 2.18, 2.19 and 2.20 show the current voltage curves for the 3 sensors after each cut. The measurements were taken (a) in the guard ring and (b) through the UBM on the chuck.

As expected, the leakage current increases reducing the dicing distance from the

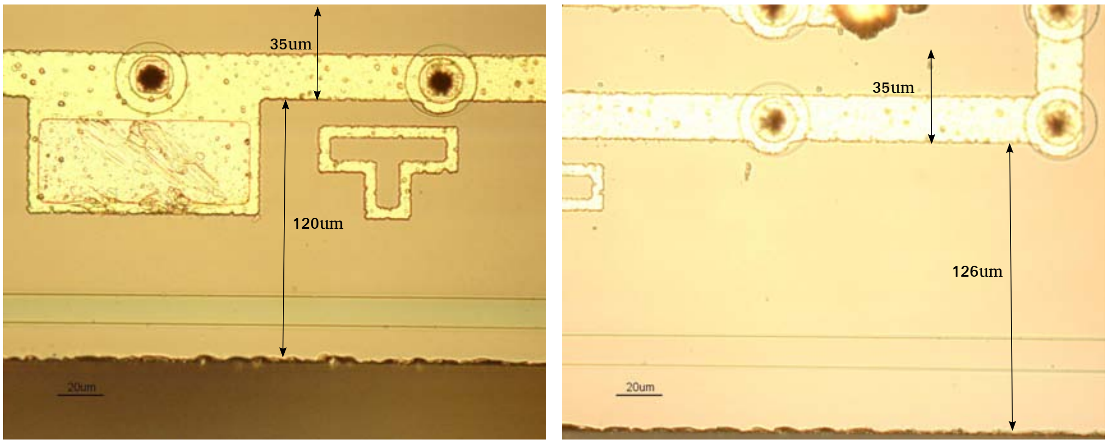

(a) Left cut (b) Right cut

Figure 2.17: Left and right images of sensor 2 cut 2.

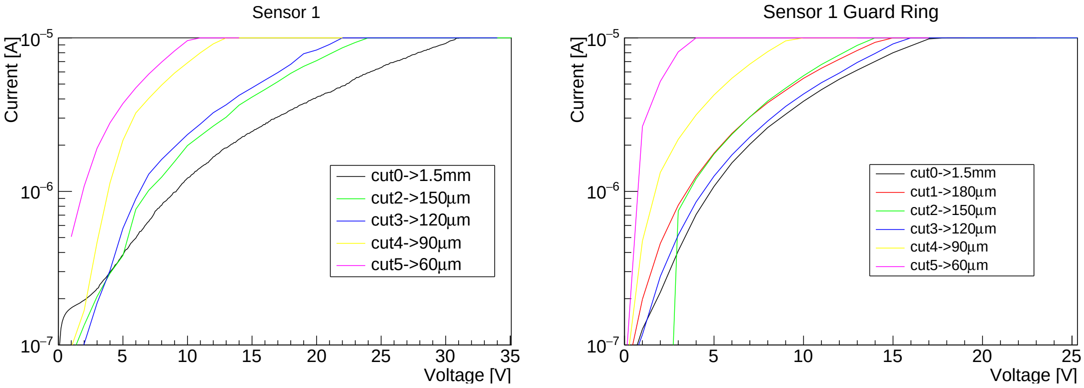

(a) Measurements from backside (b) Measurements of the guard ring

Figure 2.18: Current voltage measurements for sensor 1 after each cut.

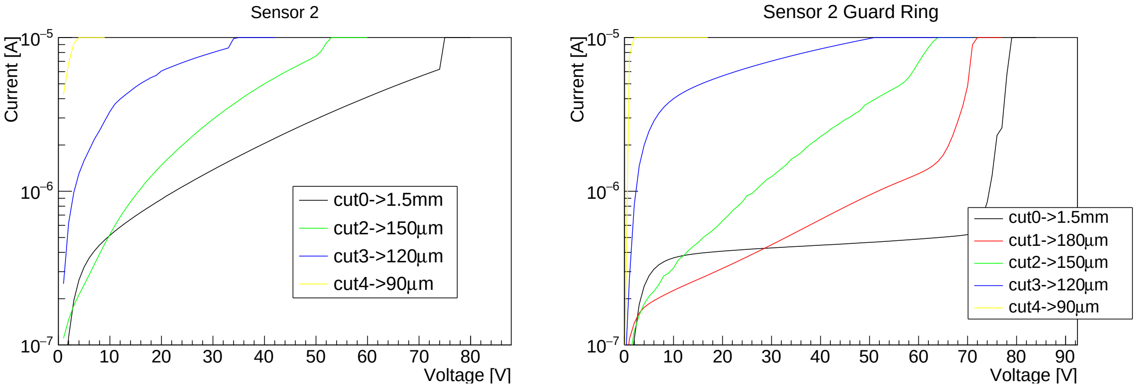

(a) Measurements from the backside (b) Measurements of the guard ring

Figure 2.19: Current voltage measurements for sensor 2 after each cut.

| | cut 0 | cut 1 | cut 2 | cut 3 | cut 4 | cut 5 |
|---|---|---|---|---|---|---|
| | Nominal distance: | [180] | [150] | [120] | [90] | [60] |
| S1 left | 1490 | 183 | 161 | 130 | 85 | 60 |
| S1 right | 1483 | 185 | 166 | 137 | 90 | 66 |
| S2 left | 1486 | 188 | 155 | 130 | 96 | |
| S2 right | 1497 | 194 | 161 | 136 | 98 | |
| S3 left | 1494 | 172 | 164 | 125 | 88 | 60 |
| S3 right | 1459 | 180 | 166 | 124 | 91 | 63 |
| Error | ±10 | ±2 | ±1 | ±1 | ±1 | ±1 |

Table 2.5: Measured dicing distances from the active area to the edge of the detector. All distances are in µm, and S1 (sensor 1), S2 (sensor 2) and S3 (sensor 3) corresponds to each one of the three detectors. The error is related to the images taken from the optical microscope.

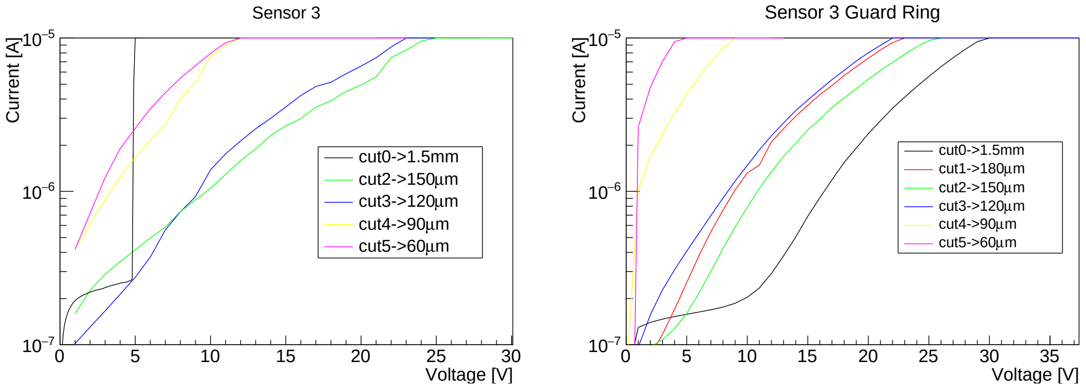

(a) Measurements from the backside (b) Measurements of the guard ring

Figure 2.20: Current voltage measurements for sensor 3 after each cut.

active area. In order to maintain the leakage current low it was decided that the detectors for the AFP experiments were diced at 175 µm from the active area.

Five wafers were fabricated for the AFP experiment with the same technology process as the IBL detectors. Figure 2.21 shows a wafer map of AFP sensors fabricated at CNM-Barcelona measured biasing the guard ring. Red detectors are the ones that have a leakage current higher than 200 nA at 25 V or a break down voltage lower than 35 V. Figure 2.22 shows the wafer map of the AFP detectors after dicing, with the current-voltage curve taken with UBM making contact to the chuck. Figure 2.23 shows the current voltages curves for the AFP detectors measured with the UBM on the chuck.

Figure 2.21: Wafer yield for detectors for AFP. Measurements at the guard ring.

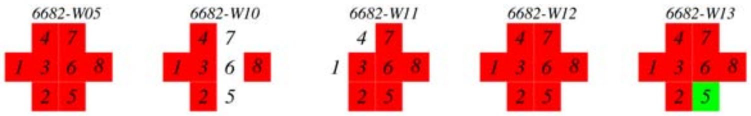

Figure 2.22: Wafer yield for detectors for AFP. Measurements taken in all the pixels after UBM. The white detectors were damaged during the dicing process.

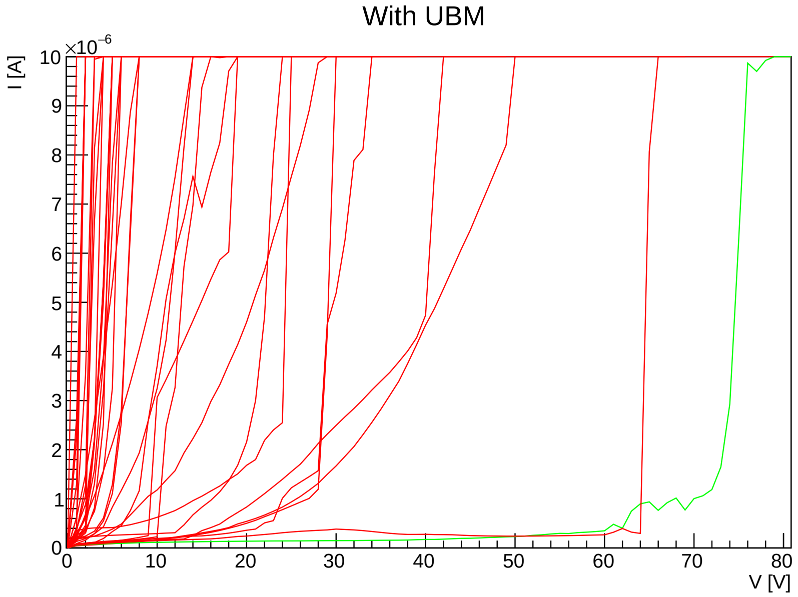

Figure 2.23: Current-voltage curves for the 3D FE-I4 detectors for AFP.

The detectors show low yield, even before dicing those detectors have low break down voltage and high current at the guard ring. Some columns were studied to know the bad performance of those detectors. The images show the polysilicon of the p-columns is over-etched which leads to an early break down. New fabrications of wafers for AFP experiment are ongoing.

## 2.3 Detectors at large $\eta$ angles

Detectors located at large $\eta$ angles in the ATLAS experiment will receive particles impinging almost perpendicularly to the columns. The IFAE group[1] carried out a test beam study of a detector in such conditions. The beam test was carried out with a FE-I4 detector tilted 80° from a 4 GeV beam of electrons[69]. The particles went through the 50 µm side of the FE-I4 detector, in order to study the performance of new pixel size of detectors for the ATLAS upgrades (with pixel size of 50 µm×50 µm, simulated in section 2.4). The FE-I4 3D detector was tilted 80° from the beam, and the data analyzed was the one that had 25 consecutively hits, thus the particle went through 25 pixels (figure 2.24 shows an sketch of the experiment). Ref. [69] shows that CNM FE-I4 detectors had low collected charge when the particle went through small $z$ positions near the n-surface, which is supposed to be related with the non crossing columns of CNM-Barcelona design (as shown in figure 2.1). Previous works of edge-TCT measurements of 3D detectors with non crossing columns show two depletion zones of the detectors, one corresponding to the volume around the column and the second one corresponding to the volume under the column [70].

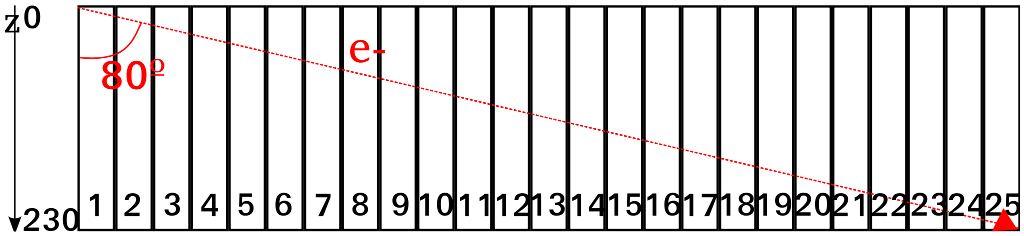

Figure 2.24: Sketch of the testbeam with the electrons impinging the detector at 80°. The rectangles are the pixels, and the particle cross 25 of them. The left axis ($z$) shows the position of the pixel for the simulation.

In order to corroborate the results presented in ref. [69], different simulations were carried out. The simulations were performed for a FE-I4 pixel cell

---

[1] IFAE: High Energy Physics Institute, Autonomous University of Barcelona, UAB

(50 µm×125 µm×230 µm), with particles impinging perpendicularly to the columns. Since the particle might strike the pixel in different positions, the simulations were run for different $z$ positions and three different $x$ planes, shown in figure 2.25 and 2.26 respectively.

The simulations were run for two bias voltages, 2 V and 30 V, the minimum and maximum bias voltage taken during the testbeam, with the detector underdepleted and the detector fully depleted. The simulations were run at 2 V since the testbeam data showed a decrease of the maximum number of pixel which the electrons went through, the maximum number of pixels which had a ToT over 1000 electrons was 21 (not 25 as for higher voltages). The testbeam data is in units of ToT (Time over Threshold), the time that the signal after the pre-amplifier is over threshold (with units of 25 ns), with the threshold set at 1000 electrons. Figures 2.27 and 2.28 show the simulation of the electric field in a diagonal cut that includes two p-columns and the n-column for 2 V and 30 V respectively. They show that the electric field at the tip of the n-column changes from the underdepleted to the depleted detector, showing a positive electric field gradient at low voltages from n to p-column, whereas at 30 V it shows a negative electric field gradient.

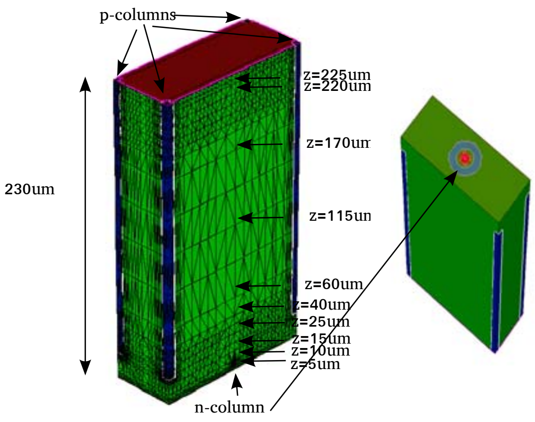

Figure 2.25: $z$ positions of the simulated particles.

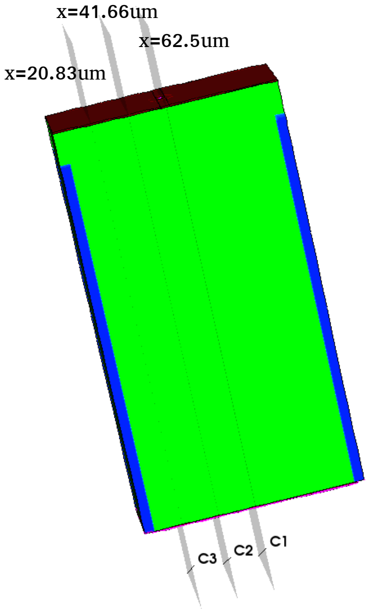

Figure 2.26: $x$ planes of the impinging MIP.

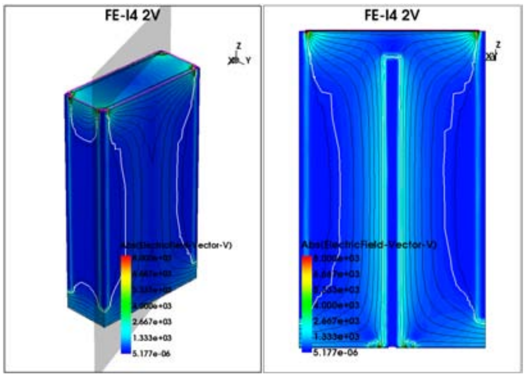

Figure 2.27: Simulation of the electric field for a FE-I4 at 2 V. The black lines are equipotential lines.

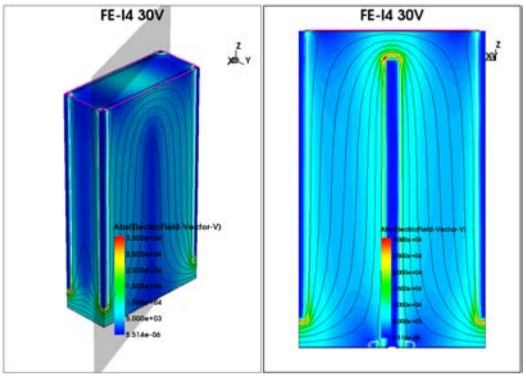

Figure 2.28: Simulation of the electric field for a FE-I4 at 30 V. The black lines are equipotential lines.

Figure 2.29 shows the simulation of the collected charge for a MIP particle crossing different positions of the FE-I4 detector at 2 V. The average charge is weighted with half the charge for $x$ =62.5 µm positions, since the position belonging to the n-column is less probable than the others:

$$Q_{average} = \frac{2Q_{x20.83} + 2Q_{x41.6} + Q_{x62.5}}{5} \tag{2.1}$$

where $Q_{x20.83}$ is the integrated charge of the position x=20.83 µm, $Q_{x41.6}$ is the integrated charge of the position x=41.6 µm and $Q_{x62.5}$ is the integrated charge of the position x=62.5 µm. The MIP crossing the n-column is less probable than the other positions because in the whole pixel cell there is one n-column but the positions $x$ =41.66 µm and $x$ =20.83 µm are in both sides of the n-column, for that reason the charge in the other two positions are weighted two times more than the charge at the n-column position.

The MIP particle is simulated with the Heavy Ion function of the Synopsys TCAD Sentaurus Device tool with a Linear Energy Transfer of $1.282 \times 10^{-5}$ pC/µm. The simulation and the testbeam data do not show a good agreement for small $z$ positions, related to the fact that the simulation do not take into account all the possible positions. For $z$ larger than 50 µm, the testbeam data and the average simulation fits well. The signal drops beyond pixel 20. The simulation shows a negative collected charge because the pulses are negative, since the electric field in that region shows a negative gradient of induced signal. Figure 2.30 shows the

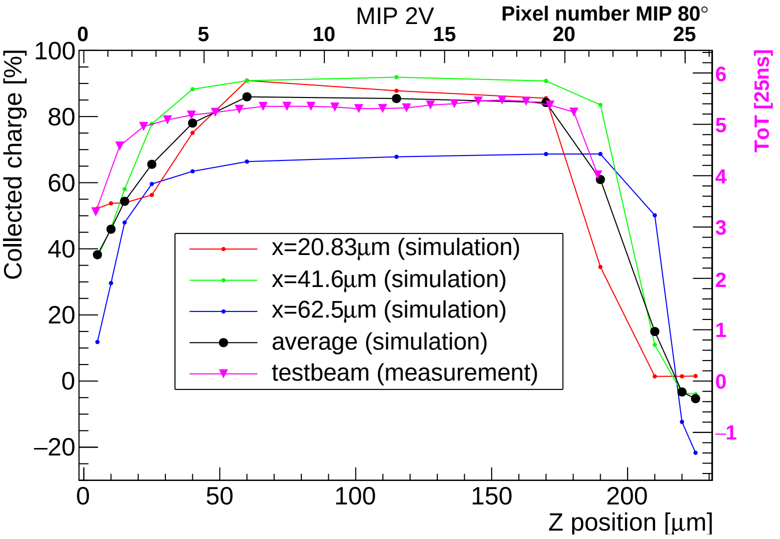

Figure 2.29: Simulation of MIP particles through different positions of the FE-I4 pixel cell at 2 V. The upper axis corresponds to the pixel number of the experiment for large $\eta$, tilted 80° from the beam. The data in purple is the testbeam real data, and the right axis shows the Time over Threshold of the testbeam particles.

simulation of a MIP at 30 V, and although they do not take into account all the possible positions, the simulation shows a good agreement with the results. The average charge is calculated with the same weighting charge as the one in equation 2.1.

## 2.4 3D pixel detectors for future ATLAS upgrades

ATLAS upcoming upgrades will cope with smaller read out pixel sizes. FE-I4 detectors have a pixel size of 50 µm× 250 µm (as specified in table 2.1). The integrated luminosity expected for LHC is 3000 $\mathrm{fb}^{-1}$ will increase the occupancy of the detector, and increase radiation damage. Smaller pixel sizes will allow more precision and will have less trapping for irradiated detectors. The two new 3D pixel sizes proposed for the ATLAS upgrade are:

- 100 µm×25 µm×200 µm
- 50 µm×50 µm×200 µm

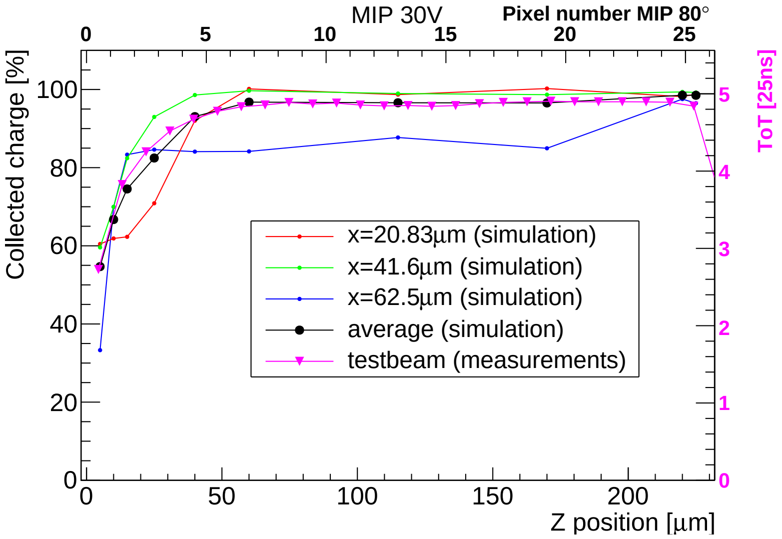

Figure 2.30: Simulation of MIP particles through different positions of the FE-I4 pixel cell at 30 V. The upper axis corresponds to the pixel number of the experiment for large $\eta$, tilted 80° from the beam. The data in purple is the testbeam real data, and the right axis shows the Time over Threshold of the testbeam particles.

Figure 2.31 shows the geometries of 3D FE-I4 and the new 3D pixel cells designed at CNM-Barcelona.

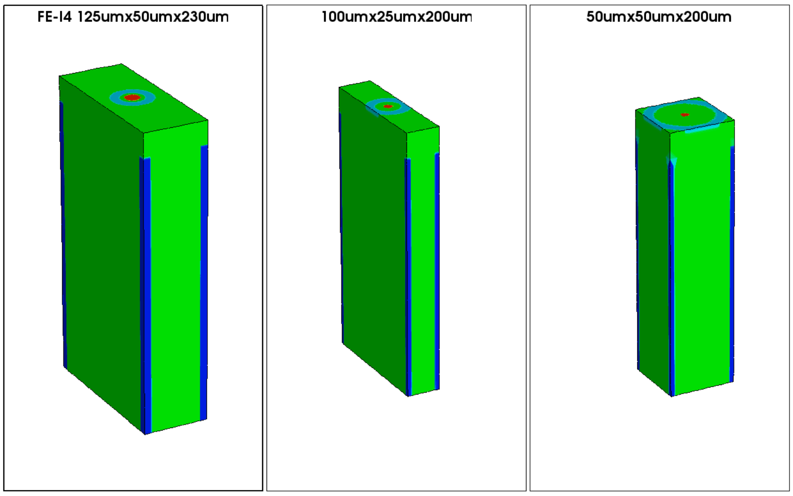

Figure 2.31: Simulated cell for FE-I4 (left) and pixel cells of 100 µm×25 µm×200 µm (center) and 50 µm×50 µm×200 µm (right).

### 2.4.1 New mask

At the moment the new pixel read out electronics is in progress, and the geometry is not defined yet[71]. The new detectors will have to be bonded and adapted to FE-I4 chips, thus, the fabricated detectors will have to adjust to FE-I4 geometry. Figure 2.32 shows the new mask of the 3D production at CNM-Barcelona. The ATLAS detectors with electronics FE-I4 are labeled A, B, C, D and E. The detector A has a standard FE-I4 configuration (defined in table 2.1).

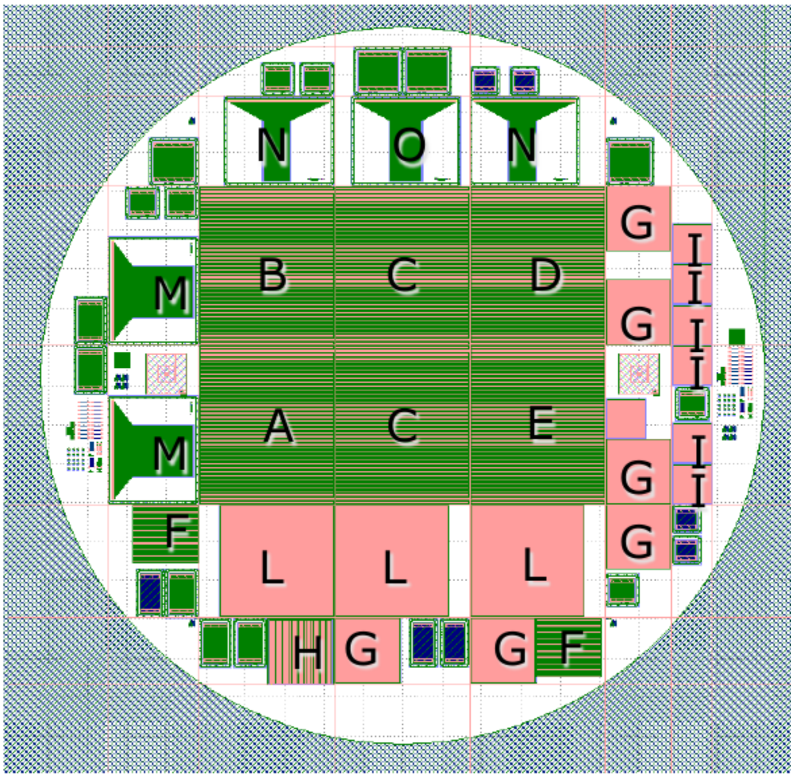

Figure 2.32: Mask for the new 3D detectors.

Figures 2.33 and 2.34 show a detail of the new mask for 50 µm×50 µm 3D pixel size adapted to FE-I4 chips with and without guard rings, C and E detectors from figure 2.32 respectively. Only part of the pixels will be bonded to the electronics, whereas the rest of the pixels are connected to the guard ring and to ground. The p-stop for C and E detectors has 25 µm of radii. The detectors have two slim edge dicing lines, at 100 µm and 200 µm from the active area, and they are designed to facilitate the dicing.

Figures 2.35 and 2.36 show the FE-I4 detectors with pixel cells 100 µm×25 µm, detectors B and D respectively. Figure 2.35 shows a configuration where five columns

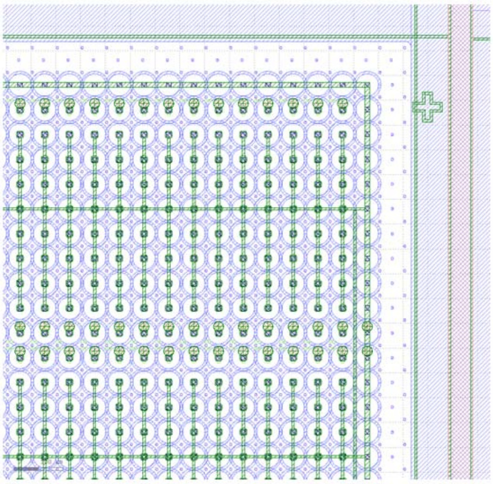

Figure 2.33: Mask detail for 50 µm×50 µm pixels adapted to the FE-I4. This detector has a 3D guard ring.

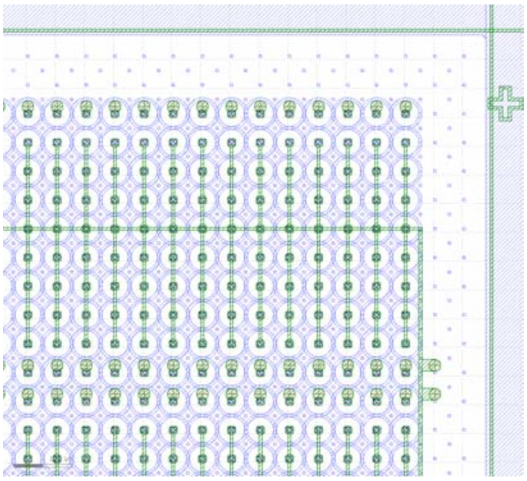

Figure 2.34: Mask detail for 50 µm×50 µm pixels adapted to the FE-I4. This detector does not have a guard ring.

are connected to one electrode, whereas the detector in figure 2.36 has 2 columns bonded (2 electrodes). Both detectors have a p-stop of 12.5 µm radii and have a guard ring surrounding all the active area. They also have two slim edge dicing lines at 100 µm and 200 µm.

The column diameter are expected to decrease to 5 µm, half the diameter of the detectors fabricated for IBL. The small aspect ratio of the columns will challenge the DRIE technology for 3D detectors, and CNM-Barcelona is working on a cryogenic DRIE process that will increase the aspect ratio of the columns, up to 40:1. As shown in ref. [56], the cryogenic DRIE increases the silicon etching rate while decreasing the resist and silicon dioxide etching rate.

### 2.4.2 Simulations

This section shows the simulation of the new 3D pixel size. The oxide charge utilized for the sensor without irradiation is $Q_{ox} = 10^{11}$ and the irradiated the charge is saturated. The simulations were run at a temperature of 258 K.

The innermost layers of pixel detectors will reach fluences up to $2 \times 10^{16}\ \mathrm{n_{eq}\ cm^{-2}}$ during the next ATLAS upgrades. The irradiation traps model used is the ones from

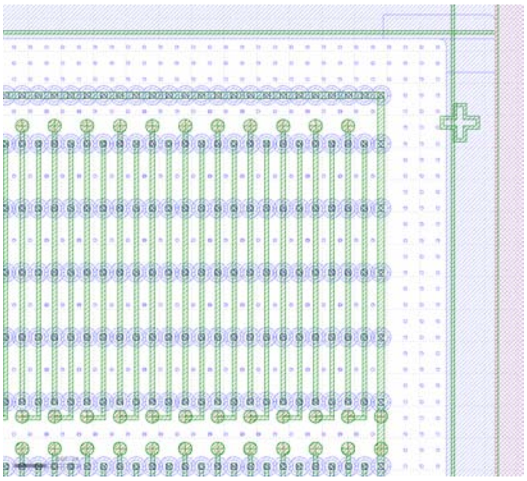

Figure 2.35: Mask detail for 100 µm×25 µm×200 µm FE-I4 pixels. This detector has a 3D guard ring. Five columns are connected to one electrode.

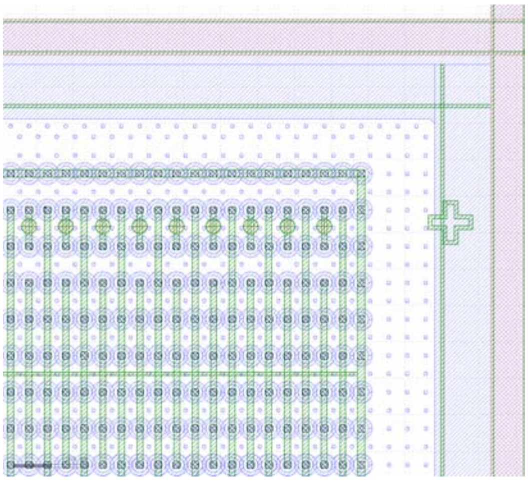

Figure 2.36: Mask detail for 100 µm×25 µm×200 µm FE-I4 pixels. This detector has a 3D guard ring. In this configuration, two columns are connected to the same electrode.

table 1.9.

### Columns 50 µm×50 µm×200 µm

The simulated structure has a volume of 50 µm×50 µm×200 µm. The p-stop is centered at the n-column and has a radii of 25 µm. Figure 2.37 shows the simulated column cell, the n-column is in red and the p-columns are in blue.

Figure 2.38 shows the current-voltage curves for different fluences, the detector does not break down before 200 V. Figure 2.39 shows the $1/C^2$-voltage curve for an unirradiated detector, the detector is depleted laterally at 5 V, although it presents a bump at 25 V corresponding to the full depletion, including the volume below the tip of the n-column.

Figure 2.40 shows the simulation of the collected charge for a MIP impinging perpendicularly the surface of the detector between the p-column and n-column (at a distance of $\sqrt{12.5^2 + 12.5^2}$ =17.7 µm between the columns) with an integration time of 25 ns. This simulation was run with a single pixel cell, and the crosstalk between neighboring columns is neglected.

Figures 2.42 and 2.43 show the simulation of the collected charge of a MIP crossing the column cell at different positions (figure 2.41 shows the simulated MIP

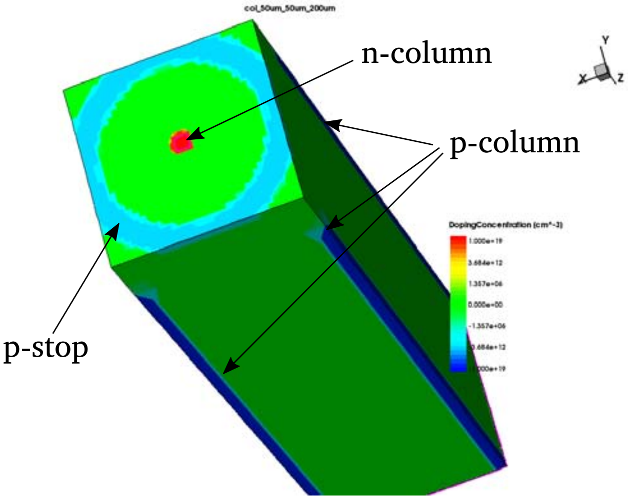

Figure 2.37: Simulated pixel cell for 50 µm×50 µm×200 µm geometry.

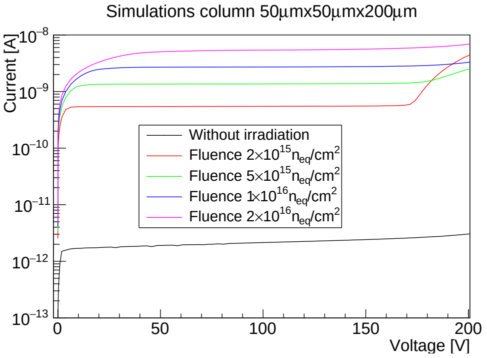

Figure 2.38: Current-voltage curve simulated for 50 µm×50 µm×200 µm.

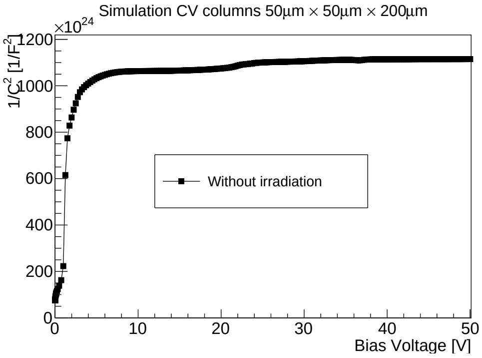

Figure 2.39: $1/C^2$-voltage curve simulated for 50 µm×50 µm×200 µm.

positions) for a non irradiated detector and for an irradiated detector with a fluence of $2 \times 10^{16}\,n_{eq}\,cm^{-2}$, respectively. As shown in figure 2.41, the simulation took into account two pixel cells, in order to integrate the possible charge collected by the neighboring column, and the integration time is always 25 ns. The integrated charge of figure 2.43 is normalized to the maximum charge of a non irradiated device, and the maximum collected charge is up to 50% when the detector is irradiated and biased at 200 V.

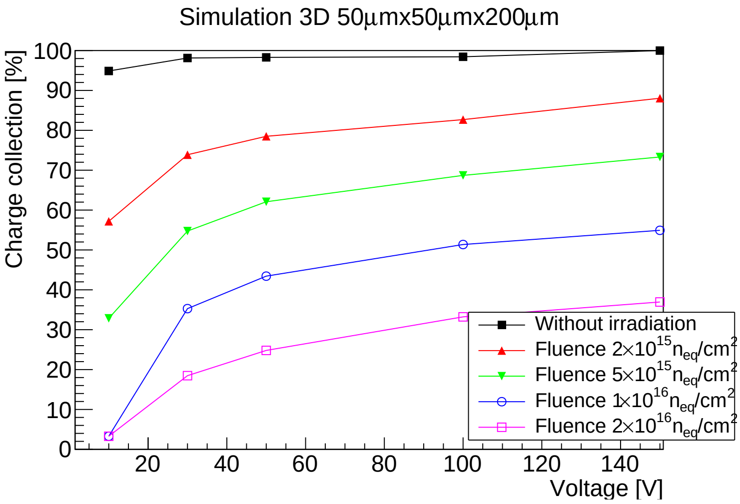

Figure 2.40: Simulation of the charge collection for a MIP crossing the detector between the p-column and the n-column for 50 µm×50 µm×200 µm.

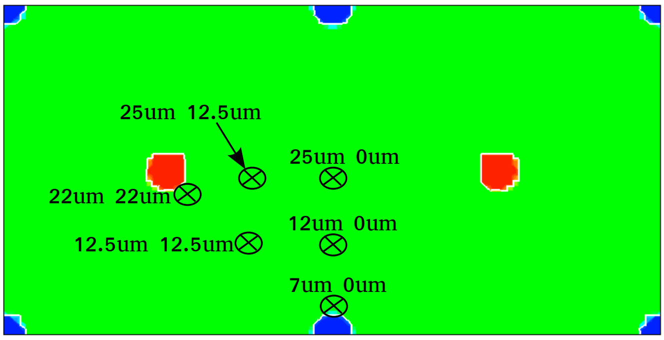

Figure 2.41: Different MIP positions for 50 µm×50 µm×200 µm.

### Detector for large $\eta$ angles

As shown in ref. [72], the new detectors might have particles impinging almost perpendicularly to the columns. A similar simulation as described in section 2.3 was carried out for a 3D detector with a pixel cell of 50 µm×50 µm×200 µm in order to study the behaviour of the detectors at large $\eta$ angles for the new ATLAS geometries. The simulation took into account two bias voltages, 2 V and 30 V as the ones simulated in section 2.3 to have a better comparison with the measurements.

Figures 2.44 and 2.45 show the electric field for 2 V and 30 V, respectively. The pixel cell show almost full depletion at 2 V (the white line show the depleted region of the detector).

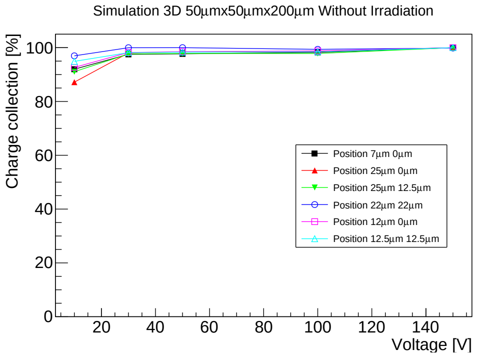

Figure 2.42: Collected charge for MIP in different positions for non irradiated sensor.

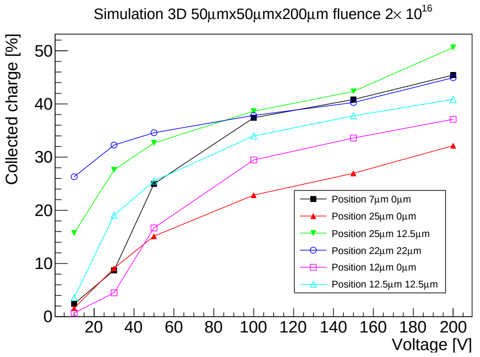

Figure 2.43: Collected charge for MIP in different positions for irradiated sensor at $2 \times 10^{16}\,\mathrm{n_{eq}\,cm^{-2}}$.

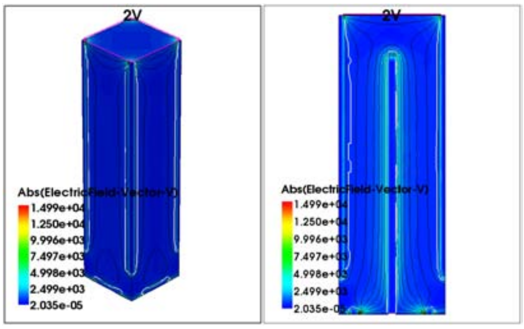

Figure 2.44: Simulation of the electric field for a FE-I4 at 2 V. The black lines are equipotential lines.

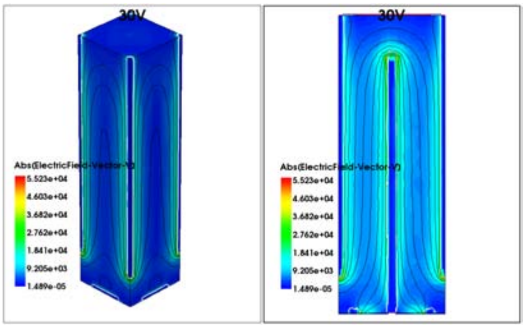

Figure 2.45: Simulation of the electric field for a FE-I4 at 30 V. The black lines are equipotential lines.

Figure 2.46 shows the simulated positions where the MIP went through perpendicularly to the columns.

Figures 2.47 and 2.48 show the simulation of the collected charge generated by a MIP crossing the position detailed in fig. 2.46 for the bias voltages of 2 V and 30 V, respectively. The average charge is calculated as:

$$Q_{average} = \frac{2Q_{x8.33} + 2Q_{x16.66} + Q_{x25}}{5} \tag{2.2}$$

where $Q_{x8.33}$ is the integrated charge of the position x=8.33 µm, $Q_{x16.66}$ is the integrated charge of the position x=16.66 µm and $Q_{x25}$ is the integrated charge of the position x=25 µm. As before, the charge belonging to the column position is

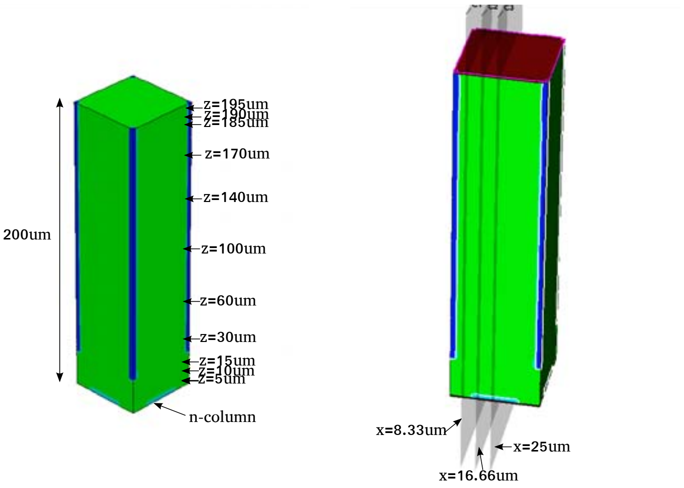

Figure 2.46: Positions of the simulations for the $z$ (left) and $x$ (right) directions.

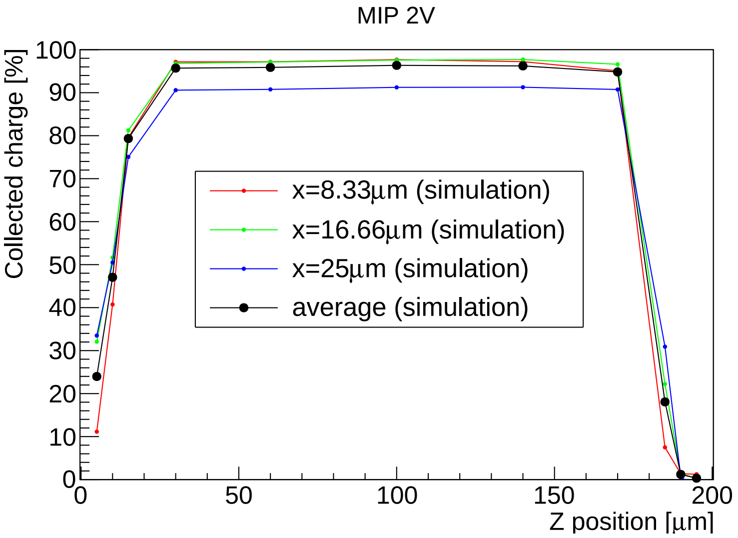

Figure 2.47: Simulation of a MIP impinging perpendicularly to the columns of a 50 µm×50 µm×200 µm 3D detector biased at 2 V.

weighted half the charge of the other positions since it is less probable.

Figure 2.47 does not show a negative signal at large $z$ positions as the simulation for the FE-I4 in figure 2.29 because this geometry the detector is almost fully depleted at 2 V. The collected charge at 30 V shows very small volume where the charge diminish, at $z$ =10 µm the charge collection efficiency almost reach 100%.

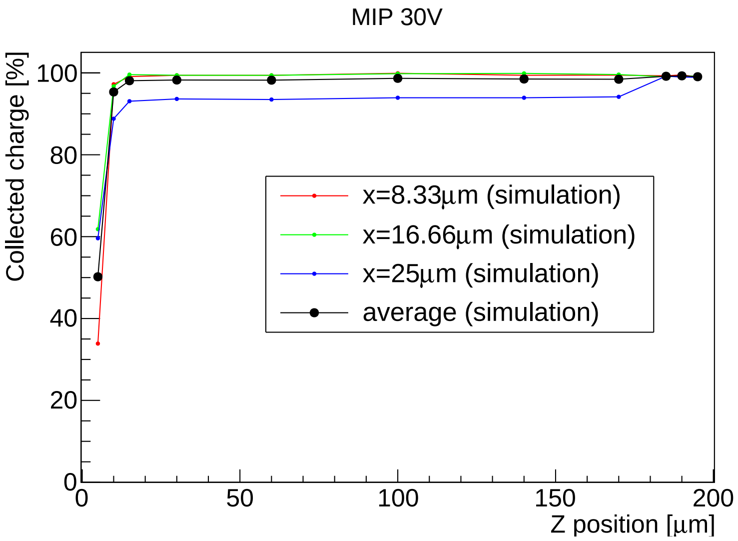

Figure 2.48: Simulation of a MIP impinging perpendicularly to the columns of a 50 µm×50 µm×200 µm 3D detector biased at 30 V.

### Columns 100 µm×25 µm×200 µm

Figure 2.49 shows the net doping profile of a 100 µm×25 µm×200 µm pixel cell. The p-stop has a radius of 12.5 µm and the columns have a diameter of 5 µm.

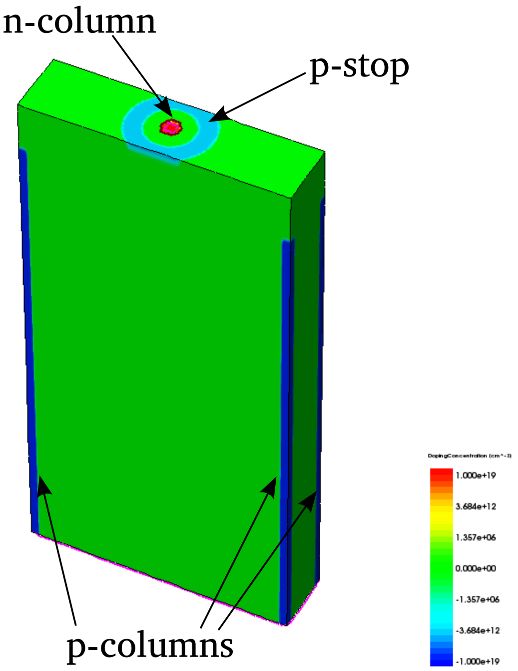

Figure 2.49: Doping profile for 100 µm×25 µm×200 µm.

Figure 2.50 shows the current-voltage curves of the detector at different fluences and up to a bias of 200 V without reaching breakdown. Figure 2.51 shows the capacitance-voltage curve of the detector for different fluences and it can be seen that the non irradiated sensor depletes at 3 V (the lateral depletion). The hump at 29 V is related to the full depletion of the detector, including the region under the n-column, as shown in [33] for simulations for similar non-crossing columns 3D detectors.

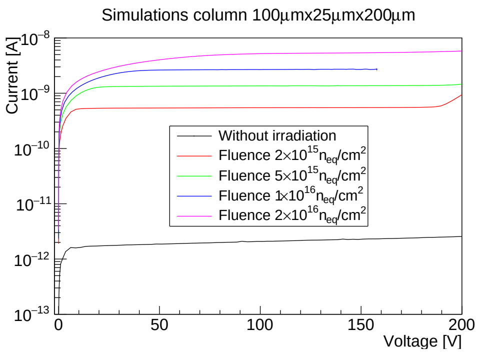

Figure 2.50: Current-voltage curves simulation for 100 µm×25 µm×200 µm.

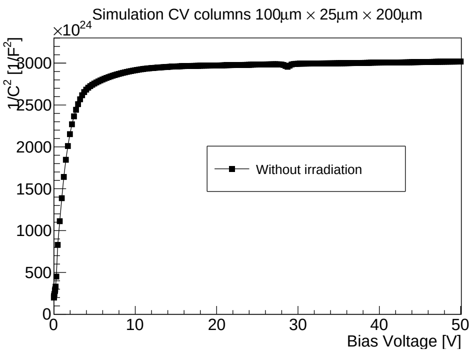

Figure 2.51: TCAD simulation of the $1/C^2$-voltage curve for 100 µm×25 µm×200 µm.

Figure 2.52 shows the collected charge of a MIP impinging the detector in a position between the two columns of the pixel (position 25 µm× 6.25 µm of figure 2.53) at different fluences. The integrated charge took into account a pixel cell, neglecting the neighboring pixels. At fluences of $2 \times 10^{16}\,\mathrm{n_{eq}\,cm^{-2}}$ the detector shows a charge collection efficiency of 30%.

Figure 2.54 shows the integrated charge of non irradiated pixel cells of 100 µm×25 µm×200 µm for a MIP crossing the pixel at different positions (shown in figure 2.53). The charge is integrated for 25 ns. The simulation used 2 pixel cells in order to take into account any collected charge by the neighboring pixel. Figure 2.55 shows the same simulation but for an irradiated device with a fluence of $2 \times 10^{16}\,\mathrm{n_{eq}\,cm^{-2}}$, normalized to the maximum charge of the non irradiated device. The collected charge after irradiation decreases to 35% efficiency.

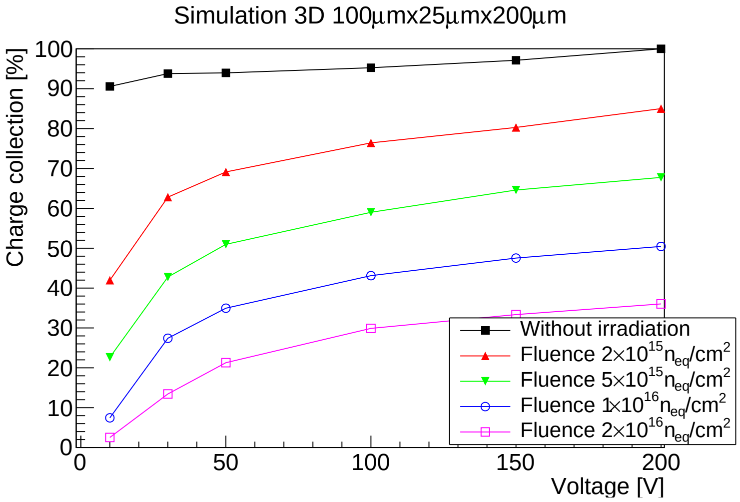

Figure 2.52: Collected charges for a MIP crossing between two columns of a 3D 100 µm×25 µm×200 µm pixel detector.

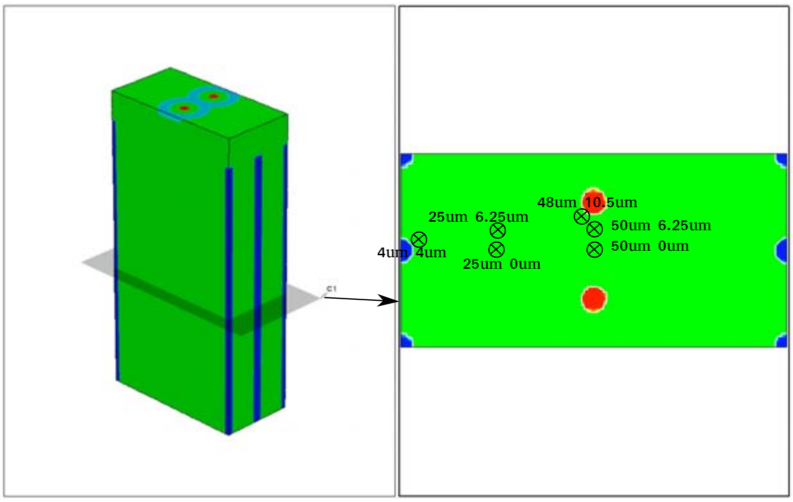

Figure 2.53: Different positions of MIP crossing the 3D 100 µm×25 µm×200 µm pixel.

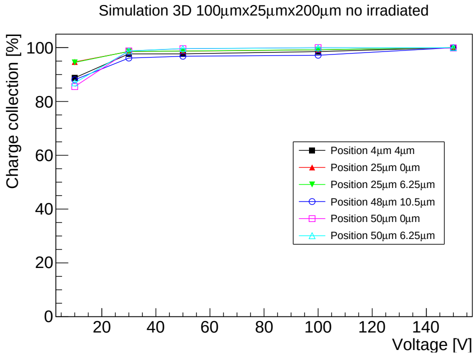

Figure 2.54: Collected charge for MIP in different positions for a non irradiated sensor.

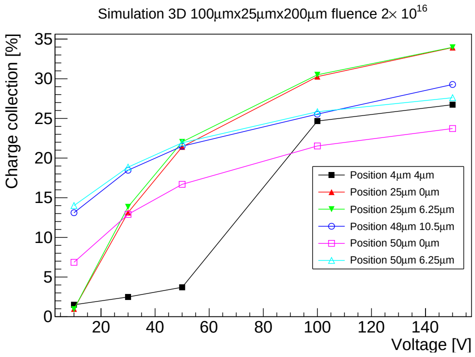

Figure 2.55: Collected charge for a MIP in different positions for an irradiated sensor at a fluence of $2 \times 10^{16}\,\mathrm{n_{eq}\,cm^{-2}}$.

### 3D single sided

Future ATLAS and LHC specifications for pixel detectors might need thinner detectors. Detectors located at large $\eta$ angles, far from the beam interaction, will receive the particles perpendicular to the column direction. In order to have a more precise detection at those positions, thinner detectors are proposed[73; 72].

Due to the complex fabrication process of the 3D detectors, the best solution to fabricate thin 3D detectors is on a Silicon-On-Oxide (SOI) wafer. A high resistivity thin silicon wafer is separated from a thicker low resistivity substrate by a Buried OXide (BOX) layer that can be removed with a wet etching process. CNM-Barcelona used this technique with several fabrications reported in [74; 75; 76], and chapter 3 covers a particular case of 3D detectors fabricated with a 50 μm low resistivity wafer in a single sided process.

Figure 2.56 shows a schematic of the 3D single sided detector proposed for the HL-LHC ATLAS experiment.

In order to test different configurations, two possible types of wafers are proposed:

- 150 μm SOI p-type wafer
- 150 μm SOI p-type wafer with a p-type backside implant

Figure 2.57 shows the simulated structures. The two structures were simulated in order to optimize the n-column depth of these 3D detectors. The simulated detectors

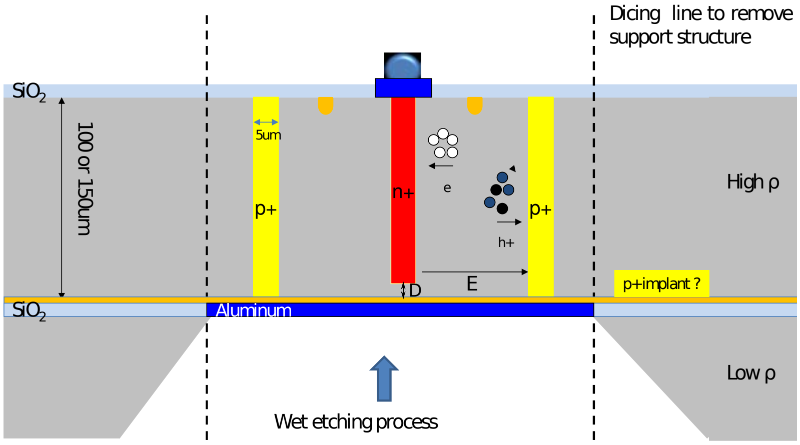

Figure 2.56: Scheme for 3D single side detector.

are single sided p-type detectors with a pixel geometry of 50 µm×50 µm×150 µm. The p-columns have a depth of 150 µm, reaching the BOX, while the n-columns will be a non crossing columns. If the n-column reach the BOX it will lead to an early break down due to the superficial currents through the silicon dioxide positive charge. The diameter of the columns are expected to be 5 µm and the p-stop will have a radius of 25 µm. The simulations are performed for different n-column depths, being $D$ the distance of the n-column to the BOX (depicted under the n-column in figure 2.56), beginning from a reference distance $d = \sqrt{25^2 + 25^2} = 35.35$ µm, which is the distance between columns. The simulated n-columns depths are:

- D=d-10 µm
- D=d-5 µm
- D=d
- D=d+5 µm
- D=d+10 µm

The simulation of those new structres is important because the DRIE process is controlled by a precision of ±10 µm.

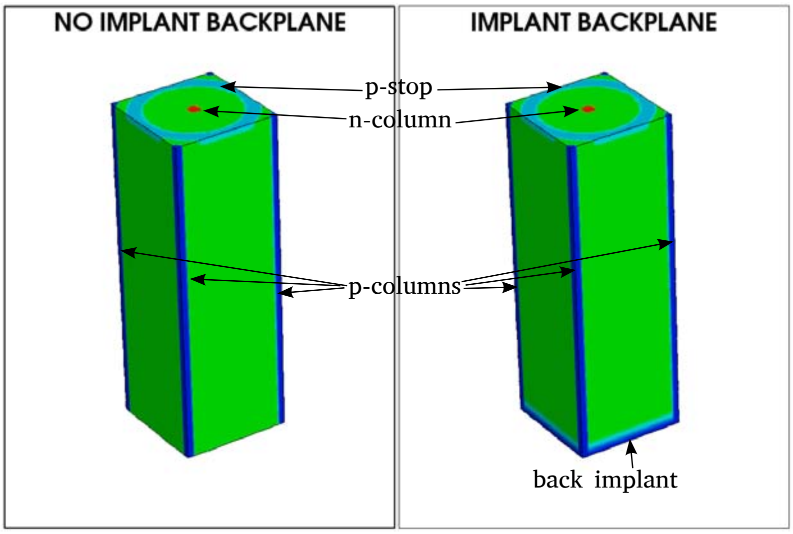

Figure 2.57: Net doping profile of the 3D single sided without implant on the backside (left) and with implant on the backside (right).

Figure 2.58 shows cross sections in a diagonal cut that includes the 2 p-columns and the n-column of the simulations of a detector without p-implant on the backside for (a) doping profiles, (b) the electric fields and (c) the electrostatic potentials.

Figure 2.59 shows the same cross sections as in figure 2.58 but with a p-implant on the backside. It shows a cross section at the n-column (including the 2 p-columns) of the simulations of a detector with p-implant on the backside for (a) doping profile, (b) the electric field and (c) the electrostatic potential.

Figure 2.60 shows the current-voltage curves of the 3D single sided detectors without p-implant in the backside (a) and with the p-implant at the backside (b).

The detector without the p-implant in the backside has slightly larger break down voltages than the detectors with the p-implant. Furthermore, the shorter the n-column the higher the break down voltage. Besides that, there is not any important difference in the leakage currents between the pixel with p-implant in the backside and without it. Anyway, the presence of the p-implant on the backside will simplify the contact of the aluminium layer deposited on the back surface of the wafer to apply the high bias voltage. In the case of the wafer without p-implant the p+ holes have to be etched through the BOX oxide in order to reach the aluminium layer used to bias the detector from the back surface.

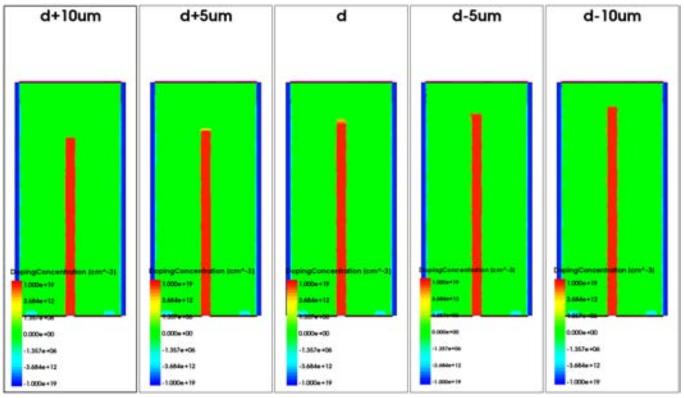

(a) Net doping profile

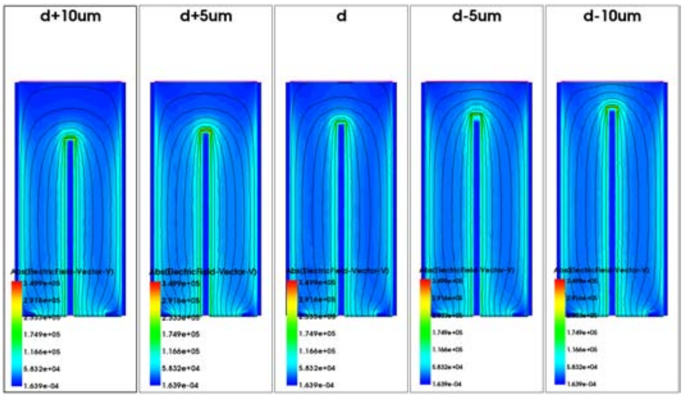

(b) Electric field, the black lines are equipotential lines

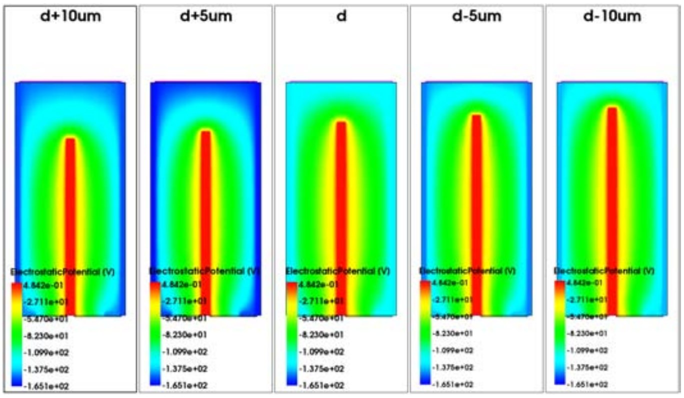

(c) Electrostatic potential

Figure 2.58: Cross sections of the simulation for the 3D single sided detectors with different depths of the columns without implant in the backplane.

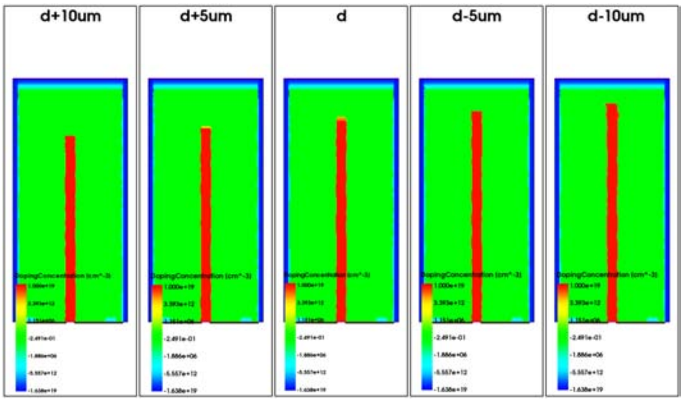

(a) Net doping profile

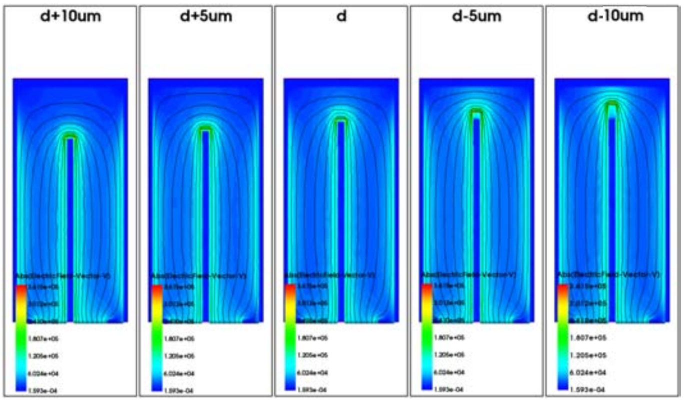

(b) Electric field, the black lines are equipotential lines

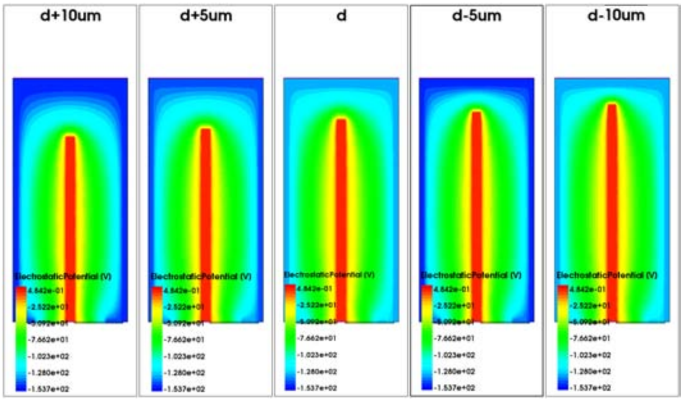

(c) Electrostatic potential

Figure 2.59: Cross sections of the simulation for the 3D single sided detectors with different depths of the columns with implant in the backplane.

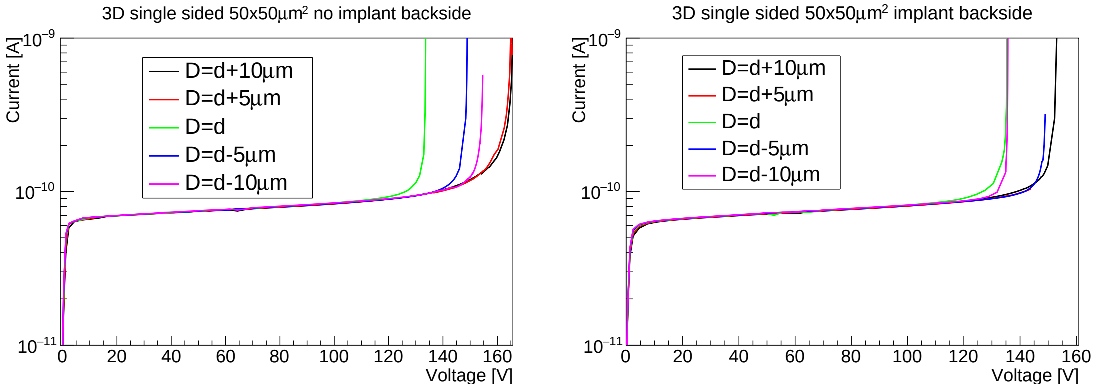

(a) No p-implant in the backside (b) P-implant in the backside

Figure 2.60: Simulation of current-voltage curves for 3D single sided 50 µm×50 µm×150 µm detector.

## 2.5 Conclusions and future work

3D detectors were first introduced into a HEP experiment at IBL in 2013 and the detectors fabricated at CNM Barcelona show a good performance. The fabrication had a good yield but one of the drawbacks was the measurement system of the detectors before and after UBM. The current-voltage curves mesured only conecting the guard ring do not show a good correlation to the measurements done after UBM with the detector diced and taking into account the current of all the contacts. New solutions to this issues are ongoing, such as the deposition of a temporary metal pads on the 3D detectors that short all the pixels together, which might have a more reliable current-voltage measurement after fabrication, and must be removed after measurement, before UBM. 3D detectors for AFP fabricated at CNM Barcelona are planned to be introduced soon in the experiment.

CNM-Barcelona is working on a cryogenic DRIE to achieve high aspect ratios up to 40:1, and fabrications of the new sensors are ongoing. The simulations of those new detectors exhibit good performance even with fluences up to $2 \times 10^{16}\,\mathrm{n_{eq}\,cm^{-2}}$, the expected fluences for the future upgrades. Simulation show that 3D detectors are a good solution for the innermost layer of the ATLAS upgrade experiment to be build in 2022.

CHAPTER

3

# 3D 50 µm single sided detectors fabricated on low resistivity wafers

As explained in the previous chapter, 3D detectors show some advantages over planar detectors:

- They are fully depleted at lower voltages.
- The probability of charge trapping is lower.
- The electric field for 3D detectors is higher and they also show charge multiplication after irradiation[44].

The fabrication of 3D detectors in thinner wafers should result in smaller column diameter (less dead area in the detector). There are two technological approaches to fabricate thin detectors:

1. Thin wafers.
2. SOI wafers.

Using thin wafers may lead to a very low yield caused by the bowing of the wafers during the fabrication process. Furthermore, the fabrication of very thin wafers (<200 µm) would be impossible with our standard technology available at CNM.

Silicon-On-Insulator (SOI) wafers offer a solution to fabricate thin detectors with thick wafers increasing the fabrication yield, since they deal with thicker wafers. The support part of the wafer can be removed after production with a wet or a dry etching process. 3D detectors on SOI wafers should be fabricated with a single sided process, and both columns should be etched from the same side (single sided 3D detector)[74; 75; 76].

This chapter is dedicated to 3D single sided (3D-SS) silicon detectors fabricated in low resistivity wafers at CNM-Barcelona. The simulations presented in [33] showed that he sensors should have high electric field that led to a charge multiplication mechanism if the correct wafer resistivity is used. Figure 3.1 shows the simulations of the full lateral depletion voltage, the breakdown voltage and the bias voltage when the gain begins (Charge Collection Efficiency CCE>100%) for wafer resistivities between 100-500Ω cm. One of the drawbacks shown by the simulations is that the use of low resistivity wafer decrease the break down voltage. Hence, the fabricated detectors might not be fully depleted before breakdown. The multiplication mechanism should appear for higher resistivity wafers which the detector will be fully depleted. This chapter reports the fabrication, electrical characterization and charge collection studies of those devices.

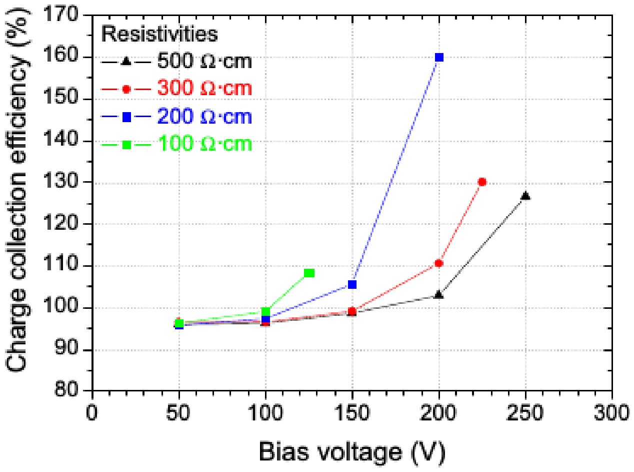

Figure 3.1: Simulation of the detector breakdown, lateral depletion voltage and voltage which CCE is higher than 100% for wafer resistivities between 100-500Ω cm[33].

## 3.1 Fabrication

The 3D-SS detectors are fabricated on a 50 µm thick SOI wafer. The total thickness of the wafer is 400 µm, and 5 wafers were processed. The wafers are p-type and have a nominal resistivity between 100-500 Ω cm. The mask used was the same as the 3D production for IBL in figure 2.3, but adapted to a single sided process and with column diameters of 5 µm. Each wafer holds 8 sensors FE-I4, 9 FE-I3, 3 CMS, 8 diodes and 4 strips detectors.

### 3.1.1 Fabrication steps

The SOI wafers were cleaned and labeled for their identification (a sketch of the wafer is in figure 3.2 (a)). As shown in figure 3.2 (b) the next step was the p-stop implantation. For that purpose, a silicon dioxide layer was grown with a wet oxidation on the silicon surface, which is typically used to grow thick oxides. The process is called wet oxidation because it uses water vapor to grow the silicon dioxide at high temperature (in this case the temperature was 1100 °C). Later, a photosensitive resist was deposited on the $SiO_2$. The resist was illuminated through the p-stop mask, exposing the p-stop parts to ultraviolet light. The exposed resist was removed with a developer solution, and afterwards, the $SiO_2$ underneath was removed with a buffered $HF$ (Hydrogen Fluoride) mixture. Then, all the resist was removed, leaving openings in the $SiO_2$ according to the pattern on the mask. After a screen oxidation (a layer of 37 nm of dry oxidation, which uses $O_2$), the wafer was implanted with boron ions.

(a) SOI wafer

(b) P-stop implantation

Figure 3.2: 3D single sided on a SOI wafer first fabrication steps. The sketch is not into scale.

Figure 3.3 (a) shows the sketch of the 35 µm deep n-columns. This process was performed with a resist mask (with a photolitographic process as explained for the p-stop, but not removing the photosensitive resist after the removal of the $SiO_2$) and the columns were etched with a Deep Reactive Ion Etching (DRIE). The DRIE is an anisotropic etching process with high aspect ratio. The DRIE used at CNM-Barcelona is the Bosch process, which alternates repeatedly a plasma etch with sulfur hexafluoride ($SF_6$) and a deposition of a passivation layer (octafluorocyclobutane $C_4F_8$). The passivation layer protects the side-wall of the holes from the etching. The DRIE was a critical process because the column should not reach the oxide of the SOI wafer (BOX) since it could lead to an early breakdown during the operation of the detector. The SEM images and photos taken after the fabrication of the device (figure 3.7 and figure 3.8) show that the n-columns reach the desired depth. After the etching of the $n^{++}$ electrodes, polysilicon was deposited on the surface and it was doped with phosphorus atoms (n-type impurity, shown in red in figure 3.3 (b)).

A $SiO_2$ layer was grown on the polysilicon to protect the n-doped zone (as shown in figure 3.4 (a)). Then 50 µm columns were etched with a DRIE process (after a photolitographic process with a resist and a $SiO_2$ mask) as shown in figure 3.4 (b). The DRIE used to etch the p-type columns was sightly different than the one from the n-type columns. The positive ions of the DRIE might be deflected by the positive charge of the BOX (buried oxide), etching the side walls of the columns instead (the side etching when the ions reach the BOX is called notching), thus a 3 gases DRIE was used to avoid the notching. Afterwards, polysilicon was deposited and doped with boron (as shown in figure 3.4 (c)). The n-columns were also filled

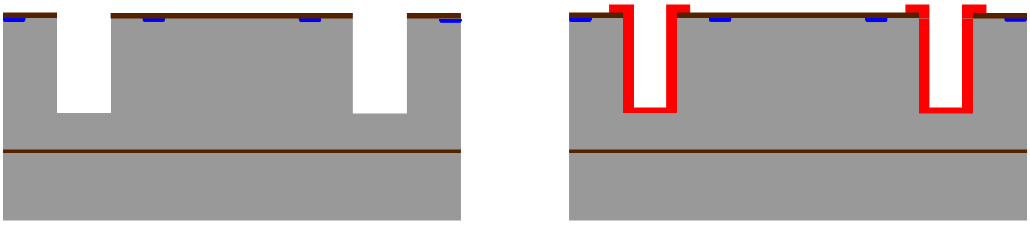

(a) DRIE 35 µm for $n^{++}$ columns (b) n-doped polysilicon

Figure 3.3: Sketch of the fabrication of the n-columns.

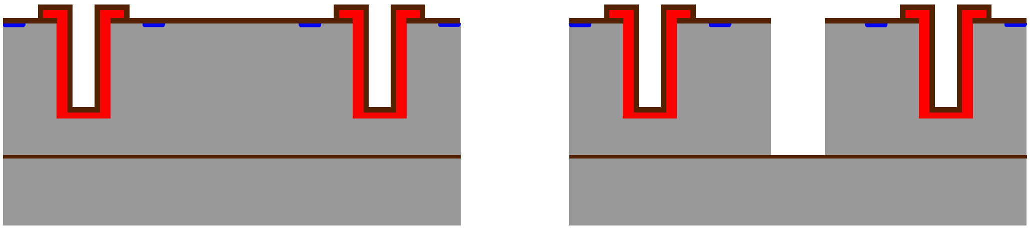

(a) Silicon dioxide

(b) DRIE 50 µm

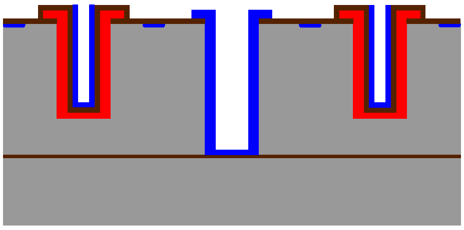

(c) p-doped polysilicon

Figure 3.4: Sketch of the fabrication of the p-column.

with p-doped polysilicon, but the silicon dioxide layer between them works as a barrier and prevents any uncontrolled diffusion.

The $SiO_2$ layer on the n-doped polysilicon was etched in order to open a contact for each column (figure 3.5 (a)). Afterwards the columns were covered with metal (aluminium) to propitiate a good contact to the electrodes (the metal is depicted in violet in figure 3.5 (b)). All the wafers were passivated in order to protect the detectors from external exposure such as humidity and scratches. Finally, the contacts were open through the passivation. Figure 3.6 shows a photo of the finished wafer.

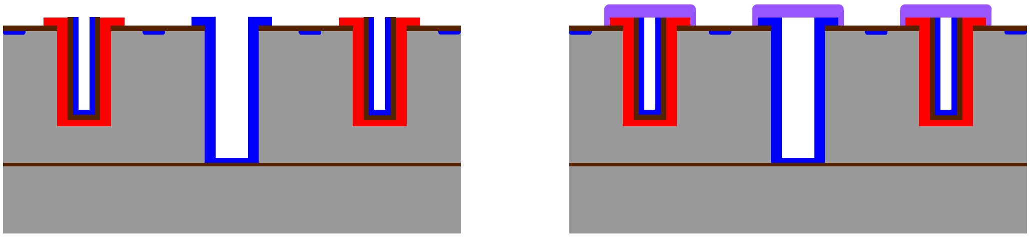

(a) Etched oxide on n-column

(b) Metal

Figure 3.5: Sketch of the etched oxide on the n-column (left) and aluminium deposition (right).

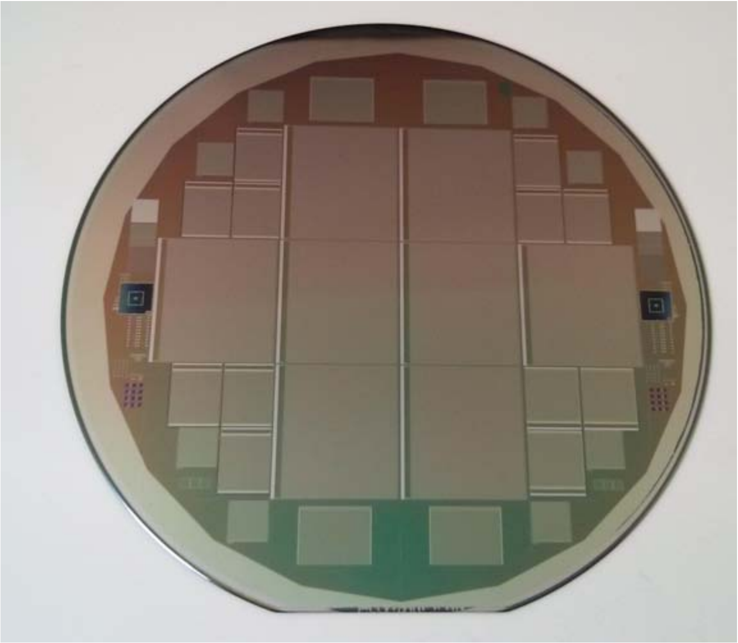

Figure 3.6: Photo of the final fabricated wafer.

### 3.1.2 Reverse engineering

Reverse engineering covers several techniques that intends to study the fabricated structures in detail. It is useful for controlling that the fabrication was as expected, such that n-columns did not reach the BOX, to observe any notching for the p-columns or to measure the size of each column. Reverse engineering slices the detector through a cross section, destroying the detector in the process and exposing the desired parts of the sensor. The detectors fabricated in this work are studied with an optical microscope and SEM images.

Figure 3.7 shows an image of the surface of a FE-I4 pixel sensor taken with a Scanning Electron Microscope (SEM). SEM uses a focused electron beam to scan the samples, giving a different response when the electrons interact with the parts of the detector. The n-electrode is different from the p-electrode since the n-columns were the first etched and they went through more fabrication steps. SEM images in figures 3.7 (b) and (c) show the detector cross section, etched with a Focused Ion Beam (FIB) in a diagonal line that included both types of columns. FIB uses a ion focused beam (usually gallium) for scanning the samples (the ions interact with the

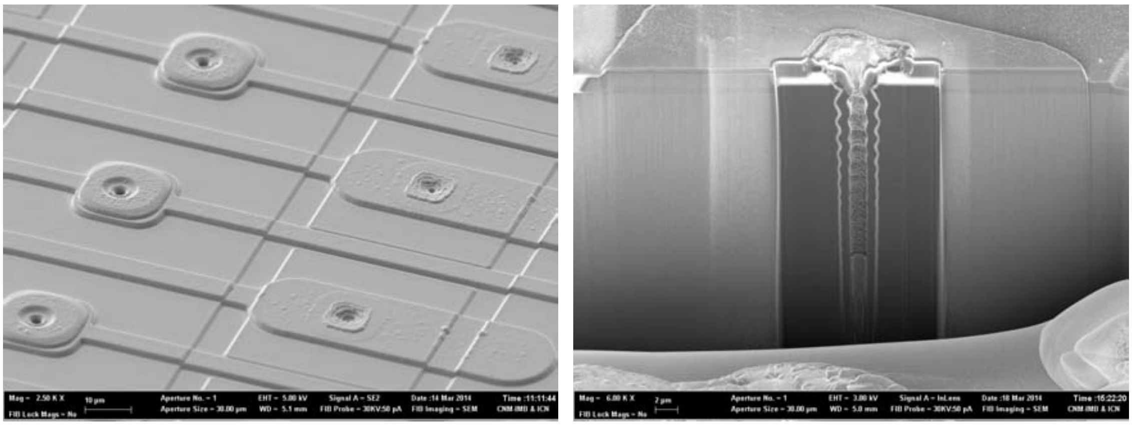

(a) Front image of FE-I4 contacts

(b) n-type column

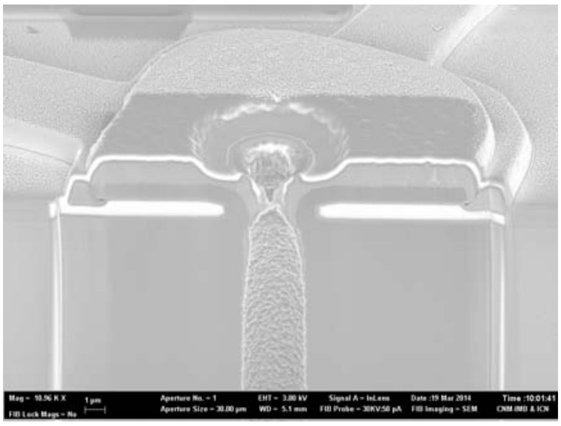

(c) p-type column

Figure 3.7: Images of the two electrodes of the FE-I4 detector taken with the scanning electron microscope at CNM. The cross section of the electrodes was done using a FIB (figures (b) and (c)).

atoms of the detector, giving a similar image as a SEM), or even etch them in a precise and slow process. The n-column in figure 3.7 (b) shows undulations at the column side wall, typical from the Bosch process.

Figure 3.8 (a) shows an image of the cross section of the columns, taken with an optical microscope. The figure shows both columns; the short one is the n-type (35 µm), the long one in the middle is the p-type (50 µm), and the horizontal line at the bottom is the BOX of the SOI wafer. The structure in the image was polished in order to reach the center of the column and take the photo, and to enhance the visibility of the n-doped and p-doped polysilicon. Figure 3.8 (b) shows a close up of the columns, where the n-column shows the n-doped polysilicon, the oxide and the p-doped polysilicon.

The columns shown in figure 3.8 are from a test structure (where the n and p-columns are aligned), and in this test structure the n-columns did not have the aluminium pad.

Table 3.1 shows the measurements of the columns width and depth, measured from figure 3.8.

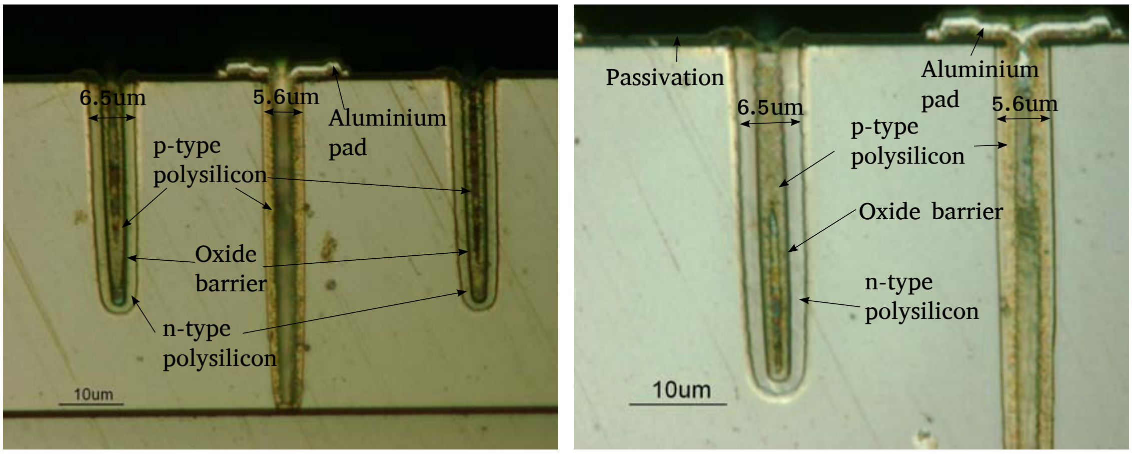

(a) Cross section of two n-columns and a p-column

(b) Cross section zoom

Figure 3.8: Cross section of the columns. The short ones are the n-columns and the long is the p-columns. The pictures are taken with an optical microscope.

| | Diameter [µm] | Depth [µm] |
|---|---|---|
| n-column | 6.5±0.1 | 35.2±0.5 |
| p-column | 5.6±0.3 | 49.7±0.5 |

Table 3.1: Measurements of the columns size.

## 3.2 Electrical characterization

The current-voltage and capacitance-voltage curves of the diodes were measured with the setup in figure 2.9. The diodes had all n-columns connected and shorted with metal lines as shown in figure 3.9. The p-columns were all connected in a similar configuration at the opposite side.

Figure 3.10 shows the current-voltage curves for all the diodes separated by wafer and the breakdown voltage is uniform at 80 V. According to the simulations in [33] the diodes are not fully depleted before they reach the breakdown.

Figure 3.11 shows the measurements of $1/C^2$-voltage for three diodes, the measurements were taken with a bridge capacitance of 10 kHz and oscillation voltage of 500 mV. They do not show any capacitance plateau before breakdown, since the $1/C^2$ curve should stabilize once the detector is depleted (as regarded in equation 1.12), hence the diodes are not fully depleted.

The capacitance for 3D detectors can be calculated as the capacitance of a concentric cylinder. Since the pad detector is not just a cylinder but an array of 69×69

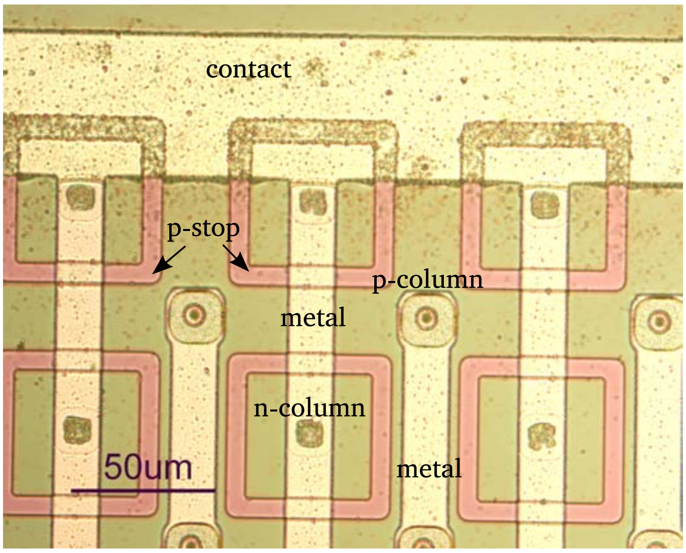

Figure 3.9: Photo of the diode contact.

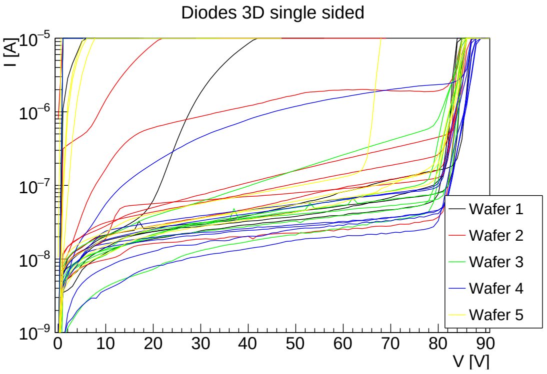

Figure 3.10: Current voltage curves for the diodes (at T=20 °C).

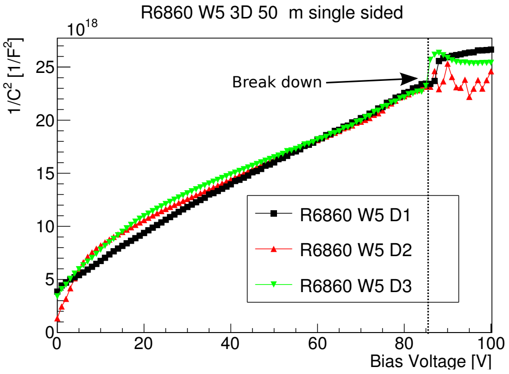

Figure 3.11: Capacitance voltage curves for 3 diodes of wafer 5 (at T=20 °C).

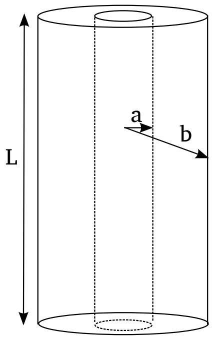

Figure 3.12: Cylinder sketch.

parallel capacitances, the total capacitance is:

$$C_{Total} = 4761 \cdot C_{cylinder} \tag{3.1}$$

The capacitance for a single cylinder is:

$$C_{cylinder} = \frac{2\pi\epsilon L}{\ln\frac{b}{a}} \tag{3.2}$$

where $\epsilon = \epsilon_0 \cdot \epsilon_{Si}$, L is the total length of the cylinder, $a$ is the inner radius and $b$ is the outer radius, as shown in figure 3.12. For a full depleted detector, the depletion voltage is given by:

$$V_d = \frac{qN_eff}{2\epsilon}\left[a^2 \ln\left(\frac{b}{a}\right) - \frac{1}{2}(b^2 - a^2)\right]$$

where $N_{eff}$ is the effective doping concentration[77]. For a not fully depleted detector, the doping profile can be calculated with the relation[78; 79]:

$$N_{eff} = \frac{1}{4\pi^2 q\epsilon b^2 L^2} \left( \frac{d(1/C^2)}{dV} \right)^{-1} \tag{3.3}$$

where $b$ is the depleted radius and can be calculated from equation 3.2, and $q$ is the electron charge. Nevertheless, the calculation for the effective doping of those wafers with the capacitance-voltage curve do not adjust to the wafer resistivity (100-500Ω cm) because the pads do not have guard ring and the active volume is not well delimited. The depleted radius cannot be measured with equation 3.2, because the depleted radius $b$ measured is very small and do not adjust to the TCT measurement of figure 3.19. During the fabrication, the measurement of the wafer resistivity was not possible with the four point probe technique due to the low resistivity of the wafer. The four point probe technique measures the sheet resistance with a current that goes through the outer probes inducing a voltage at the inner probes.

## 3.3 Charge collection characterization

### 3.3.1 Measurements with trialpha radioactive source

A 3D pad diode was glued to a PCB board and their electrodes were connected to an amplifier (setup in figure 3.13). A trialpha radioactive source was located in front of the detector, the trialpha source has three radioactive isotopes of three different elements ($Am^{241}$, $Pu^{239}$ and $Cm^{244}$), and has an alpha decay with energies detailed in table 3.2. The amplitude of the signal was collected through a MCA (Multichannel Analyzer, Pocket 9000A Amp Tek) that shows the counts per channel. The MCA requires positive pulses, thus an inverter was connected between the amplifier and the MCA.

Figure 3.14 shows the measurements taken with the MCA for the PIN diode (a) and a 3D-SS diode (b). The measurements were taken with a trialpha radioactive source located at the front of the detector, at the same distance from both detectors. The x axis shows the channel, and the y axis shows the number of counts. The measurements were taken at $-27\,°\mathrm{C}$ in order to minimize the noise.

Figure 3.15 shows the collected data of the 3D single sided diode compared with a n-on-p diode 300 µm thick, the figure shows the mean value of the gaussian fit

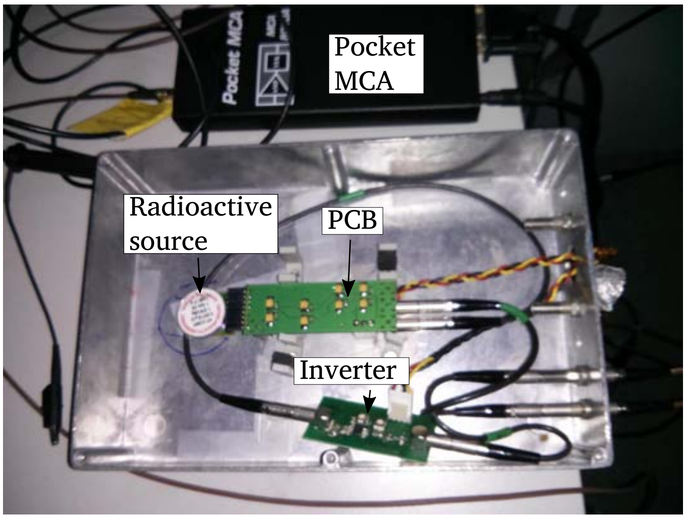

Figure 3.13: Radioactive source setup at CNM-Barcelona. The PCB is connected to a MCA through a pulse inverter. The data is collected with a laptop.

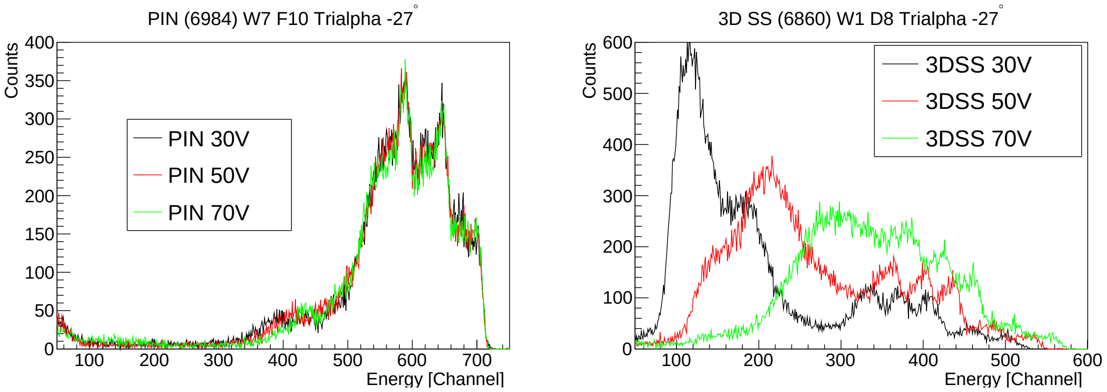

(a) PIN diode measurement with trialpha source T=−27 °C

(b) 3D-SS diode measurement with trialpha source T=−27 °C

Figure 3.14: Spectra of a PIN diode for trialpha radioactive source measurements and a 3D-SS detector.

| | $Am^{241}$ | $Pu^{239}$ | $Cm^{244}$ |
|---|---|---|---|
| Kinetic Energy [MeV]<br>(percent branching) | 5.48574±0.00012<br>85 | 5.1554±0.0007<br>73.3 | 5.80496±0.00005<br>76.4 |
| Kinetic Energy [MeV]<br>(percent branching) | 5.44298±0.00013<br>12.8 | 5.1429±0.0008<br>15.1 | 5.76283±0.000030<br>23.6 |
| Kinetic Energy [MeV]<br>(percent branching) | | 5.1046±0.0008<br>11.5 | |

Table 3.2: Energies of the isotopes of the trialpha radioactive source[1].

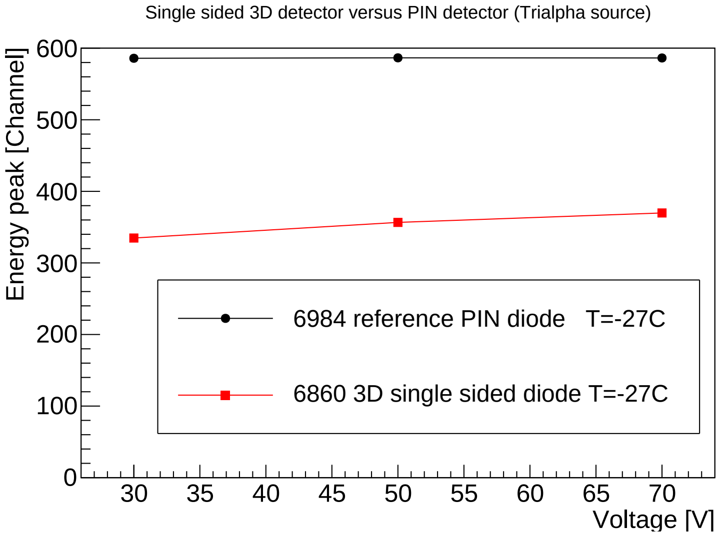

Figure 3.15: Trialpha measurements of the 3D single sided detector compared to a PIN detector.

for the less energetic peak ($Pu^{239}$). The energy collected with the 3D-SS sensor is smaller than the PIN detector, due to the fact that the 3D-SS is not fully depleted.

### 3.3.2 $Sr^{90}$ measurements

Measurements of a 3D-SS diode with the setup detailed in [80] were carried out by the experimental particle physics group of The Institute Jožef Stefan at Slovenia[81]. They used a $Sr^{90}$ radioactive source for the measurements, which emits electrons with an energy of 0.546 MeV. Two power supplies, a Keithley 2010 and a Wentzel source were used to bias the detector. Considering that MIP creates 80 electron-holes pair $\mu m^{-1}$, those electrons through the 3D single sided detector will create:

$$80 \text{ electron-hole pair } \mu m^{-1} \times 50\,\mu m = 4000 \text{ electron-holes pairs}$$

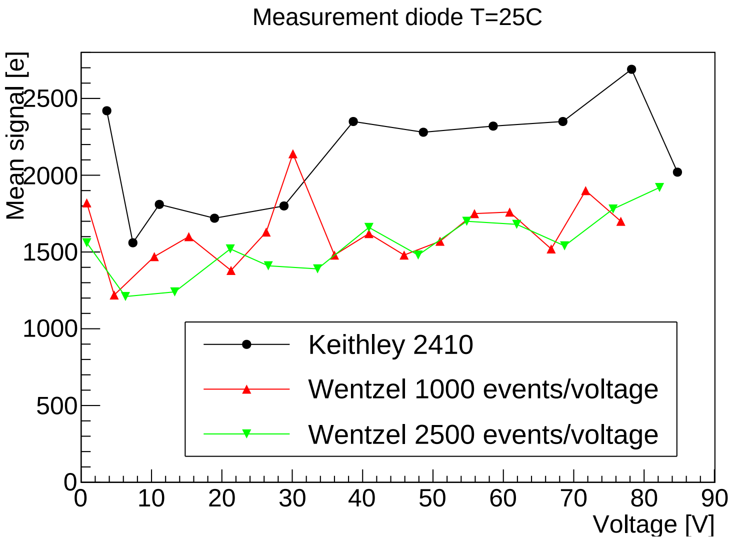

Figure 3.16: Measurements of a 3D-SS with a $Sr^{90}$ source.

As shown in figure 3.16, the measurements show only half of the signal, and this agrees with figure 3.15 which the collected energy is approximately half of the energy collected for the PIN diode. This is due to the fact that the 3D single sided detector is not fully depleted during the measurements.

### 3.3.3 TCT laser measurements

One 3D-SS diode was characterized at CERN (Geneva) with a Transient Current Technique (TCT) setup (figure 3.17). The TCT measurement collects the drifting charge carriers created in the silicon bulk, allowing to reconstruct the electric field of the detector. The setup induces the charges with a laser light in the red and infrared (IR) wavelengths ($\lambda_{red} = 660\,\mathrm{nm}$ and $\lambda_{IR} = 1064\,\mathrm{nm}$). The measurements were taken at $-20\,^{\circ}\mathrm{C}$ to reduce the noise. All scans where carried out focusing the laser from the top of the detector. The beam spot of the red and IR laser is about $10\,\mu\mathrm{m}$, the laser pulses had a frequency of $200\,\mathrm{Hz}$ and the pulse width is about $100\,\mathrm{ps}$.

The setup had a Keithley power supply to bias the sensor, laser controls, trigger control, peltier controls and an oscilloscope to collect the signal (figure 3.18 shows a photo of the electronics). The setup was controlled with a LabView program.

Figure 3.19 shows the collected signal when a region is illuminated, the charge is integrated for $25\,\mathrm{ns}$. The left image shows the TCT measurements of IR light with the detector biased at 70 V and the right image shows a photo of the scanned area of the diode. The metal lines have a width of 16 µm and they reflect the light and blind the signal from the laser (red or IR), for that reason the metal areas in figure 3.19 do not show collected charge.

The depleted volume of the detector can be extracted from figure 3.19 (left),

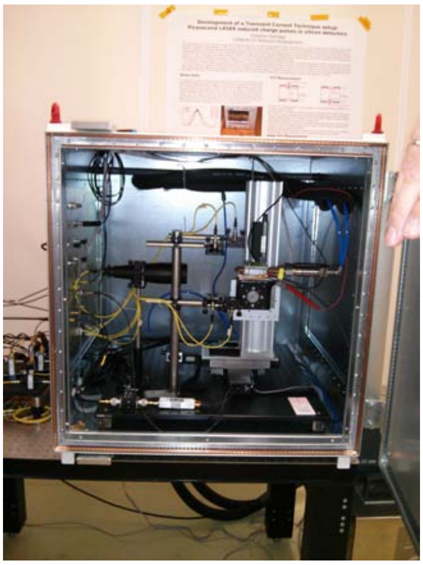

Figure 3.17: CERN laser setup.

Figure 3.18: CERN laser setup electronics.

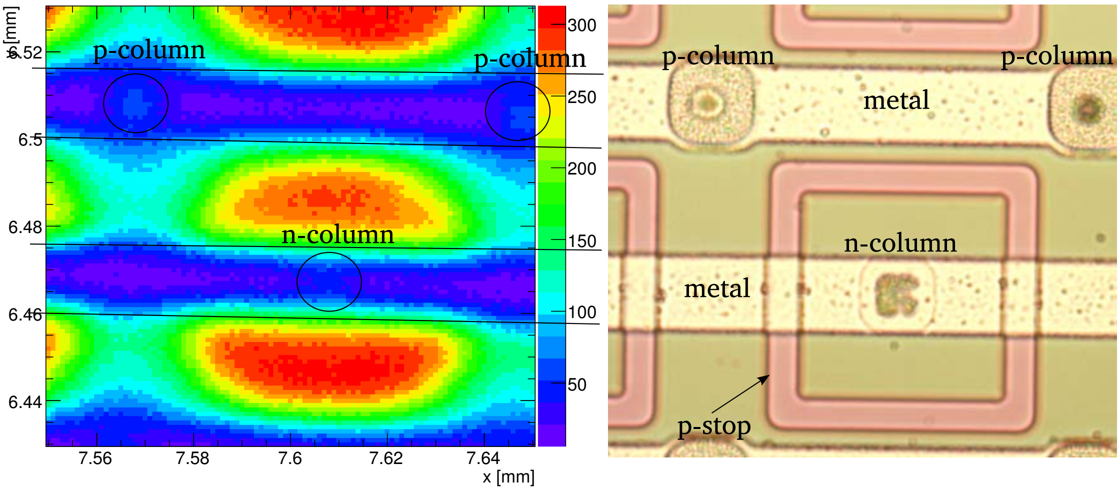

Figure 3.19: Collected charge at 70 V with IR laser (left) and front image of the diode (right).

considering the depleted radii as the Full Width Half Maximum (FWHM) of the total signal. The calculated radii is $r_d$ =36 µm ±3 µm, the error is quite big since the detector is slightly tilted (the calculation is the average of 8 different points). Using the value of that radii at 70 V, the equations 1.12 and 3.2, and $L$ =50 µm, the calculated resistivity of the wafer is 150 Ω cm ± 50 Ω cm.

Figure 3.20 shows an XY scan for the IR laser for 4 different bias voltages (10 V, 30 V, 50 V, 70 V). The data was collected for an area of 80 µm×80 µm (the pitch of the columns is 80 µm). The scan for the red laser is shown in figure 3.21. The red light penetrates only few microns into the silicon whereas the IR goes through all the volume of the detector (as shown in figure 1.13).

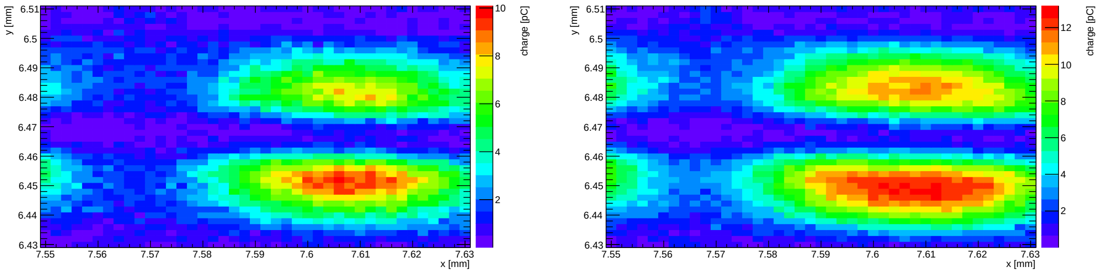

(a) V=10 V

(b) V=30 V

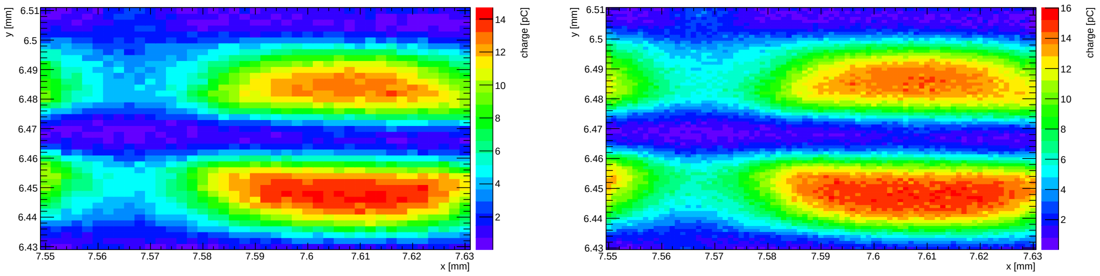

(c) V=50 V

(d) V=70 V

Figure 3.20: IR laser scan, $\lambda_{IR}$ = 1064 nm.

The signal collected at the electrodes with the laser is proportional to the electric field (equations 1.1 and 1.2 show the correlation of the drift current and the electric field). The electric field is higher near the n-electrode whereas it is almost zero near the p-electrode. Figure 3.19 (left) shows a small signal on the metal position (top left side of the scan) in the position of the p-column. It might be that the laser goes through the spot of the column in the metal and reaches the silicon creating some electron-holes pairs (due to some tilt angle of the detector). It is not visible with

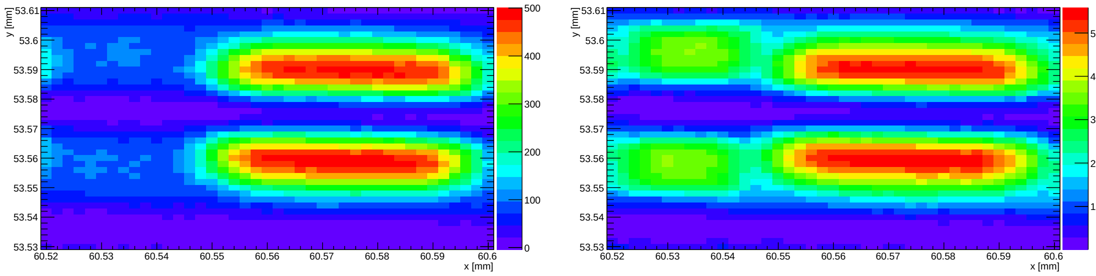

(a) V=10 V (b) V=30 V

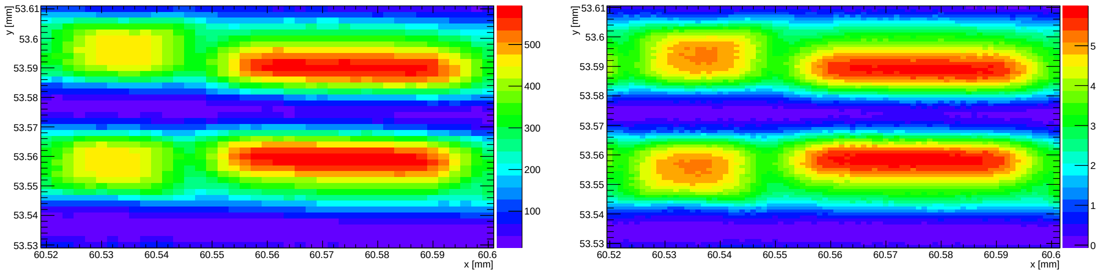

(c) V=50 V (d) V=70 V

Figure 3.21: Red laser scan, $\lambda_{red} = 660\,\text{nm}$.

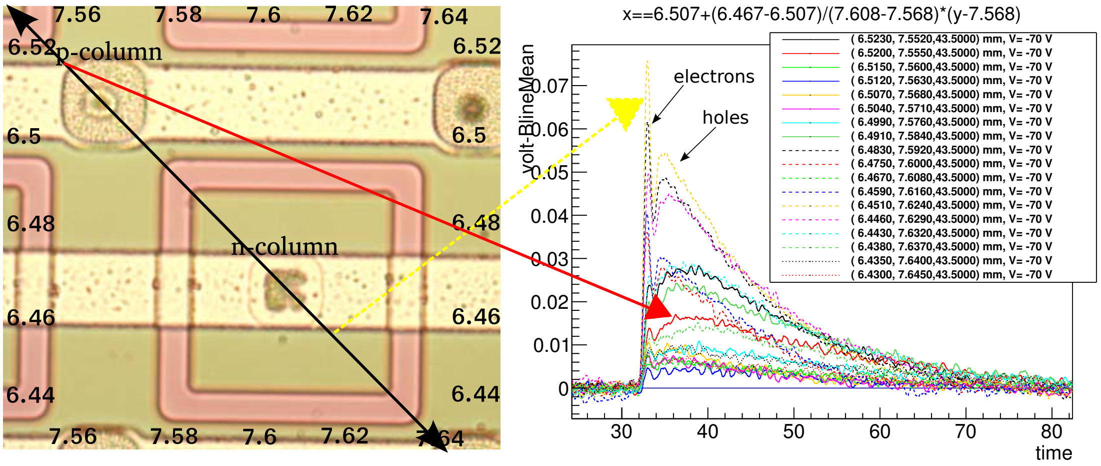

Figure 3.22: Charge collection through the line between two different columns at 70 V with IR laser.

the red laser because its light is absorbed by the polysilicon.

Figure 3.22 (right) shows the collected charge through a diagonal line between the n and the p-column, as shown in figure 3.22 (left). The first sharp pulse in figure

3.22 (right) corresponds to electrons, and the long slower pulse corresponds to holes. When the position of the laser is near the p-type column the detector is not fully depleted, thus some of the carriers are recombined, whereas for positions near the n-type columns the electrons dominate. The lower charge collected corresponds to the metal positions, where almost no charge is collected.

## 3.4 Irradiated detectors

Two pad detectors were irradiated at TRIGA Nuclear Reactor[82] with neutrons at fluences:

- $1 \times 10^{15}\,\mathrm{n_{eq}\,cm^{-2}}$
- $5 \times 10^{15}\,\mathrm{n_{eq}\,cm^{-2}}$

After irradiation, the detectors were annealed during 8 min at 80 °C[30]. Figure 3.23 shows the current-voltage curves of the detectors before and after irradiation. Although the leakage current for the irradiated devices is higher than the non irradiated detectors, the breakdown voltage is higher. Figure 3.24 shows the $1/C^2$-voltage curves for unirradiated and irradiated devices. The detector irradiated at fluences of $1 \times 10^{15}\,\mathrm{n_{eq}\,cm^{-2}}$ show a plateau after 90 V.

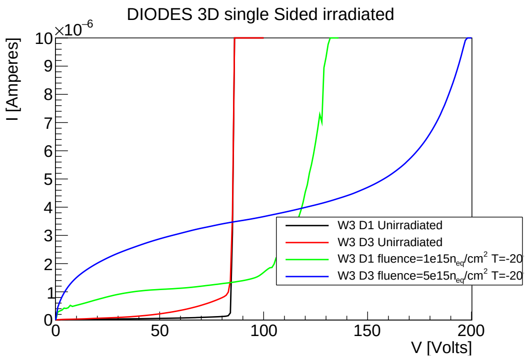

Figure 3.23: Current voltage curve for the irradiated devices. The irradiated detectors were measured at −20 °C.

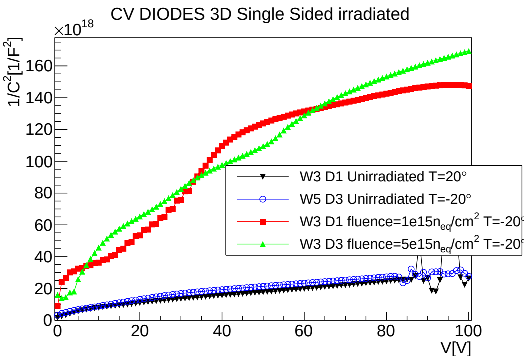

Figure 3.24: Capacitance-voltage curve for the irradiated devices. The irradiated detectors were measured at −20 °C.

The capacitance decrease after irradiation, which means that the $N_{eff}$ has decreased. This results are in agreement with [80; 83] where a decrease of the effective

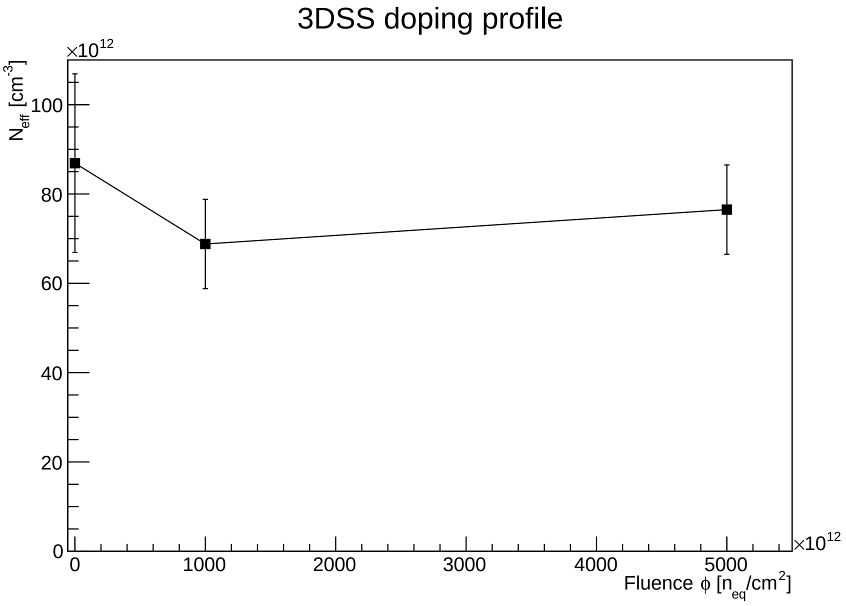

Figure 3.25: Calculations of the doping profile for the unirradiated and irradiated detectors.

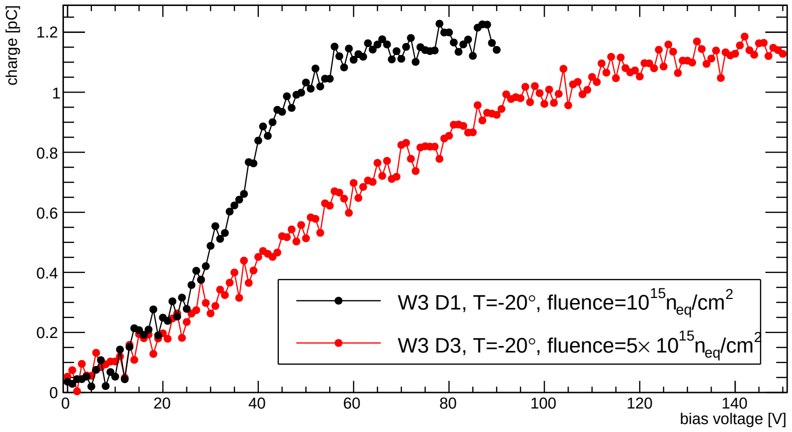

Figure 3.26: Collected infrared charge between columns of the irradiated diodes.

doping for highly doped p-implants in LGAD's and HV-CMOS low resistivity wafers are reported. Figure 3.25 shows the doping profile versus the fluence of the 3 detectors, calculated with equations 1.12 and 3.2.

The exponential fitting as described in [80] was not possible since the few data induce big error to the function. More irradiations are needed to have a more accurate study of the effective doping.

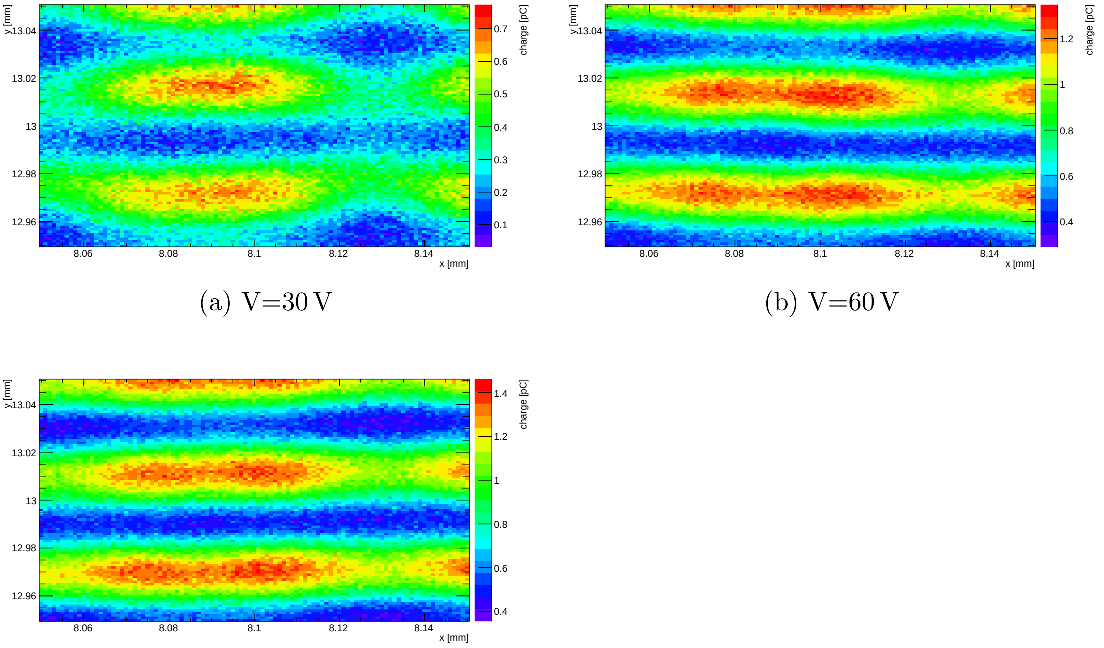

(a) V=30 V

(b) V=60 V

(c) V=90 V

Figure 3.27: IR laser scan for detector D1 irradiated at fluences of $1 \times 10^{15}\,\mathrm{n_{eq}\,cm^{-2}}$, $\lambda_{IR} = 1064\,\mathrm{nm}$.

The irradiated detectors were measured with the TCT setup at CERN (figures 3.17 and 3.18) with the IR laser, at $-20\,°\mathrm{C}$. Figure 3.26 shows the collected charge in a position between the p and n-column, with an integration time of 25 ns. The diode irradiated at fluences $1 \times 10^{15}\,\mathrm{n_{eq}\,cm^{-2}}$ reach a plateau at 60 V whereas the diode irradiated at fluences $5 \times 10^{15}\,\mathrm{n_{eq}\,cm^{-2}}$ reach the plateau at 120 V. The plateau means that the detector is depleted at the laser position, between the n and p-column.

Figure 3.27 shows the XY scan of a surface of $100\,\mu\mathrm{m}\times 100\,\mu\mathrm{m}$ for the irradiated detector at fluence $1 \times 10^{15}\,\mathrm{n_{eq}\,cm^{-2}}$ at three different bias voltages. The n-column is located at (8.09 mm, 12.99 mm) and the p-column is located at the position (8.13 mm, 13.03 mm). Figure 3.30 shows the TCT image with the location of the columns.

Figure 3.29 shows the XY scan of a surface of $100\,\mu\mathrm{m}\times 100\,\mu\mathrm{m}$ for the irradiated detector at fluence $5 \times 10^{15}\,\mathrm{n_{eq}\,cm^{-2}}$ at six different bias voltages. The n-column is located at (8.065 mm, 12.97 mm) and the p-column is located (8.105 mm, 13.01 mm). Figure 3.30 shows the TCT image with the position of the columns.

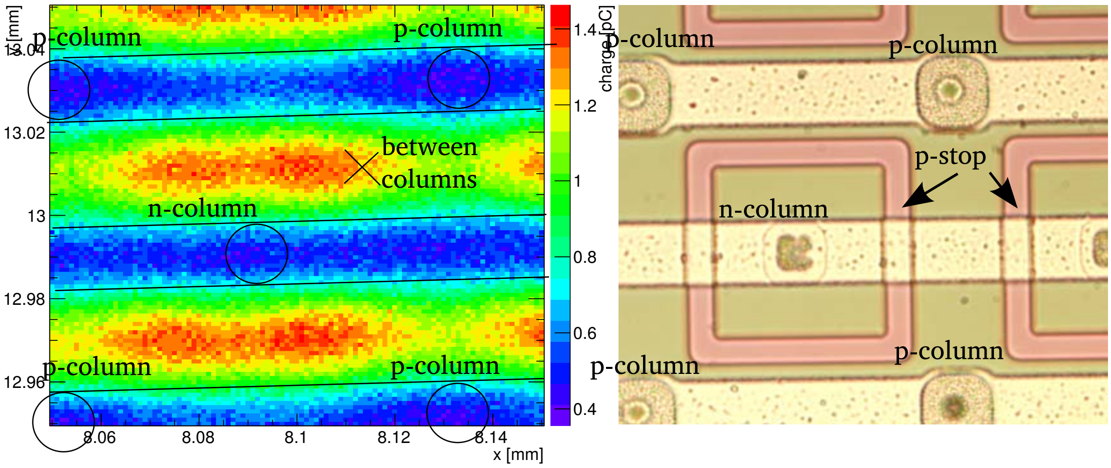

Figure 3.28: Collected charge of the irradiated sensor with a fluence of $1 \times 10^{15}\,\mathrm{n_{eq}\,cm^{-2}}$ at 90 V (left) and front image of the detector (right).

## 3.5 TCAD Simulation

TCAD simulations were carried out for a pixel cell of dimensions $80\,\mu\mathrm{m} \times 80\,\mu\mathrm{m} \times 50\,\mu\mathrm{m}$. The considered resistivity of the wafer for the simulations is $150\,\Omega\,\mathrm{cm}$ (that corresponds to a boron concentration of $9 \times 10^{13}\,\mathrm{cm}^3$). Figure 3.31 shows the simulated cell, a $80\,\mu\mathrm{m} \times 80\,\mu\mathrm{m} \times 50\,\mu\mathrm{m}$ structure with the $50\,\mu\mathrm{m}$ p-columns in blue and the $35\,\mu\mathrm{m}$ n-column in red. All the simulations were carried out with a temperature of $-20\,°\mathrm{C}$, and the oxide dioxide charge considered for the unirradiated device is $Q_{ox} = 10^{11}$ and $Q_{ox} = 1.5 \cdot 10^{12}$ for the irradiated devices.

Figure 3.32 shows the electric field at breakdown (114 V). The white line shows the depleted volume of the structure, and it does not reach all the volume of the pixel, showing a non fully depleted structure.

The simulations were run for non irradiated device, for an irradiated device with a fluence of $1 \times 10^{15}\,\mathrm{n_{eq}\,cm^{-2}}$ and for an irradiated device with a fluence of $5 \times 10^{15}\,\mathrm{n_{eq}\,cm^{-2}}$ (as the detectors measured previously). The traps model used is detailed in table 1.9.

Figure 3.33 shows the simulated current-voltage curves (multiplied by the number of columns at the detector) compared to the measured data of figure 3.10 and

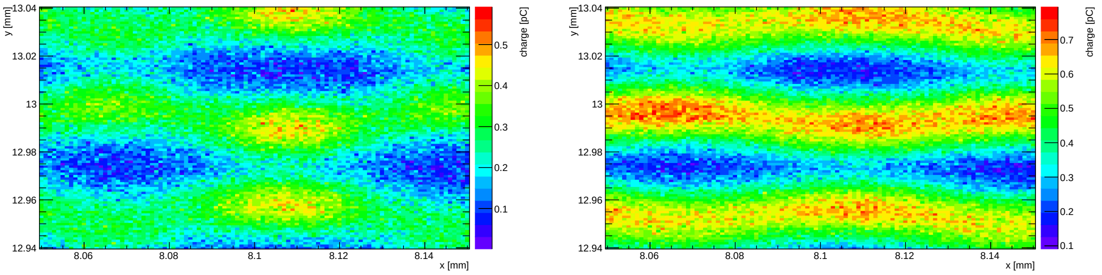

(a) V=25 V (b) V=50 V

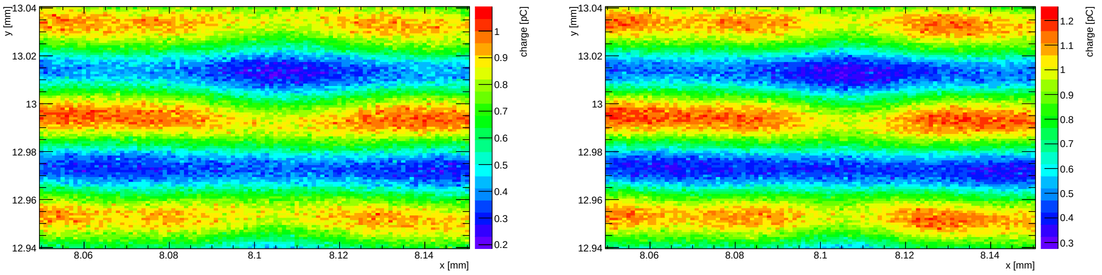

(c) V=75 V (d) V=100 V

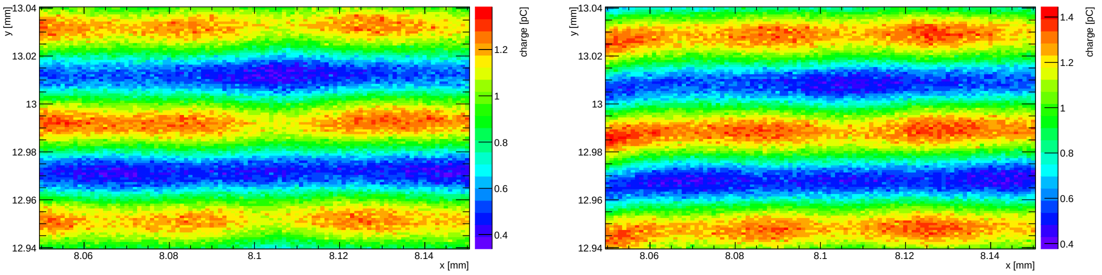

(e) V=125 V (f) V=150 V

Figure 3.29: IR laser scan for detector D3 irradiated at fluences of $5 \times 10^{15}\,\mathrm{n_{eq}\,cm^{-2}}$, $\lambda_{IR} = 1064\,\mathrm{nm}$.

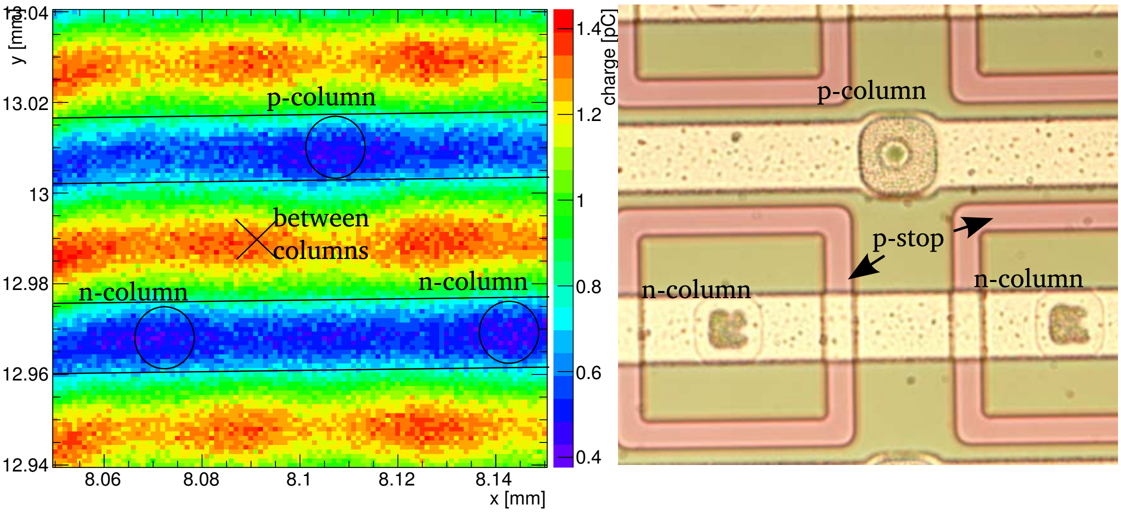

Figure 3.30: Collected charge of the irradiated sensor with a fluence of $5 \times 10^{15}\,\mathrm{n_{eq}\,cm^{-2}}$ at 150 V (left) and front image of the detector (right).

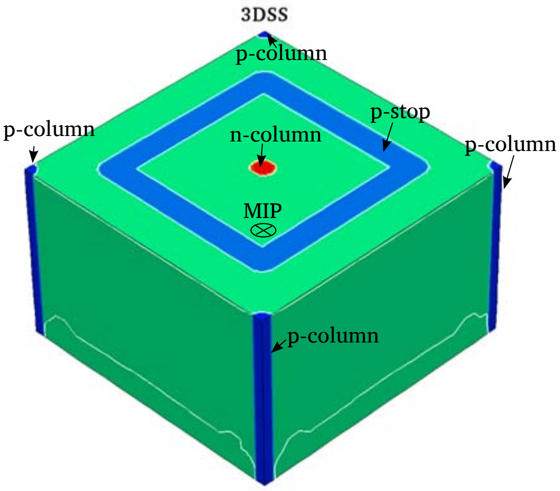

Figure 3.31: Design of the simulated 3D single sided structure.

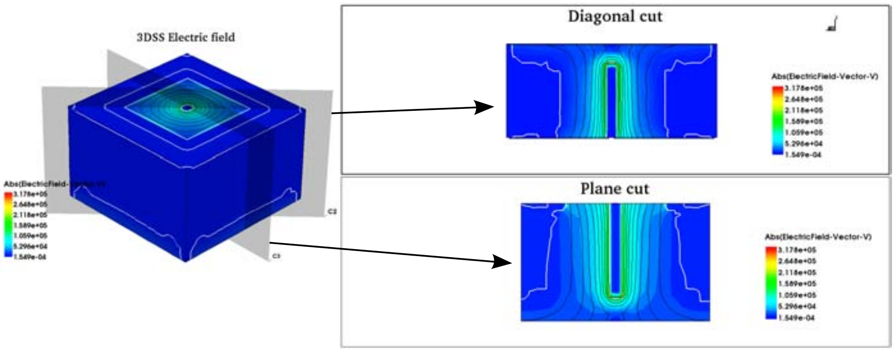

Figure 3.32: Electric field at breakdown for all the cell (left) and through a diagonal cut (right). The black lines are the equipotential lines.

they show a fairly good agreement although the break down voltage is not the same. Figure 3.34 shows the simulation of the capacitance compared to the measured data of figure 3.11 (the simulation took into account all the columns as explained in equation 3.1). The measured data have higher leakage current because the lack of guard ring and the error associated to the substrate resistivity of the wafer. Besides, the capacitance-voltage curve simulations do not fit the measured data because the simulation does not take into account the change of the effective doping profile.

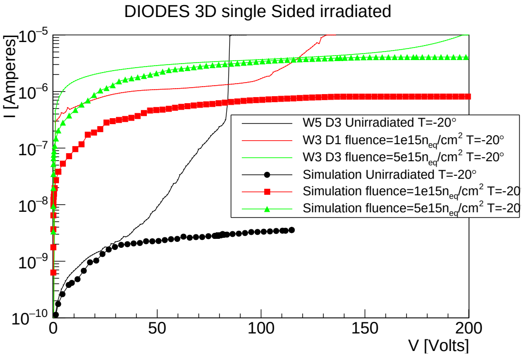

Figure 3.33: Current voltage curves for the irradiated devices compared with the simulations.

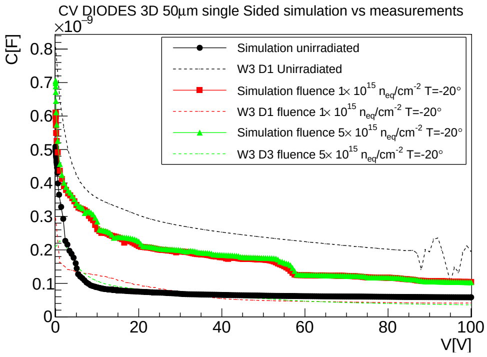

Figure 3.34: Capacitance-votage curves for the irradiated devices compared with the simulations.

Figure 3.35 shows the electric field at breakdown for the unirradiated and irradiated devices, and the simulation of the irradiated detectors shows the detector fully depleted.

Figure 3.36 shows the comparison of the TCT measurement and the charge collection simulation of the unirradiated structure. The measurement is taken from

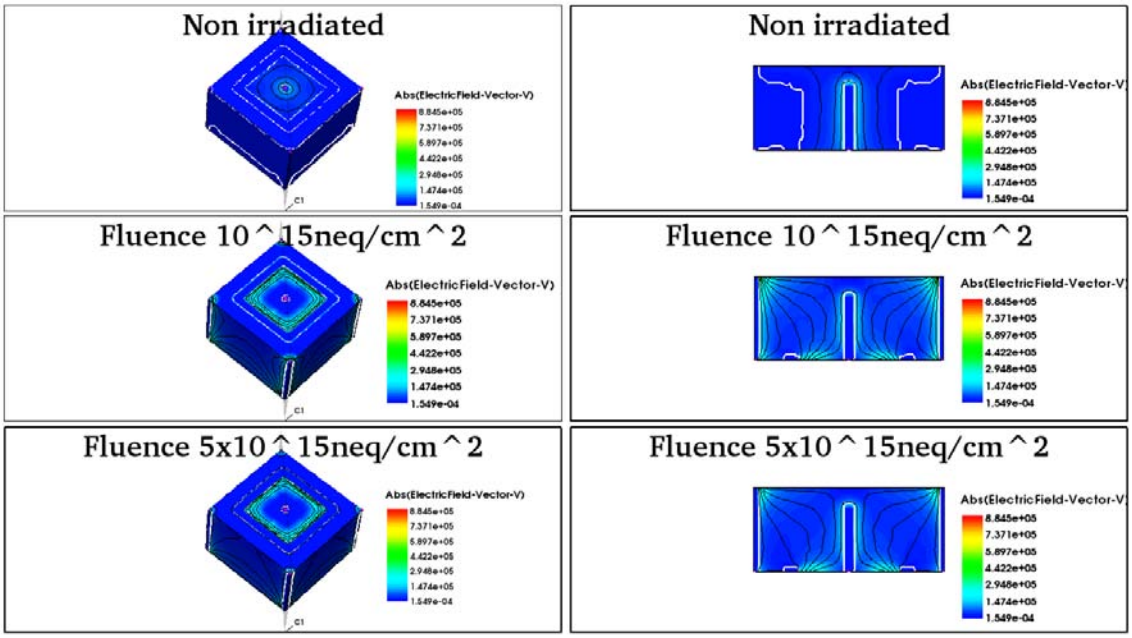

(a) Electric field

(b) Electric field at a diagonal cut

Figure 3.35: Simulation of the electric field at breakdown for different irradiations.

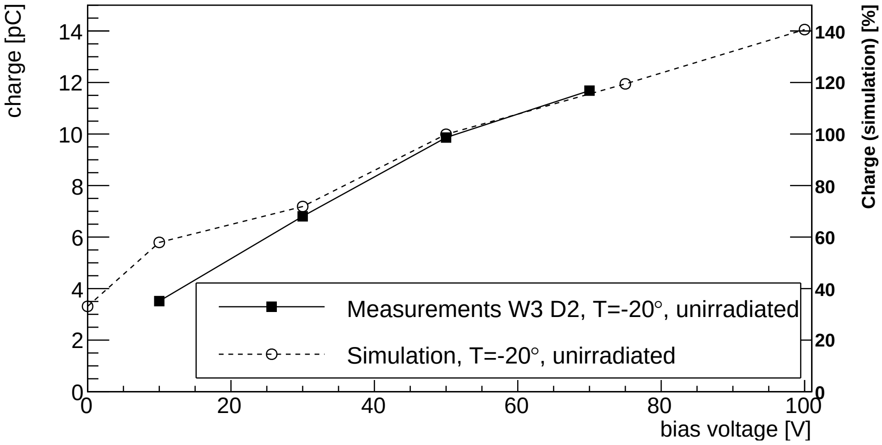

Figure 3.36: Simulation of a MIP particle impinging between the n and p-column, compared with the data from figure 3.20.

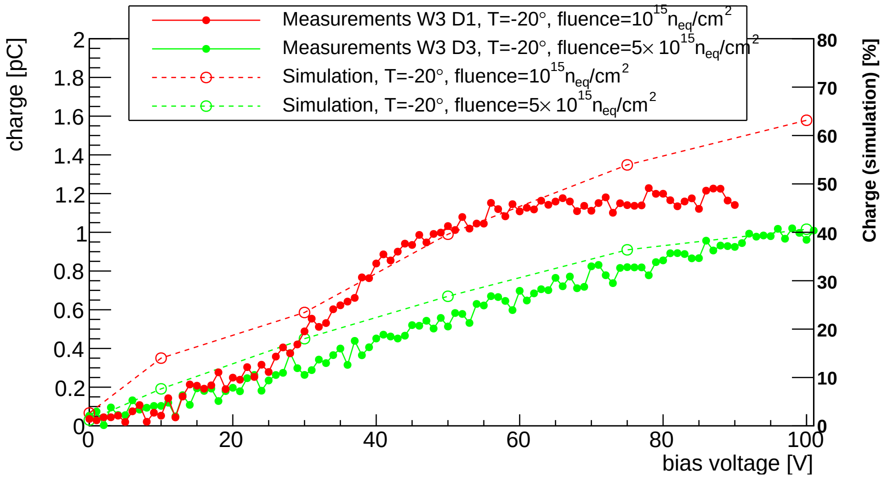

Figure 3.37: Simulation of a MIP particle impinging between the n and p-columns, compared with the data from figure 3.26.

figure 3.20, integrating the charge at the position between the two columns. Since the unirradiated measurements and irradiated measurements were not taken in the same moment, they are not comparable because the setup was changed, and the unirradiated ones are not callibrated. The unirradiated simulations show some charge multiplication but when the detector is not fully depleted, after 70 V, after the detector break down. Figure 3.37 shows the simulation of a MIP going through the irradiated detector in a position between the n and p-column (shown in figure 3.31) compared with the measurements taken in 3.26. The simulation shows an increment of the collected charge with the bias voltage, as expected by in results[84].

## 3.6 Conclusions and future work

This chapter reports 3D single sided detector fabricated in a low resistivity substrate wafer. The detectors fabricated are fully functional, although they break down before the full depletion of the sensors. The calculated resistivity of the wafer is 150 Ω cm ± 50 Ω cm which is given by the wafer, far from the optimal one according to the simulations which at 500 Ω cm the detector would be fully depleted and show some multiplication after irradiation. Diodes were measured before and after irradiation with the transient current technique, showing a depleted radius of $r_d$ = 36 µm ±3 µm. The measurements and the simulations do not show a good agreement due to the non delimited area of those diodes and the change of the effective doping concentration after irradiation. Pixel detectors with FE-I4 and FE-I3 electronics will soon be bump bonded for measurements, since the detectors are interesting for the ATLAS upgrade for their thickness.

New fabrication of thin detectors are planned although using high resistivity wafers in order to ensure that they can be operated at full depletion before breakdown.

CHAPTER

4

# Strip and pad sensors with Low Gain Avalanche Detectors (LGAD) fabricated in epitaxial wafers

Standard silicon detectors have a response time of a few nanoseconds. The 3D configuration has a shorter response time than the planar one, since the drift path in a 3D detector is typically shorter than in a planar. Thinner wafers were proposed for faster planar detectors, known as Ultra Fast Silicon Detectors (UFSD)[85]. On the other hand, when the thickness of the detector decreases, the signal decreases significantly.

The collected charge in a silicon detector increases with the electric field, and as pointed out in chapter 1, implanting a p-layer beneath the n-electrode in an n-on-p detector, creates a high electric field region, which can lead to a multiplication mechanism (Low Gain Avalanche Detectors or LGAD). This chapter presents the simulation, fabrication, electrical characterization and charge collection for segmented and pad LGAD fabricated on FZ and thin epitaxial wafers.

## 4.1 Motivation

### 4.1.1 Ultra Fast Silicon Detectors (UFSD)

Thinner detectors should provide a readout chain with[85]:

- Ultra-fast timing resolution [10's of ps]
- Precision location information [10's of µm]

Those detectors are candidates for aplications such as medical PET, mass spectroscopy or particle tracking[86]. Those applications need fast rising time of the pulse, which provides fast signals.

P-type epitaxial layers grown on thick support wafers should provide thin detectors with ultra fast timing resolution. The support wafers must have a low resistance (highly p-doped) that will work as an ohmic contact. Different thicknesses of epitaxial wafers were proposed (shown in table 4.1) to study its collection time.

| Wafer thickness [µm] | Capacitance [fF] | Signal [# of e-] | Collection Time [ps] | Gain required for 2000 e- |
|---|---|---|---|---|
| 0.1 | 2500 | 8.3 | 1.3 | 241.0 |
| 1 | 250 | 83 | 12.5 | 24.1 |
| 2 | 125 | 166 | 25.0 | 12.0 |
| 5 | 50 | 415 | 62.5 | 4.8 |
| 10 | 25 | 830 | 125.0 | 2.4 |
| 20 | 13 | 1660 | 250.0 | 1.2 |
| 100 | 2.5 | 8300 | 1250.0 | 0.2 |
| 300 | 0.8 | 24900 | 3750.0 | 0.1 |

Table 4.1: Collection times for different wafer thicknesses proposed in [85].

According to the results in table 4.1, the convenient thicknesses are 2 µm, 5 µm and 10 µm since they need a moderate gain but they are fast enough to improve the time resolution[87].

As shown in the right column of table 4.1, thin detectors need some gain to reach the minimum signal of 2000 electrons, therefore some gain is required.

### 4.1.2 Low Gain Avalanche Detectors (LGAD)

CNM-Barcelona developed high energy particle detectors, called LGAD, with an intrinsic charge multiplication[18]. As explained in chapter 1, those detectors have a n-contact with a p-doped implant beneath (multiplication layer), creating a junction with high electric field where an avalanche mechanism takes place. Figure 4.1 shows a scheme of a $5 \times 5$ mm$^2$ LGAD pad, the phosphorus is colored in red and the boron in blue. The metal contacts are located at the edge of the detector and underneath them a deep phosphorus layer is implanted (known as Junction Termination Extension, or JTE) that avoids high electric fields at the edge of the detectors[88].

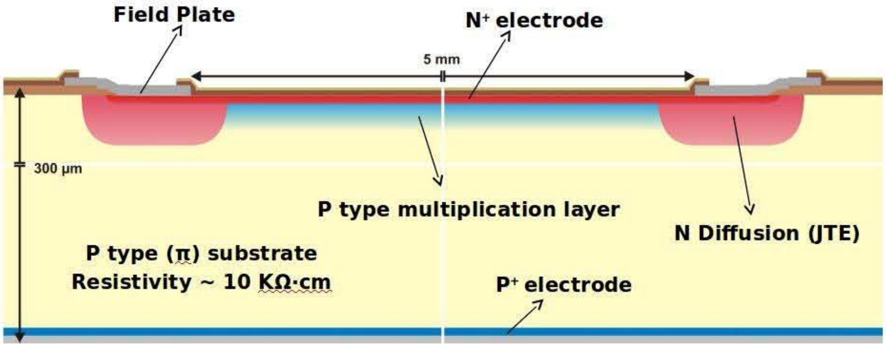

Figure 4.1: LGAD detector [18].

LGAD reported moderate gain (between 10 and 20 at 1000 V)[89; 19]. Increasing the boron dose in the multiplication layer increases the gain, as well as the slope of the current-voltage curve and decreases the break down voltage[18]. Ref. [90] shows LGAD simulations which considered the gain associated with the boron concentration and the boron peak. Figure 4.2 shows the current-voltage curves of LGAD fabricated in wafers with different boron doses, whereas figure 4.3 shows the measurement of the gain for a LGAD detector. The gain is calculated with the Charge Collection Efficiency (CCE) of LGAD and normalizing with the CCE of a PIN reference detector[18].

Figure 4.4 shows three TCT measurements, taken with an $Am^{241}$ radioactive source located at the back of the detector, for diodes of three doping profiles biased at 800 V. W13 (in black) does not have an intrinsic gain, W7 has a boron dose of $1.8 \times 10^{13}$ cm$^{-2}$ and W8 has a boron dose of $2 \times 10^{13}$ cm$^{-2}$. The initial pulse, which is the same for the three of them, shows the electrons generated by the incoming particles. The second part of the pulse, from 4 ns to 10 ns, is only present for the

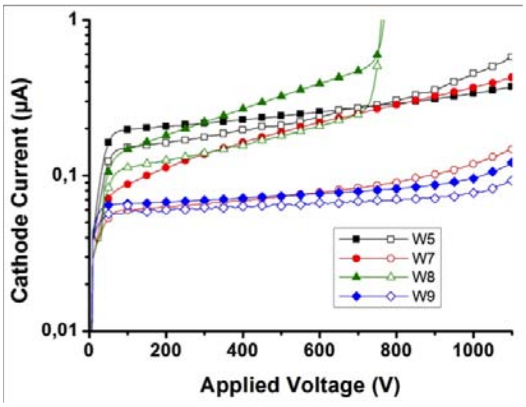

Figure 4.2: Current-voltage curves for wafers with different boron doses.

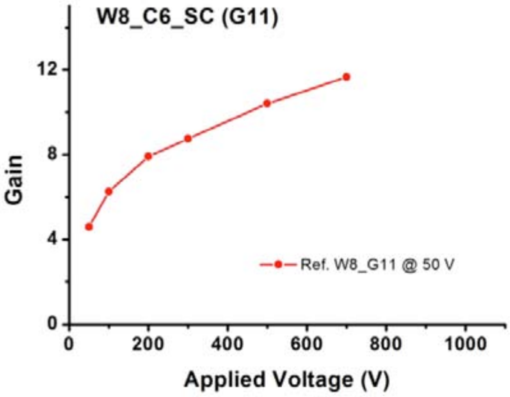

Figure 4.3: Gain for LGAD measured in a pad detector.

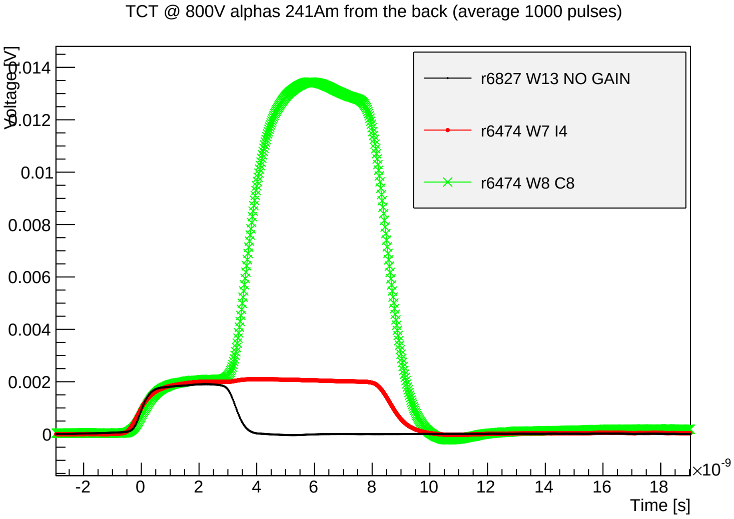

Figure 4.4: Three TCT measurements for different sensors. W13 in black is a detector without gain, W7 in red shows a gain of approximately 2 and W8 in green has gain up to 14. The initial pulse is the same for the three detectors. The second part of the pulse corresponds to the multiplied carriers[91].

pads with gain and corresponds to the multiplied signal. Wafer 8, in green, has higher boron dose and it shows larger gain.

However, LGAD showed that, after irradiation, the boron dose decreases and consequemtly the multiplication decreases, reaching values similar to those of standard PIN[80]. Currently, efforts for fabricating the multiplication layer with heavier ions than boron, such as gallium[92], are ongoing.

### 4.1.3 LGAD fabricated on epitaxial wafers

This chapter covers the fabrication, characterization and simulation of UFSD with LGAD fabricated in epitaxial wafers with intrinsic gain. The goal is to compensate the loss of signal in thin UFSD with the gain provided by LGAD. The fabrication used four different kinds of wafers:

1. Epitaxial 10 µm
2. Epitaxial 50 µm
3. Epitaxial 75 µm
4. Float Zone (285 µm)

RD50 collaboration[11] bought the epitaxial wafers for this fabrication, and their thickness and resistivity were fixed. Each type of wafers were fabricated with three different doping profiles, modifying the diffusion times and temperatures for the activation of the ions in the crystal lattice. These three doping profiles should induce different electric fields on each detector bearing in mind that a high electric field in the junction or at the edge of the detector can lead to an early break down. The three doping profiles are refererred as:

1. Shallow
2. Standard
3. Deep

## 4.2 Device design

The wafer mask holds different detectors such as FE-I4, FE-I3, CMS pixels detectors, AC and DC strips and pad detectors. The mask was designed using the software Cadence Design Systems, Inc.[93], which offers a suite to design the different layers. Figure 4.5 shows all the layers of the full wafer mask, and the position of the different detectors.

AC strips were designed with different strip and metal widths, the details are reported in table 4.2. Figure 4.6 shows a sketch of three different strip widths

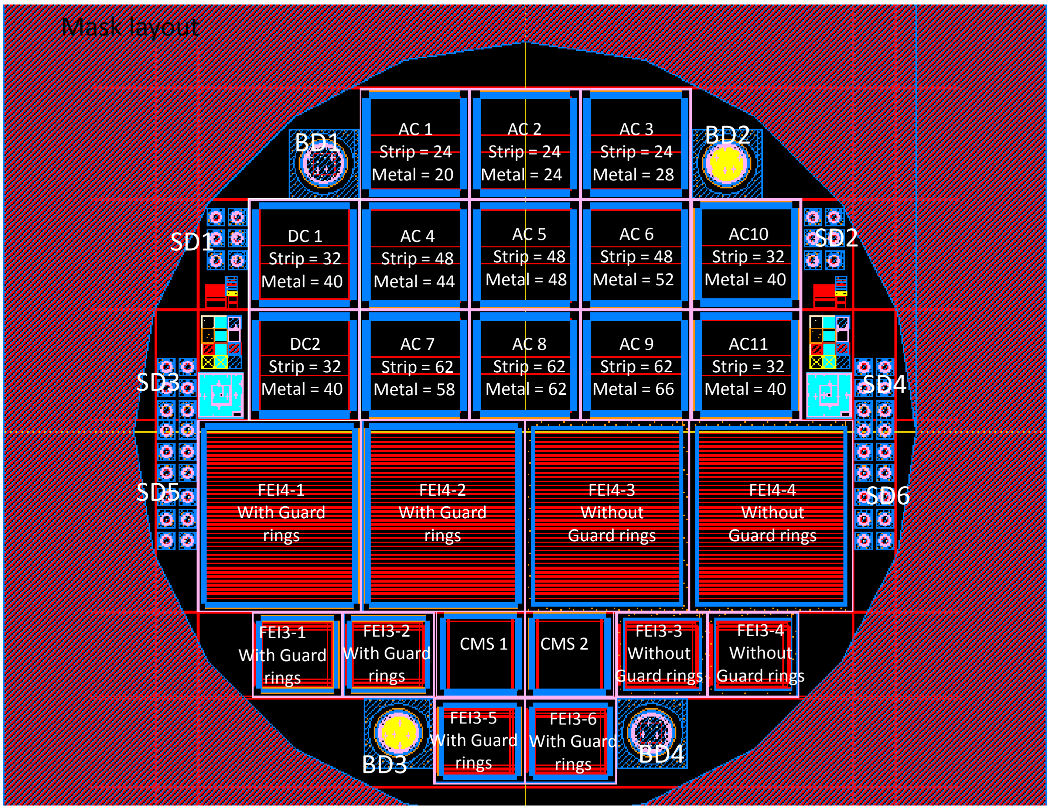

Figure 4.5: Wafer layout. The border of the wafer holds pad detectors with and without gain of 4 mm and 1 mm diameter.

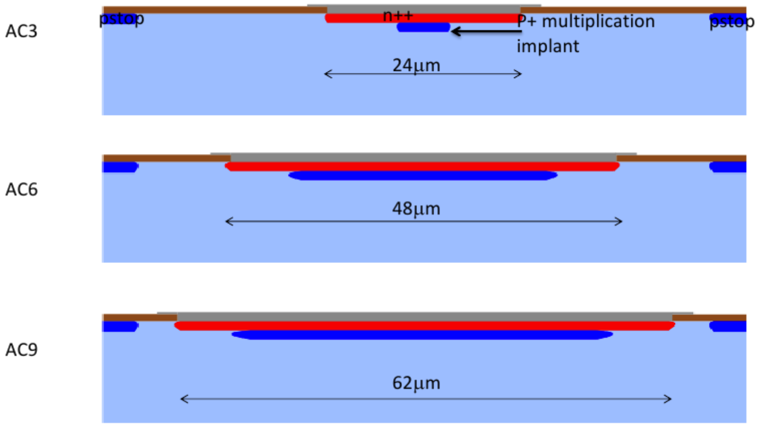

Figure 4.6: AC3, AC6 and AC9 strips layout. The phosphorus implant is coloured in red and the boron in blue.

| | Strip [µm] | Metal [µm] | P-implant [µm] | $w/p$ |
|---|---|---|---|---|
| AC1 | 24 | 20 | 6 | 0.3 |
| AC2 | 24 | 24 | 6 | 0.3 |
| AC3 | 24 | 28 | 6 | 0.3 |
| AC4 | 48 | 44 | 30 | 0.6 |
| AC5 | 48 | 48 | 30 | 0.6 |
| AC6 | 48 | 52 | 30 | 0.6 |
| AC7 | 62 | 58 | 44 | 0.775 |
| AC8 | 62 | 62 | 44 | 0.775 |
| AC9 | 62 | 66 | 44 | 0.775 |
| AC and DC | 32 | 40 | 14 | 0.4 |

Table 4.2: Widths of the AC strip detectors. The strip pitch (distance between strips) is $p$ =80 µm. The last column of the table shows the strip width divided by the pitch.

(AC3, AC6 and AC9). All the strips have a pitch (distance between two strips) of $p$ =80 µm. The multiplication layer should be isolated from the wafer surface otherwise it can lead to an early breakdown. Therefore, the p-layer beneath the n-implant is 9 µm narrower than the n-contact on each side (18 µm in total).

The strips are designed with different strip widths to observe different multiplication behavior, and the metal has different widths to observe any change in the electric field, which might lead to more multiplication.

Table 4.3 shows the wafer specifications. The epitaxis is grown on a substrate 525 µm thick wafer with resistivity of 0.006 Ω cm. The silicon orientation for all wafers is $< 100 >$ and all are p-type doped.

| | Thick [µm] | Resistivity [Ω cm] | Substrate resistivity [Ω cm] | Substrate thickness [µm] |
|---|---|---|---|---|
| Epitaxial | 9.8 | 110.5 | 0.006 | 525 |
| Epitaxial | 50.4 | 96.7 | 0.006 | 525 |
| Epitaxial | 75.2 | 104.6 | 0.006 | 525 |
| FZ | 285 | 12000 ± 7000 | | |

Table 4.3: Wafer details.

### 4.2.1 Mask Design

The mask includes pixel, strip and pad detectors. Figure 4.7 and figure 4.8 show details of the mask of AC and DC strips respectively. The difference between AC

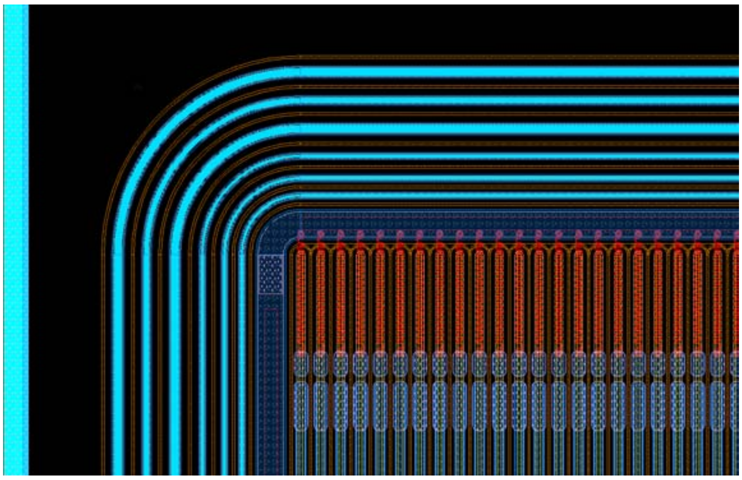

Figure 4.7: Mask of AC strip (upper-left edge detail). In red is the polysilicon resist that connects the strips to the bias ring. The detector has one bias ring and 6 floating guard rings.

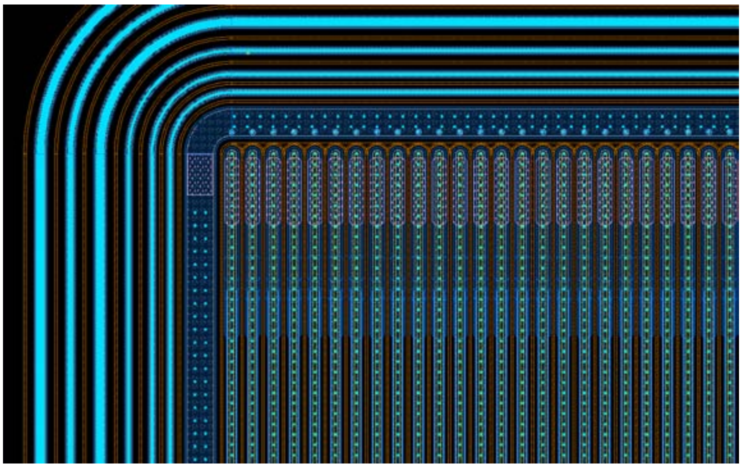

Figure 4.8: Mask of DC strip (upper-left edge detail). The detector has one bias ring and 6 floating guard rings. These sensors do not have polysilicon resist.

and DC strips is that the AC strips has a coupling oxide between the n+ contact and the aluminium line. The bias ring has a purple square that is an opening in the passivation layer to make contact. The strips have a pitch of 80 µm, a length of 1 cm and each detector has 130 strips.

Figure 4.9 shows the mask for FE-I3 pixel detectors. There are 6 FE-I3 pixel detectors per wafer, four of them have 10 guard rings (figure 4.9 (a)) and two of them do not have any guard ring (figure 4.9 (b)), designed for slim edge dicing.

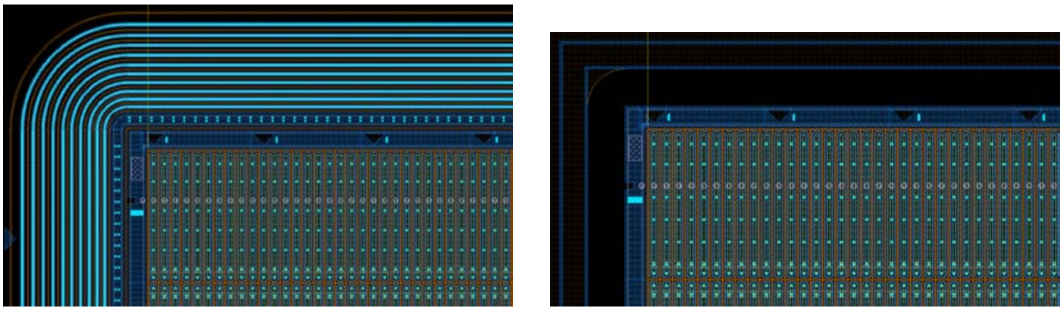

(a) FE-I3 with GR (b) FE-I3 without GR

Figure 4.9: Detail of the mask of the FE-I3 pixel detectors with guard ring (a) and without guard ring (b).

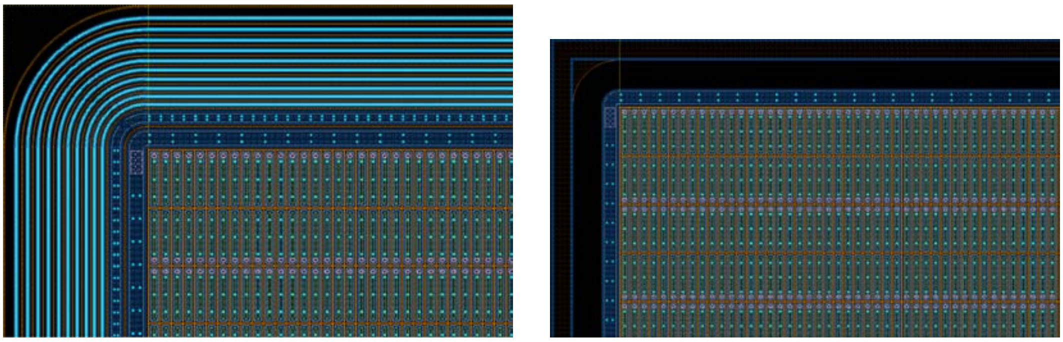

(a) FE-I4 with GR (b) FE-I4 without GR

Figure 4.10: Detail of the FE-I4 pixel detectors mask,(a) with guard ring and (b) without guard ring.

Figure 4.10 shows the mask for FE-I4 pixel detectors. There are 4 FE-I4 pixel detectors per wafer, 2 of them have 10 guard rings (figure 4.10 (a)) and 2 of them do not have any guard ring (figure 4.10 (b)). The detectors without guard ring are designed for slim edge dicing. The pixel and detector size for FE-I4 and FE-I3 are shown in table 2.1.

Figure 4.11 shows a detail of the mask for CMS detectors. CMS detectors have a polysilicon resistence surrounding each pixel which allow to bias the pixel before bump bonding. The resistance is $R \approx 1\,\mathrm{M\Omega}$.

The wafer also included pad detectors with a diameter of 1 mm and 4 mm. Figure 4.12 shows a detail of the mask for pad detectors of 1 mm. Some of them had the multiplication layer (yellow area in figure 4.12) while others did not. Therefore, the gain can be calculated comparing the charge of a detector with multiplication layer and the charge of one without multiplication layer, both from the same wafer.

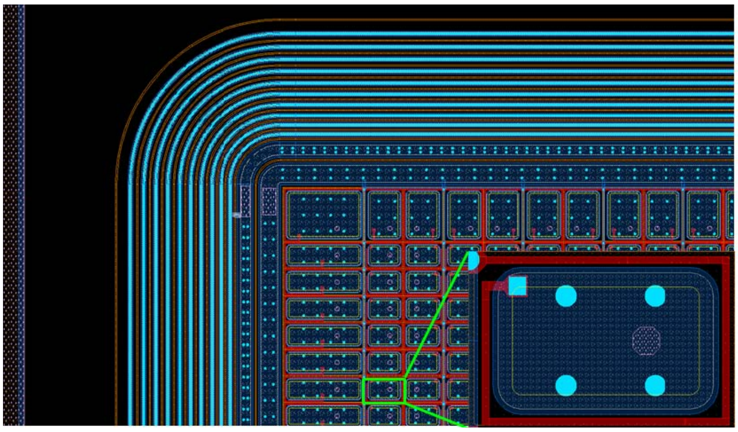

Figure 4.11: CMS detector. The CMS pixels have a polysilicon resist (in red) surrounding each pixel.

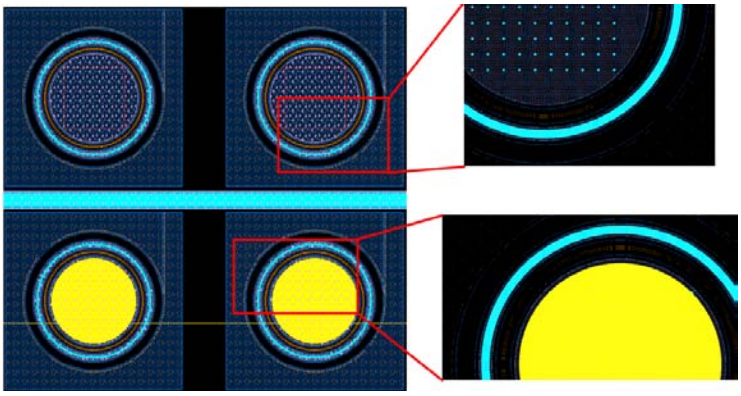

Figure 4.12: Mask detail of diodes with a diameter of 1 mm. The ones at the bottom have a multiplication layer colored in yellow.

## 4.3 Simulations

Technology Computer Aided Design (TCAD) toolkits assist the fabrication with a simulation software which adjust to the fabrication and the device characterization. The TCAD simulations of this work are run with Synopsys Sentaurus TCAD toolkit[47]. The technological and electrical simulations in this section are cross sections of strips in 2 dimensions. For two dimensions simulations, the software takes into account a 1 µm deep volume of the 2D cross section.

### 4.3.1 Technological simulations

Sentaurus Process [94] provides a simulation tool for the fabrication process of silicon devices, and all the technological simulations in this work are run with this software. The technological simulation is done only on a single side, it takes into account the high temperature processes and the implantation of phosphorus and boron. Figure 4.13 shows the net doping profile of a technological simulation for FZ wafers with standard doping profile. In order to minimize the computational time, the simulations takes into account half of the strip and at the end it mirrors the structure. Only the upper 10 µm are simulated, since it is enough for computing the doping profiles. The simulation shows the p-stop implantation, the boron of the multiplication layer and the phosphorus implantation.

Figure 4.14 shows the three different doping profiles (shallow, standard and deep) for FZ wafers. The doping profiles were designed to agree with the ones in

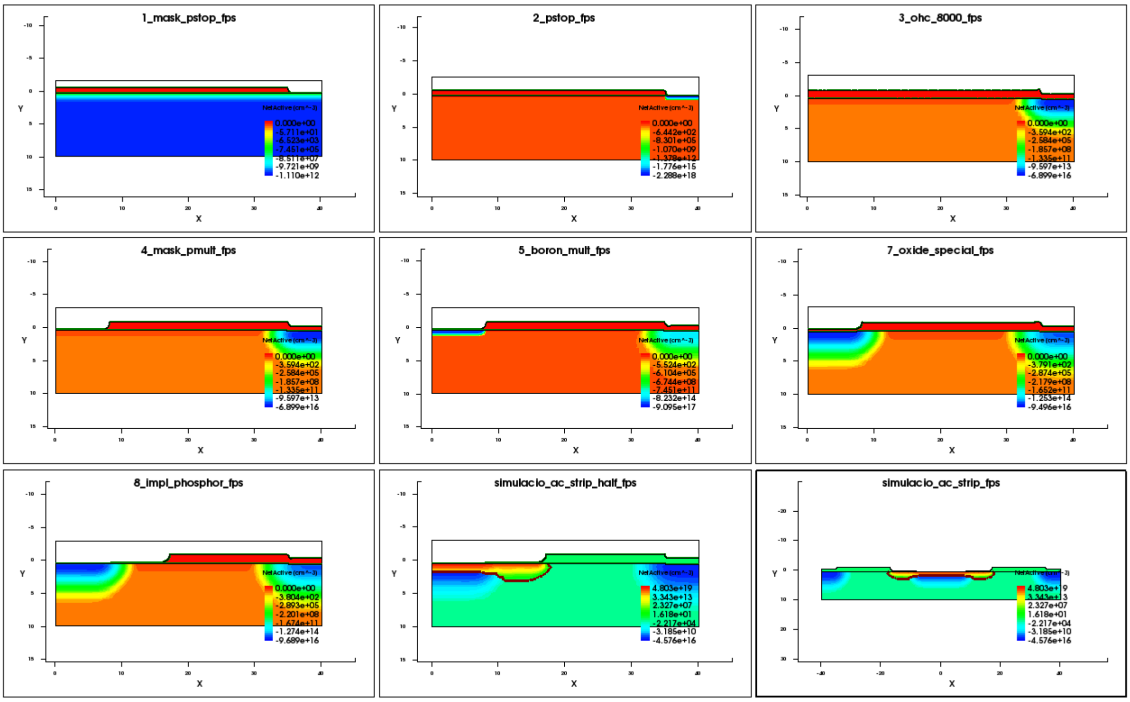

Figure 4.13: Technological simulation for a FZ wafer with standard doping profile. The simulation shows the net doping profile. The three first plots show the p-stop boron implantation, the middle three ones show the implantation of the multiplication layer, and the last three steps show the implant of the phosphorus, the annealing and the mirrored structure (which shows the final net doping profile).

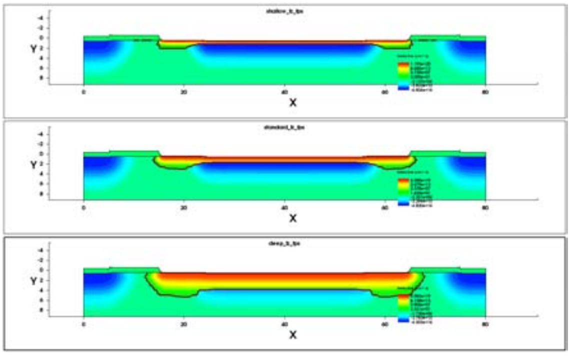

Figure 4.14: Technological simulations for the three different doping profiles: From top to bottom: shallow, standard and deep profile. The p-type implants are shown in blue and the n-type implants are shown in red.

ref. [90; 18].

### Technological simulation for wafers with a 10 µm epitaxy layer

Detectors fabricated on wafers with a 10 µm epitaxy are grown on a low resistivity 525 µm thick p-doped wafers. After the fabrication of the devices, the boron in the highly doped support wafer will diffuse to the epitaxy, reducing the active volume of the detector. Figure 4.15 shows the simulation of the doping profiles after the fabrication process in a cross section in the middle of the strip for a wafers with a 10 µm epitaxy layer. The simulations show that the boron of the substrate wafer will almost reach the boron of the multiplication layer, leaving a depleted volume of 2 µm for the deep doping profile.

After these results, the fabrication with 10 µm epitaxy and deep implantation was descarted since the volume of the detectors would be insufficient to collect a signal at the electrodes.

## 4.3.2 Electrical simulations

The critical point for LGAD is the multiplication layer, where the high electric field can lead to an early break down.

AC7, AC8 and AC9 detectors with 62 µm wide strips have a distance of 5 µm from the p-stop. Figure 4.16 shows the simulation of the electric field of the AC9 strip detector at 600 V. The high electric field is expected at the junction of the $n^{++}$ and $p^{++}$ implant (for the multiplication mechanism), but high electric field appears

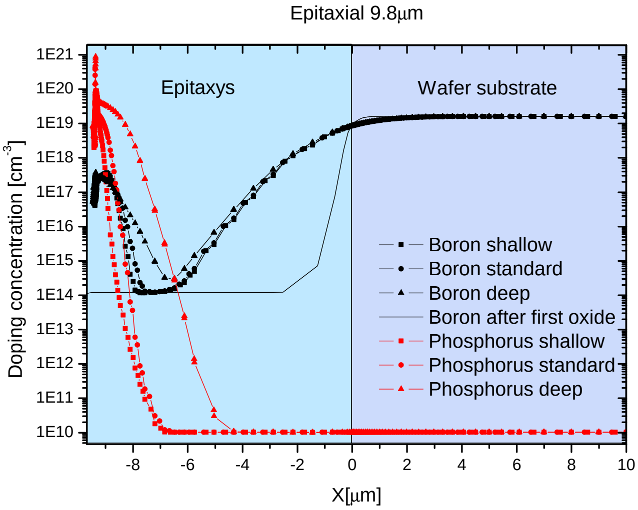

Figure 4.15: Doping profile simulations in the middle of the strip for 10 µm epitaxial wafer. The phosphorus is shown in red and the boron is in black.

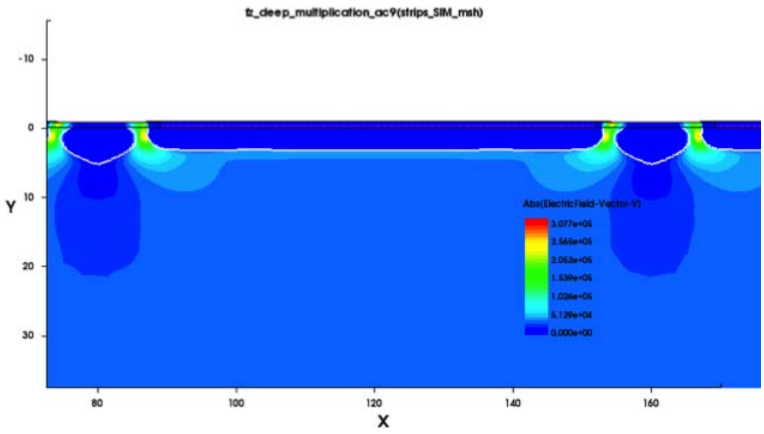

Figure 4.16: Simulation of AC9 geometry electric field at 600 V.

at the edge of the strip, leading to a break down around 600 V.

### Comparison of AC3 and AC6 with gain and no gain

Simulations for AC3 and AC6 in a 2D structure of 3 strips were carried out in order to study if larger multiplied area leads to more gain. The simulations are performed for 3 strips, with a 285 µm thick FZ wafer standard doping profile. The chosen structures are strips of 24 µm and 48 µm width, which have a high break down voltage. The simulation of the current-voltage curve is showed in figure 4.17, and shows similar results for detectors with and without gain. Figure 4.18 shows capacitance-voltage curves simulated for the strip detectors with and without gain. The AC6 strip detector with gain shows a foot in the curve, corresponding to the depletion of the multiplication layer. According to the simulations, the strip detectors AC3 with and without gain and the AC6 without gain are fully depleted at 70 V, whereas the AC6 strip detector with gain does not fully deplete until the voltage reaches 80 V.

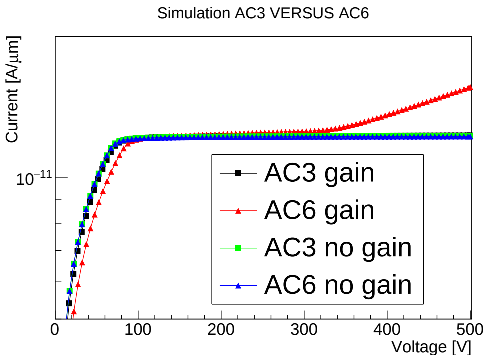

Figure 4.17: Simulations of the current voltage for the AC3 and AC6 strips with standard doping profile in a FZ wafer in 2D with 3 strips.

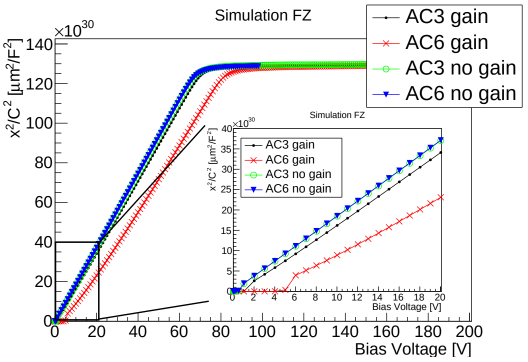

Figure 4.18: Simulations of the capacitance voltage for the AC3 and AC6 strips with standard doping profile in a FZ wafer in 2D with 3 strips.

The dashed lines belong to the detectors without gain and the solid lines are for the detectors with gain. The collected charge pulses are around 50 ns and the AC6 strip detector only shows multiplication after biasing it at 250 V.

Figure 4.19 shows the collected charge of an alpha particle impinging from the back of the detector for different voltages ranging from 50 V to 500 V for an integration time of 25 ns. The simulated alpha particle is injected in the back of the detector, in the middle of the central strip and with an energy of 5 MeV. The simulations show no gain for AC3 strip detector, whereas AC6 has, due to the fact that AC6 has a bigger multiplication area than AC3.

## 4.4 Fabrication Process

28 wafers were fabricated in this project, 14 of them had the boron implant (the multiplication layer) while 14 were standard wafers used as reference. The basic parametres for each wafer are detailed in table 4.4.

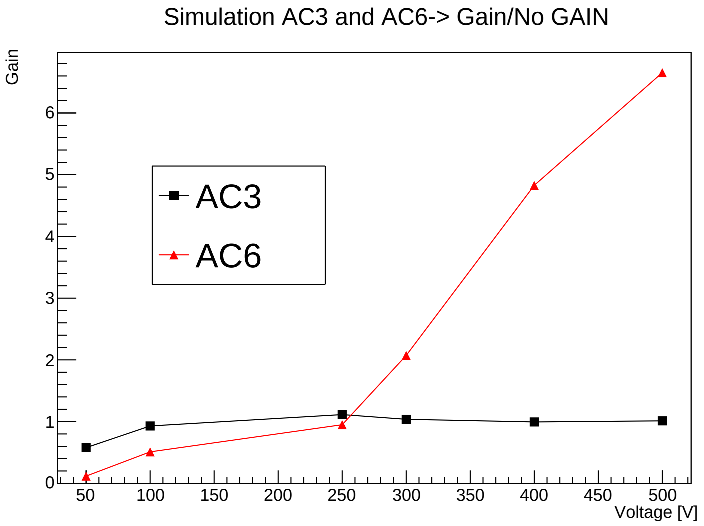

Figure 4.19: Simulation of the gain for the AC3 and AC6 for generated by an alpha particle. The gain is calculated integrating 25 ns of the detector with the multiplication layer and dividing its signal for the detector without the multiplication layer.

| Wafer # | Wafer type | Diffusion | P-stop |
|---|---|---|---|
| 1 | Epi 10 µm | Shallow | yes |
| 2 | Epi 10 µm | Shallow | yes |
| 3 | Epi 10 µm | Standard | no |
| 4 | Epi 10 µm | Standard | yes |
| 5 | Epi 50 µm | Shallow | yes |
| 6 | Epi 50 µm | Standard | yes |
| 7 | Epi 50 µm | Standard | no |
| 8 | Epi 50 µm | Deep | yes |
| 9 | Epi 75 µm | Shallow | yes |
| 10 | Epi 75 µm | Standard | yes |
| 11 | Epi 75 µm | Deep | yes |
| 12 | FZ | Shallow | yes |
| 13 | FZ | Standard | yes |
| 14 | FZ | Deep | yes |

Table 4.4: List of wafers fabricated. Each wafer was fabricated with and without multiplication layer.

The wafers without multiplication underwent the same fabrication process except for the implantation of the multiplication layer. The shallow process is done using a Rapid Thermal Anneal (RTA), the RTA equipment heats the wafer with a lamp, and the standard and deep annealings are dry oxidations.

### 4.4.1 Fabrication steps

Since the fabrication steps of the wafers with and without multiplication is the same, except for the implant of the multiplication layer, both will be described together.

First, the wafers were individually labeled in the backside for future identification, engraving the run and the wafer number. Then, after cleaning the wafers, a wet silicon dioxide was grown and removed (with a buffered $HF$ mixture) in order to clean the surface of any impurity. Typically, the grown silicon dioxide is 8000 Å but the wafers with 10 µm epitaxy it was 1000 Å, because the high temperature process will diffuse the dopants of the substrate wafer to the epitaxial wafer and therefore the wafer with 10 µm epitaxy will suffer a drastic reduction of the active thickness.

#### Implantation of the p-stop

The first implanted structure is the p-stop, which is a boron implant that surrounds the n-electrodes and it is used to compensate the electron layer at the surface and therefore to isolate the structures of surface currents. The fabrication steps involved in the implantation of the p-stop are sketched in figure 4.20.

A photosensitive resist is deposited on the $SiO_2$ (the resist is shown in yellow in figure 4.20 (c)). The photosensitive resist is exposed to ultraviolet light through the mask, illuminating the p-stop positions. The parts of illuminated resist were removed with a developer solution (shown in figure 4.20 (e)). Then, the exposed silicon dioxide was removed with a buffered $HF$ mixture (step shown in figure 4.20 (f)). Afterwards, all the resist was removed with a developer solution (figure 4.20 (g)), and boron ions are implanted on the surface of the substrate.

Figure 4.21 shows a photo of the p-stop implant for a strip detector taken with an optical microscope during fabrication.

#### Multiplication layer

The next fabrication step is the implantation of the boron ions to create the multiplication layer. Boron is implanted through a silicon dioxide mask, using the same process as explained for the p-stop. Figure 4.22 shows the steps for the multiplication layer. After the p-stop implantation, a wet growth of a silicon dioxide activates the boron of the p-stop in the crystalline silicon lattice (figure 4.22 (a)). This is a high temperature process that activates the dopands, and it diffuses the boron ions deep into the silicon substrate.

This part of the fabrication was skipped for the fabrication of the wafers without multiplication. Figures 4.23 (a) and (b) show two pictures of the strip and pixel devices after the implantation of the multiplication layer, taken with an optical microscope during the fabrication.

The boron doses and energies are different for each doping profile and are de-

(a) Silicon (b) Oxidation (c) Deposition of the resist

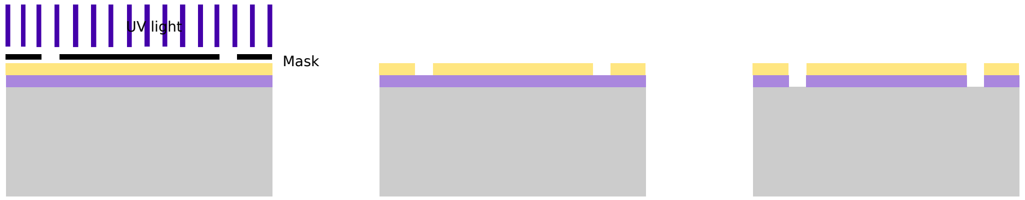

(d) Ultraviolet exposure of the mask (e) Develop resist (f) Etch oxide

(g) Remove resist (h) Implant boron

Figure 4.20: Fabrication steps for the p-stop implantation. The bulk silicon is in gray, the oxidation is in violet, the resist is in yellow and the implanted boron in blue.

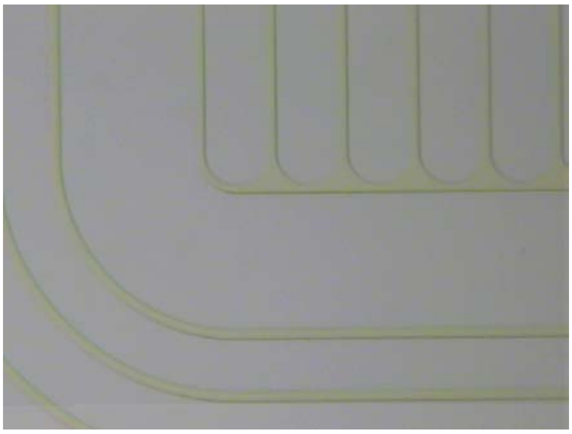

Figure 4.21: Picture of the p-stop structures of a strip detector.

(a) Silicon dioxide

(b) Deposit resist

(c) Develop resist

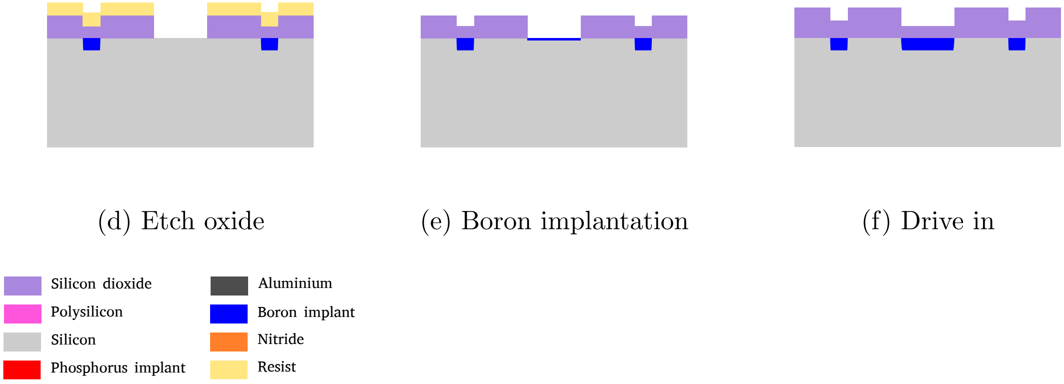

(d) Etch oxide

(e) Boron implantation

(f) Drive in

Figure 4.22: Steps for the multiplication layer.

signed in such a way that the accumulated charge in the multiplication layer is as similar as possible to the samples fabricated in ref. [18], which proved to have a gain in the range of 8.

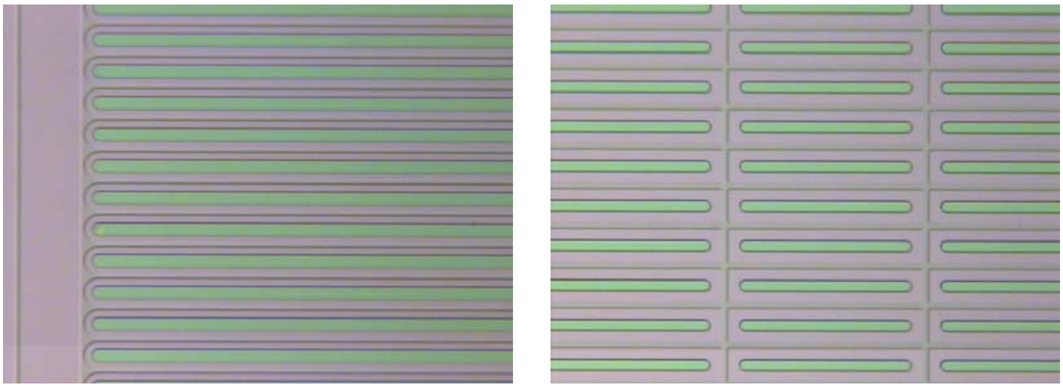

(a) AC6 strip detector (b) FE-I4 pixel detector

Figure 4.23: Pictures taken with an optical microscope of strip and pixel detectors. The greenish part is the boron implant.

### Contact implants

The following step after the multiplication layer is the implantation of the $n$-contacts and the ohmic $p+$ contact on the backplane. Although the epitaxial wafers have a highly doped support wafer, the backplanes were implanted with boron in order to ensure a low resistance contact between the metal and the silicon.

The n-contacts are created using a highly doped phosphorus implant with a mask, while the p-contact on the bottom is created using a highly doped boron implant that covers the entire backplane wafer surface. Figure 4.24 shows the fabrication steps for the phosphorus (in red) and boron implants.

Figure 4.25 shows a picture taken with an optical microscope of the FE-I4 pixels after the contacts implantation.

### Polysilicon resist and annealing

The next step is the deposition of 50 nm of tetraethylorthosilicate $Si(OC_2H_5)_4$ (TEOS oxide) with PECVD (Plasma Enhanced Chemical Vapor Deposition) to minimize pin-holes.

After the TEOS deposition, polysilicon resist is deposited and doped with p-type impurities (boron). The resistance of the polysilicon should be 2 MΩ, and it will depend on the following annealing time and temperature steps. The polysilicon deposition is sketched in figure 4.26 and it has two boron implantations, (c) is to dope the polysilicon and (f) is the implant at the windows position to propiciate a

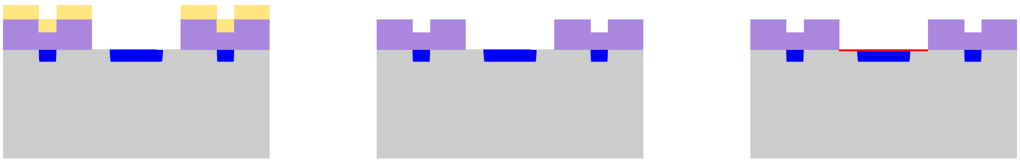

(a) Etch silicon dioxide (b) Remove resist (c) Implant phosphorus

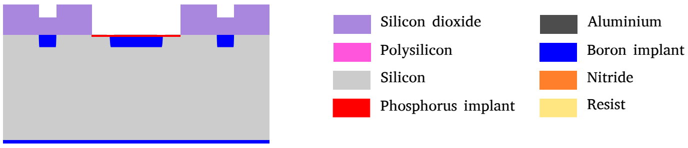

(d) Implant boron at the backplane

Figure 4.24: Steps for the fabrication of the contact implants, the phosphorus is sketched in red and the boron in blue.

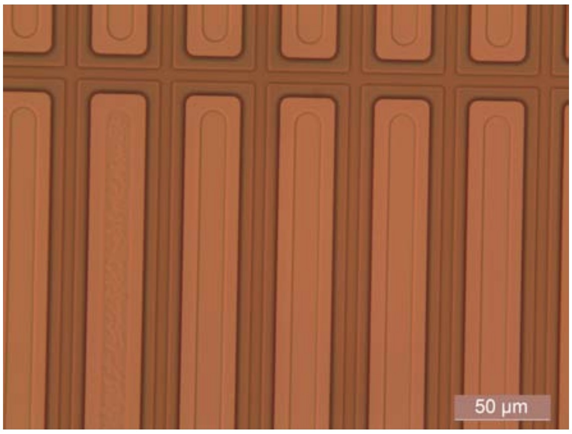

Figure 4.25: Picture of the FE-I4 pixel detector after the n-contacts implantation.

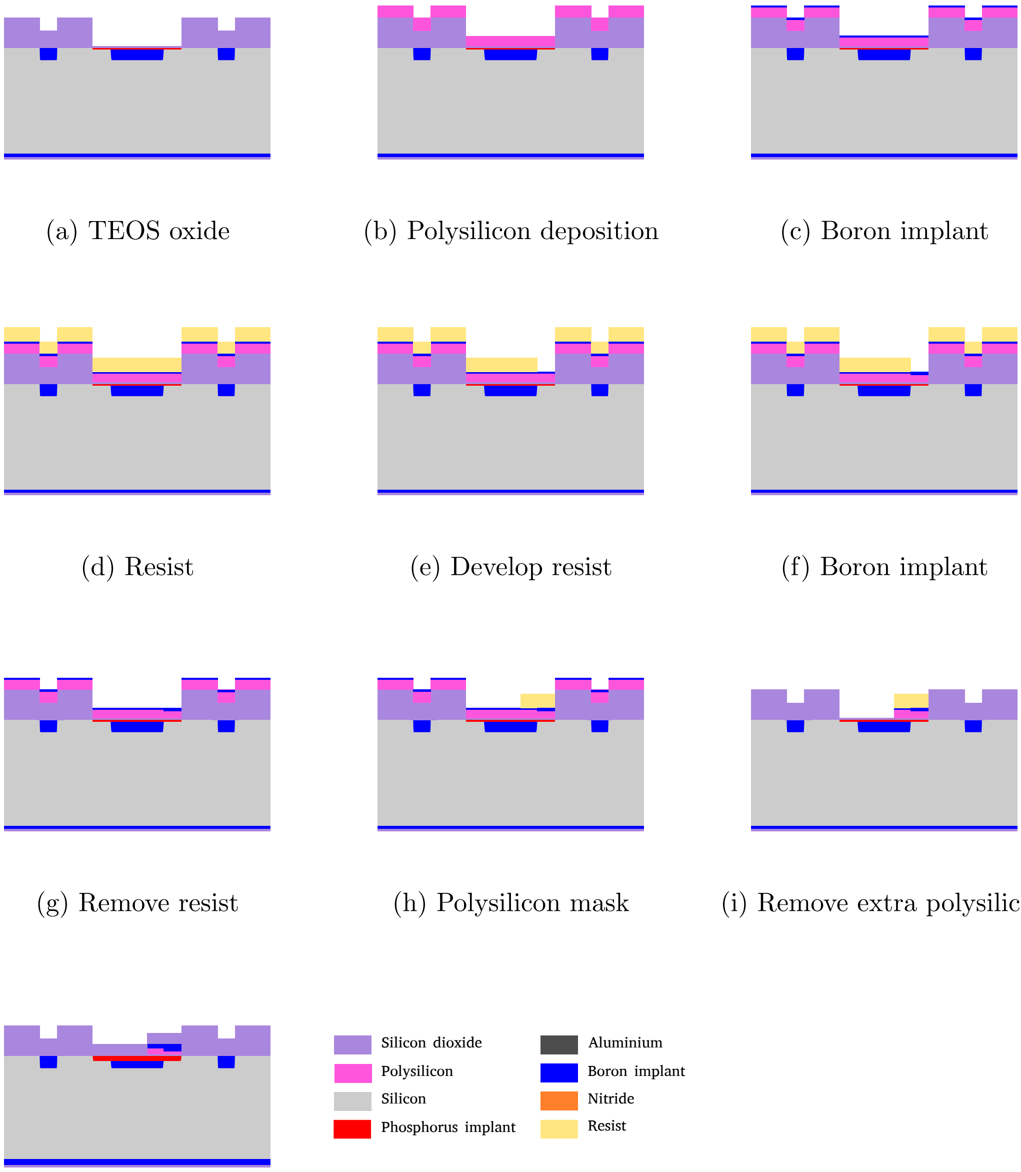
(a) TEOS oxide
(b) Polysilicon deposition
(c) Boron implant
(d) Resist
(e) Develop resist
(f) Boron implant
(g) Remove resist
(h) Polysilicon mask
(i) Remove extra polysilicon
(j) Annealing

Figure 4.26: Steps for the polysilicon resist of the AC strip and CMS detectors. The polysilicon is sketched in pink.

better contact between the polysilicon and the metal pads. The polysilicon resist is needed for AC strip detectors and the CMS detectors. The polysilicon resist in the AC strip detectors decouples the bias voltage from the signal of the strips.

The annealing shown in figure 4.26 (j) will activate the atoms in the crystalline lattice, and depending on the annealing time and temperature it will have a shallow, standard or deep doping profile of the phosphorus and boron of the contacts. The thickness of the silicon dioxide after the annealing will depend on the time and temperature of the annealing, the shorter the time the thinner the $SiO_2$ (no silicon dioxide was grown for the shallow doping profile with the RTA).

### Window opening and metalization

The next step is the deposition of an aluminium metal layer on the contacts in the front and on the backplane of the wafers. First, it is necessary to etch the oxide to reach contact, and deposit the metal on the front side. Figure 4.27 shows a sketch of the window opening and the metal deposition. Once the windows are etched, the metal is deposited and after a photolithographic process the exceeding metal is removed. Afterwards, an aluminium layer is deposited on the backplane without a mask, covering all the backplane surface.

### Passivation and end of the fabrication

The last steps of the fabrication are the deposition of 400 nm of oxide and 200 nm of nitride. These processes create a passivation layer on the surface of the wafer protecting the fabricated structures from scratches and humidity. The passivation is removed from the contacts to allow the bump bonding, wire bonding, or probing the test structures and diodes in the probe station. Those steps are sketched in figure 4.28. Figure 4.29 shows a picture of the finished wafer.

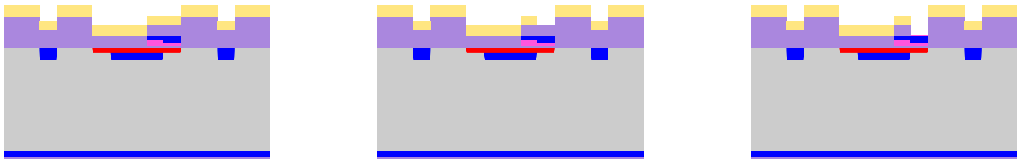

(a) Resist (b) Etch resist (c) Etch oxide

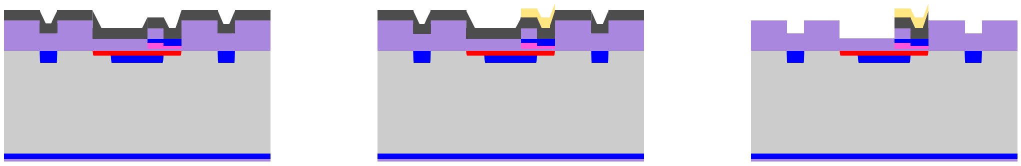

(d) Deposit metal (e) Resist (f) Remove metal

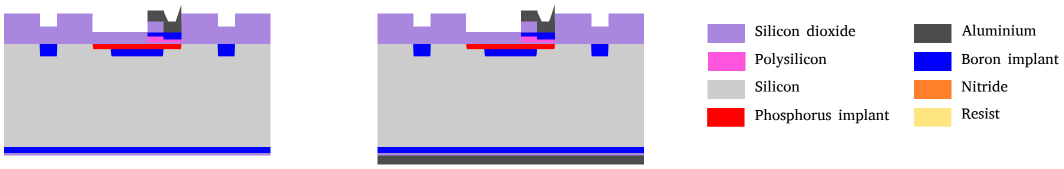

(g) Remove resist (h) Deposition of metal on the backside

Figure 4.27: Steps for the window opening and the metalization.

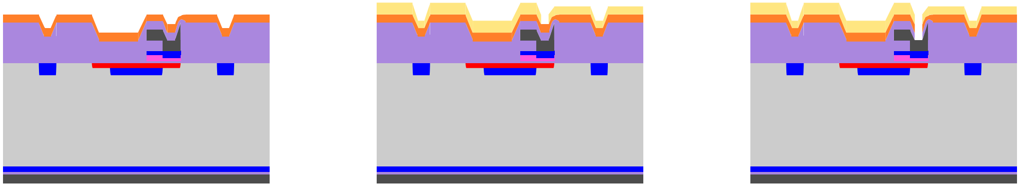

(a) Deposit passivation (b) Resist (c) Etch resist and oxide

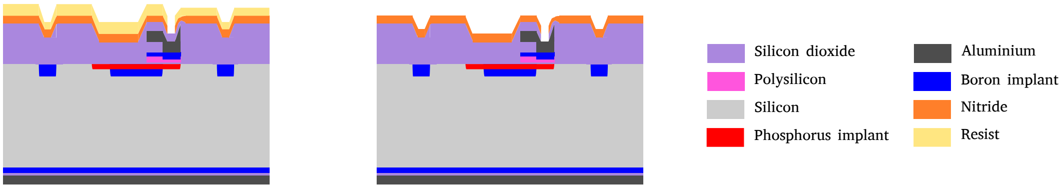

(d) Etch nitride (e) Remove resist

Figure 4.28: Passivation steps. The nitride is shown in orange.

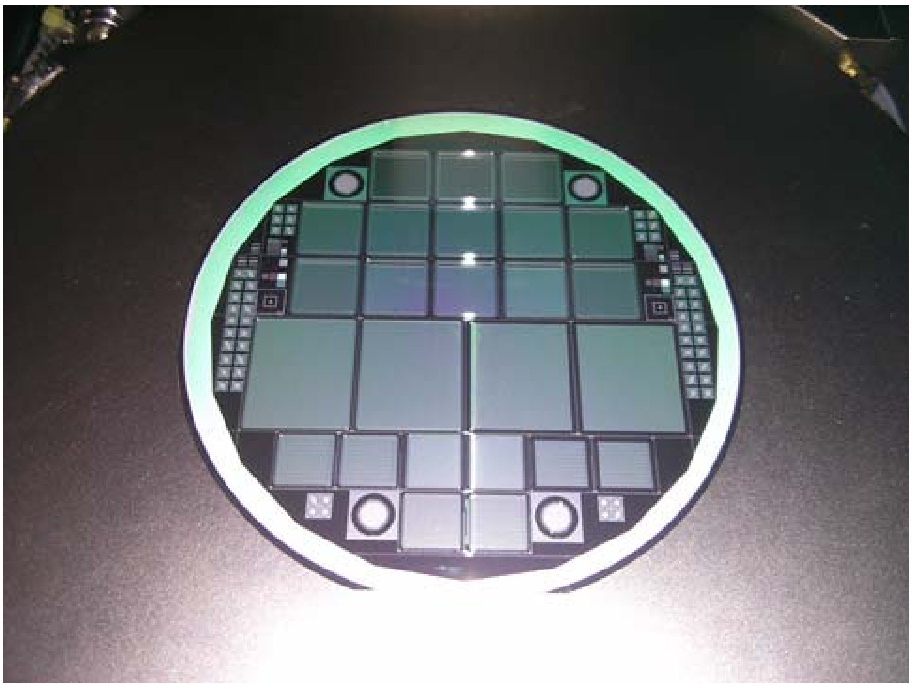

Figure 4.29: Photo of the finished wafer.

## 4.5 Characterization

The ensure the good performance and electrical response of the fabricated devices, the detectors are tested electrically, with current-voltage and capacitance-voltage curves. The measurements of current-voltage gives information of the leakage current and the break down voltage of the detectors. Capacitance voltage curves give the full depletion voltage when $1/C^2$ reaches a plateau, and also gives the effective doping profile of the detector. Pixel detectors could not be measured before bump-bonding, but measurements of the AC strip detectors and pad detectors are shown in this section.

### 4.5.1 Reverse engineering

Two strips and a pad detectors were used to take micro-sections for reverse engineering. The detectors were diced in a plane perpendicular to the strip direction and, afterwards, they were polished to enhance the visibility of phosphorus and boron. Figures 4.30 (a) and (b) show microsections of 10 µm epitaxial wafer with shallow implantation. It is possible to observe the diffusion of the substrate wafer to the epitaxis. Figures 4.30 (c), (d) and (e) show strip detectors from a FZ wafer with standard implant. From figures (d) and (e) it is possible to observe the phosphorus dopant. Figure 4.30 (f) shows a micro-section of the FZ big diode from wafer 13 (standard doping profile).

### 4.5.2 Electrical characterizations

The electrical measurements of those detectors were carried out in the radiation detectors lab at CNM-Barcelona and at UCSC lab. The current voltage measurements at CNM-Barcelona were taken with a Cascade probe station biasing the detectors with a 2410 Keithley power supply (figure 2.9) at room temperature. The measurements taken at UCSC were carried out in a probe station biasing the detector with a 2410 Keithley power supply at room temperature. The capacitance voltage measurements were taken with an Agilent 4284A LCR using a capacitance bridge of 10 kHz and an oscillation voltage of 500 mV.

#### Wafers with 10 µm epitaxy

The nominal full depletion of the 10 µm thick epitaxial wafers is 9.3 V. Figures 4.31 and 4.32 show the current-voltage curves for the shallow implant (wafers 1 and 2

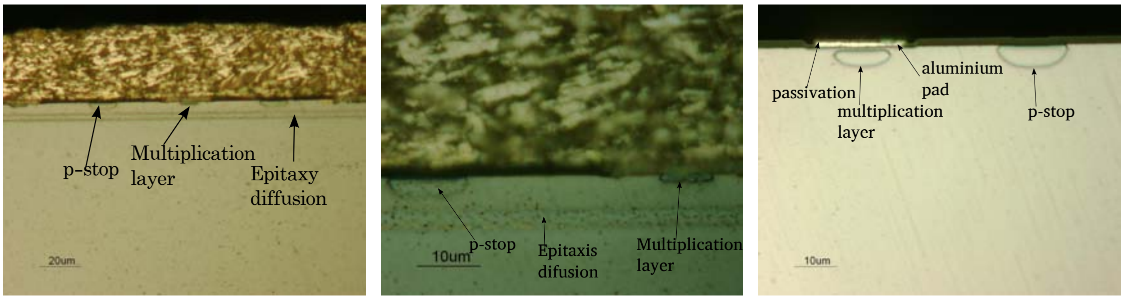

(a) 6827 W1 AC1 (b) 6827 W1 AC1 (c) 6827 W13 AC1

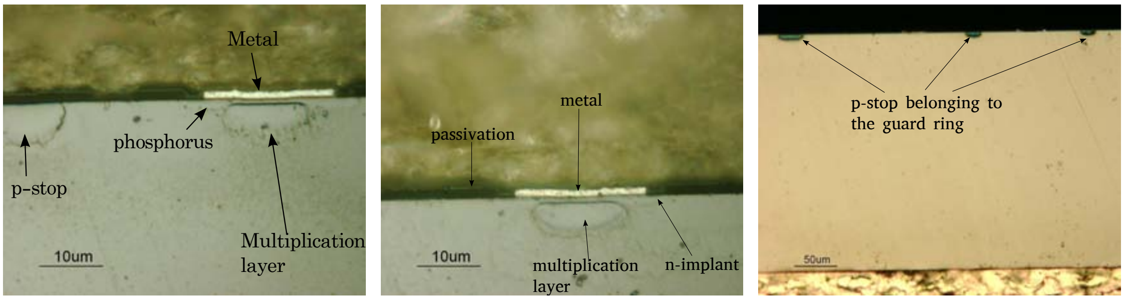

(d) 6827 W13 AC1 (e) 6827 W13 AC1 (f) 6827 W13 big diode 2

Figure 4.30: Strips and diodes microsections.

respectively).

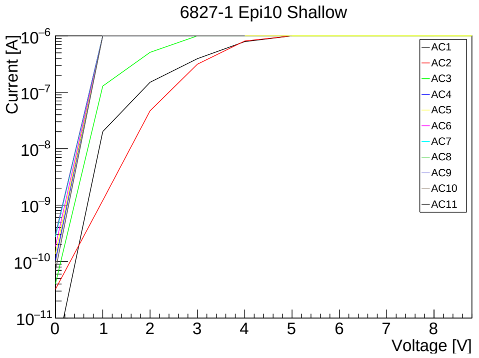

Figure 4.31: IV curves for the AC strip detectors of the 10 µm epitaxial wafer 1 with multiplication (shallow annealing).

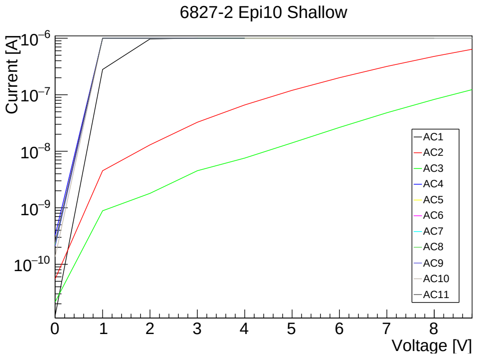

Figure 4.32: IV curves for the AC strip detectors of the 10 µm epitaxial wafer 2 with multiplication (shallow annealing).

Figure 4.33 shows the current-voltage curves for wafer 4 with gain. Figure 4.34 shows the current-voltage curves of wafer 4 with no gain. The measured leakage currents are lower for the wafers without multiplication layer than for those with the multiplication layer.

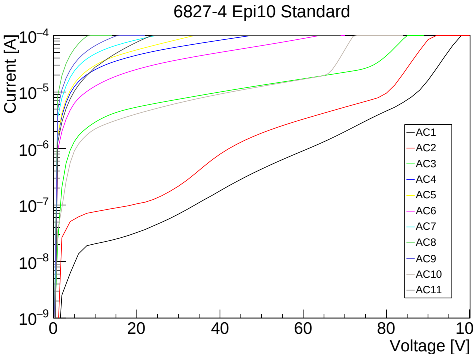

Figure 4.33: IV curves for the AC strip detectors of 10 µm epitaxial wafer with multiplication layer (standard annealing).

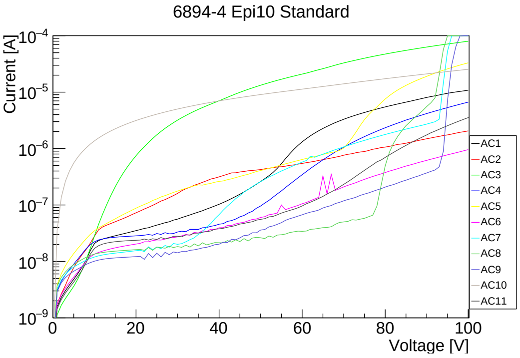

Figure 4.34: IV curves for the AC strip detectors of 10 µm epitaxial wafer without multiplication layer (standard annealing).

Figure 4.35 shows the capacitance-voltage curves for strip detectors from wafer 2 (shallow doping profile). Those curves show very high capacitances for AC strip detectors. Furthermore, the capacitance does not decrease with voltages but it increases, untill break down is reached at 10 V, not showing a diode behaviour.

Figures 4.36 and 4.37 show the capacitance-voltage curves ($1/C^2$) for strip detectors with standard doping profile for the fabrication with and without multipli-

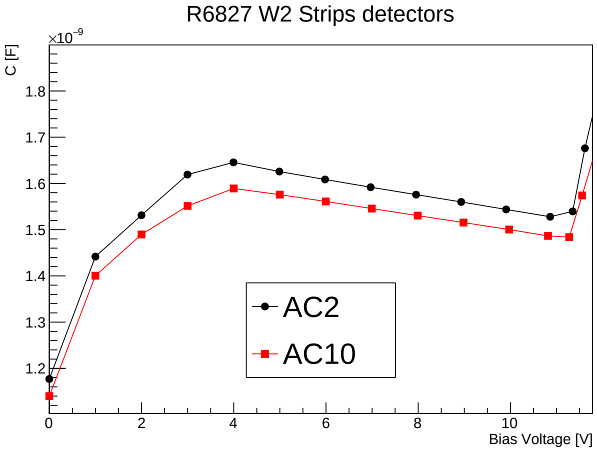

Figure 4.35: Capacitance-voltage curves for the AC strip detectors of 10 µm epitaxial wafer with multiplication (shallow doping profile).

cation, respectively. The detectors measured are AC2 (24 µm of strip width), AC10 (32 µm of strip width), AC5 (48 µm of strip width) and AC8 (62 µm of strip width). The capacitance reaches a plateau for all the detectors, thus the detectors are fully depleted. All the detectors without multiplication reach the plateau around 12 V, whereas the detectors with multiplication reach the plateau at different voltages (between 10 V and 20 V).

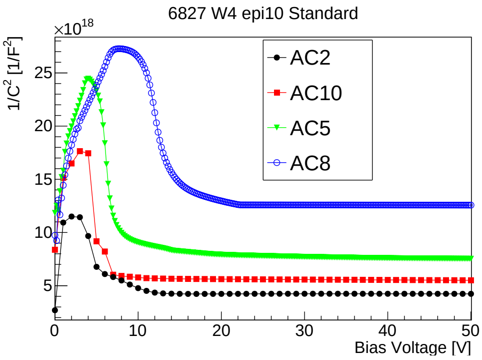

Figure 4.36: CV curves for the AC strip detectors of 10 µm epitaxial wafer with multiplication (standard doping profile).

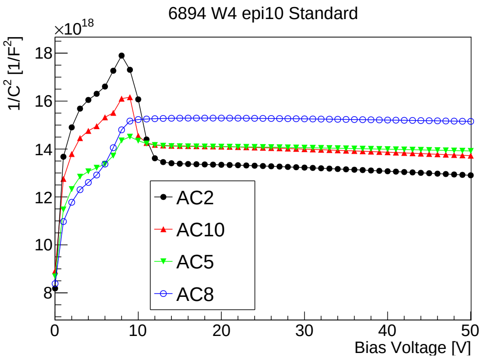

Figure 4.37: CV curves for the AC strip detectors of 10 µm epitaxial wafer without multiplication (standard doping profile).

The bulk capacitance for a single strip is [16]:

$$C_b = \epsilon \frac{pl}{d} \tag{4.1}$$

where $p$ is the pitch of the detector, $l$ is the length of the strip, and $d$ is the wafer thickness. For a strip detector, the fringing capacitance to neighbouring electrodes dominates, and it can be approximated by[95]:

$$\frac{C_s}{l} = \left(0.03 + 1.62\frac{w + 20\mu m}{p}\right)\left[\frac{pF}{cm}\right]$$

where $w$ is the width of the strip. The total capacitance is:

$$C_{tot} = C_b + C_s$$

$1/C^2$ increases with the depleted thickness and decreases when the depleted strip increases. For detectors without multiplication fabricated in 10 µm epitaxial wafers (figure 4.37), since the thickness of the wafer is smaller than the area of the detector, the detector is depleted first in volume and then laterally. The wafers with and without multiplication behave differently because the detectors with multiplication deplete first the multiplication layer.

Figure 4.38 shows the simulation of the electric field at 100 V for strips AC3 (24 µm), AC10 (32 µm), AC6 (48 µm) and AC9 (62 µm). The widest strips (AC9) show a larger area with high electric field than their thinner counterparts. The results come from a technological simulation of the complete fabrication process for a 2D structure of a 10 µm support wafer and a 10 µm epitaxy, and it takes into account three strips. According to simulations, the depleted volume of the detectors is 5 µm thick.

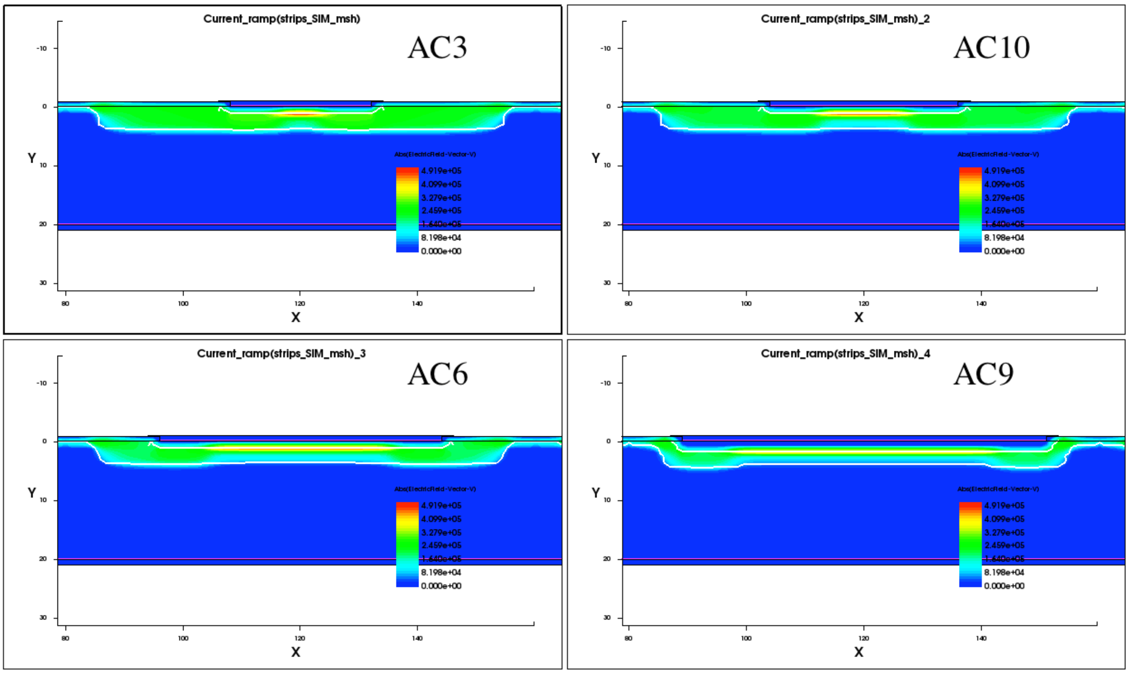

Figure 4.38: Electric field for the 4 different geometries of the strips at 100 V, in a simulation of 3 strips.

### Wafers with 50 µm epitaxy

Four wafers with 50 µm epitaxy were fabricated with three different doping profiles as detailed in table 4.4. The nominal full depletion voltage calculated with equation 1.7 is 267 V. Figure 4.39 shows the current-voltage curves for AC strip detectors fabricated on wafers with 50 µm epitaxis. The wafers without multiplication (figure

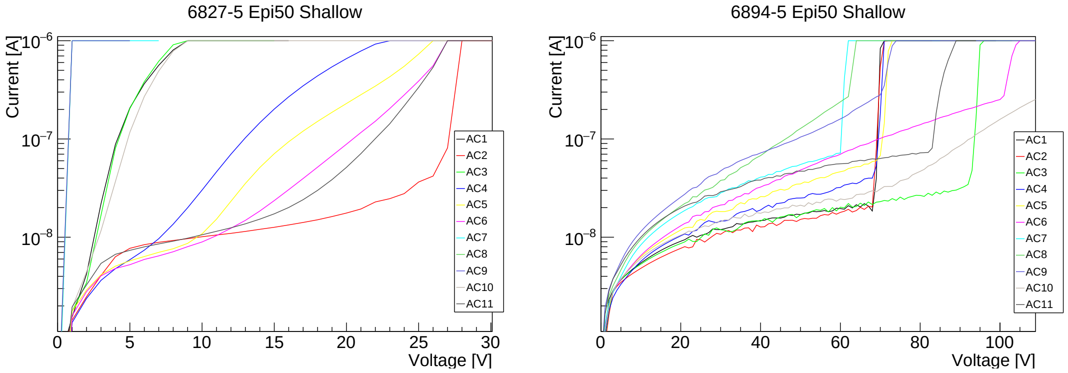

(a) 6827 W5 AC strip sensors with gain (b) 6894 W5 AC strip sensors without gain

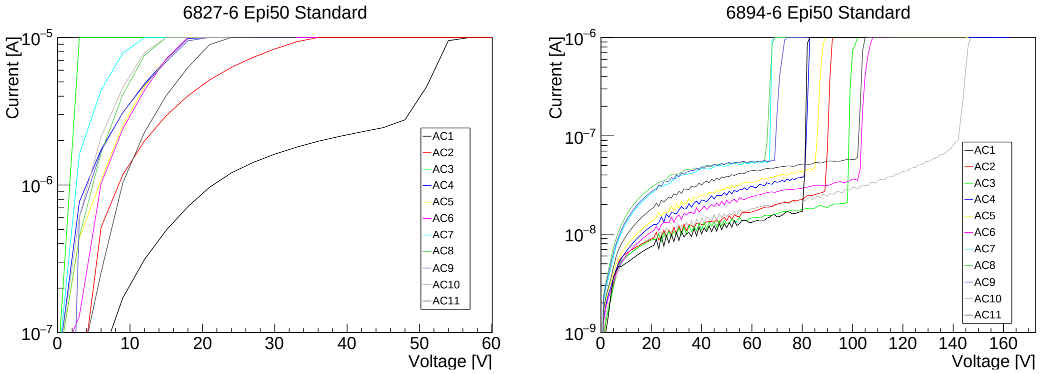

(c) 6827 W6 AC strip sensors with gain (d) 6894 W6 AC strip sensors without gain

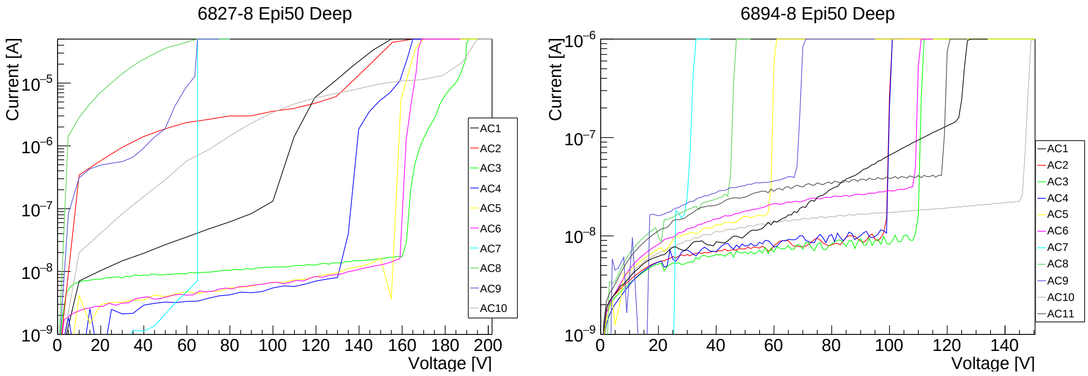

(e) 6827 W8 AC strip sensors with gain (f) 6894 W8 AC strip sensors without gain

Figure 4.39: Current voltage measurements for the strips fabricated on the 50 µm thick epitaxy.

4.39 (b), (d) and (f)) have lower leakage currents than their counterpart with multiplication (figure 4.39 (a), (c) and (e)). Wafers with deep doping profile show the highest break down voltage. All strip detectors show a break down voltage below 200 V.

Wafer 7 is not presented since the detectors reach the compliance level of the power supply at low voltages, because those detectors do not have a p-stop to isolate the strips and to stop the surface current. The current-voltage curves for wafer 8 were taken after dicing and they show a lower current due to the fact that the measured area does not take into account all the back wafer surface.

Figure 4.40 shows the $1/C^2$ versus voltage of two big diodes (4 mm diameter) from wafer 8 (epitaxial 50 µm, deep doping profile). The capacitance reaches a plateau at 150 V, when the detector is considered fully depleted. The curves show a foot at low voltages for the diode with gain. This foot is associated to the depletion of the multiplication layer (already observed in ref. [18]). Figure 4.41 shows the doping profile calculated with equation 1.13. The wafer with gain shows a peak in the net doping at 1 µm depth, which reaches values of $1 \times 10^{16}\,\mathrm{cm}^{-3}$, and it corresponds to the multiplication layer.

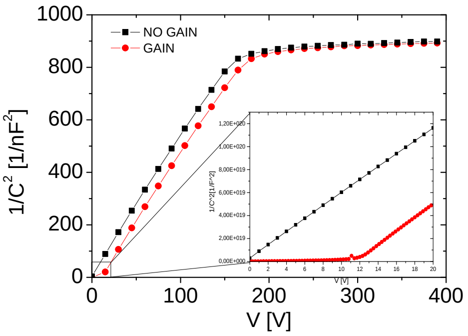

Figure 4.40: Capacitance-voltage measurements of the diodes with and without gain.

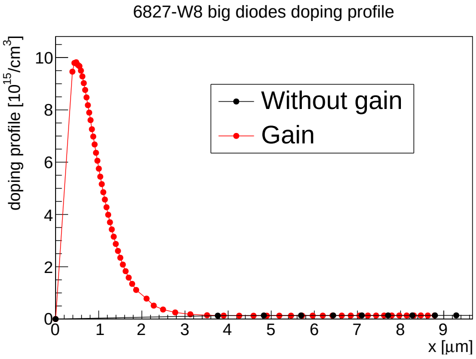

Figure 4.41: Doping profile calculated from the curves of figure 4.40 for wafer 8 (epitaxial 50 µm, deep).

### Wafers with 75 µm epitaxy

Three wafers with 75 µm epitaxy were fabricated with three different doping profiles as detailed in table 4.4. The nominal full depletion voltage is 550 V. Figure 4.42 shows the current-voltage curves of the strip detectors fabricated on 75 µm epitaxy wafers, figures 4.42 (a), (c) and (e) have multiplication whereas figures 4.42 (b), (d) and (e) belong to the wafers without multiplication. The measurements of wafers 9 and 10 are taken before dicing and the measurements of the currents for wafer 11 are taken after dicing.

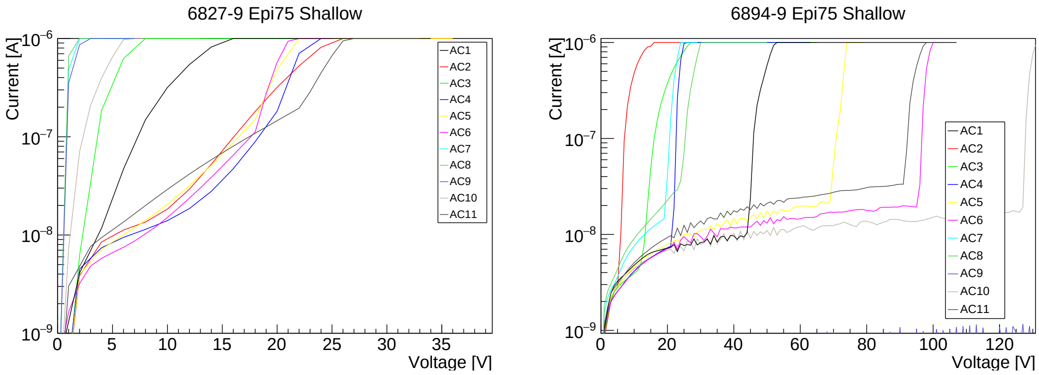

(a) 6827 W9 AC strip sensors with gain (b) 6894 W9 AC strip sensors without gain

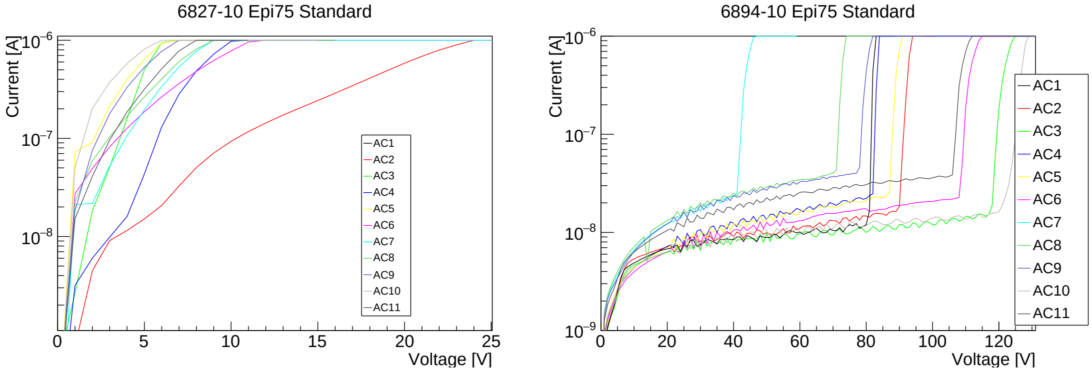

(c) 6827 W10 AC strip sensors with gain (d) 6894 W10 AC strip sensors without gain

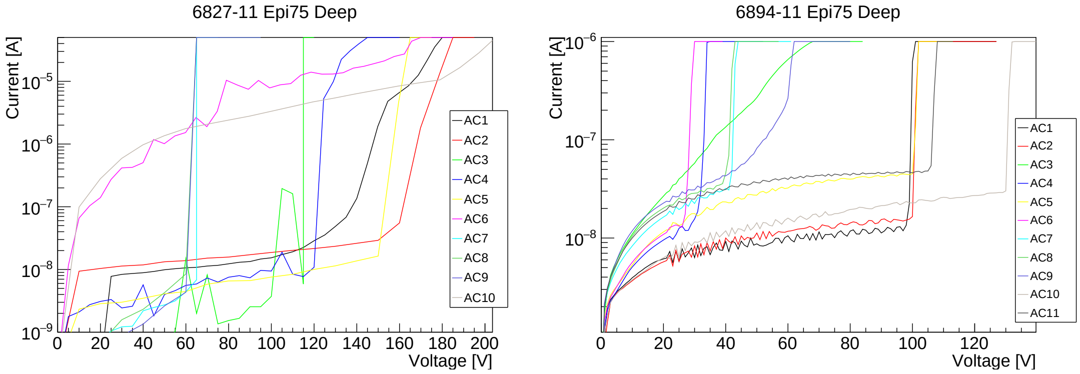

(e) 6827 W11 AC strip sensors with gain (f) 6894 W11 AC strip sensors without gain

Figure 4.42: Current-voltage measurements for the strips fabricated on the 75 µm thick epitaxy wafer.

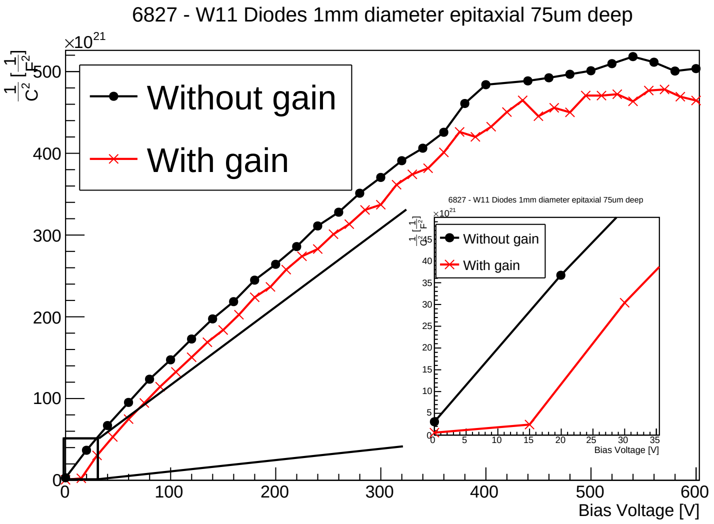

Figure 4.43: Capacitance versus voltage measurements of 1 mm diameter pad, with and without gain, from wafer 11.

Figure 4.43 shows $1/C^2$ versus voltage for 1 mm diameter pad diodes with gain and without gain of wafer 11 (75 µm epitaxial deep doping profile). The depletion voltage is around 400 V.

All the strip detectors have the break down voltage below 200 V, hence no strip detector reaches the full depletion voltage before breakdown. Considering that the detctors fabricated on 75 µm epitaxy have a full depletion voltage at 400 V (larger than the strips break down voltage) those detectors were not further used.

All the epitaxial wafers have a nominal full depletion voltage larger than the measured one. It may be related to the fact that the substrate wafer, after fabrication, diffuses to the epitaxy decreasing the active volume of the wafer and therefore the full depletion voltage.

### Float Zone wafers

Three FZ wafers were fabricated with three different doping profiles as detailed in table 4.4. The nominal full depletion voltage is 70 V. Figure 4.44 shows the current-voltage curves for FZ wafers, (a), (c) and (e) are for wafers with the multiplication layer and (b), (d) and (f) are for the reference wafers. Wafers with shallow doping profile (wafer 12) have high leakage current (figures 4.44 (a) and (b)), whereas wafers with deep doping profile exhibit a high break down voltage (figures 4.44 (e) and (f)).

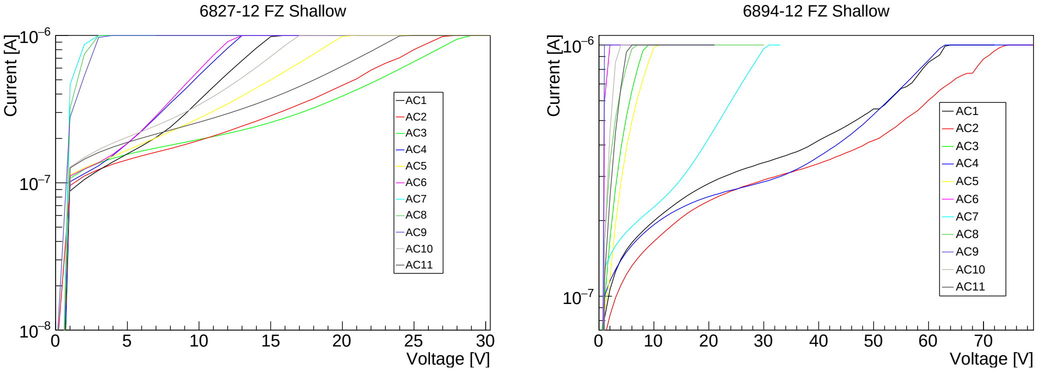

(a) 6827 W12 AC strip detectors with gain (b) 6894 W12 AC strip detectors without gain

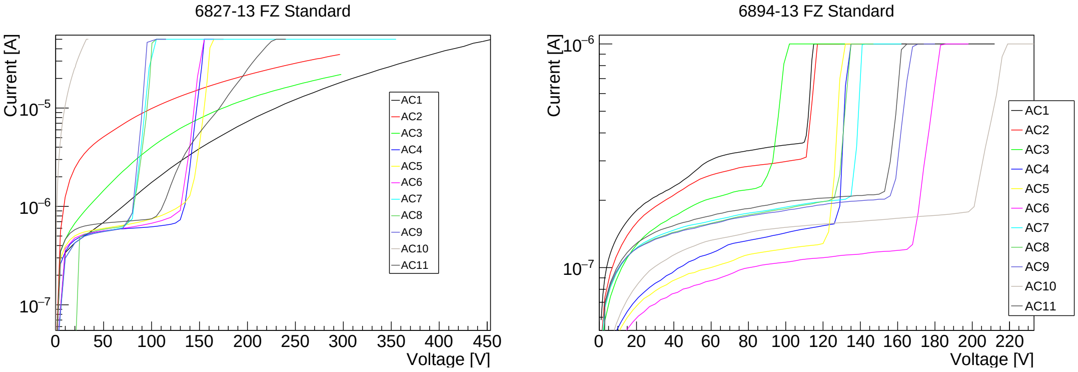

(c) 6827 W13 AC strip detectors with gain (d) 6894 W13 AC strip detectors without gain

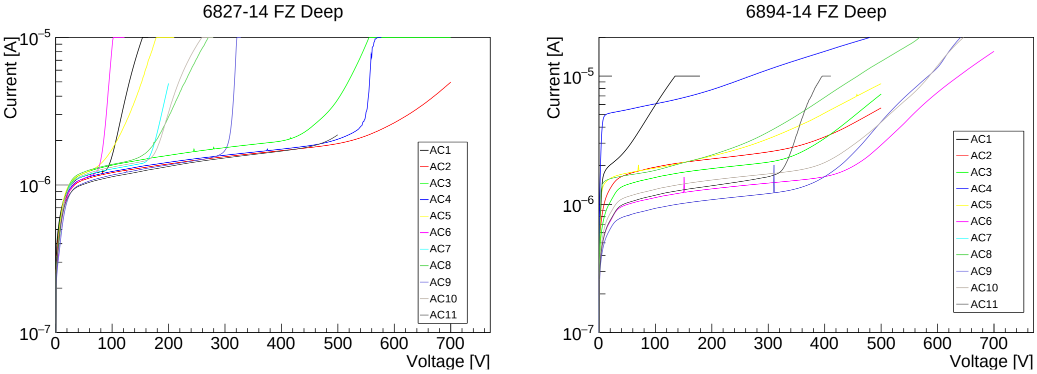

(e) 6827 W14 AC strip detectors with gain (f) 6894 W14 AC strip detectors without gain

Figure 4.44: Current-voltage measurements for the strips fabricated on FZ wafers.

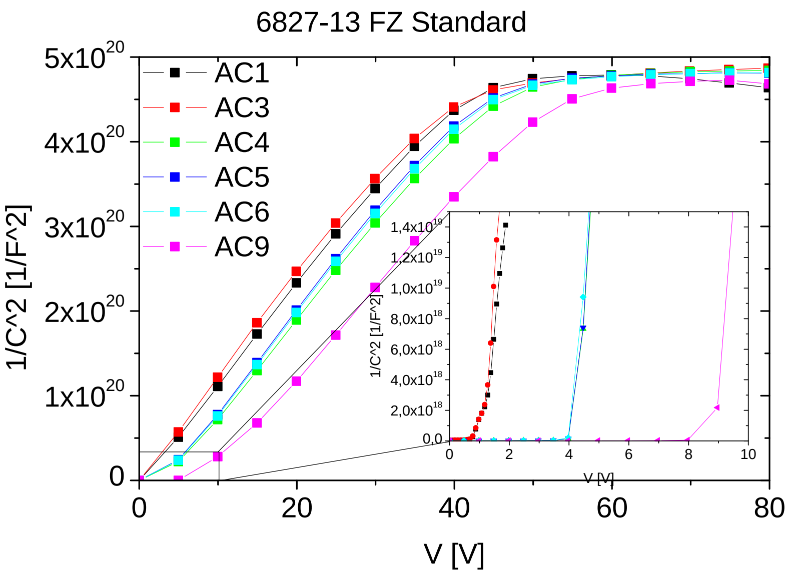

Figure 4.45: Capacitance versus voltage measurements of AC sensors from wafer 13. The different foot in the initial voltage corresponds to sensors with different width. The wider the sensor, the higher the voltage required to achieve full depletion of the multiplication layer.

Figure 4.45 shows the $1/C^2$-voltage curves for AC strip detectors from wafer 13 (standard doping profile). They show different foot depending on the width of the strip (and aggrees with the simulations of figure 4.18), which aggrees to the fact that strips with more p-implant surface need more bias voltage to deplete the multiplication layer and should show higher gain (as shown in simulations from figure 4.19).

Figures 4.46 and 4.47 show the measurements of $1/C^2$-voltage curves for AC strip detectors from wafer 14 (with and without gain respectively). Curves in figure 4.46 show a small foot at low voltages, which is related to the depletion of the multiplication layer.

Figure 4.48 shows the $1/C^2$-voltage curve for two pad detectors of wafer 14 (FZ deep) and the pad with gain depletes the multiplication layer at 14 V. Figure 4.49 shows the calculation of the doping profile for the same diodes with equation 1.13.

Diodes with gain from wafers 12 and 13 showed high current at low voltages. This can be explained because those diodes do not have a Junction Termination Extension (JTE) as the diode in figure 4.1. The JTE is a deep n-implant at the edge of the diodes that smoothes the electric field. The absence of that structure, which

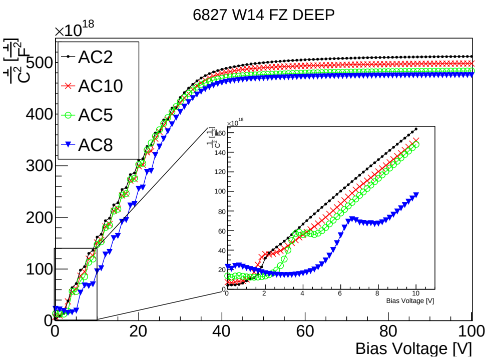

Figure 4.46: Capacitance versus voltage for AC strip detectors with 4 different widths from wafer 14 (with gain).

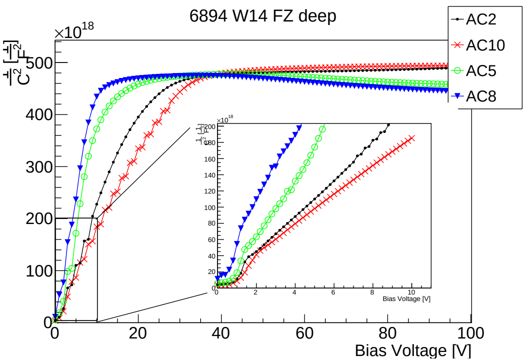

Figure 4.47: Capacitance versus voltage for AC strip detectors with 4 different widths from wafer 14 (without gain).

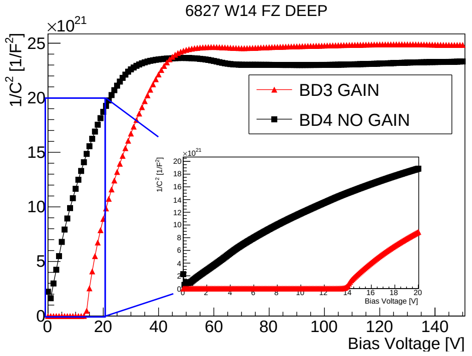

Figure 4.48: Capacitance versus voltage measurements for one diode with gain and one without gain, 4 mm diameter, of wafer 14 (FZ deep). The inset shows the region between 0 and 20 V in more detail.

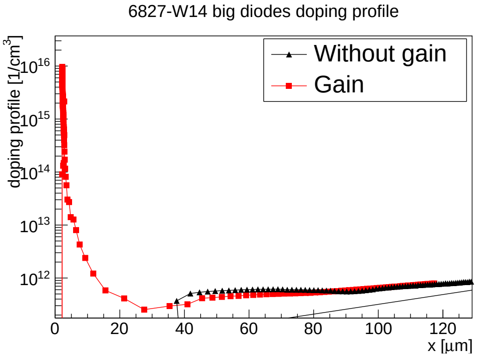

Figure 4.49: Doping profile extracted from the CV curves for the 4 mm pad diodes fabricated in FZ wafers, deep doping profile and with gain (calculated with equation 1.13).

is implanted with an extra photolitographic step, might lead to a high electric field at the edge of the pad junction which, in turn, would lead to an early breakdown.

### 4.5.3 Inter-strip resistance and bias resistance measurements

The strips are separated by p-stop structures, which compensate the inversion layer of superficial electons of the silicon dioxide. Inter-strip resistance measurements give information on the insulation resistance between strips.

The inter-strip resistance and bias resistance were measured with a HP4155 Semiconductor Parameter Analyzer (SPA) and a Cascade probe station at CNM-Barcelona. The backplane was polarized to a negative voltage, and three consecutive strips were tested with three probes[96]. The fourth probe of the SPA was used to ground the bias ring. A small voltage was applied to the middle strip while the neighboring strips read the current from the middle strip. Figure 4.50 shows the distribution of the probes during the measurement.

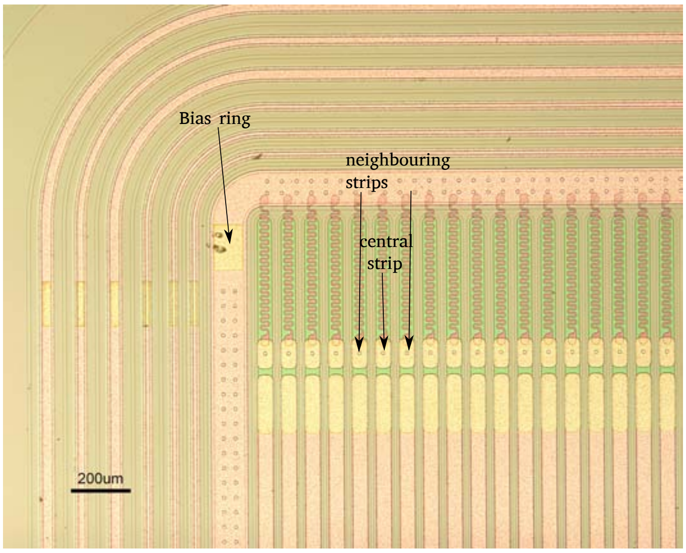

Figure 4.50: Inter strip resistance and bias resistance probes positions.

The bias resistance $R_{Bias}$ is calculated as:

$$R_{Bias} = \left[ \frac{dI_{Center}}{dV_{Center}} \right]^{-1}$$

and the inter-strip resistance is calculated as:

$$R_{Inter-strip} = \left[ \frac{dI_{Center}}{dV_{Neighbour}} \right]^{-1}$$

where $I_{Center}$ is the current of the central strip and $V_{Centre}$ is the voltage applied to the central strip. Figure 4.51 shows the inter strip resistance measurements. The wafer with deep doping profile presents lower interstrip resistance due to the longer and higher temperature thermal annealing. Figure 4.52 shows the measurement of bias resistance for three different wafers, and again, the wafers with deep profile show lower bias resistance than the standard ones.

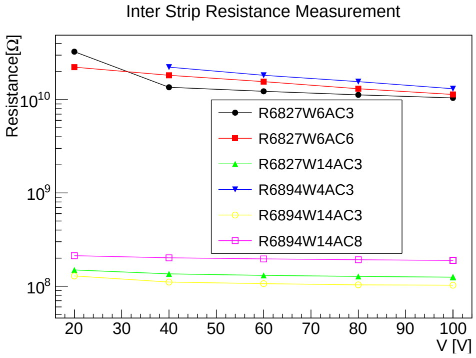

Figure 4.51: Inter strip resistance measurements.

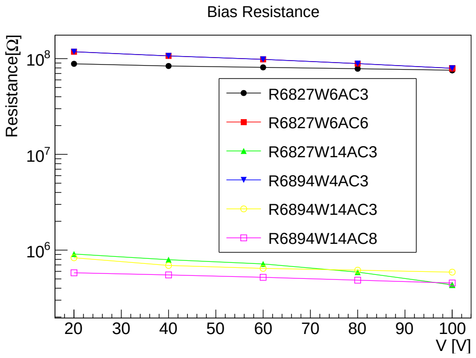

Figure 4.52: Bias resistance measurements for several sensors.

### 4.5.4 TCT measurements

Some sensors were tested with the Transient Current Technique (TCT) at UCSC (University of California Santa Cruz) during a short stay abroad financed by the FPI scholarship. Figure 4.53 shows the TCT setup used for the measurements, and figure 4.54 shows the aluminium box which contained the detector under test. The setup consists of a Faraday cage which contains the detector connected to a bias tee, which is connected to an RC circuit and an amplifier, and the amplified signal is collected by an oscilloscope. The amplifier is biased at 12 V and it provides an amplification of around 120. The radioactive source used for those measurements is an $Am^{241}$, which emits alpha particles with energy $E$ =5.486 MeV and $E$ =5.443 MeV (table 3.2).

Figure 4.55 shows the measurement of the big diodes from wafer 8 with and without gain with $Am^{241}$ compared to TCT measurements with laser of 1060 nm wavelength. Since the diodes have a support wafer of 525 µm, the alpha source was located in front of the detector. The laser measurements present an increment in the gain with the voltage and reach values of 2.5. The gain is calculated integrating the charge collected by the diode with gain and normalizing the value with the integrated charge of the reference diode.

Figure 4.56 shows the TCT measurements of 4 detectors, two big diodes from wafer 8 with and without gain (the same used in figure 4.55) and the TCT mea-

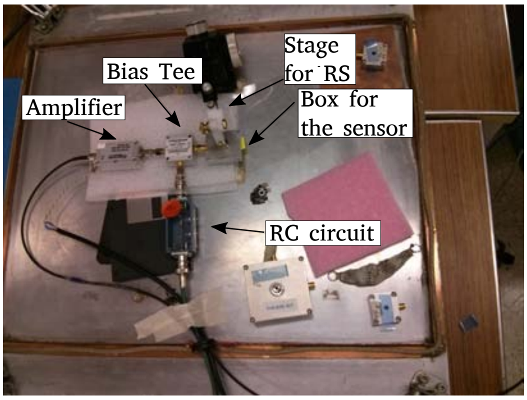

Figure 4.53: Photo of the setup at UCSC. The setup was inside a Faraday cage and the output signal was connected to an oscilloscope. The sensor was biased with a Keithley power supply and the amplifier was biased at 12 V.

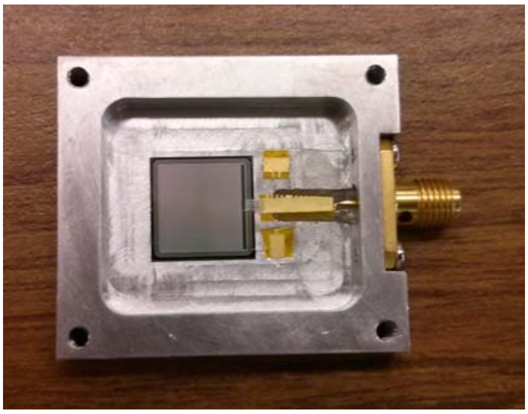

Figure 4.54: Photo of a strip sensor wire bonded to the connections (16 strips bonded together and shorted).

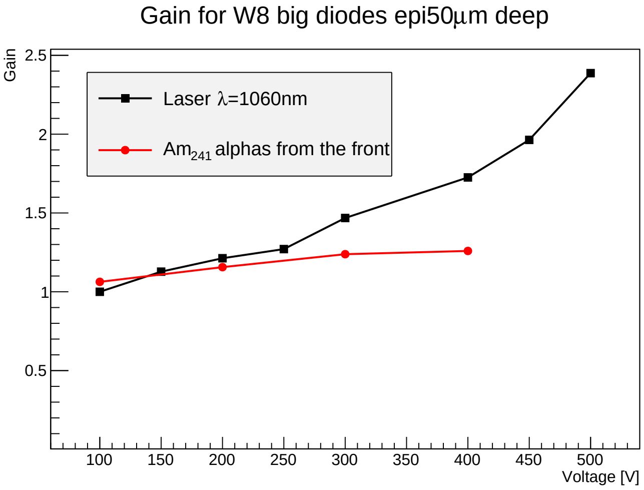

Figure 4.55: Gain measurements for the diodes from wafer 8 illuminated from the front with an $Am^{241}$ radioactive source and with an IR laser of 1060 nm wavelength.

surements of a diode without gain. The TCT measurements from figure 4.56 are an average of 1000 pulses biased at 400 V. Table 4.5 shows the rising times (the time the signal takes to go from 10% of the pulse to 90% of the pulse) for the diodes measured in figure 4.56. The epitaxial detectors show a faster signals than the FZ detector, since they are thinner and therefore they collect the charge faster.

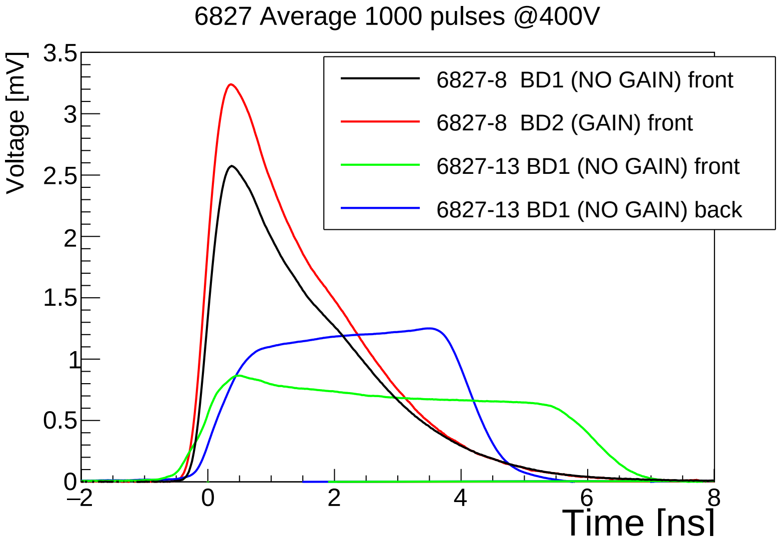

Figure 4.56: Rising times of different sensors with gain and without gain, from the front and from the back. The detectors were biased at 400 V.

Nevertheless, the signal from the sensor with multiplication layer has a higher pulse and a slower rise time, or higher slew rate, than the one without multiplication[97]. Detectors with high slew rate are better for detectors dedicated to medical PET, mass spectroscopy or particle tracking[86].

| Sensors | Sensors description | Rise time [ps] | Height [mV] |
|---|---|---|---|
| 6827-8 BD1 | Epi50, NO gain, front | 425 | 2.575 |
| 6827-8 BD2 | Epi50, gain, front | 445 | 3.240 |
| 6827-13 BD1 | FZ, NO gain, front | 705 | 0.865 |
| 6827-13 BD1 | FZ, NO gain, back | 765 | 1.1 |

Table 4.5: Rising times of the pulses from figure 4.56 at 400 V. The pulses are an average of 1000 pulses.

### 4.5.5 Measurements with trialpha radioactive source

Big diodes (4 mm diameter) from wafer 14 (FZ deep) were tested with a trialpha radioactive source ($Am^{241}$, $Pu^{239}$ and $Cm^{244}$) that has an approximate energy of 5 MeV (table 3.2 shows the energy of the trialpha radioactive source). Two diodes were measured, one with gain and the other without gain. The measurements were carried out at CNM radiation lab with the setup from figure 3.13. The detector was illuminated from the backplane and the alpha particles were entering through the ohmic contact, and since the output was a negative signal, an inverter was needed.

Figure 4.57 shows the measurements, and it can be seen that the difference between the energy peak for the detector with gain and the one without gain is small.

The tri-alpha measurement shows three peaks, and one of them was fitted with a gaussian function. The peak chosen for the fitting was the most energetic one (the Curium alpha particles). The data shown in figure 4.57 have a small error bars (almost negligible) which correspond to the error of the gaussian fitting. The gain at 900 V is 1.06 which is very small compared to what was expected. Such small gain can be explained because the deep difusion soften the electric field peak, leading to lower gain signal.

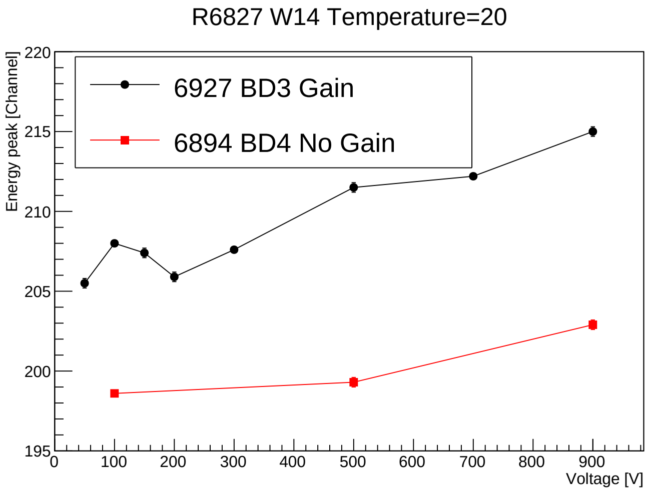

Figure 4.57: Energy peaks of the big diodes from wafer 14, measured with the tri-alpha radioactive source. The diode with gain shows a slightly higher energy peak than the diode without gain. The gain at 900 V is 1.06.

### 4.5.6 Measurements at Diamond Light Source

Some strip detectors were tested on B16 beam line at Diamond Light Source synchrotron (Oxford[98]), with a micro-focused beam of photons at 15 keV (X-rays). These measurements were taken during the short stay of the FPI scholarship at the University of Glasgow. The strip detectors prepared for testing were:

- R6827 W4 AC9 - wafer with 10 µm epitaxy, standard, gain
- R6894 W4 AC9 - wafer with 10 µm epitaxy, standard, no gain
- R6827 W13 DC2 - FZ, standard, gain (breakdown at 300 V)

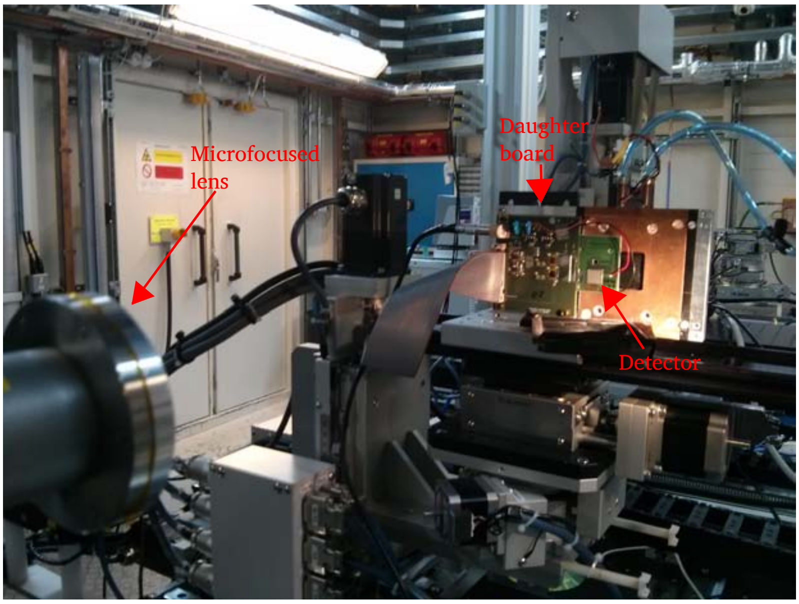

Figure 4.58: Photo of the setup in Diamond light source B16 beam-line.

- R6827 W14 AC11 - FZ, deep, gain (up to 900 V)
- R6894 W14 AC11 - FZ, deep, no gain (up to 500 V)

128 strips of the detectors were wire bonded to the Alibava systems daughter board[99]. Figure 4.58 shows the Diamond Light Source B16 beam-line setup, the lens that focus the beam is located in the left of the image, and the sensor connected to the daughter board of the Alibava setup is in the right part of the image. The setup had a micrometric stage, all the measurements were taken at room temperature, and the detectors were located perpendicular to the beam. The DUT was biased with a Keithley 2410 and the data were taken with Alibava Systems hardware.

The photons impinged the detector without a trigger, using the pedestal modes of the Alibava software. Figure 4.59 shows the analysis files of the measurements. Figure 4.59 (a) shows the amplitude of the spectrum, and the bottom right plot shows the amplitude of the data taken, which maximum value is then plotted in the analysis. Although the fitting has an error associated, the plots do not show any error bar for simplification of the figures. Figure 4.59 (b) shows the channel number, figure 4.59 (c) shows the cluster size of the data and figure 4.59 (d) shows the pedestals of the measurement.

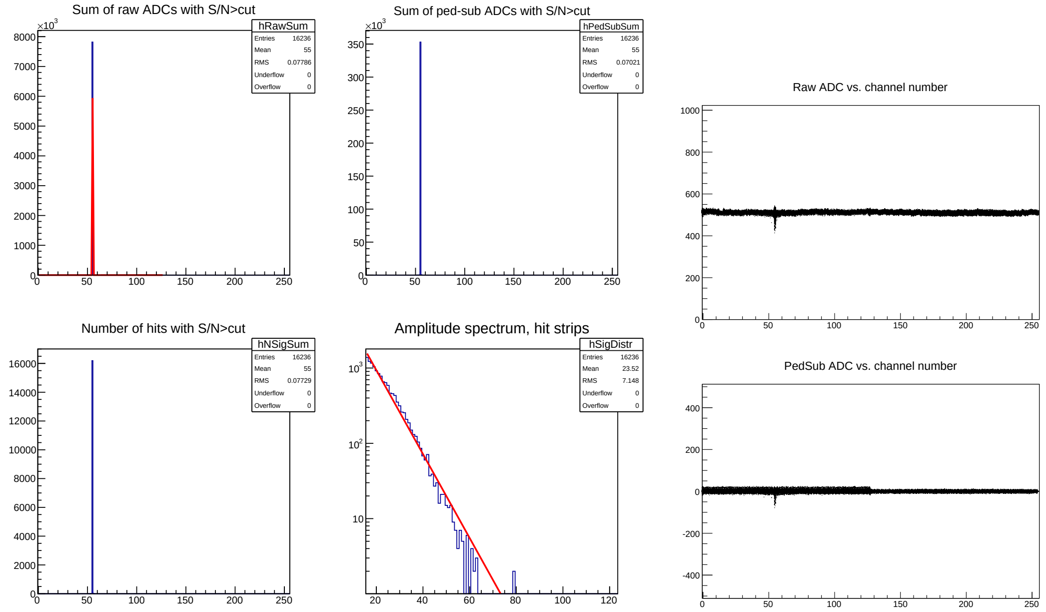

(a) Amplitude spectrum. The plot on the bottom right shows the amplitude of the signal

(b) Channel number

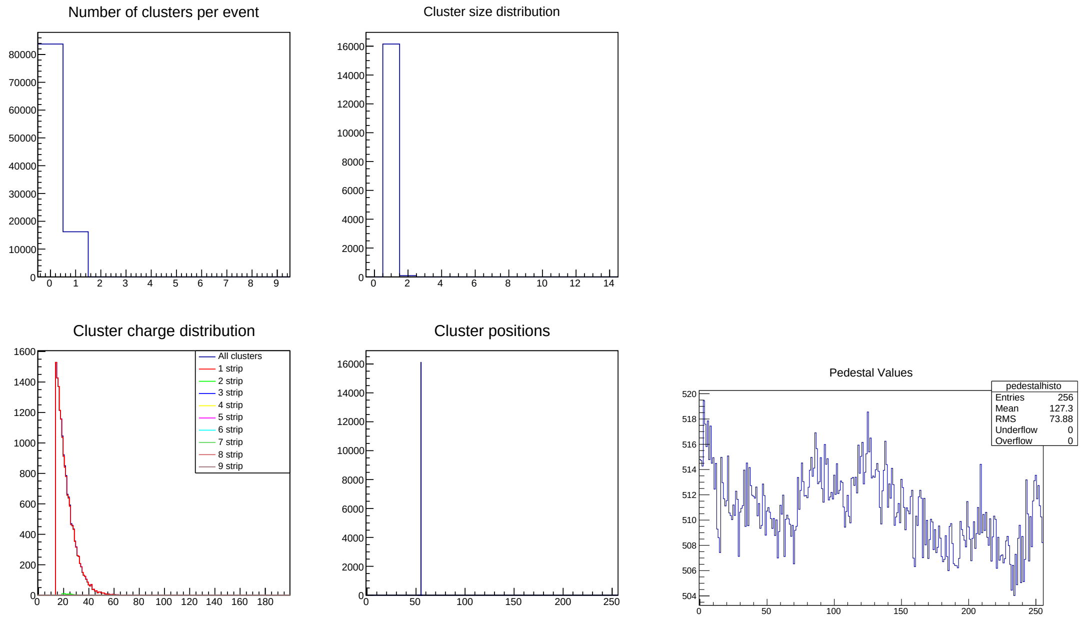

(c) Cluster

(d) Pedestals

Figure 4.59: Analysis data for the Diamond Light Source Alibava setup.

### R6827 W4 AC9 - wafer with 10 µm epitaxy, standard with gain

The sensor had very high current (200 µA at 20 V). The data showed no difference between the hit and the noise, and therefore it was impossible to subtract any signal at all.

### R6894 W4 AC9 - wafer with 10 µm epitaxy, standard without gain

The current for wafer with 10 µm with standard doping profile without gain was much lower than its counterpart with gain, although the signal was difficult to observe for events with low rate. The real thickness of the wafers with a 10 µm epitaxy is only 5 µm thus in order to have enough statistics to analyze the data the number of events to be recordered were more than $10^6$. Figure 4.60 (b) shows the amplitude of the signal at four different points (separated by 5 µm), for the sensor AC9 from wafer 4 without gain biased at 80 V. Since the software had to record $10^6$ events, no more points were taken for this device ignoring the position of the strip during the scan of figure 4.60 (b).

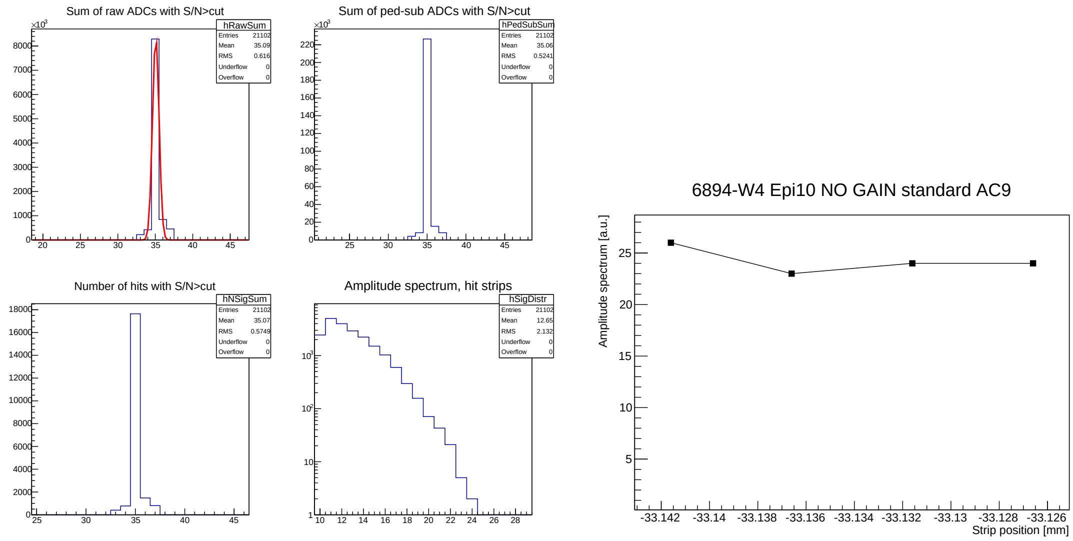

(a) Example of the amplitude spectrum for one of the measurements.

(b) Collected amplitude at 4 different positions

Figure 4.60: Maximum amplitude of the detector fabricated on 10 µm thick epitaxis with standard doping profile for 1M events collected. The sensor was biased at 80 V.

A beam of monoenergetic photons with an incident intensity $I_0$ penetrating a layer of material of thickness $x$ and density $\rho$ emerges with an energy with exponential attenuation, as reported with the Beer-Lambert's law in equation 1.14. The attenuation coefficient at 15 keV is calculated from tables from [100], and table 4.6 shows the absorbed probability for two silicon thicknesses (the ones measured during the Diamond Light Source testbeam).

| x [µm] | Absorbed probability [%] |
|---|---|
| 5 | 0.06 |
| 300 | 0.98 |

Table 4.6: Absorbed probability of 15 keV x-rays for different silicon thicknes.

The number of photons at Diamond Light Source synchrotron is approximately 5 each 25 ns[101], and the probability of the photon interacting with the detector follows a binomial distribution:

$$\binom{N}{k} P^k (1-P)^{N-k}$$

where $k$ is the number of successes, $N$ the number of photons and $P$ the probability of interaction. Thus, the probability for 5 photons to interact with silicon is given by:

- 0 photons: $(1-P)^N$
- 1 photon: $N \cdot P \cdot (1-P)^{(N-1)}$
- 2 photons: $10 \cdot P^2 \cdot (1-P)^{(N-2)}$
- 3 photons: $10 \cdot P^3 \cdot (1-P)^{(N-3)}$
- 4 photons: $N \cdot P^4 \cdot (1-P)^{(N-4)}$
- 5 photons: $P^N$

The calculation of the number of photons that interact with silicon is given in table 4.7. For 5 µm of silicon the probability of interaction is very low, for each bunch, 72.04% will not interact with silicon, whereas for 300 µm of silicon most photons will interact with the silicon substrate. This results explains the number of events taken with the software and the low signal of figure 4.60.

| | 5 µm | 300 µm |
|---|---|---|
| 0 photons | 72.04% | 0% |
| 1 photon | 24.42% | 0% |
| 2 photons | 3.30% | 0% |
| 3 photons | 0.23% | 0.36% |
| 4 photons | 0.01% | 9.05% |
| 5 photons | 0% | 90.58% |

Table 4.7: Probability of 15 keV x-rays photons of being absorbed for different silicon thicknes.

### R6827 W13 DC2 - FZ Standard with gain

Figure 4.61 shows a 100 µm scan of a strip with steps of 5 µm for the sensor R6827 W13 DC2. The sensor was fabricated in a FZ wafer with standard doping profile with gain, and has a strip width of 32 µm. Since it is a DC coupled strip detector, it needs an external AC circuit to decouple the signal of the sensor from the bias. The scan was carried out at 100, 200 and 300 V and each point took $10^5$ events.

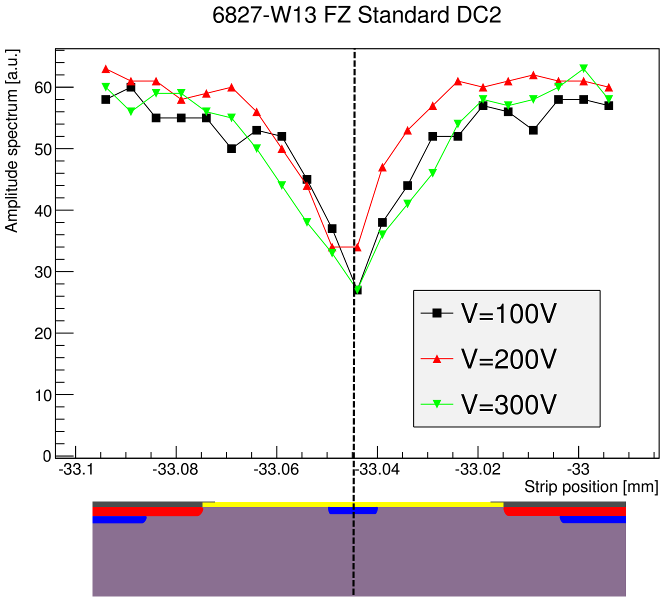

Figure 4.61: 15 keV x-ray measurement for the sensor R6827 W13 DC2 at 3 different bias voltages.

Each scan crossed two adjacent strips and the signal at the middle point between two strips was half the maximum signal. The measurements show no significant difference at different voltages, and therefore, these sensors do not show any appreciable gain.

### R6827 W14 AC11 - FZ Deep with gain

Figure 4.62 shows a 100 µm scan of a strip with steps of 5 µm for the sensor R6827 W14 AC11. The sensor was fabricated in a FZ wafer with deep doping profile with gain, and has a strip width of 32 µm. The sensor reached 900 V before breakdown. Figure 4.62 shows the scan for three bias voltages. $10^5$ events were recored at each step.

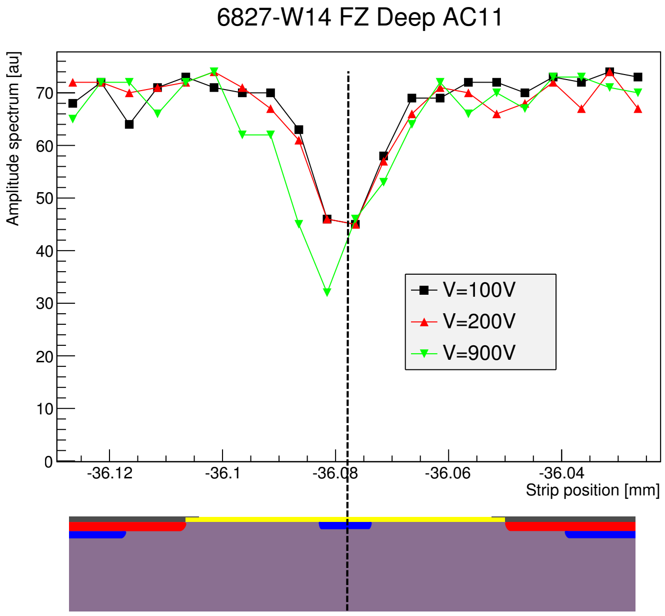

Figure 4.62: X-ray measurements of the sensor R6894 W14 AC11 at three different bias voltages.

Each scan crossed two adjacent strips and the signal at the middle point between two strips was half the maximum signal. The measurements show no significant difference at different voltages, and therefore, these sensors do not show any appreciable gain.

### R6894 W14 AC11 - FZ Deep without gain

Figure 4.63 shows a 100 µm scan of a strip with steps of 5 µm for the sensor R6827 W14 AC11. The sensor was fabricated in a FZ wafer with deep doping profile without gain, and has a strip width of 32 µm. The sensor reached 400 V before breakdown. Figure 4.63 shows the scan for four bias voltages, and each measurement collected $10^5$ events.

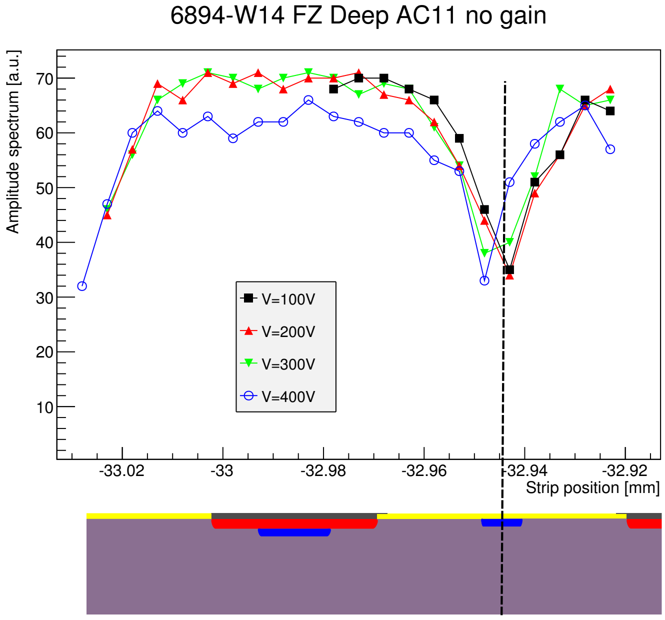

Figure 4.63: Measurement of sensor R6894 W14 AC11 at 4 different bias voltages.

The scan shows an entire strip and a small part of the adjacent one. The amplitude spectrum has similar values as the sensor with gain, as expected, hence no gain is observed during those measurements.

The measurements of FZ wafers do not show any gain, on agreement with the results presented in references [102; 103].

### 4.5.7 IBIC measurements

Two strip sensors were taken to the Centro Nacional de Aceleradores (CNA[104]) in Sevilla and they were measured with the IBIC (Ion Beam Induced Charge) technique[105]. 20 strips were bonded through the DC pads and all the charge were collected for the same output. The measured detectors were:

- W8 AC5, 50 µm Epitaxial wafer with deep implant, with strips 48 µm wide with multiplication.
- W14 AC4, FZ wafer with deep implant, with strips 48 µm wide with multiplication.

Those detectors were chosen since the diodes showed some multiplication (figures 4.55 and 4.57). The particles used to illuminate the detector were protons with a beam spot around 4 µm × 4 µm with two energies: 2 MeV and 4 MeV. The protons came from a high-voltage Tandem accelerator, which accelerates ions twice by means of high voltage configuration. SRIM [106] (The Stopping and Range of Ions in Matter) is a software that allows to simulate the interaction of ions with matter and predict their penetration range. Table 4.8 shows the calculated range of penetration of protons in silicon and the corresponding deposited energy in wafers of 50 µm and 300 µm thick. Table 4.9 shows the simulation with SRIM of the range of protons through 1 µm of aluminium and 1 µm of $SiO_2$, in order to reproduce the detector in maximum detail. The range of the protons do not change significantly through the aluminium or the silicon dioxide.

| Energy MeV | Silicon range [µm] | Deposited energy for 300 µm Si [MeV] | Deposited energy for 50 µm Si [MeV] |
|---|---|---|---|
| 2 | 48.4 | 2 | 2 |
| 4 | 150 | 4 | 0.9 |

Table 4.8: Range of the protons in silicon and deposited energy calculated with SRIM[106].

| Energy MeV | Silicon range [µm] | Silicon range for 1 µm Al [µm] | Silicon range for 1 µm $SiO_2$ [µm] |
|---|---|---|---|
| 2 | 48.4 | 48.3 | 48.3 |
| 4 | 150 | 149 | 149 |

Table 4.9: Range of the protons in silicon calculated with SRIM[106].

Figure 4.64 shows a simulation run with Geant4 software[107] of deposited energy of protons at 2 MeV through 300 µm of silicon through 1 µm of aluminium and 1 µm of $SiO_2$.

The range of protons for a silicon detector 50 µm thick stands in the border of the detector. The dopants from the low resistance substrate wafer diffused during fabrication will reduce the thickness of the epitaxys by 4 µm. Moreover the protons will go through the implant of the detector, whose doping profile depth is 6 µm, thus it will have a dead area around 3 µm and 6 µm where the protons will loose energy but will not be collected due to recombination. Figure 4.65 shows the simulation with Geant4 of the energy deposited in silicon with a 6 µm of non-detecting layer (the doping thickness) and with 40 µm of active silicon, and the possible case of

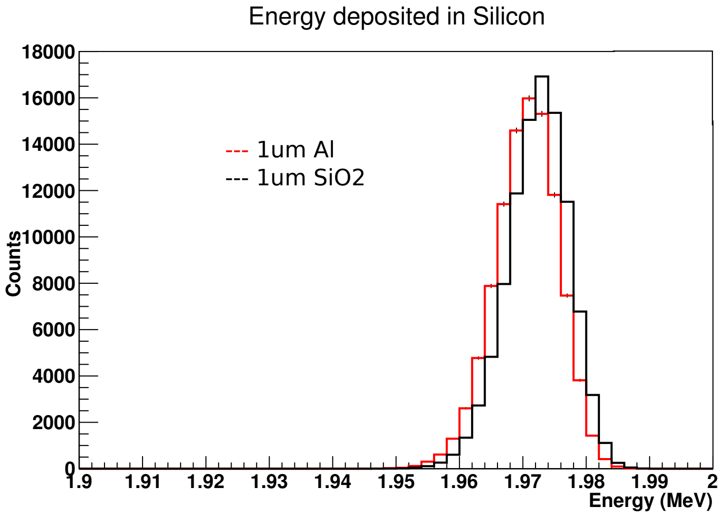

Figure 4.64: Geant4 simulation of the deposited energy by 2 MeV protons passing through 300 µm of silicon.

3 µm of non-detecting layer (the doping thickness) with 43 µm of active silicon. The real case will be between those extreme possible cases. The simulation is run for 10000 protons and for energies of 2 MeV and 4 MeV. The simulations show that for 2 MeV the energy deposited is close to the maximum possible energy, whereas the deposited energy for 4 MeV is around 0.7 MeV, slightly smaller than the simulation with SRIM represented in table 4.8. The simulations with 2 MeV energy show two peaks, one at lower energy and a smaller one at higher energy, which corresponds to the Bragg peak as it corresponds to the deposited energy for a detector with 100 µm which will leave all the energy inside the detector. The peak at lower energy corresponds to the particles that go through the detector and do not deposit all the energy within the silicon.

The measurements in the IBIC experiment were taken with the DUT located perpendicular to the beam inside a vacuum chamber at room temperature. The detector was connected to a PCB that amplified the signal that was then collected with an MCA (figure 4.66 shows a picture of the setup). Since the MCA reads only positive pulses an inverter was used (the PCB and inverter used are the ones from figure 3.13). The MCA was synchronized to the beam spot, scanning a matrix of 100×100 points. The measurement took the collected charge for different energy ranges as well as its spectrum.

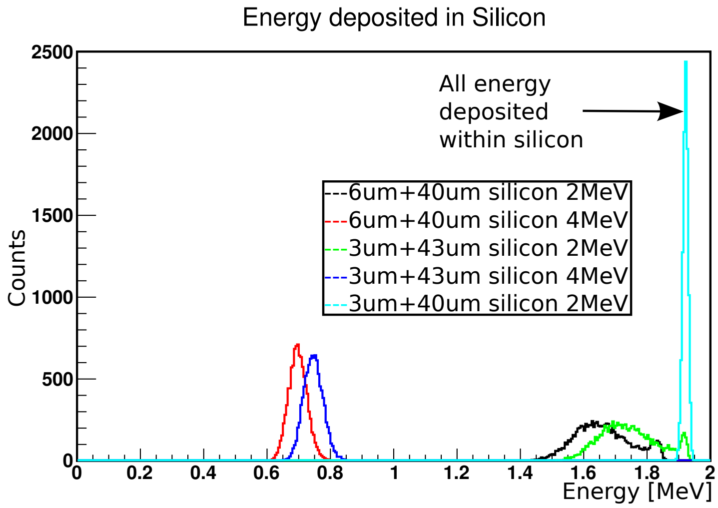

Figure 4.65: Geant4 simulation of the deposited energy by 2 MeV and 4 MeV protons through 46 µm of silicon. The simulation took into account 10000 protons.

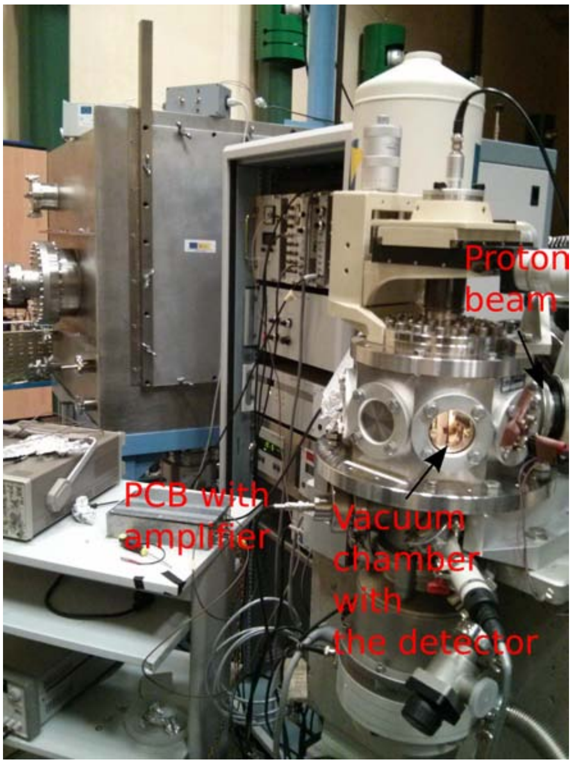

Figure 4.66: Setup at CNA for the tandem experiment.

Both detectors have a strip width of 48 µm, with a multiplication layer of 30 µm wide and a distance between strips of 32 µm (the pitch is 80 µm), sometimes the position of the strip is not clear since the distance between strips and the width of the multiplication layer only differs 2 µm.

### Measurements of W8 AC5

The detector is fully depleted at 150 V and the break down voltage is at 140 V, thus it was not possible to measure the detector fully depleted. Figure 4.67 shows the IBIC measurement for protons at 2 MeV with a beam spot resolution of 5 µm×5 µm. Figure 4.67 (a), (b) correspond to an area of 100 µm×100 µm and (c), (d) correspond to an area of 1000 µm×1000 µm. (a) and (c) correspond to an energy range of $E1$ =1.37 MeV-1.69 MeV and (b) and (d) correspond to an energy of $E2$ =1.78 MeV-1.92 MeV. Figure 4.68 shows the spectrum of the IBIC measurements for protons at 2 MeV, and it shows the spectrum windows for $E1$ and $E2$.

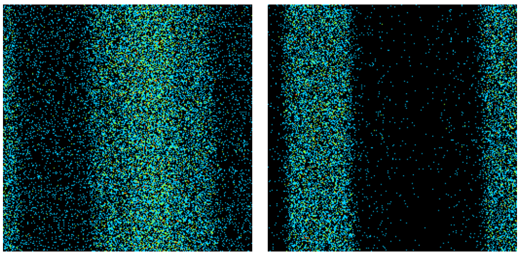

(a) $E1$ =1.37 MeV-1.69 MeV (b) $E2$ =1.78 MeV-1.92 MeV

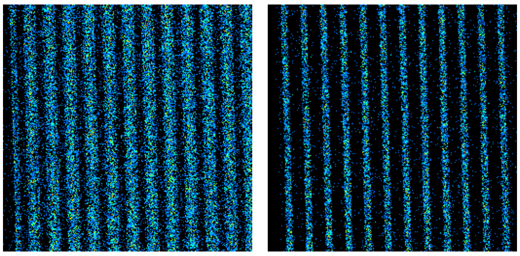

(c) $E1$ =1.37 MeV-1.69 MeV (d) $E2$ =1.78 MeV-1.92 MeV

Figure 4.67: IBIC measurement at 100 V. (a, b) show a 100 µm×100 µm window and (c, d) show an area of 1000 µm×1000 µm.

Figure 4.67 (c) and (d) show the edge of the bonded strips (bottom left part of the figure), thus the strip is the blue line shown in figure (d) corresponding to the high energies E2. The images were taken for different channels (given by the

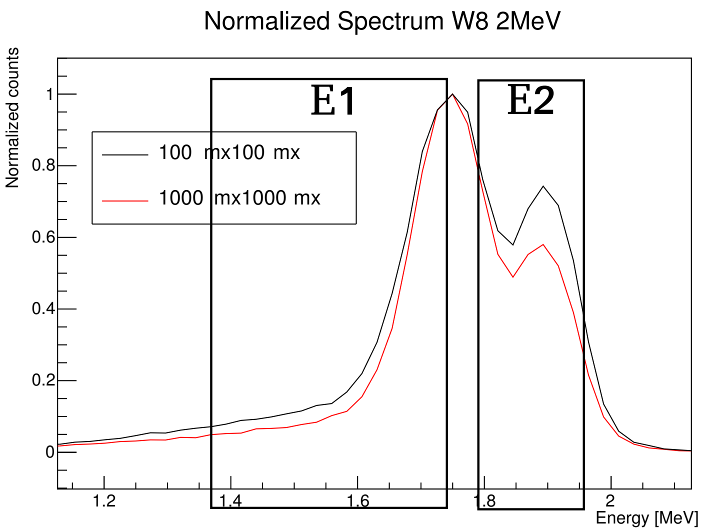

Figure 4.68: Spectrum of the W8 AC5 strip detector.

MCA), and this channel corresponds to an energy. The correlation between channel and energy can be calibrated with a pulse test. A pulse generator created pulses of known energy and the channel was read. The linear fit for channel with energy was calculated with three points, which can generate some error. Nevertheless, the maximum deposited energy corresponds to 2 MeV, as expected (figure 4.68).

The detector was measured with protons at 4 MeV, but the data is more noisy and it did not show any relevant result.

The images of figure 4.67 show 2 different regions of the strips, (b) corresponds to the center of the strip with a width of 30 µm, and (a) shows the position between the strip. The maximum energy of the spectrum is located at 2 MeV as the protons energy, which according to the simulations is slightly higher than the expected energy.

### Measurements of W14 AC4

The detector was fully depleted at 150 V and was measured using protons with two energies: 2 MeV and 4 MeV.

Figure 4.69 shows IBIC images of the detector with protons at 2 MeV with the detector biased at two voltages (150 V and 400 V), and the images are separated in three different energies, E1=1.56 MeV-1.66 MeV, E2=1.78 MeV-1.87 MeV and E3=1.96 MeV-2.16 MeV. The figure shows a region of 100 µm×100 µm. Figure

**150V**

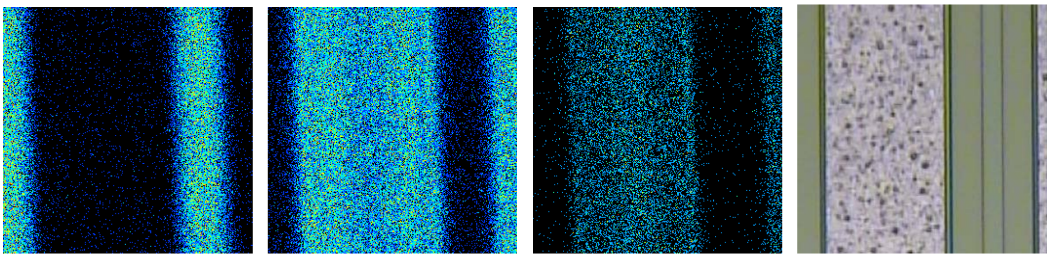

(a) E1=1.56 MeV-1.66 MeV (b) E2=1.78 MeV-1.87 MeV (c) E3=1.96 MeV-2.16 MeV (d) Photo of the strip front

**400V**

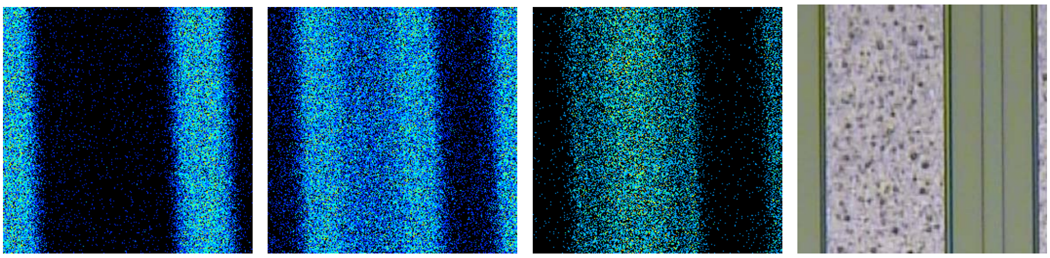

(e) E1=1.56 MeV-1.66 MeV (f) E2=1.78 MeV-1.87 MeV (g) E3=1.96 MeV-2.16 MeV (h) Photo of the strip front

Figure 4.69: IBIC measurement at 150 V (a, b, c) and 400 V (e, f, g). They show a region of 100 µm×100 µm, and the protons had an energy of 2 MeV.

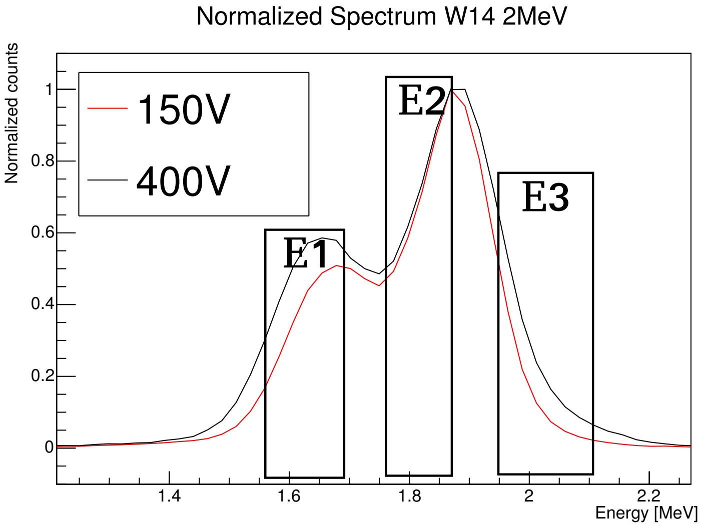

Figure 4.70: Spectrum of the W14 AC4 strip detector for protons at 2 MeV.

4.70 shows the spectrum corresponding to the scans of the W14 AC4 detector for protons with energy of 2 MeV, and the three energy ranges E1, E2 and E3. The maximum energy of the spectrum is higher than 2 MeV, which is related to the multiplication mechanism, since the simulation in figure 4.64 shows that the deposited energy at 300 µm thick silicon should deposit slightly less than 2 MeV. The diodes showed a gain of 1.06, which agrees with the results obtained (figure 4.57). As reported in the previous measurement (figure 4.68), the spectrum shows two peaks, although for this detector the peak corresponding to the lower energy is smaller than the peak corresponding to the highest energy. The IBIC measurements were taken in three energy regions: E1 corresponds to the first peak and collects charge between the strips; the second region E2 collects charge at the edge of the strips; finally the region with highest energy, E3, shows most of the charge in the middle of the strip.

Figure 4.71 shows the IBIC measurement for the same detector for protons at 4 MeV. The measurements were taken at 50 V (under-depleted), 150 V and 400 V (fully depleted detector). Figure 4.71 shows an area of 200 µm×200 µm, and the images are separated in three energy regions, E1, E2 and E3. Figure 4.71 (a) shows charge collected in the middle of the strip, but at 400 V it disapears and moves to a high energy spectrum (figure 4.71 (k)). Figure 4.71 (d), (h) and (l) show a front photo of the strips, corresponding to the position of the strips during the measurement.

Figure 4.72 corresponds to the spectrum of figure 4.71, and shows the three energy regions of figure 4.71 (E1, E2 and E3). The amplifier of the PCB had to be recalibrated since the energy saturated the signal. Then the spectrum might be shrunk and thus, only one peak is visible. The maximum energy does not reach the energy of the protons of 4 MeV and it might be to the error associated to the calibration or that not all the protons energy is deposited into the silicon bulk (which desaggrees with SRIM calculations of table 4.8).

**50V**

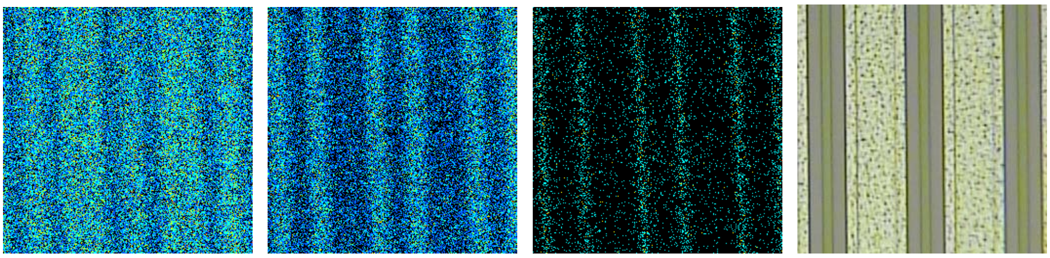

(a) $E1$ =3.18 MeV-3.25 MeV (b) $E2$ =3.32 MeV-3.40 MeV (c) $E3$ =3.43 MeV-3.50 MeV (d) Photo of the strips

**150V**

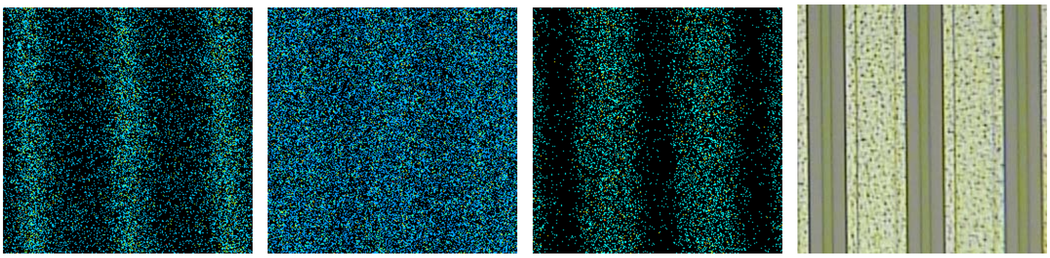

(e) $E1$ =3.18 MeV-3.25 MeV (f) $E2$ =3.32 MeV-3.40 MeV (g) $E3$ =3.43 MeV-3.50 MeV (h) Photo of the strips

**400V**

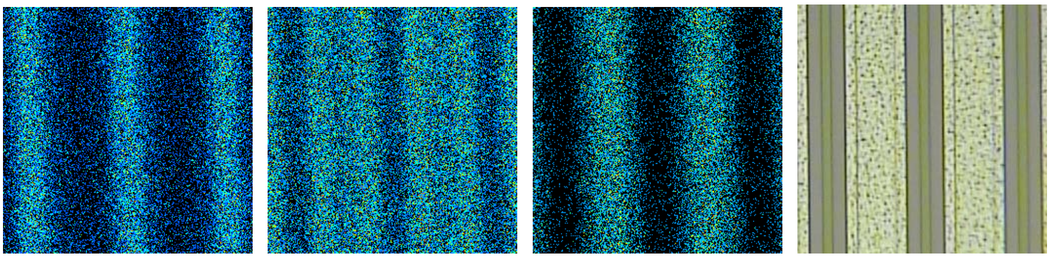

(i) $E1$ =3.18 MeV-3.25 MeV (j) $E2$ =3.32 MeV-3.40 MeV (k) $E3$ =3.43 MeV-3.50 MeV (l) Photo of the strips

Figure 4.71: IBIC measurement for 50 V (a, b, c), 150 V (e, f, g) and 400 V (i, j, k). The pictures show a region of 200 µm×200 µm and the protons had an energy of 4 MeV.

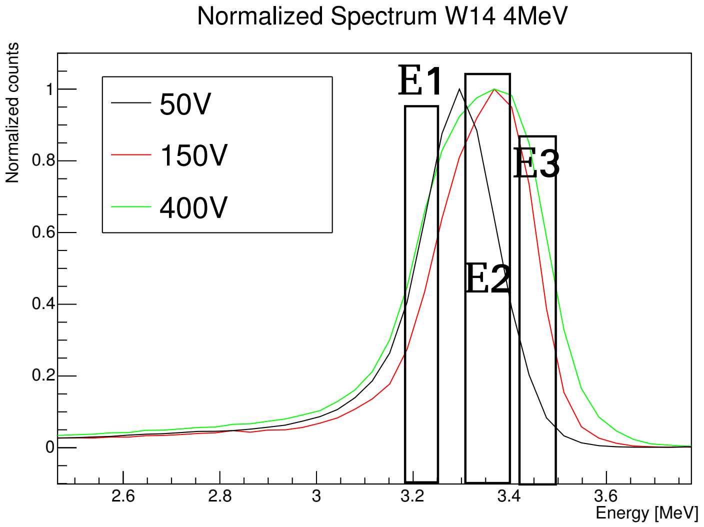

Figure 4.72: Spectrum of the W14 AC4 strip detector with energy of 4 MeV protons.

Due to limited beam time, we did not measure detectors without gain, but this measurement would be interesting for comparison.

### TCAD simulations for a MIP in different positions of the strip

IBIC measurements showed different collected charge at different energies in different strip locations. For this purpose, simulations were run for different MIP positions. The simulated structure is a 2D three strips detector equal to the FZ wafer AC6 (46 µm) type. Figure 4.73 shows the 3 strips simulated (the wafer simulated is 285 µm thick), and the three different positions of the MIP particles are:

1. Center of the strip
2. Edge of the strip (without the multiplication layer underneath)
3. P-stop region

Figure 4.74 shows the gain of the MIP for the three different positions. The gain is calculated integrating the collected charge for a strip with multiplication divided by the charge of the same strip and the same MIP position without multiplication, with an integration time of 25 ns. The MIP is simulated with the Heavy Ion Synopsys Sentaurus sdevice model, with a linear energy transfer (LET_f) of $1.282 \times 10^{-5}$ pC/µm. The figure shows that, once the detector is depleted, the charge is multiplied at the center of the strip.

According to the simulations in figure 4.74, the higher energy expected with the depleted detector is at the center of the strip. This results agrees with figure 4.71 (k), which shows the strip signal at higher energies.

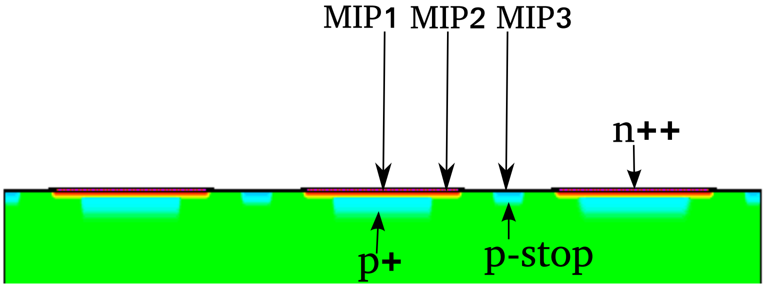

Figure 4.73: Positions for the MIP crossing the strip detector.

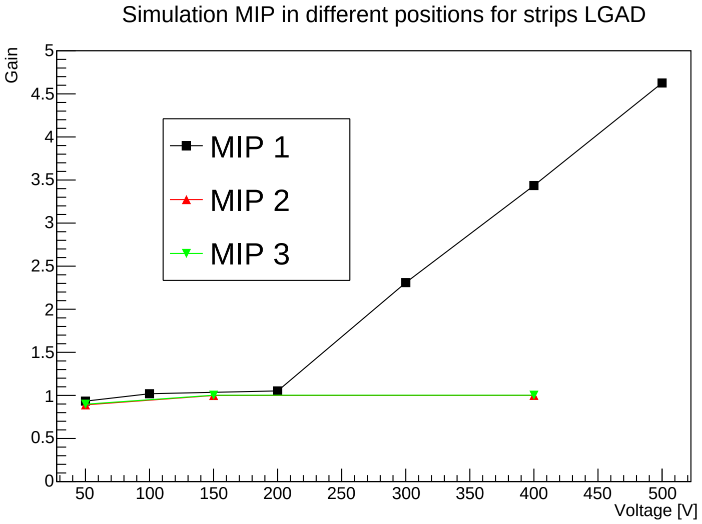

Figure 4.74: Simulation of the gain for a MIP crossing a strip at different positions.

## 4.6 New structure

Since segmented LGAD do not present an homogeneous multiplication through all the surface as presented in figure 4.74, the possibility to fabricate p-on-p detectors with the multiplication layer located in the backside was considered. The name proposed for these detectors is iLGAD (*inverse* LGAD)[108; 97]. Figure 4.75 shows a scheme of the p-on-p configuration. Since the entire surface will have the multiplication layer all the strips will have homogeneous charge collected[109]. The fabrication for iLGAD will be a double sided process, and since the detector will be depleted

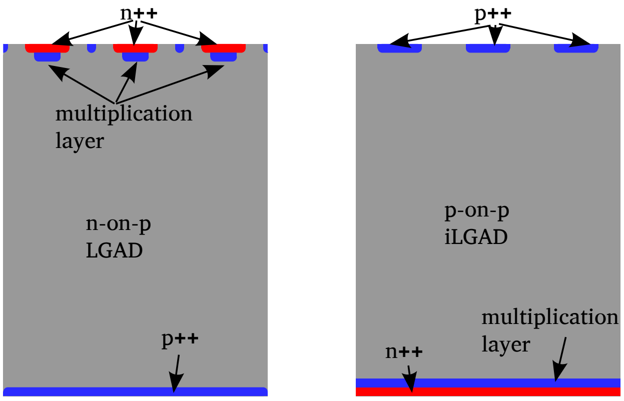

Figure 4.75: Scheme of n-on-p LGAD structure (left) and p-on-p iLGAD (right) structure of 3 strips.

from the back, once irradiated the depleted volume will not reach the strip or pixels. Besides p-on-p detectors collect holes, which are slower and are more likely to be trapped, hence they should be fabricated in thin wafers for faster signals. The thin iLGAD detectors are suitable for fast detectors applications such as medical PET, mass spectroscopy or particle tracking where the pulse amplitude is more important than the pulse area[86; 110], but not as radiation hard detectors.

### 4.6.1 Simulations

Figure 4.76 shows the electric field at 500 V for the LGAD (left) and iLGAD with and without p-stop (center and right respectively). LGAD and iLGAD structures show high electric field at the junction side, however, the iLGAD with p-stop presents a high electric field region near the strip due to the p-stop.

Figure 4.77 shows the comparison of the IV curves for the simulation of the p-on-p and n-on-p structures with and without p-stop. The curve corresponding to the thin iLGAD (24 µm) with p-stop overlaps with the current of the strips without p-stop. iLGAD has higher currents because it has more multiplication surface, and the iLGAD strips 48 µm width with p-stop has a higher current because of the high electric field at the edge of the p-stop. Figure 4.78 shows the CV simulation of iLGAD strip detector. The full depletion voltage is 120 V and it takes more than 50 V to deplete the multiplication layer.

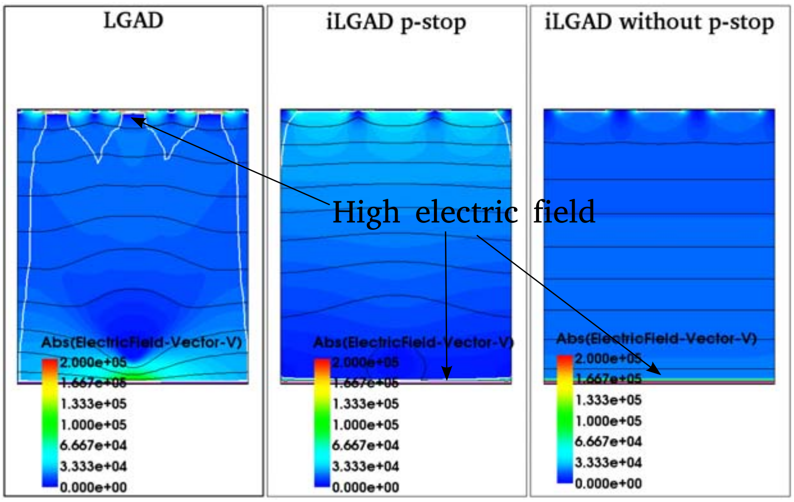

Figure 4.76: Electric field for LGAD (left) and iLGAD detectors with and without p-stop at 500 V.

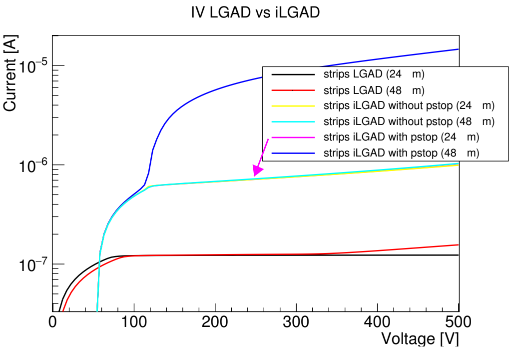

Figure 4.77: IV simulations for the p-on-p structure and n-on-p structure of 3 strips into 285 µm thick silicon wafer for two different widths of the strips.

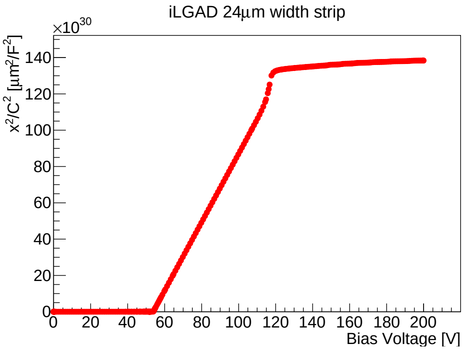

Figure 4.78: CV simulation for the p-on-p structure for a strip 24 µm width (AC3).

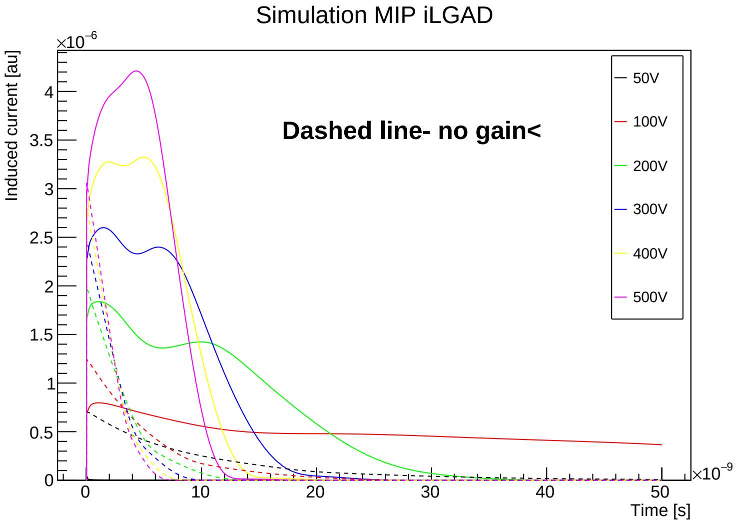

Figure 4.79: Simulation of MIP particles crossing the iLGAD center of the strip (solid lines) and the center of a PIN strip (dashed lines) at different voltages.

Figure 4.79 shows the induced current for a iLGAD detector of 48 µm width with and without gain for different bias voltages. The iLGAD show slow pulses although they have faster rise time.

Figure 4.80 shows the integration of the collected charge for a LGAD and an iLGAD (a n-on-p and p-on-p strip detector without gain, respectively) integrated during 50 ns. The MIP crosses the strip in the middle of the collecting electrode normalized to the charge collected.

Figure 4.81 shows the gain of a MIP particle crossing different positions of an iLGAD for 300 µm FZ silicon wafer. The simulated positions are the same as the ones in figure 4.74 for the LGAD. The gain is homogeneous through all the detector surface although the gain in the middle of the strip is slightly lower. Comparing the iLGAD charge collection with the LGAD in different positions (figure 4.74), the iLGAD shows more homogeneous gain along the surface than the LGAD.

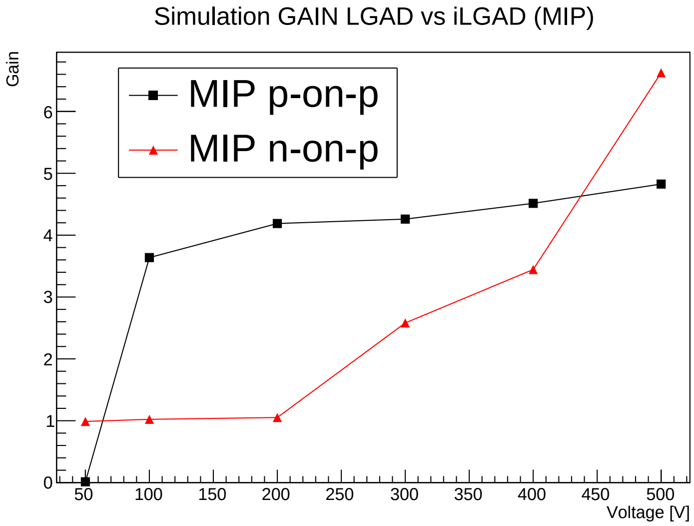

Figure 4.80: Simulation of gain for LGAD and iLGAD for a MIP particle passing through the middle of the central strip.

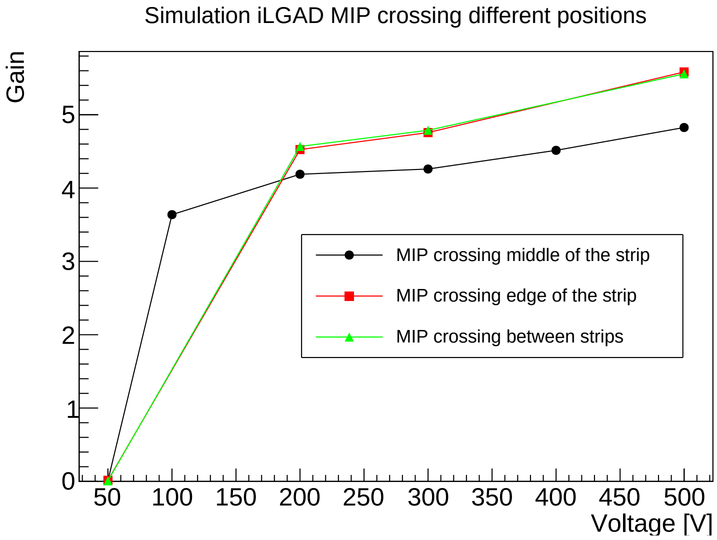

Figure 4.81: Simulation of gain for an iLGAD with a MIP passing through different positions of the strip (central of the strip, edge of the strip and between strips).

## 4.7 Conclusions and Future Work

The segmented LGAD fabricated on thin wafers are fully functional by the end of this work. Different detectors fabricated at CNM-Barcelona were characterized by their current-voltage curves, capacitance-voltage curves, charge collection, TCT and IBIC measurements. Some pixel detectors were bonded and measured among other groups in the RD50 CERN collaboration, such as the ones reported in [102]. The shallow doping profile presents a high leakage current, and usually those detectors were discarded for measurements. The standard doping profile shows an early break down, and the strips do not reach voltages higher than 160 V, which makes them difficult to measure since they are not fully depleted. The deep doping profile shows low leakage current and reaches high voltages before breakdown, anyway multiplication of the charge has achieved gain between 1 and 3.

The boron of the support wafer for detectors fabricated on 10 µm epitaxy diffused during the fabrication, decreasing the detector volume. 50 µm epitaxial wafers with deep doping profile showed good behaviour and the diodes showed gain of 2.5. Detectors fabricated on 75 µm epitaxial wafers were depleted at high voltage which made it difficult to measure at full depletion. FZ wafers showed good electrical behaviour and IBIC measurements confirmed that the detector have multiplication.

There are new ongoing fabrication projects with segmented LGAD detectors which shows moderate leakage current and high break down voltage. Those strip detectors present higher gain at low voltages.

iLGAD are a promising new design, although they are not radiation hard and will have applications such as medical PET, mass spectroscopy or particle tracking[86]. First fabrication of iLGAD detectors at CNM-Barcelona will be finished during the following months.

CHAPTER 5

# Conclusions

The next upgrades of the ATLAS experiments will have to cope with fluences up to $2 \times 10^{16}\,\mathrm{n_{eq}cm^{-2}}$ and higher occupancy detectors will be needed. This thesis developed two different possible advanced silicon detectors for the ATLAS experiment:

1. 3D detectors for the innermost pixel layer
2. LGAD detectors suitable for pixel or strip layers

Chapter 2 overviews the performance of 3D FE-I4 silicon fabricated at CNM detectors for IBL. Although the detectors show a good performance, the measurements of the electrical response (break down voltage and leakage current) for those detectors was not optimized and their measurements previous to flip chip was not very reliable. For the new fabrications, a temporary metal pad that will cover all the detector surface will give a more accurate measurement of the detector performance. Chapter 2 also covers the simulation of new 3D silicon detectors for the upcoming ATLAS upgrades, which will have smaller pixel size for the increasing ocupancy. CNM-Barcelona is working through a cryogenic DRIE in order to enhance the actual aspect ratio. The simulations of the new devices presents good performance after the expected maximum fluences of $2 \times 10^{16}\,\mathrm{n_{eq}\,cm^{-2}}$ for the next ATLAS upgrades. The next steps will be to fabricate those new structures and evaluate their performance under testbeams.

Chapter 3 reports the fabrication, electrical characterization, charge collection efficiency and TCT measurements of 3D 50 µm single sided detectors fabricated in low resistivity (100-500 Ω cm) SOI wafers. The reverse engineering images of those detectors show that the fabrication was performed as expected. Nevertheless, the electrical characterization shows that the pad diodes have a break down voltage at 80 V, before the detector reach the full depletion. The charge collection measurements show similar results and the laser TCT measurements shows a depleted radius at 70 V of $r_d = 36$ µm ±3 µm, which corresponds to a wafer resistivity of 150 Ω cm. Two diodes were irradiated with neutrons and they have a higher break down voltage and higher leakage current than the unirradiated device. The simulations of those structures show good agreement with the measurements.

Chapter 4 reports the device design, the fabrication, simulation, electrical characterization, TCT, IBIC and x-rays testbeam of segmented LGAD fabricated on epitaxial wafers (UFSD). The fabrication was performed in 4 different kind of wafers: 10 µm epitaxys, 50 µm epitaxys, 75 µm epitaxys and Float Zone (285 µm) and with three doping profiles: shallow, standard and deep.

During the fabrication, the low resistivity substrate diffused to the epitaxy, decreasing the volume of the wafers with 10 µm epitaxys to half. Detectors fabricated on 75 µm epitaxial wafers are not studied due to the high depletion voltage and the low break down voltage. Pad diodes fabricated on 50 µm epitaxial wafers show a multiplication up to 2.5 at 500 V although the strips presents a break down voltage before the detector is fully depleted. FZ wafers with deep doping profile presents good electrical response although the measured gain is 1.06, as shown in the measurements at the IBIC experiments and the testbeam at Diamond light source syncrothron testbeams. New LGAD fabrications with segmented detectors are being tested. The fabrication of the detectors with the inverted geometry (iLGAD) is ongoing and expected to be ready during the next months. Although iLGAD detectors are not radiation hard, they are promising candidates for timing applications when fabricated on thin wafers.

# Bibliography

[1] G. F. Knoll. Radiation Detection and Measurement. *Phoenix Usa*, 3:830, 2010.

[2] J. Kemmer. Fabrication of low noise silicon radiation detectors by the planar process. *Nuclear Instruments and Methods*, 169:499–502, 1980. ISSN 0029554X. doi: 10.1016/0029-554X(80)90948-9.

[3] F. Hartmann. Silicon tracking detectors in high-energy physics. *Nuclear Instruments and Methods in Physics Research Section A: Accelerators, Spectrometers, Detectors and Associated Equipment*, 666:25–46, February 2012. ISSN 01689002. doi: 10.1016/j.nima.2011.11.005. URL `http://linkinghub.elsevier.com/retrieve/pii/S0168900211020389`.

[4] http://www.imb-cnm.csic.es/.

[5] http://www.imb-cnm.csic.es/index.php/en/research/research-groups/radiation-detectors.

[6] G. Aad and et al. Combined Measurement of the Higgs Boson Mass in pp Collisions at $\sqrt{s}$=7 and 8 TeV with the ATLAS and CMS Experiments. *Physical Review Letters*, 114(19):1–33, 2015. doi: 10.1103/PhysRevLett.114.191803. URL `http://journals.aps.org/prl/pdf/10.1103/PhysRevLett.114.191803`.

[7] http://home.web.cern.ch/topics/large-hadron-collider, .

[8] C. Lippmann. Particle identification. *Nuclear Instruments and Methods in Physics Research Section A: Accelerators, Spectrometers, Detectors and Associated Equipment*, 666:148–172, February 2012. ISSN 01689002. doi: 10.1016/j.nima.2011.03.009. URL `http://linkinghub.elsevier.com/retrieve/pii/S0168900211005419`.

[9] http://atlas.ch/.

[10] http://www.atlas.ch/etours_exper/experiment-07.html.

[11] http://rd50.web.cern.ch/RD50/.

[12] C. Da Via, M. Boscardin, G. F. Dalla Betta, G. Darbo, C. Fleta, C. Gemme, P. Grenier, S. Grinstein, T. E. Hansen, J. Hasi, C. Kenney, A. Kok, S. Parker, G. Pellegrini, E. Vianello, and N. Zorzi. 3D silicon sensors: Design, large area production and quality assurance for the ATLAS IBL pixel detector upgrade. *Nuclear Instruments and Methods in Physics Research, Section A: Accelerators, Spectrometers, Detectors and Associated Equipment*, 694:321–330, 2012. ISSN 01689002. doi: 10.1016/j.nima.2012.07.058. URL `http://www.sciencedirect.com/science/article/pii/S0168900212008509`.

[13] http://perneg.web.cern.ch/perneg/IBL070514/html/index.html.

[14] S. M. Sze. *Semiconductor Devices: Physics and Technology*. John edition, 2006. ISBN 0471333727.

[15] L. Rossi, P. Fischer, T. Rohe, and N. Wermes. *Pixel Detectors*. Particle Acceleration and Detection. Springer-Verlag, Berlin/Heidelberg, 2006. ISBN 3-540-28332-3. doi: 10.1007/3-540-28333-1. URL `http://www.springerlink.com/index/10.1007/3-540-28333-1`.

[16] H. Spieler. *Semiconductor Detector Systems*. Oxford Science Publications, first edit edition, 2005. ISBN 0-19-852784-5 978-0-19-852784-8.

[17] G. Lutz. *Semiconductor radiation detectors*, volume 40. 1999. ISBN 3540648593. doi: 10.1049/sqj.1970.0033.

[18] P. Fernández-Martínez. *Diseño, Fabricación y Optimización de Detectores con Multiplicación (LGAD) para Experimentos de Física de Altas Energías*. PhD thesis, Universitat Autònoma de Barcelona, 2014.

[19] G. Pellegrini, P. Fernández-Martínez, M. Baselga, C. Fleta, D. Flores, V. Greco, S. Hidalgo, I. Mandić, G. Kramberger, D. Quirion, and M. Ullan. Technology developments and first measurements of Low Gain Avalanche Detectors (LGAD) for high energy physics applications. *Nuclear Instruments and Methods in Physics Research, Section A: Accelerators, Spectrometers, Detectors and Associated Equipment*, 765:12–16, 2014. ISSN 01689002.

doi: 10.1016/j.nima.2014.06.008. URL http://www.sciencedirect.com/science/article/pii/S0168900214007128.

[20] W. Shockley and W. T. Read. Statistics of the Recombination of Holes and Electrons. *Physical Review*, 87(46):835–842, 1952. ISSN 0031-899X. doi: dx.doi.org/10.1103/PhysRev.87.835. URL http://journals.aps.org/pr/abstract/10.1103/PhysRev.87.835.

[21] R. N. Hall. Electron-Hole recombination in Germanium. *Physical Review*, 87 (3):387, 1952. ISSN 0031899X. doi: 10.1103/PhysRev.175.823.

[22] W. R. Leo. *Techniques for Nuclear and Particle Physics Experiments*. Springer-Verlag, Würzburg, 1994.

[23] http://www.pveducation.org/pvcdrom/materials/optical-properties-of-silicon.

[24] K. Nakamura. REVIEW OF PARTICLE PHYSICS * Particle Data Group. *Physics*, 37(7A):075021, 2010. ISSN 09543899. doi: 10.1088/0954-3899/37/7A/075021. URL http://stacks.iop.org/0954-3899/37/i=7A/a=075021?key=crossref.de0390bfb70101fa23c6dbe588ea1324.

[25] H.-G. Moser. Silicon detector systems in high energy physics. *Progress in Particle and Nuclear Physics*, 63(1):186–237, July 2009. ISSN 01466410. doi: 10.1016/j.ppnp.2008.12.002. URL http://linkinghub.elsevier.com/retrieve/pii/S0146641008000951.

[26] http://cerncourier.com/cws/article/cern/49691, .

[27] S. I. Parker, C. J. Kenney, and J. Segal. 3D - A proposed new architecture for solid-state radiation detectors. *Nuclear Instruments and Methods in Physics Research, Section A: Accelerators, Spectrometers, Detectors and Associated Equipment*, 395(3):328–343, 1997. ISSN 01689002. doi: 10.1016/S0168-9002(97)00694-3. URL http://www.sciencedirect.com/science/article/pii/S0168900297006943.

[28] C. Kenney, S. Parker, J. Segal, and C. Storment. Silicon detectors with 3-D electrode arrays: Fabrication and initial test results. *IEEE Transactions on Nuclear Science*, 46(4 PART 3):1224–1236, 1999. ISSN 00189499. doi: 10.1109/23.785737. URL http://ieeexplore.ieee.org/xpl/login.jsp?

tp=&arnumber=785737&url=http%3A%2F%2Fieeexplore.ieee.org%2Fxpls%2Fabs_all.jsp%3Farnumber%3D785737.

[29] S. Ramo. Currents Induced by Electron Motion. *Proceedings of the IRE*, 27(9): 0–1, 1939. ISSN 0096-8390. doi: 10.1109/JRPROC.1939.228757. URL http://lartpc-docdb.fnal.gov/0005/000532/001/ramo_pire_27_584_39.pdf.

[30] M. Moll. *Radiation Damage in Silicon Detectors - microscopic defects and macroscopic properties -*. PhD thesis, University of Hamburg, 1999.

[31] I. Dawson and P. S. Miyagawa. ATLAS upgrade radiation background simulation. Sheffield University.

[32] C. Fleta Corral. *Tecnología de detectores de partículas de silicio resistentes a la radiación*. PhD thesis, 2006.

[33] J. P. Balbuena Valenzuela. *Development of innovative silicon radiation detectors*. PhD thesis, Universitat Autònoma de Barcelona, 2012.

[34] R. Radu, I. Pintilie, L. C. Nistor, E. Fretwurst, G. Lindstroem, and L. F. Makarenko. Investigation of point and extended defects in electron irradiated silicon—Dependence on the particle energy. *Journal of Applied Physics*, 117(16):164503, 2015. ISSN 0021-8979. doi: 10.1063/1.4918924. URL http://scitation.aip.org/content/aip/journal/jap/117/16/10.1063/1.4918924.

[35] M. Huhtinen. Simulation of non-ionising energy loss and defect formation in silicon. *Nuclear Instruments and Methods in Physics Research, Section A: Accelerators, Spectrometers, Detectors and Associated Equipment*, 491(1-2):194–215, 2002. ISSN 01689002. doi: 10.1016/S0168-9002(02)01227-5. URL http://www.sciencedirect.com/science/article/pii/S0168900202012275.

[36] G. Lindstroem, M. Moll, and E. Fretwurst. Radiation hardness of silicon detectors - a challenge from high-energy physics. *Nuclear Instruments and Methods in Physics Research, Section A: Accelerators, Spectrometers, Detectors and Associated Equipment*, 426(1):1–15, 1999. ISSN 01689002. doi: 10.1016/S0168-9002(98)01462-4. URL http://www.sciencedirect.com/science/article/pii/S0168900298014624.

[37] F. Hartmann. *Evolution of Silicon Sensor Technology in Particle Physics*. 2009. ISBN 0367-0325.

[38] V. A. J. van Lint, T. M. Flanagan, R. E. Leadon, J. A. Naber, and V. C. Rogers. *Mechanisms of radiation effects in electronic materials.* John Wiley & Sons, Inc., 1980.

[39] A. Vasilescu. Fluence normalization based on the NIEL scaling hypothesis. In *DESY-PROCEEDINGS*, page 2, 1998.

[40] G. Casse, A. Affolder, P. P. Allport, H. Brown, and M. Wormald. Enhanced efficiency of segmented silicon detectors of different thicknesses after proton irradiations up to 1x$10^{16} n_{eq}/cm^2$. *Nuclear Instruments and Methods in Physics Research, Section A: Accelerators, Spectrometers, Detectors and Associated Equipment*, 624(2):401–404, 2010. ISSN 01689002. doi: 10.1016/j.nima.2010.02.134. URL http://dx.doi.org/10.1016/j.nima.2010.02.134.

[41] M. Baselga. Radiation hard semiconductor devices for very high luminosity colliders. In *Vertex2015*, Santa Fe, 2015. Proceedings of Science. URL http://pos.sissa.it/archive/conferences/254/032/VERTEX2015_032.pdf.

[42] R. Wunstorf. *Systematische Untersuchungen zur Strahlenresistenz von Silizium-Detektoren für die Verwendung in Hochenergiephysik-Experimenten.* PhD thesis, DESY, 1992. URL http://www-library.desy.de/cgi-bin/showprep.pl?DESY-FH1K-92-01.

[43] I. Mandić, V. Cindro, A. Gorišek, G. Kramberger, M. Mikuž, and M. Zavrtanik. Observation of full charge collection efficiency in heavily irradiated n+p strip detectors irradiated up to 3x1015 neq/cm2. *Nuclear Instruments and Methods in Physics Research, Section A: Accelerators, Spectrometers, Detectors and Associated Equipment*, 612(3):474–477, 2010. ISSN 01689002. doi: 10.1016/j.nima.2009.08.004.

[44] M. Köhler, R. Bates, C. Fleta, K. Jakobs, M. Lozano, C. Parkes, U. Parzefall, G. Pellegrini, and J. Preiss. Comparative measurements of highly irradiated n-in-p and p-in-n 3D silicon strip detectors. *Nuclear Instruments and Methods in Physics Research, Section A: Accelerators, Spectrometers, Detectors and Associated Equipment*, 659(1):272–281, 2011. ISSN 01689002. doi: 10.1016/j.nima.2011.08.041.

[45] G. Casse, P. P. Allport, and A. Watson. Effects of accelerated annealing on p-type silicon micro-strip detectors after very high doses of proton irradiation.

*Nuclear Instruments and Methods in Physics Research, Section A: Accelerators, Spectrometers, Detectors and Associated Equipment*, 568(1):46–50, 2006. ISSN 01689002. doi: 10.1016/j.nima.2006.05.200.

[46] I. Pintilie, E. Fretwurst, and G. Lindstroem. Cluster related hole traps with enhanced-field-emission—the source for long term annealing in hadron irradiated Si diodes. *Applied Physics Letters*, 92(2):024101, 2008. ISSN 00036951. doi: 10.1063/1.2832646. URL `http://scitation.aip.org/content/aip/journal/apl/92/2/10.1063/1.2832646`.

[47] http://www.synopsys.com/tools/tcad/Pages/default.aspx.

[48] R. Escoffier, W. Fichtner, D. Fokkema, E. Lyumkis, O. Penzin, B. Polsky, A. Schenk, and B. Schmithüsen. *DESSIS 10.0 Manual*. 1996.

[49] Synopsys. *Sentaurus Device User Guide*. 2012.

[50] G. Masetti, M. Severi, and S. Solmi. Modeling of Carrier Mobility Against Carrier Concentration in Arsenic, Phosphorus, and Boron Doped Silicon. *IEEE Transactions on Electron Devices*, 30(7):764–769, 1983.

[51] R. Häcker and A. Hangleiter. Intrinsic upper limits of the carrier lifetime in silicon. *Journal of Applied Physics*, 75(11):7570–7572, 1994. ISSN 00218979. doi: 10.1063/1.356634.

[52] M. Petasecca, F. Moscatelli, D. Passeri, G.U. Pignatel, and C. Scarpello. Numerical simulation of radiation damage effects in p-type silicon detectors. *Nuclear Instruments and Methods in Physics Research Section A: Accelerators, Spectrometers, Detectors and Associated Equipment*, 563(1):192–195, 2006. ISSN 01689002. doi: 10.1016/j.nima.2006.01.093. URL `http://linkinghub.elsevier.com/retrieve/pii/S0168900206002166`.

[53] M. Petasecca, F. Moscatelli, D. Passeri, and G.U. Pignatel. Numerical simulation of radiation damage effects in p-type and n-type FZ silicon detectors. *IEEE Transactions on Nuclear Science*, 53(5):2971–2976, 2006. doi: 10.1109/TNS.2006.881910.

[54] D. Pennicard. *3D detectors for synchrotron applications*. PhD thesis, University of Glasgow, 2010. URL `http://theses.gla.ac.uk/694/`.

[55] M. Petasecca. Modeling radiation damage effects in oxygenated silicon detectors. CERN, 2006.

[56] B. Wu, A. Kumar, and S. Pamarthy. High aspect ratio silicon etch: A review. *Journal of Applied Physics*, 108(5), 2010. ISSN 00218979. doi: 10.1063/1.3474652. URL http://scitation.aip.org/content/aip/journal/jap/108/5/10.1063/1.3474652.

[57] RD53 Collaboration. RD Collaboration Proposal : Development of pixel readout integrated circuits for extreme rate and radiation. 2013. URL https://cds.cern.ch/record/1553467/files/LHCC-P-006.pdf.

[58] M. Capeans, T. Flick, R. Vuillermet, G. Darbo, H. Pernegger, K. Einsweiler, M. Garcia-Sciveres, M. Elsing, O. Rohne, and C. Gemme. ATLAS Insertable B-Layer Technical Design Report. (September), 2010. URL http://cds.cern.ch/record/1291633.

[59] G. Pellegrini, J. P. Balbuena, D. Bassignana, E. Cabruja, C. Fleta, C. Guardiola, M. Lozano, D. Quirion, and M. Ullán. 3D double sided detector fabrication at IMB-CNM. *Nuclear Instruments and Methods in Physics Research, Section A: Accelerators, Spectrometers, Detectors and Associated Equipment*, 699:27–30, 2013. ISSN 01689002. doi: 10.1016/j.nima.2012.05.087.

[60] G. Pellegrini, M. Lozano, M. Ullán, R. Bates, C. Fleta, and D. Pennicard. First double-sided 3-D detectors fabricated at CNM-IMB. *Nuclear Instruments and Methods in Physics Research Section A: Accelerators, Spectrometers, Detectors and Associated Equipment*, 592(1-2):38–43, July 2008. ISSN 01689002. doi: 10.1016/j.nima.2008.03.119. URL http://linkinghub.elsevier.com/retrieve/pii/S0168900208004828.

[61] http://www.izm.fraunhofer.de/en.html.

[62] ATLAS IBL Collaboration. Prototype ATLAS IBL modules using the FE-I4A front-end readout chip. *Journal of Instrumentation*, 7(11): P11010–P11010, 2012. ISSN 1748-0221. doi: 10.1088/1748-0221/7/11/P11010. URL http://stacks.iop.org/1748-0221/7/i=11/a=P11010?key=crossref.1607afc402756d2e7218f7327961358c.

[63] M. Backhaus. Characterization of new hybrid pixel module concepts for the ATLAS Insertable B-Layer upgrade. *Journal of Instrumentation*, 7(01): C01050–C01050, January 2012. ISSN 1748-0221. doi: 10.1088/1748-0221/7/01/C01050. URL http://stacks.iop.org/1748-0221/7/i=01/a=C01050?key=crossref.a18f5ca45638737d755e8eaebb611e38.

[64] I. Lopez. Experience with CNM 3D sensors for the ATLAS IBL Insertable B-Layer. In *9th Trento Workshop*, Genova, 2014. URL http://indico.cern.ch/event/273880/session/3/contribution/45/attachments/493716/682252/ILopez-trento-final.pdf.

[65] G. Darbo. Experience on 3D Silicon Sensors for ATLAS IBL. *Journal of Instrumentation*, 10:C05001, 2014. doi: 10.1088/1748-0221/10/05/C05001. URL http://arxiv.org/abs/1411.6937http://dx.doi.org/10.1088/1748-0221/10/05/C05001.

[66] ATLAS Collaboration. Cluster Properties and Lorentz Angle Measurement in the 4-Layer Pixel Detector Using Cosmic Rays. *ATLAS note*, (June): 1–8, 2015. URL https://preprints.cern.ch/record/2020918/files/ATL-COM-PHYS-2015-477.pdf.

[67] ATLAS Collaboration. ATLAS Letter of Intent Phase-I Upgrade. *Scientific Committee Paper*, 2011. URL http://cds.cern.ch/record/1402470/files/LHCC-I-020.pdf.

[68] G. Pellegrini, M. Baselga, M. Christophersen, S. Ely, V. Fadeyev, C. Fleta, A. Gimenez, S. Grinstein, I. Lopez, M. Lozano, A. Micelli, B. F. Phlips, D. Quirion, Sadrozinski, H.F.-W., and S. Tsiskaridze. Recent results on 3D double sided detectors with slim edges. *Nuclear Inst. and Methods in Physics Research, A*, 731:198–200, 2013. ISSN 0168-9002. doi: 10.1016/j.nima.2013.05.145. URL http://dx.doi.org/10.1016/j.nima.2013.05.145.

[69] I. Lopez, E. Cavallaro, S. Grinstein, J. Lange, and D. Vazquez. Recent testbeam results of 50um pitch 3D sensors at high incidence angle for HL-LHC. In *26th RD50 workshop*, Santander, 2015. URL https://indico.cern.ch/event/381195/session/1/contribution/20.

[70] G. Stewart, R. Bates, C. Fleta, G. Kramberger, M. Lozano, M. Milovanovic, and G. Pellegrini. Analysis of edge and surface TCTs for irradiated 3D silicon strip detectors. *Journal of Instrumentation*, 8(03): P03002–P03002, 2013. ISSN 1748-0221. doi: 10.1088/1748-0221/8/03/P03002. URL http://stacks.iop.org/1748-0221/8/i=03/a=P03002?key=crossref.7768f4d3b676ad926ab0196f553105c1.

[71] http://rd53.web.cern.ch/RD53/.

[72] S. Viel, S. Banerjee, G. Brandt, R. Carney, M. Garcia-Sciveres, A. S. Hard, L. S. Kaplan, L. Kashif, A. Pranko, J. Rieger, J. Wolf, S. L. Wu, and H. Yang. Performance of Silicon Pixel Detectors at Small Track Incidence Angles for the ATLAS Inner Tracker Upgrade. *Nuclear Instruments and Methods in Physics Research, Section A: Accelerators, Spectrometers, Detectors and Associated Equipment*, Article in Press, 2015.

[73] A. Macchiolo, R. Nisius, B. Paschen, and S. Terzo. Development of thin n-in-p pixel modules for the ATLAS upgrade at HL-LHC. In *10th International "Hiroshima" Symposium on the Development and Application of Semiconductor Tracking Detectors*, Xi'an, China, 2015.

[74] C. Fleta, C. Guardiola, S. Esteban, C. Jumilla, G. Pellegrini, D. Quirion, J. Rodríguez, A. Lousa, L. Martínez-de Olcoz, and M. Lozano. Erratum: Fabrication and nuclear reactor tests of ultra-thin 3D silicon neutron detectors with a boron carbide converter. *Journal of Instrumentation*, 9(05): E05001–E05001, 2014. ISSN 1748-0221. doi: 10.1088/1748-0221/9/05/E05001. URL http://stacks.iop.org/1748-0221/9/i=05/a=E05001?key=crossref.6ca241367b447ddfb2e268e4bd984b7f.

[75] F. García, G. Pellegrini, M. Lozano, J. P. Balbuena, C. Fleta, C. Guardiola, and D. Quirion. Ultra thin 3D silicon detector for plasma diagnostics at the ITER tokamak. *IEEE Nuclear Science Symposium Conference Record*, pages 199–201, 2012. ISSN 10957863. doi: 10.1109/NSSMIC.2011.6154479.

[76] L. T. Tran, D. A. Prokopovich, M. Petasecca, M. L. F. Lerch, C. Fleta, G. Pellegrini, C. Guardiola, M. I. Reinhard, and A. B. Rosenfeld. Ultra-Thin 3-D Detector : Charge Collection Characterization and Application for Microdosimetry. *IEEE Nuclear Science Symposium Conference Record*, 61(6):3472–3478, 2014.

[77] G. Pellegrini. *Technology Development of 3D Detectors for High Energy Physics and Medical Imaging*. PhD thesis, University of Glasgow, 2002.

[78] B. Birkenbach, B. Bruyneel, G. Pascovici, J. Eberth, H. Hess, D. Lersch, P. Reiter, and a. Wiens. Determination of space charge distributions in highly segmented large volume HPGe detectors from capacitancevoltage measurements. *Nuclear Instruments and Methods in Physics Research, Section A: Accelerators, Spectrometers, Detectors and Associated Equipment*, 640(1):

176–184, 2011. ISSN 01689002. doi: 10.1016/j.nima.2011.02.109. URL http://dx.doi.org/10.1016/j.nima.2011.02.109.

[79] B. Bruyneel, B. Birkenbach, and P. Reiter. Space charge reconstruction in highly segmented HPGe detectors through capacitance-voltage measurements. *Nuclear Instruments and Methods in Physics Research, Section A: Accelerators, Spectrometers, Detectors and Associated Equipment*, 641(1): 92–100, 2011. ISSN 01689002. doi: 10.1016/j.nima.2011.02.110. URL http://dx.doi.org/10.1016/j.nima.2011.02.110.

[80] G. Kramberger, M. Baselga, V. Cindro, P. Fernández-Martínez, D. Flores, Z. Galloway, A. Gorišek, V. Greco, S. Hidalgo, V. Fadeyev, I. Mandić, M. Mikuž, D. Quirion, G. Pellegrini, H.F-W. Sadrozinski, A. Studen, and M. Zavrtanik. Radiation effects in Low Gain Avalanche Detectors after hadron irradiations. *Journal of Instrumentation*, 10(07): P07006–P07006, 2015. ISSN 1748-0221. doi: 10.1088/1748-0221/10/07/P07006. URL http://stacks.iop.org/1748-0221/10/i=07/a=P07006?key=crossref.06fa9a7a22e1804bc316f2c2477f9aa7.

[81] http://www.ijs.si/ijsw/JSI.

[82] TRIGA Reactor, Jozef Stefan Institute, Jamova 39, 1000 Ljubljana, Slovenia. URL http://www.rcp.ijs.si/ric/index-a.htm.

[83] G. Kramberger, V. Cindro, I. Mandić, M. Mikuž, and M. Zavrtanik. Studies of initial acceptor removal in p-type silicon. In *26th RD50 workshop*, Genova, 2015. URL https://indico.cern.ch/event/381195/session/0/contribution/12.

[84] D. Pennicard, G. Pellegrini, C. Fleta, R. Bates, V. O'Shea, C. Parkes, and N. Tartoni. Simulations of radiation-damaged 3D detectors for the Super-LHC. *Nuclear Instruments and Methods in Physics Research Section A: Accelerators, Spectrometers, Detectors and Associated Equipment*, 592(1-2):16–25, 2008. ISSN 01689002. doi: 10.1016/j.nima.2008.03.100. URL http://linkinghub.elsevier.com/retrieve/pii/S0168900208004762.

[85] H.F.-W. Sadrozinski, A. Seiden, and N. Cartiglia. Ultra-Fast Silicon Detectors. In *20th RD50 Workshop*, Bari, 2012. URL https://indico.cern.ch/event/175330/session/8/contribution/18.

[86] H.F.-W. Sadrozinski, S. Ely, V. Fadeyev, Z. Galloway, J. Ngo, C. Parker, B. Petersen, A. Seiden, A. Zatserklyaniy, N. Cartiglia, F. Marchetto, M. Bruzzi, R. Mori, M. Scaringella, and A. Vinattieri. Ultra-fast silicon detectors. *Nuclear Instruments and Methods in Physics Research, Section A: Accelerators, Spectrometers, Detectors and Associated Equipment*, 730: 226–231, 2013. ISSN 01689002. doi: 10.1016/j.nima.2013.06.033. URL `http://dx.doi.org/10.1016/j.nima.2013.06.033`.

[87] N. Cartiglia, G. Dellacasa, S. Garbolino, F. Marchetto, G. Mazza, A. Rivetti, R. Arcidiacono, M. Obertino, V. Fadeyev, H.F-W. Sadrozinski, A. Seiden, N. Spencer, A. Zatserklyaniy, R. Bellan, F. Cenna, V. Monaco, A. Picerno, F. Ravera, R. Sacchi, A. Solano, G. Pellegrini, P. Fernández-Martínez, M. Baselga, V. Greco, S. Hidalgo, and D. Quirion. Timing Capabilities of Ultra-Fast Silicon Detectors. *Acta Physica Polonica B Proceedings Supplement*, 7(4):657, 2014. ISSN 1899-2358. doi: 10.5506/APhysPolBSupp.7.657. URL `http://www.scopus.com/inward/record.url?eid=2-s2.0-84910627213&partnerID=tZOtx3y1`.

[88] B. Jayant Baliga. *Fundamentals of Power Semiconductor Devices.* Springer, 2008. ISBN 9780387473147.

[89] S. Hidalgo, G. Pellegrini, D. Quirion, and M. Baselga. Simulation and Technology development of Low Gain Avalanche Detectors ( LGAD ) for High Energy Physics applications. In *22nd RD50 Workshop*, Albuquerque, 2013. URL `https://indico.cern.ch/event/209612/session/3/contribution/4/attachments/325744/454300/Gain_Diodes_RD50_New_Mexico_v6.pdf`.

[90] I. Cortés, P. Fernández-Martínez, D. Flores, S. Hidalgo, and J. Rebollo. Gain estimation of RT-APD devices by means of TCAD numerical simulations. In *Proceedings of the 8th Spanish Conference on Electron Devices, CDE'2011*, volume 2, pages 4–7, 2011. ISBN 9781424478637. doi: 10.1109/SCED.2011.5744152.

[91] H.F.-W. Sadrozinski, M. Baselga, S. Ely, V. Fadeyev, Z. Galloway, J. Ngo, C. Parker, D. Schumacher, A. Seiden, A. Zatserklyaniy, N. Cartiglia, G. Pellegrini, P. Fernández-Martínez, V. Greco, S. Hidalgo, and D. Quirion. Sensors for ultra-fast silicon detectors. *Nuclear Instruments and Methods in Physics Research Section A: Accelerators, Spectrometers, Detectors and Associated Equipment*, pages 1–5, May 2014. ISSN 01689002. doi: 10.1016/j.

nima.2014.05.006. URL `http://linkinghub.elsevier.com/retrieve/pii/S0168900214005051`.

[92] A. Khan, M. Yamaguchi, Y. Ohshita, N. Dharmaraso, K. Araki, V. T. Khanh, H. Itoh, T. Ohshima, M. Imaizumi, and S. Matsuda. Strategies for improving radiation tolerance of Si space solar cells. *Solar Energy Materials & Solar Cells*, 75(1/2):271, 2003. ISSN 09270248. doi: 10.1016/S0927-0248(02)00169-1. URL `http://www.sciencedirect.com/science/article/pii/S0927024802001691`.

[93] http://www.cadence.com/en/default.aspx.

[94] Synopsys. *Sentaurus* $^{TM}$ *Process User Guide*. Number December. 2012.

[95] N. Demaria, S. Albergo, M. Angarano, P. Azzi, E. Babucci, N. Bacchetta, A. Bader, G. Bagliesi, A. Basti, U. Biggeri, G.M. Bilei, D. Bisello, D. Boemi, G. Bolla, F. Bosi, L. Borrello, D. Bortoletto, C. Bozzi, S. Braibant, H. Breuker, M. Bruzzi, A. Buffini, S. Busoni, A. Candelori, A. Caner, R. Castaldi, A. Castro, E. Catacchini, B. Checcucci, P. Ciampolini, C. Civinini, D. Creanza, R. D'Alessandro, M.Da Rold, M. de Palma, R. Dell'Orso, R.Della Marina, S. Dutta, C. Eklund, A. Elliott-Peisert, G. Favro, L. Feld, L. Fiore, E. Focardi, M. French, K. Freudenreich, A. Fürtjes, A. Giassi, M. Giorgi, A. Giraldo, B. Glessing, W.H. Gu, G. Hall, R. Hammerstrom, T. Hebbeker, J. Hrubec, M. Huhtinen, A. Kaminsky, V. Karimaki, St. Koenig, M. Krammer, P. Lariccia, M. Lenzi, M. Loreti, K. Luebelsmeyer, W. Lustermann, P. Mättig, G. Maggi, M. Mannelli, G. Mantovani, A. Marchioro, C. Mariotti, G. Martignon, B.Mc Evoy, M. Meschini, A. Messineo, E. Migliore, S. My, A. Paccagnella, F. Palla, D. Pandoulas, A. Papi, G. Parrini, D. Passeri, M. Pieri, S. Piperov, R. Potenza, V. Radicci, F. Raffaelli, M. Raymond, A. Santocchia, B. Schmitt, G. Selvaggi, L. Servoli, G. Sguazzoni, R. Siedling, L. Silvestris, K. Skog, A. Starodumov, I. Stavitski, G. Stefanini, P. Tempesta, G. Tonelli, A. Tricomi, T. Tuuva, C. Vannini, P.G. Verdini, G. Viertel, Z. Xie, Li Yahong, S. Watts, and B. Wittmer. New results on silicon microstrip detectors of CMS tracker. *Nuclear Instruments and Methods in Physics Research Section A: Accelerators, Spectrometers, Detectors and Associated Equipment*, 447(1-2):142–150, 2000. ISSN 01689002. doi: 10.1016/S0168-9002(00)00182-0. URL `http://www.sciencedirect.com/science/article/pii/S0168900200001820`.

[96] S. Lindgren, C. Betancourt, A. Chilingarov, N. Dawson, V. Fadeyev, H. Fox, K. Hara, H. Hatano, T. Kohriki, Y. Ikegami, S. Mitsui, H. F W Sadrozinski, S. Terada, Y. Unno, J. Wright, and M. Yamada. Interstrip characteristics of n-on-p FZ silicon detectors. *IEEE Nuclear Science Symposium Conference Record*, pages 157–162, 2009. ISSN 10957863. doi: 10.1109/NSSMIC.2009.5401828.

[97] N. Cartiglia, R. Arcidiacono, M. Baselga, R. Bellan, M. Boscardin, F. Cenna, G.F. Dalla Betta, P. Fernández-Martínez, M. Ferrero, D. Flores, Z. Galloway, V. Greco, S. Hidalgo, F. Marchetto, V. Monaco, M. Obertino, L. Pancheri, G. Paternoster, A. Picerno, G. Pellegrini, D. Quirion, F. Ravera, R. Sacchi, H.F.-W. Sadrozinski, A. Seiden, A. Solano, and N. Spencer. Design optimization of ultra-fast silicon detectors. *Nuclear Instruments and Methods in Physics Research Section A: Accelerators, Spectrometers, Detectors and Associated Equipment*, 796:141–148, 2015. ISSN 01689002. doi: 10.1016/j.nima.2015.04.025. URL `http://linkinghub.elsevier.com/retrieve/pii/S0168900215004982`.

[98] http://www.diamond.ac.uk/Home.html. .

[99] R. Marco-Hernández. A Portable Readout System for Microstrip Silicon Sensors (ALIBAVA). *IEEE Transactions on Nuclear Science*, 56(3):1–8, 2009.

[100] J. H. Hubbell and S. M. Seltzer. Tables of X-Ray Mass Attenuation Coefficients and Mass Energy-Absorption Coefficients from 1 keV to 20 MeV for Elements Z = 1 to 92 and 48 Additional Substances of Dosimetric Interest. *NIST*, 1996. URL `http://www.nist.gov/pml/data/xraycoef/`.

[101] http://www.diamond.ac.uk/Beamlines/Materials/B16/status.html. .

[102] E. Cavallaro, J. Lange, I. Lopez Paz, S. Grinstein, M. Baselga, V. Greco, D. Quirion, and G. Pellegrini. First measurements of segmented silicon tracking detectors with built-in multiplication layer. *Nuclear Instruments and Methods in Physics Research Section A: Accelerators, Spectrometers, Detectors and Associated Equipment*, 796:136–140, 2015. ISSN 01689002. doi: 10.1016/j.nima.2015.05.023. URL `http://linkinghub.elsevier.com/retrieve/pii/S0168900215006336`.

[103] C. Betancourt, K. Jakobs, S. Kühn, K. Lohwasser, R. Mori, U. Parzefall, A. Hasenfratz, and M. M. Hauser. An investigation on the charge collection reduction of silicon sensor. In *10th RESMDD*, Florence, 2014.

[104] http://acdc.sav.us.es/cna/.

[105] M. B. H. Breese, E. Vittone, G. Vizkelethy, and P. J. Sellin. A review of ion beam induced charge microscopy. *Nuclear Instruments and Methods in Physics Research, Section B: Beam Interactions with Materials and Atoms*, 264(2):345–360, 2007. ISSN 0168583X. doi: 10.1016/j.nimb.2007.09.031.

[106] http://www.srim.org/.

[107] http://geant4.web.cern.ch/geant4/.

[108] S. Hidalgo. New iLGAD detector development at CNM. In *26th RD50 workshop*, Santander, 2015. URL `https://indico.cern.ch/event/381195/session/2/contribution/3`.

[109] G. Pellegrini, M. Baselga, M. Carulla, V. Fadeyev, P. Fernández-Martínez, D. Flores, Z. Galloway, S. Hidalgo, Z. Liang, A. Merlos, M. Moll, D. Quirion, H.F.-W. Sadrozinski, M. Stricker, and I. Vila. Recent Technological Developments on LGAD and iLGAD Detectors for Tracking and Timing Applications. *Nuclear Instruments and Methods in Physics Research Section A: Accelerators, Spectrometers, Detectors and Associated Equipment*, Article in press.

[110] H.F.-W. Sadrozinski, A. Anker, J. Chen, V. Fadeyev, P. Freeman, Z. Galloway, B. Gruey, H. Grabas, C. John, Z. Liang, R. Losakul, S. N. Mak, C. W. Ng, A. Seiden, N. Woods, A. Zatserklyaniy, B. Baldassarri, N. Cartiglia, F. Cenna, M. Ferrero, G. Pellegrini, S. Hidalgo, M. Baselga, M. Carulla, P. Fernández-Martínez, D. Flores, A. Merlos, D. Quirion, M. Mikuz, G. Kramberger, V. Cindro, I. Mandic, and M. Zavrtanik. Ultra-Fast Silicon Detectors (UFSD). *Nuclear Instruments and Methods in Physics Research Section A: Accelerators, Spectrometers, Detectors and Associated Equipment*, Article in press.

# Resum en català

Aquesta tesi tracta el desenvolupament de detectors de silici de tecnologia avançada per experiments de Física d'Altes Energies (HEP en anglès). La mida dels detectors de silici per determinar traces en experiments de HEP ha de disminuïr per millorar la resolució espacial en les mesures i millorar l'ocupancia en l'electrònica. Els experiments al CERN hauran de funcionar amb fluencies de fins a $2 \times 10^{16}\,\mathrm{n_{eq}/cm^2}$, i els detectors de silici més petits tindran menys atrapament de les parelles electró-forat generats al volum, que porta a un millor comportament sota un medi amb alts nivells de radiació.

Aquesta tesi estudia detectors de silici fabricats al CNM-Barcelona per aplicacions de HEP amb dos tipus d'arquitectura nou: 3D i detectors d'allau amb guany moderat (LGAD en anglès). Els detectors 3D afavoreixen la reducció de la mida de la regió buidada dins del detector i permet treballar a voltatges més baixos, mentres que els detectors LGAD tenen guany intern que incrementa la senyal col·leccionada amb un mecanisme de multiplicació.

El capítol 1 introdueix els detectors de silici aplicats a HEP. Els capítols 2 i 3 exploren els dissenys de detectors 3D de silici fabricats al CNM-Barcelona. Els detectors 3D de silici van ser introduïts per primera vegada a un experiment de HEP durant el 2013 per una nova capa del experiment ATLAS, la Insertable B-Layer (IBL), i alguns d'aquests detectors han sigut caracteritzats durant aquest treball. Actualment, detectors 3D de silici amb dimensions de píxel més petites seran operatius per noves posades a punt de l'ATLAS, i aquests detectors s'han simulat en aquest treball. El capítol 4 està dedicat a detectors LGAD segmentats i fabricats en oblies epitaxials amb la intenció de disminuïr el gruix dels detectors i augmentar la càrrega col·leccionada amb el mecanisme de multiplicació. Aquesta tesi mostra simulacions tecnològiques, el procés de fabricació, simulació elèctrica i caracterització elèctrica i de càrrega d'aquests detectors.

# List of Figures

# List of Tables